DOCTOR OF PHILOSOPHY

Seismic performance of pile-reinforced slopes

Al-Defae, Asad Hafudh Humaish

Award date:
2013

DOCTOR OF PHILOSOPHY

Seismic performance of pile-reinforced slopes

Asad Hafudh Humaish Al-Defae

2013

University of Dundee

College of Art, Science & Engineering
School of Engineering, Physics and Mathematics
Department of Civil Engineering

Seismic performance of pile-reinforced slopes

By:
Asad Hafudh Humaish Al-Defae

A dissertation submitted for the
Degree of Doctor of Philosophy
University of Dundee
September, 2013

To the souls of all those who have fallen because of terrorism in the world and particularly in my country, Iraq

Declaration

This is to certify that, except where specific reference to other investigation is made, the work described in this thesis is entirely my own work. None of this work has been previously submitted for any other degree at this or any other university.

Asad Hafudh Humaish Al-Defae (Candidate), Dundee, (/ /2013)

Dr Jonathan A. Knappett (Supervisor), Dundee, (/ /2013)

Acknowledgements

I am extremely grateful to my supervisor Jonathan A. Knappett for his help, encouragement and patience throughout this period of research. I have been extremely fortunate to have had a supervisor who, without his enormous knowledge, would not have made this possible and who always made the time and effort to respond to my queries. Under his supervision and teachings, I have improved as researcher and gained new insight.

Thanks also go to other members of the technical staff at University of Dundee, starting from their manager, Dr. Gary Callon, Mark Truswell, Chris Walker, Grant Kydd, Willie Henderson, Mike McKernie, John Anderson, Dave Ritchie, Colin Stark and others. Thank you all for your help, encouragement, and for simply making my time here doing a PhD a more interesting experience.

I would like also to acknowledge the financial supporter of my PhD studies from the Ministry of Higher Education and Scientific Research (MOHESR) of my country, the Republic of Iraq and special thanks to my University, Wasit University.

Finally, I will not forget to thank my father, my mother, all my brothers and my sister, who made me more insistent when I hear their voice via mobile.

Special thanks also to my wife, Nagham who has stood beside me and shouldered the burden of my children, Safa, Mustafa and Zainab during this critical period.

Abstract

Shallow embankment slopes are commonly used to support elements of transport infrastructure in seismic regions. In this thesis, the seismic performance of such slopes in non-liquefiable granular soils has been investigated and an extensive programme of centrifuge testing was conducted to quantify the improvements to seismic slope performance which can be achieved by installing a row of discretely spaced vertical precast concrete piles. This study focussed on permanent movement and dynamic response at different positions within the slope, especially at the crest, which would form key inputs into the aseismic design of supported infrastructure. In contrast to previous studies, the evolution of this behaviour under multiple sequential strong ground motions is studied through dynamic centrifuge modelling, analytical (sliding-block) and numerical (Finite Element) models. This thesis makes three major contributions.

Firstly, an improved sliding-block ('Newmark') approach is developed for estimating permanent deformations of unreinforced slopes during preliminary design phases, in which the formulation of the yield acceleration is fully strain-dependent, incorporating the effects of both material hardening/softening and geometric hardening (re-grading). This is supported by the development of numerical (Finite Element) models which can additionally predict the settlement profile at the crest of the slope and also the dynamic ground motions at this point, for detailed seismic design were also developed. It is shown that these new models considerably outperform existing state-of-the art models which do not incorporate the geometric changes for the case of an earthquake on a virgin slope. It is further shown that only the improved models can correctly capture the behaviour under further earthquakes (e.g. strong aftershocks) and therefore can be used to determine the whole-life performance of a slope under a suite of representative ground motions that the slope may see during its design life, and allow improved estimates of the seismic performance of slopes beyond their design life. The finite element models can accurately replicate the settlement profile at the crest (important for highway or rail infrastructure) and quantify the dynamic motions which would be input to supported structures, though these were generally over-predicted.

Secondly, the principles of physical modelling have been used to produce realistically damageable model piles using a new model reinforced

concrete (both a designed section specifically detailed to carry the bending moments induced by the slipping soil mass and a nominally reinforced section with low moment capacity). This was used to investigate how piles can stabilise slopes under earthquake events and how the permanent deformation and the dynamic response of stabilised slope are strongly influenced by the pile spacing (S/B) especially at the minimum pile spacing (i.e. S/B=3.5). This is consistent with previous suggestions made for the optimal S/B ratio for encouraging soil arching between piles at maximum spacing both under monotonic conditions, and for numerical investigations of the seismic problem. These were supported by further centrifuge tests on conventional 'elastic' piles which were instrumented to measure seismic soil-pile interaction. The importance of reinforcement detailing was also highlighted, with the nominally reinforced section yielding early in the earthquake; the damaged piles subsequently only offer a small (though measureable) reduction in seismic slope performance compared to the unreinforced case. It was demonstrated that both permanent deformations at the slope crest (e.g. settlement) and dynamic ground motions at the crest can be significantly reduced as pile spacing reduced.

Finally, a coupled P-y and elastic continuum approach for modelling soil-pile interaction has been used to develop a Newmark procedure applicable for pile-reinforced slopes. It was observed that the single pile resistance is mobilising at beginning of the earthquake's time and it is strongly influenced by pile stiffness properties, pile spacing and the depth of the slip surface. It was observed also that the depth of the slip surface and pile spacing (S/B) play an important role in the determination of the permanent deformation of the slope. The results show great agreement to centrifuge test data in term of the permanent deformation (settlement at the crest of the slope) with slight differences between the measured (centrifuge) and calculated (this procedure) maximum bending moments.

Notations and abbreviations

A_c	Cross sectional area of concrete section
A_{red}	Acceleration reduction factor
A_s	Cross sectional area of steel section
a	Ground acceleration
a^*	Centrifuge acceleration
a_g	Underlying bedrock peak acceleration
a_{slip}	Slip acceleration
B	Width of soil model
b	Width of section
CN	Cyanoacrylate adhesive
C_k	Stiffness-proportional Rayleigh damping coefficient
C_m	Mass-proportional Rayleigh damping coefficient
c'	Effective cohesion parameter
c_u	Uniformity Coefficient
c_z	Coefficient of curvature
D_b	Longitudinal bar diameter
DAQ	Data acquisition system
D_{eq}	Equivalent pile diameter
D_{10}	Particle diameter at which 10% passing soil
D_{30}	Particle diameter at which 30% passing soil
D_{60}	Particle diameter at which 60% passing soil
d	Slope parallel slip
d_i	Instantaneous slip of unstable soil
E_c	Young's modulus of concrete
E_{oed}	Tangent stiffness for oedometer
E_s	Young's modulus of steel
E_{ur}	Unloading/reloading stiffness

EI	Pile bending stiffness
$EI_{elastic}$	Pre-earthquake bending stiffness
EI_{res}	Residual bending stiffness
E_{50}	Secant stiffness in drained triaxial test
e_o	Natural void ratio
e_{max}	Maximum void ratio
e_{min}	Minimum void ratio
FS	Factor of safety
$f_{c_{100}}$	The compressive strength of concrete for 100x100mm cube
$f_{c_{150}}$	The compressive strength of concrete for 150x150mm cube
f'_c	The concrete compressive strength
f_{cu}	Concrete compressive
f_r	Rupture modulus
f_n	Natural frequency
f_y	Yield strength for concrete
G	Shear modulus
G_c	Average shear modulus
G_o	Small strain modulus
G_o^{ref}	Small strain stiffness
G_s	Specific gravity
g	Gravity acceleration
H	Slope height above toe
$HST95$	Congleton silica sand
I_D	Relative density
K_o	Earth pressure at rest condition
K_a	Active earth pressure
k	Initial subgrade reaction
kd	Un-cracked depth

k_h	Pseudo-static seismic horizontal acceleration (g)
k_{hy}	Yield acceleration (g)
K_p	Passive earth pressure
L	Length of soil model
L_c	Critical length of pile
L_i	Instantaneous slope plane length
$LVDT$	Linear variable differential transformer
M	Soil mass
M_{max}	Maximum induced moment in the pile
M_p	Plastic moment resistance
M_{res}	Normalised residual moment capacity
M_{ult}	Ultimate pile moment capacity
M_y	Pre-earthquake measured moment capacity
m	Power law index for stress level dependency of stiffness
$N-1$	Coating of Neoprene rubber
P	Single pile resistance
P_m	Force multiplier
P_u	Ultimate soil resistance
p_{ref}	Reference stress (= 100 kPa)
PGA	Peak ground acceleration (at soil surface)
SPI	Soil-pile interaction
PSD	Particle size distribution
R	Radius of centrifuge to the base of the model
R_f	Ratio of deviatoric failure stress to asymptotic limiting deviator stress
r	Effective radius of centrifuge
r_d	Stress reduction coefficient
S	Soil factor (Eurocode 8)

S_{red}	Spectral reduction factor
S_T	Topographic amplification factor
S/B	Pile spacing ratio
T	Natural period
t	Shear band thickness
u	Pore water pressure
V_u	Flexural shear capacity
Y_{red}	Yield acceleration reduction factor
y_p	Lateral pile displacement
y_r	Reinforced crest settlement
y_u	Unreinforced crest settlement
z	Depth of slip plane
Δ_u	Ultimate displacement
Δ_y	Yield displacement
α	Inclination angle of the container to keep the resultant acceleration perpendicular to the model
β	Slope angle
θ	Angular distortion
β_0	Initial slope angle (pre-earthquake)
γ	Soil unit weight
γ_d	Dry unit weight
γ_{sat}	Saturated unit weight
δ	Interface friction angle
ε_c	Strain of concrete
ε_s	Strain of steel
$\varepsilon_{s,pk}$	Shear strain at peak state
$\varepsilon_{s,cs}$	Shear strain at critical state
η	Modular ratio for concrete section

κ	Curvature
μ	Displacement ductility
v_{ur}	Poisson ratio (unload/reload)
ς_{add}	Viscous damping ration
ρ	Soil density
ρ_c	Homogeneity factor
σ'	Normal effective stress
$\tau_{applied}$	Applied shear stress
τ_{ult}	Shear strength
φ'	Ground acceleration
φ'_{cs}	Critical effective angle of friction
φ'_{pk}	(Secant) Peak angle of friction
ψ'	Effective angle of dilation
ω	Angular velocity

Table of Contents

List of Figures

List of tables

Chapter One
Introduction

1.1 Preface

Earthquakes are natural disasters that engineers should take into consideration in the design criteria of any infrastructure project more than any other disaster in seismic areas. Many landslides caused by earthquakes have been observed in the world such as in China (Wenchuan earthquake 2008), Taiwan (Chi-Chi earthquake 1999) and in Japan (Niigata earthquake 2005), Figures (1-1) and (1-2) whereas more than 5000 people were died and 300,000 became homeless after a very short earthquake (20 sec only) in Kobe 1995. Also, the largest earthquake in March 2011 in Japan causes many landslides (www.geogonline.org.uk) (Figures 1-2 and 1-3).

Figure (1- 1): Cross section of slope failure during Wenchuan Earthquake in china (Yin, 2009)

Figure (1- 2): Landsliding during the recent large earthquakes in Japan 2011 (www.geogonline.org.uk)

Figure (1- 3): Landslide observation by USGS team (USGS webpage)

In some of these earthquakes, villages have been buried under soil due to slope failure. An example of such a big landslide occurred on 13 of January 2001 when an earthquake triggered more than 500 landslides across EI-Salvador. As many as 500 people were buried and one hundred thousand houses were fully destroyed under the collapsed soil and sudden landslide (Jibson and Corne, 2001). Figure (1-4) shows how the landslide buried tens of houses of the village.

Figure (1- 4): Landslide due to EI-Salvador earthquake, 2001 (USGS)

Earthquake-induced landslides have caused a massive amount of damage in the world and these landslides, many times, have been responsible for more damage than the combined effects of all other seismic hazards. Billions of dollars have been lost because of earthquake damage during the last few decades. More than 50% of the total cost of damage was caused by landslides in the 1964 Alaska earthquake (Wilson and Keefer, 1985). Kobayashi (1981) showed that more than half of the fatalities due to earthquakes in Japan between 1964 and 1980 were caused by landslides. Investigation of seismic slope stability can be classified as one of the most important activities for geotechnical earthquake engineers (Kramer, 1996). Keefer (1984) suggested that the landslide type depends on the distance of the slope to the fault and the epicentre of the earthquake (Figure 1-5) and that the area affected by earthquake-induced landsliding also increases with increasing earthquake magnitude Figure (1-6)

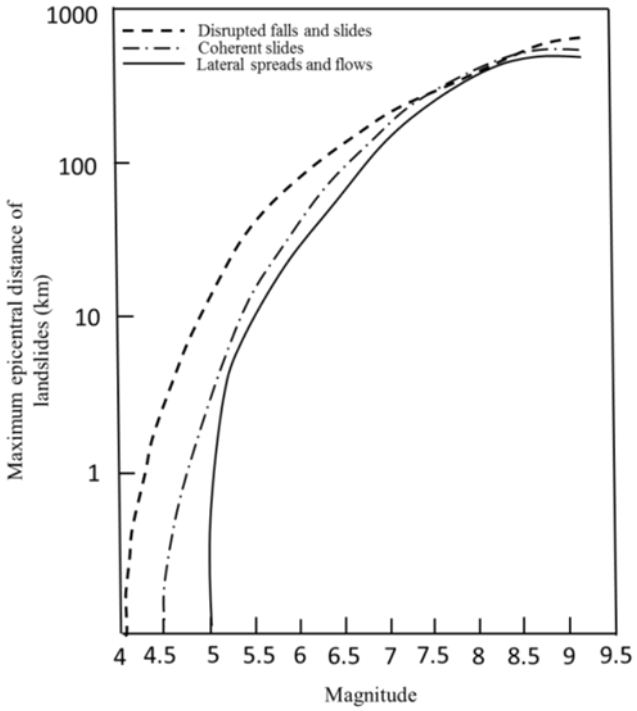

Figure (1- 5): Maximum epicentral distance for different kinds of landslides (Keefer, 1984)

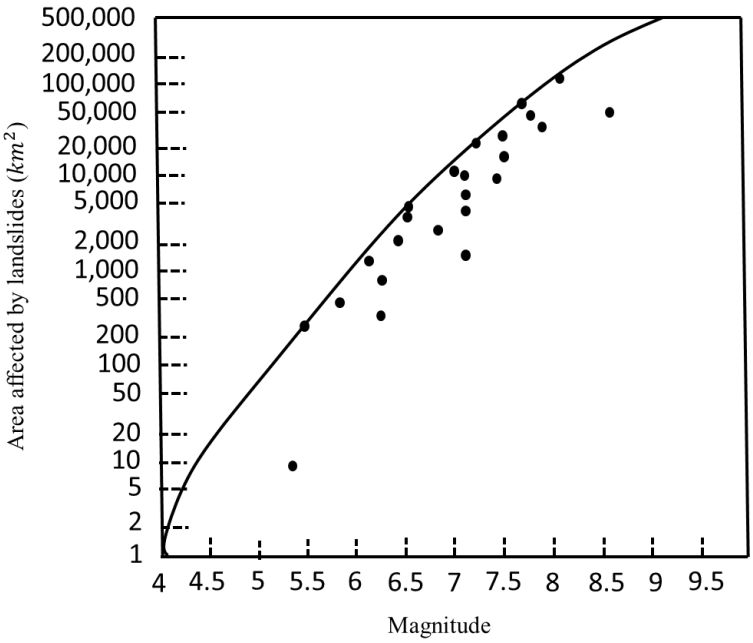

Figure (1- 6): Area affected by landslides for earthquakes of different (Keefer, 1984)

Slope remediation using piles has become an increasingly common technique around the world over the last two decades to reduce soil movement in the down slope direction. The lateral forces applied to the pile face generate bending moment along it

and lead to pile head displacement. Bending of the piles will not prevent the slope from moving, but it will reduce the size of these movements and potentially prevent a sudden collapse, provided that the piles do not fail structurally under the induced bending moments.

Due to the development of centrifuge techniques in the last two decades, many physical studies of slope problems have been conducted to study the seismic performance of slopes (and soil-pile interaction as a special case) and other related problems resulting from earthquakes in general (e.g Yu-Zhen et al., 2008). There is still not enough understanding of the problems of slope failure during real earthquakes because many of the previous researchers (e.g. Ng et al., 2004; Madabhushi et al., 2002; and Hayashi et al., 1998) used harmonic waves as input motions with a constant frequency and amplitude. This research aims to address these issues by studying the performance of unreinforced and pile-reinforced slopes using centrifuge modelling, applying predominantly real-earthquake motions, and realistically modelling the structural behaviour of the piles.

1.2 Types of landslides and slopes failure

'Landslide' is a term that refers to any sudden movement of a soil mass downward whether the soil is clayey, sandy, silty or rocky or a combination of them. Most slope failures occur in mountainous regions, but also occur as cut and fill failure (e.g. in the case of highways, building excavations and electrical pylons). Landslides occur also when there is a weak zone that separates weak surface material from more stable strata underlying it. In the United Kingdom in 1966, a flow slide from a colliery spoil tip travelled down the valley side directly above the village of Aberfan in Wales at an average speed of about 16 km/hour and destroyed a primary school and led to death 144 pupils in addition to five of their teachers. Many major landslides in the world occurred during the last century, for example: London highway landslide in 1970, San Luis dam slide 1981, Olmsted dam Land slide in Ohio 1988 and Panama Canal Landslides in 1986 (Duncan and Wright, 2005).

There are two major kinds of slope failure, rotational failure and translational failure which are explained below:

-**Rotational slide**: in this type of slide, the soil mass movement occurs rotationally about a point representing the centre of an arc; see Figure (1-7a). This type is also known as a deep slide and is most widely seen in cohesive soils.

-**Translational slide**: this is a slide in which the soil mass moves as a planar surface parallel to the slope surface with little or no rotation; see Figure (1-7b).

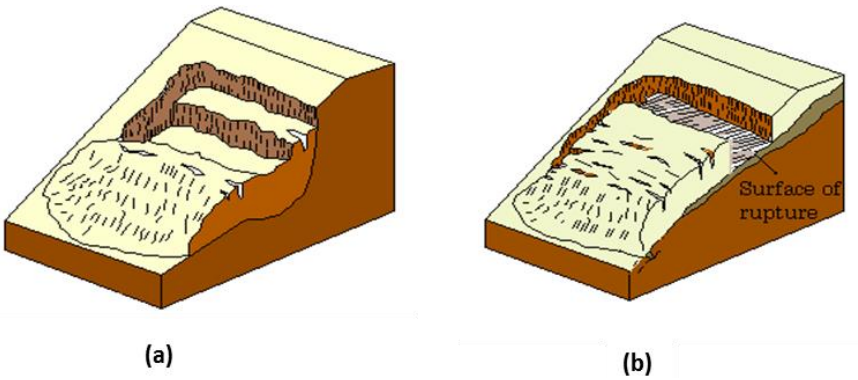

Figure (1- 7): The main types of Slope failure; (a) Rotational Slip; (b) Translational slip

There are also other types of slope failure, including Creep failure, toppling, rock fall, debris flow and lateral spreading. All these types of failure are shown in Figure (1-8) and can be summarized below:

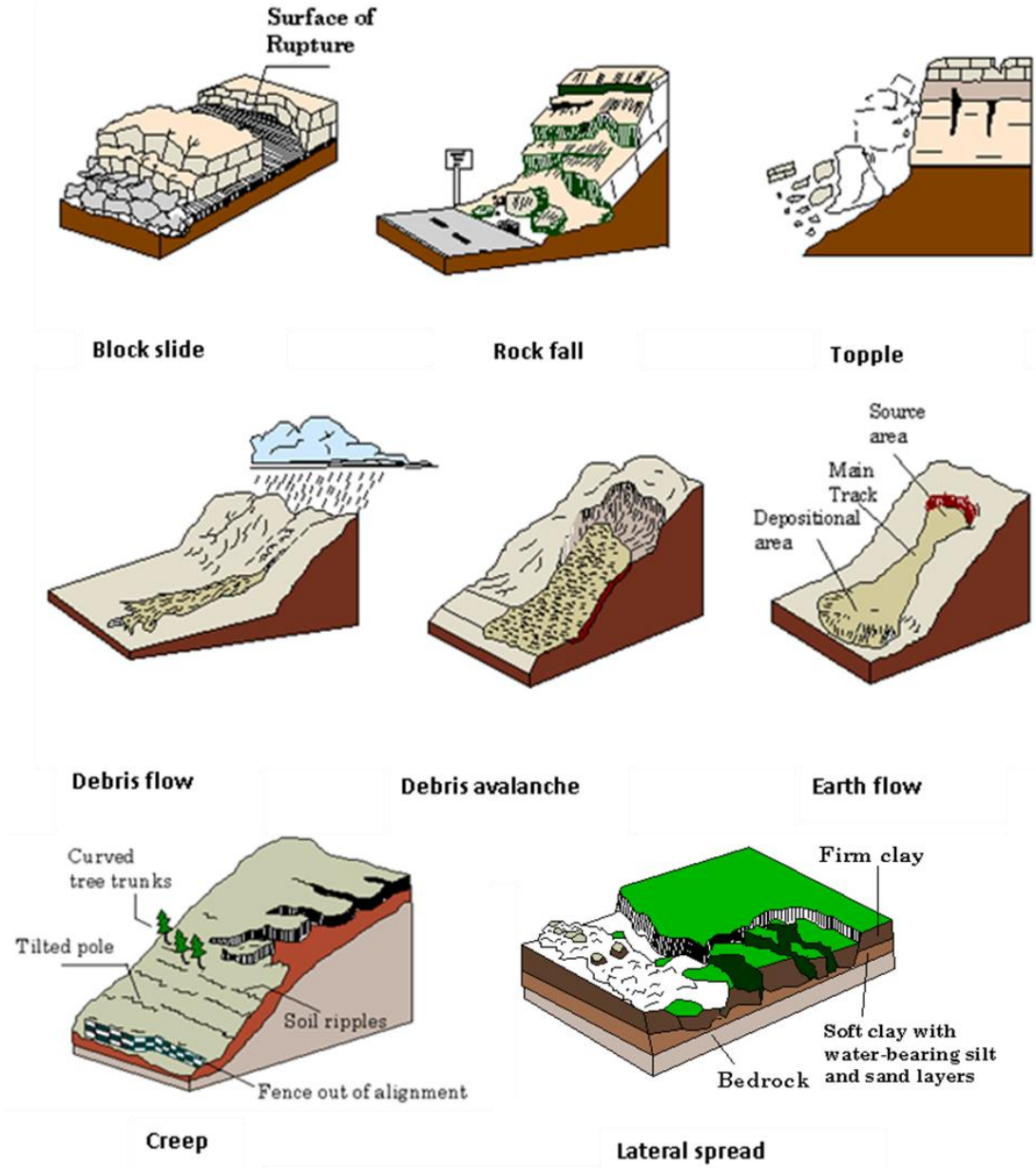

Figure (1- 8): Slope failure modes (redrawing from USGS factsheet)

- *Falls*: Due to sudden movement and geological changes and erosion, rocks and boulders may fall from steep slopes. Falls may also be induced by gravity, mechanical weathering and water dissipation into clefts.
- *Topples*: Occur due to the action of gravity or forces exerted by adjacent units of soil or by water in cracks.
- *Flows:* there are many categories of flows such as debris flow, debris avalanche, earth flow and creep.
- *Lateral spreads*: Usually occur in very gentle slopes or near-flat terrain due to soil liquefaction.

1.3 Statement of problem

Slope stabilisation methods are varied and dependent on many factors including the angle of the slope, soil material type and variation of water table during seasons, amongst others. Installing piles in a sloping soil mass is a frequently used technique under non-seismic conditions. Use of a single row of piles to resist slope failure due to seismic shaking is shown schematically in Figure (1-9). Many important factors should be taken into account by geotechnical engineers, namely: (1) the size of the piles and their structural detailing/properties; (2) spacing between piles (max. spacing between piles for best soil arching at minimum cost); (3) embedded pile length into the stable soil; (4) location of piles with respect to the slope toe or crest; (5) the forces affecting the piles due to the moving mass so that the structural design of piles can meet the capacity requirements.

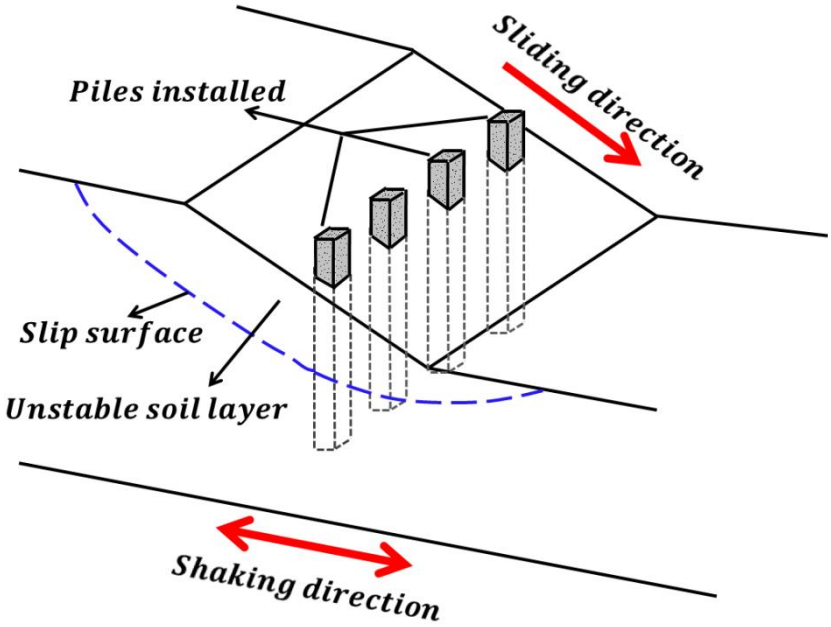

Figure (1- 9): Statement of problem

In seismic geotechnical problems, most of the previous studies of pile stabilization of slopes do not provide full understanding due to many of the idealizing assumptions made by previous researchers. The analysis of seismic pile-reinforced slope behaviour including the kinematic forcing from the slipping soil mass and the resistance of the stable soil is still uncertain due to the small amount of experimental data or field studies. Thus, there is still a lack of understanding of the mechanism of soil-pile

interaction under earthquake shaking. For the reasons mentioned above, geotechnical centrifuge modelling will be used to study the seismic performance of pile-reinforced slopes using different models and cases under real earthquake motions and cyclic motion.

1.4 Aim and objectives

The main aims of this thesis are: (i) to investigate the dynamic behaviour of cohesionless slopes under earthquake events, and develop new approaches for predicting this behaviour; (ii) to investigate the seismic performance of pile-reinforced slope systems and (iii) to develop analytical tools for predicting the performance of pile-reinforced slope systems.

The following objectives were achieved to attain the above aims:

1- Dynamic geotechnical centrifuge modelling was used to investigate non-remediated and pile-remediated cohesionless slopes at different pile spacing;
2- A new reinforced cementitious model material is used to cast damageable pile model elements for use in centrifuge testing;
3- Finite element procedures have been developed for predicting the full dynamic behaviour of unreinforced slopes. These methods were validated against the centrifuge test data;
4- An analytical solution based on the Newmark sliding block method has been developed to quantify permanent slope movements under earthquake shaking. The method can take into account the variation of soil strength due to strain softening and hardening, geometric changes to the slope with slip (re-grading) and soil pile interaction due to a row of discretely spaced piles. The method can also be used to estimate the bending moments in the piles for subsequent structural design/detailing.

1.5 Structure of thesis

This thesis is presented in eight chapters, and each chapter is described in the following sections:

***Chapter 2*:** The thesis starts with a literature review. This will focus on summarising previous research in the areas of dynamic slope stability analysis, methods of seismic analysis of slopes, pile behaviour when used to stabilise slopes under monotonic and dynamic loads, laterally loaded pile behaviour and at the end of the literature review some information concerning the dynamic response of cohesionless soils.

***Chapter 3*:** The bulk of the research work in this thesis is conducted using geotechnical centrifuge techniques and physical modelling principles. Chapter 3 describes the experimental methods used in this work and explains the principles of centrifuge testing and scaling laws. The design and fabrication of the novel pile models is described along with details of the characterisation tests conducted on the pile models. The soil properties and instrumentation used are also explained in detail.

The results and discussion of the dynamic centrifuge tests are contained within Chapters 4, 5 and 6.

***Chapter 4*:** This chapter considers unreinforced cohesionless slopes. The results of the first three dynamic centrifuge tests are included here. An analytical solution based on the Newmark method was improved to determine the permanent seismic slope movements and the results are validated against the centrifuge test results.

Chapter 5: This chapter follows on from Chapter 4, presenting 2D Finite Element modelling of the seismic performance of unreinforced cohesionless slopes. Constitutive modelling of the dynamic behaviour of sands is also included and the results are validated against the centrifuge test data reported in Chapter 4.

Chapter 6: Presents the results from the remaining dynamic centrifuge tests modelling pile-reinforced cohesionless slopes with different pile spacing ratios (*S/B*) with both elastic instrumented piles to investigate the dynamic soil-pile interaction (SPI), and using new damageable model reinforced-concrete (RC) piles. A further damageable RC pile section was tested (with nominal steel reinforcement) to demonstrate how the

designed pile capacity against bending is important if the piles are to be effective in improving slope performance during earthquakes.

Chapter 7: A significant development of the modified Newmark procedure developed in Chapter Four is made to incorporate non-linear soil pile interaction within the formulation of the yield acceleration. This new method is validated against the centrifuge tests results of the instrumented piles from Chapter 6.

Chapter 8 The results of the work are summarised and suggestions for future work are made.

Chapter Two
Literature Review

2.1 Introduction

Slope failures can be classified as one of the major causes of damage and losses in earthquakes. In October, 2004 in Japan, a strong earthquake (M=6.8) hit the middle of Niigata and led to many landslides and structural collapses. More recently, the 1999 Chi-Chi earthquake (M=7.3) triggered more than 10,000 landslides of various types in the steep mountainous terrain of Central Taiwan, throughout an area of approximately 11,000 km^2 (Khazai and Sitar, 2004). Understanding the failure mechanism of slopes during earthquakes is therefore important for reducing damage and loss of life in future earthquakes, and could lead to the development of mitigation techniques for improving seismic slope performance.

Earthen slopes are of two main types: (i) naturally formed and (ii) man-made. Natural slopes are formed by environmental processes, such as slopes in hilly areas. Examples of man-made slopes include embankments constructed for railway lines, roads and canals and earth dams. Slopes can also generally be classified by their failure mode, typically as either 'finite' (also termed 'rotational' or 'short') or 'infinite' (also termed 'translational' or 'long') slopes. In this thesis, term infinite slope is used to designate a slope.

The important factors that can cause instability in slopes under static conditions (after Murthy, 2003) and lead to failure are: (1) gravitational force; (2) hydraulic force due to seepage; (3) erosion of the surface of the slope due to flowing water; (4) the sudden lowering of water adjacent to the slope ('drawdown') and (5) additional inertia loads due to earthquakes. Figure (2-1) shows schematically these common forces and causes of slope failure. It should be noted that in the case of earthquakes, adverse seepage effects (e.g. liquefaction) can also be generated, and the resistive strength of the soil may be reduced due to the dynamic behaviour of the soil (including liquefaction).

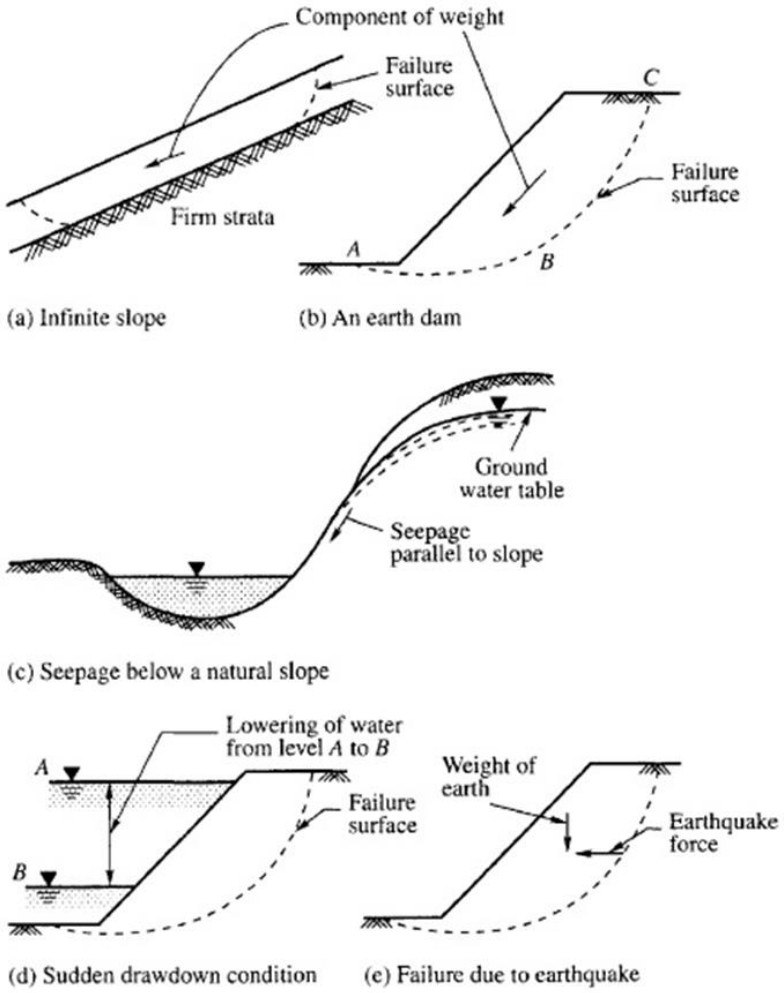

Figure (2- 1): Forces acting on slopes (Murthy, 2003)

The analysis of slope movement and deformation can be considered one of the most important steps to understand slope failure (Terzaghi, 1950). Leroueil et al. (1996) classified the failure process of slopes into four main stages: (1) pre-failure, (2) post-failure stage, (3) occasional reactivation and (4) active failure. Figure (2-2) shows these main stages. Skempton (1985) showed that the third and fourth stages start when the shear band has completely developed and the soil material is sliding at the critical or residual strength as shown in Figure (2-3). The slope's failure point (dividing stages 1 and 2) occurs when the soil material just exceeds its peak shear strength, leading to a large drop in shear strength to critical or residual shear strength (Massey, 2010).

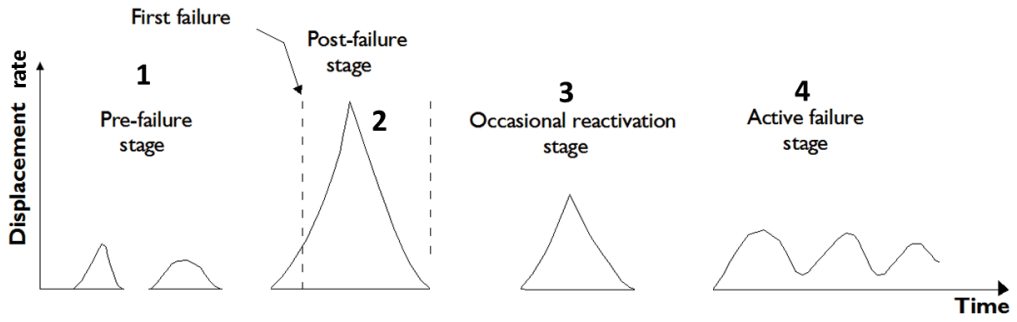

Figure (2- 2): Slope movement stages (Leroueil et al., 1996)

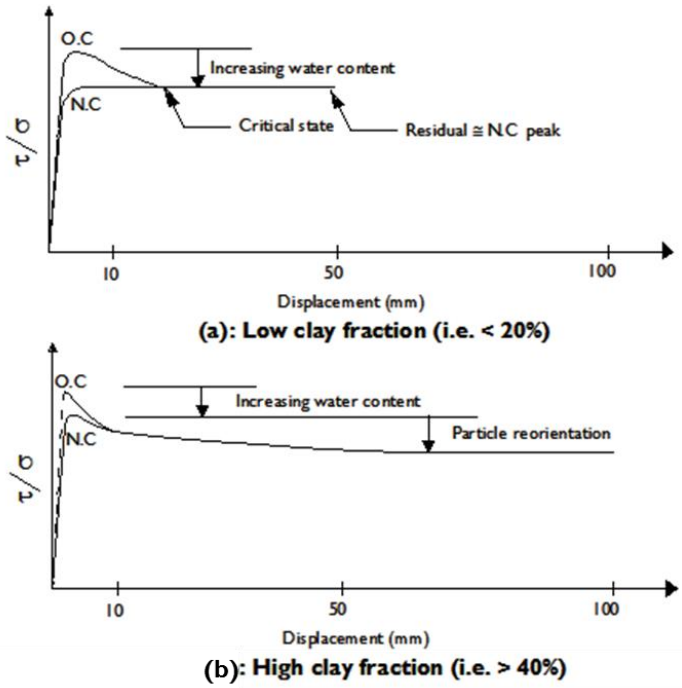

Figure (2- 3): Stress-displacement curve at constant normal effective stress (Skempton, 1985)

The effect of earthquake shaking is normally to increase the inertial loading and reduce the resistive strength of the soil transiently, resulting in soil slip during shaking. When earthquake shaking stops, the resistive strength will usually recover and the additional inertial forces are no longer acting, so that slope deformation ceases and it becomes stable again. However, in the case of undisturbed soils with low residual strengths, the earthquake may cause reduction in strength which result in the slope being statically unstable and suffering stage (4) deformations post-earthquake (Ambraseys and Srbulov, 1995).

Kramer (1996) classified the instability of the slope due to earthquake-induced dynamic loads into two main kinds, either 'inertial instability', in which the slope is deformed due to the additional destabilising dynamic earthquake stresses (with the soil strength unaffected). The second type is 'weakening instability', where the earthquake–induced stresses lead to instability of the soil due to a significant reduction in the soil strength.

2.2 Slope stability analysis

The stability of slopes depends on many parameters including the type of soil, failure mechanism, variation of water table within the slope and surcharge loads from structures near the slope. Slope stability considers the ratio of available strength to applied forces, defining the triggering of slope failure.

2.2.1 Static slope stability analysis

Two dimensional slope stability analyses are widely used by geotechnical engineers. Most slope stability analysis methods are based on principles of limit equilibrium employing the same definition of the factor of safety, which is defined as the ratio between the available shear strength (τ) to the applied shear stress ($\tau_{applied}$):

$$FS = \frac{\tau}{\tau_{applied}} \tag{2-1}$$

This factor of safety represents the factor by which the shear strength must be reduced so that the reduced strength is just in equilibrium with the shear stress $\tau_{applied}$ (Duncan and Wright, 2005). By the Mohr Coulomb criterion, the applied shear that will cause failure (factor of safety less than 1.0) can be represented as:

$$\tau_{applied} = \frac{c' + (\sigma - u)\tan\varphi'}{FS} \tag{2-2}$$

where c' and φ' are the apparent cohesion and angle of internal friction of the soil, σ is the total normal stress on the shear plane, and u is the pore pressure, also on the slip plane (Figure 2-4).

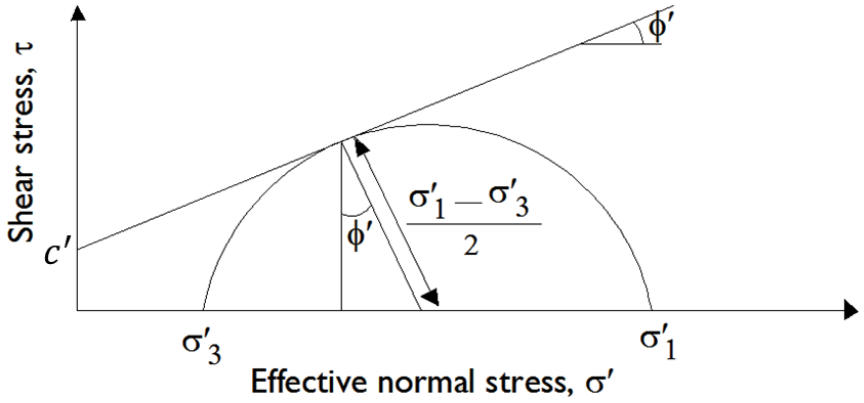

Figure (2- 4): Mohr-Coulomb failure envelope

The factor of safety is calculated by assuming different slip surface positions and calculating the value of FS for each (Duncan and Wright, 2005). Figure (2-5) shows some of the most well-known types of slope failure mechanism. The 'critical slip surface' refers to the slip surface giving the minimum factor of safety which represents the most likely slip surface.

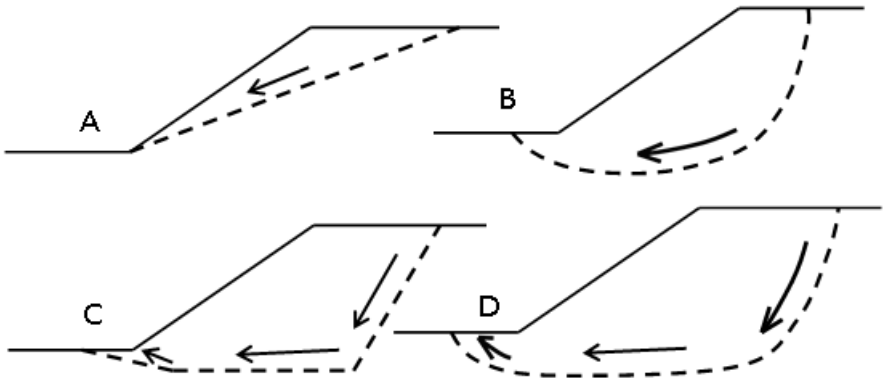

Figure (2- 5): Types of failure mechanism; (A) planar failure; (B) Circular failure; (C) multi-planar failure; (D) non-uniform failure (Re-drawn from Kramer, 1996)

When the factor of safety is less than one, a section of the slope will slide along the failure surface and only come to rest again at a place where the new stresses do not exceed the available strength, due to the change of the geometry and soil properties during the sliding process. It is therefore obvious that a factor of safety less than one cannot be permitted under static conditions. A value of FS = 1.5 is the minimum value generally considered by geotechnical engineers for long term loading conditions

(Kramer, 1996). The following subsections describe some of the most popular slope stability analysis methods.

2.2.1.1. Infinite slope method

In this procedure, the slope is assumed to be of infinite length and width and the soil is sliding as a block, parallel to the slope surface. From free-body equilibrium diagram in Figure (2-6) the equilibrium equation at limit state (Equation 2.1) can be defined as:

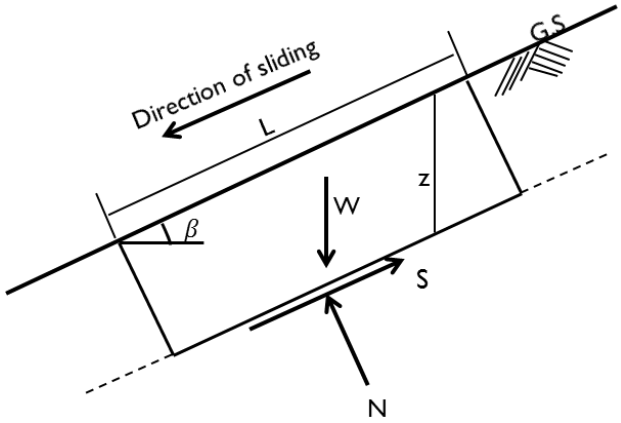

Figure (2- 6): Failure mechanism and free-body equilibrium diagram for infinite slope.

$$S = W\sin\beta \tag{2-3}$$

$$N = W\cos\beta \tag{2-4}$$

where β is the angle of the slope and W is the weight of the soil block, which for block of unit depth, is equal to:

$$W = \gamma L z\cos\beta \tag{2-5}$$

where γ is the total unit weight of the soil, L is the length along the slip plane between the two ends of the block and z is the vertical depth of the shear plane. By combining Equations (2-2) – (2-5), the factor of safety can be written in terms of effective stresses as:

$$FS = \frac{c' + (\gamma z \cos^2 \beta - u) \tan \varphi'}{\gamma z \cos \beta \sin \beta} \quad (2\text{-}6)$$

In cohesionless soil, and in terms of drained conditions ($c' = 0$, $u = 0$), the computed value of FS by the infinite slope procedure is independent of the depth z of the slip surface:

$$FS = \frac{\tan \varphi'}{\tan \beta} \quad (2\text{-}7)$$

This type of analysis is more appropriate for cohesionless slopes as the critical slip surface tends to be very shallow, and because of the independence of FS on the depth of the slip surface.

2.2.1.2. Slices method

The failure surface in this method is assumed to be a circular arc with centre *O* and radius *r*. The soil body above the proposed slip surface is divided by vertical planes to form many slices with a constant width *b* as shown in Figure (2-7). For each slice, the angle of the base line of the slice, measured from the horizontal line, is α and the height of the centre of mass of the slice is *h*. The factor of safety can be defined as before as the ratio between the available shear strength (τ) along the whole length of the slip plane to the sum of the applied shear stresses (τ_{app}). The forces acting on each slice are detailed below:

- Total weight of the slice: $W = \gamma bh$.
- Normal force on the base of slice, per metre length of slope: $N = \sigma.L$. (Two components form this force, namely the effective normal force, $N' = \sigma' L$, and the boundary water force, $U = u.L$. $N = N' + U$).
- The shear force on the base of the slice: τ .
- The normal forces on the two sides E_1 and E_2.
- The shear forces on the two sides, X_1 and X_2.

This is a statically indeterminate problem, and to obtain a solution, an assumption must be made regarding the inter-slice forces *E* and *X*.

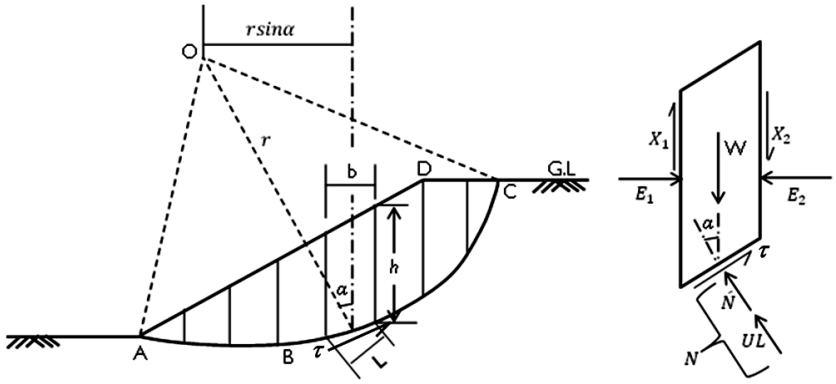

Figure (2- 7): analysis of slices method (redrawn from Duncan and Wright, 2005)

By taking moments about point *O*, sum of shear forces multiplied by radii from *O* along the slip failure surface AC should be equal to the moment generated by the weight of the soil body above the slip surface, thus, for any slice:

$$\sum \tau = r.\sum W\sin\alpha \tag{2-8}$$

And by substitution the above forces acting on each slice, the factor of safety will be:

$$FS = \frac{\sum (c' + \sigma' \tan\varphi')L}{\sum W\sin\alpha} \tag{2-9}$$

or

$$FS = \frac{c'L_t + \tan\varphi' \sum N'}{\sum W\sin\alpha} \tag{2-10}$$

where L_t is the total length of arc AC.

2.2.1.3. Bishop's Method

The assumption in this method is that the inter-slice forces acting on the two sides of each slice are horizontal (i.e. the shear stress between the two slices is neglected). Therefore, the normal forces (weight of slices and the components of the normal and shear stresses acting on the base of the slice) satisfy equilibrium as shown in Figure (2-8).

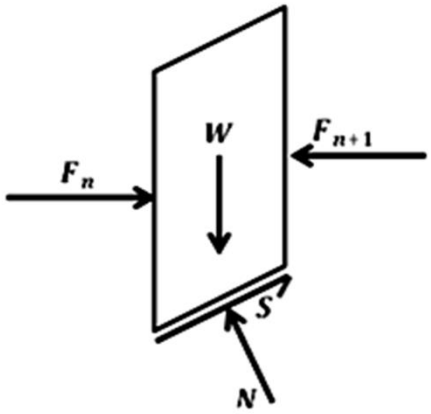

Figure (2- 8): Forces acting on Bishop's slice.

By Bishop's method, the Factor of safety becomes:

$$FS = \frac{\sum \frac{c'l\cos\alpha + (W - ul\cos\alpha)\tan\varphi'}{\cos\alpha + \frac{\sin\alpha\tan\varphi'}{FS}}}{\sum W\sin\alpha} \qquad (2\text{-}11)$$

The Bishop's method is accurate when pore water pressures are high (Duncan and Wright, 2005).

2.2.2 Seismic slope stability analysis

In seismic slope stability analysis, the extension to the static analysis approaches described previously is known as pseudo-static slope stability analysis. In this method a constant horizontal acceleration is applied to the whole slope. In pseudo static analysis, the vertical components of earthquake accelerations are neglected. A factor of safety can be defined in the same way as for the static case. However, a better parameter to describe the seismic safety of a slope is the critical or yield acceleration (k_{hy}). The yield acceleration is defined as the acceleration that, when applied to the mass between the slip and the slope surfaces, produces a state of primary failure along that surface. If the applied acceleration (earthquake acceleration) is larger than the yield acceleration of the slope, then the mass of slope soil will move along the slip surface. This principle underpins Newmark's method for determining seismic slip/deformation, as will be discussed in Section 2.3.1 (Newmark's Rankine lecture). It can be noted that the factor of safety (or yield

acceleration) is evaluated for a given slip surface while the minimum factor of safety (or yield acceleration) is a characteristic of the slope.

Any vertical component of earthquake acceleration can be easily accommodated by simply changing the unit weight of materials to take care of the additional vertical acceleration, then finding the horizontal critical acceleration for the modified unit weight and then the resulting critical acceleration can be adjusted for the modified unit weight. If case of excess pore pressure in the slope, the unit weight of water should also be modified accordingly.

2.2.2.1. Infinite slope method

The horizontal yield acceleration of a shallow translational (infinite) slip can be determined using standard limit equilibrium techniques, incorporating a pseudo static acceleration component due to the seismic ground motion (see Figure 2-9). For a slip plane at depth z beneath the slope surface, the applied downslope shear stress is

$$\tau_{applied} = \gamma z \sin\beta \cos\beta + k_h \gamma z \cos^2\beta \tag{2-12}$$

where the first term relates to the static shear stress due to the ground slope, and the second term relates to the additional peak dynamic shear stress induced by the earthquake. The shear strength of the soil along the slip plane, assuming that the soil can be idealised as a Mohr-coulomb at failure is given by:

$$\begin{aligned} \tau_{ult} &= c' + \sigma' \tan\phi' \\ &= c' + \left(\gamma z \cos^2\beta - k_h \gamma z \sin\beta \cos\beta - u\right)\tan\phi' \end{aligned} \tag{2-13}$$

The soil yields when $\tau_{applied} = \tau_{ult}$. The value of k_h at which this occurs (the yield acceleration, k_{hy}) can be determined from Equations (2-12) and (2-13) as:

$$k_{hy} = \frac{c' + \left(\gamma z \cos^2\beta - u\right)\tan\phi' - \gamma z \sin\beta \cos\beta}{\gamma z \cos^2\beta + \gamma z \sin\beta \cos\beta \tan\phi'} \tag{2-14}$$

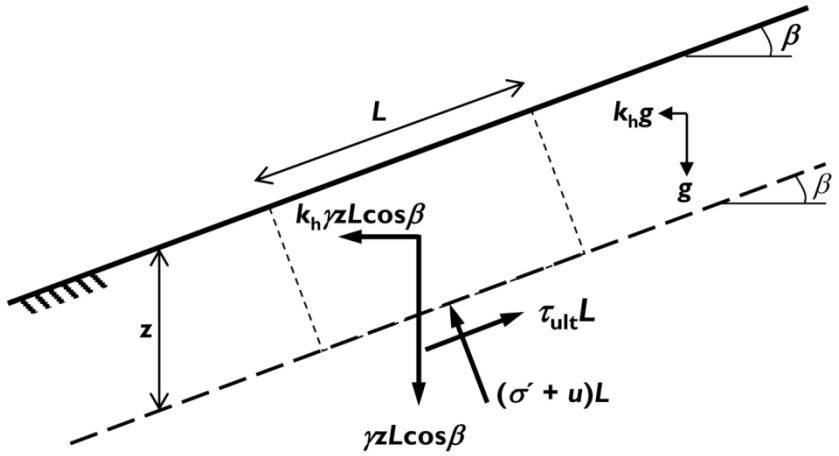

Figure (2- 9): Forces acting within an infinite slope.

2.2.2.2. *Slices method*

Kim and Sitar (2004) determined the yield acceleration for rotational slip failures. This procedure is based on the principles of slices method, previously described in Section 2.2.1.2). The concept of this method is that the slipping mass is divided into many vertical slices of equal width (*b*) as shown in Figure (2-10). By analysing the forces acting on every slice (forces perpendicular to and along the slip surface and the weight of each slice) and ensuring that equilibrium is maintained over the whole set of slices, the yield acceleration k_{hy} can be determined:

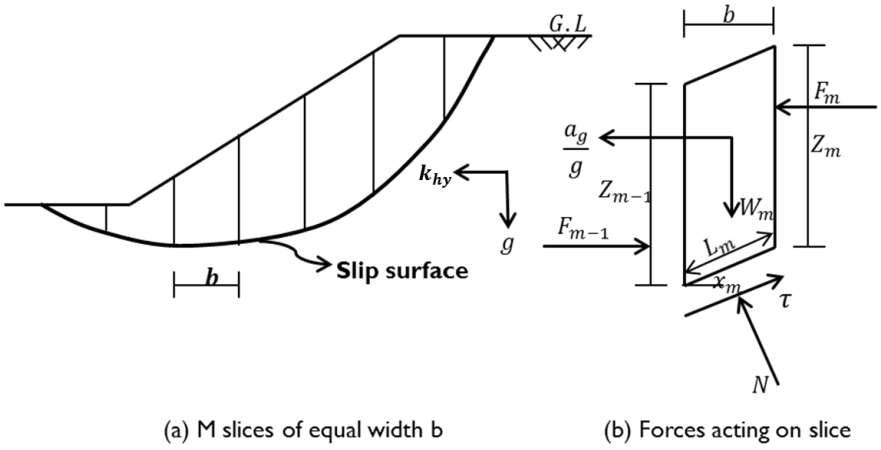

Figure (2- 10): Principles of yield acceleration determination (Kim and Sitar, 2004)

$$k_{hy} = \frac{\sum_M [c - \frac{W_M}{L_M}\sin X_M + (\frac{W_M}{L_M}\cos X_M - u_M)\tan\varphi]}{\sum_M (\frac{W_M}{L_M}\cos X_M + \frac{W_M}{L_M}\sin X_M \tan\varphi)} \quad (2\text{-}15)$$

where

$$W_M = \frac{\gamma b}{2}(Z_{M-1} + Z_M) \quad (2\text{-}16)$$

$$L_M = \frac{b}{\cos X_M} \quad (2\text{-}17)$$

Many trials must be made changing the position of slip surface to determine the critical (lowest) value of the yield acceleration.

Terzaghi (1950) suggested that the pseudostatic inertia forces act through the centre of gravity of each slice when using the slice procedure. However, this is not true because the acceleration is not constant within the soil mass when the shear plane is deep below the surface of the slope. Seed (1979) studied the effect of the position of the pseudostatic force on the factor of safety of an earth dam. He found that changing the position of the pseudo static force from the center of gravity of the slice to the bottom reduces the factor of safety from 1.32 to 1.21 for a ground motion having a PGA of 0.1g. According to many dynamic analyses reported for different earth dams (i.e., Seed, 1979; Okamoto, 1984; Meen and Hsien, 2009) the peak acceleration is magnified from the bottom of the dam to the top. Thus, the location of the seismic force resultant should be above the center of the gravity of the slice in the case of translational slip surface (Makdisi and Seed, 1978). Makdisi and Seed (1978) also suggested that the computed factor of safety provides an indication of the possible magnitude of seismically induced displacement. However, pseudostatic analysis is not perfect because in many cases seismic factors of safety have been calculated well above 1.0 for many embankment dams that later failed during earthquakes, such as the Sheffield Dam and many tailings dams (Kramer, 1996).

Ding (2006) presented a procedure to determine the critical slip surface based on pseudostatic analysis within the limit equilibrium framework. The procedure was extensively validated by a series of simulations performed using the Imperial College Finite Element Program with an elastic perfectly plastic Mohr-Coulomb model. In these simulations different strength parameters and initial stress fields were assumed to check the independency of these conditions. Good agreement was achieved

between the proposed procedure and finite element analysis, in terms of the critical acceleration, the critical slip surface and the stress distribution along the critical slip surface, both for homogenous and non-homogenous slopes.

Deng (2006) used stress acceptability as a prerequisite to derive a system of nonlinear equations to determine the slip surface slice by slice upward. He used an iterative approach to overcome the divergence near the corner point of the slope and a slip-path approach is employed to account for the variety of potential failures at the boundaries of different soil layers. In the homogeneous cases without pore water pressures, the shows that the equations can be expressed analytically; however for inhomogeneous slopes or when pore water pressures are considered, he shows that the equations can only be solved numerically. For homogenous slopes, the method is summarised below (Deng, 2006):

(1) A possible slip surface is selected from experience and the associated yield acceleration for that surface is found using an established stability analysis method, e.g. Sarma (1973) or Sarma (1979). The initially assumed slip surface may not be acceptable in terms of stress and kinematical acceptability.
(2) A starting point is picked from the slope surface and the yield acceleration found in step (1) is used as an initial approximation of the yield acceleration.
(3) A slip surface path is designated.
(4) A slip surface is defined slice by slice. The increment Δx in the horizontal direction along with the two inclination angles of the two sides defines the geometry of a standard slice. Each slice is then solved separately using special algorithm.
(5) Comparing the yield accelerations obtained from different slip surface paths, the slip surface path with the minimum acceptable yield acceleration was selected.
(6) Steps (2) to (5) are repeated for different starting points. From the second loop, the yield acceleration obtained from the previous loop can be used as the initial approximation of the critical acceleration.

Deng (2006) shows that by repeating steps (2) to (5), every starting point on the slope surface can be analysed and then the slip surface and associated yield acceleration can be determined for each starting point. Another possible option he explained to obtain

the critical slip surface is that the starting point can be generated randomly within the possible area for starting points. Provided that the number of random points is large enough, the minimum value of the yield accelerations is close to the statistical global minimum.

Figure (2-11) shows an example from Deng's procedure where three slip surface paths are designated for inhomogeneous soil with three layers and three different sets of properties. The first one was defined as when the slip surface encounters the first soil layer interface; it was clearly shown that slip surface was developed along the interface and then carried on. The second one was defined as that when the slip surface crosses the first soil layer interface but develops along the second soil layer interface. The third one was defined as that when the slip surface crosses all the soil layer interfaces. Figure (2-12) shows the comparison between the Zolfagari et al., (2005) approach based on genetic algorithms and the new procedure proposed by Ding (2006).

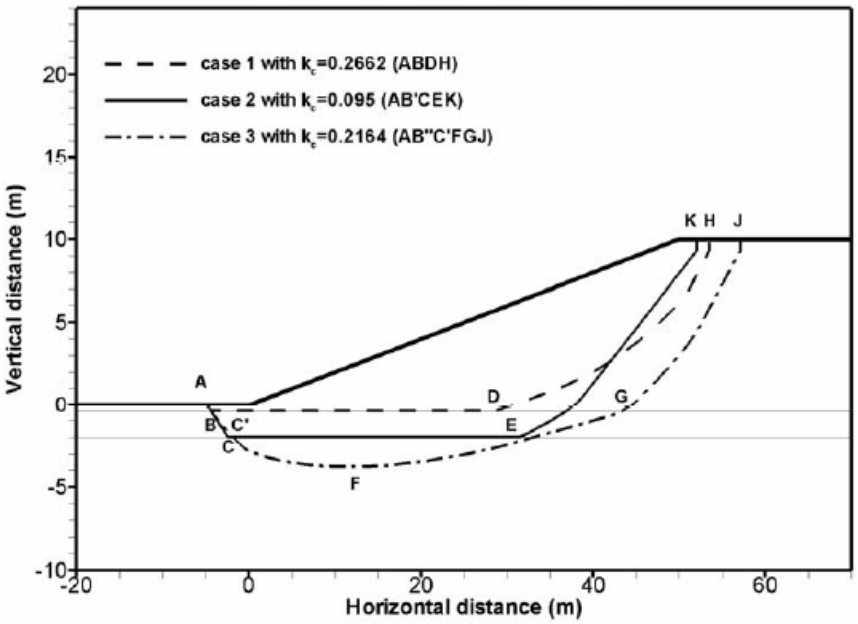

Figure (2- 11): Slip surface path example. Note that different surfaces encounter the first soil layer boundary at three different points near B but the differences are too small to be seen (Ding, 2006)

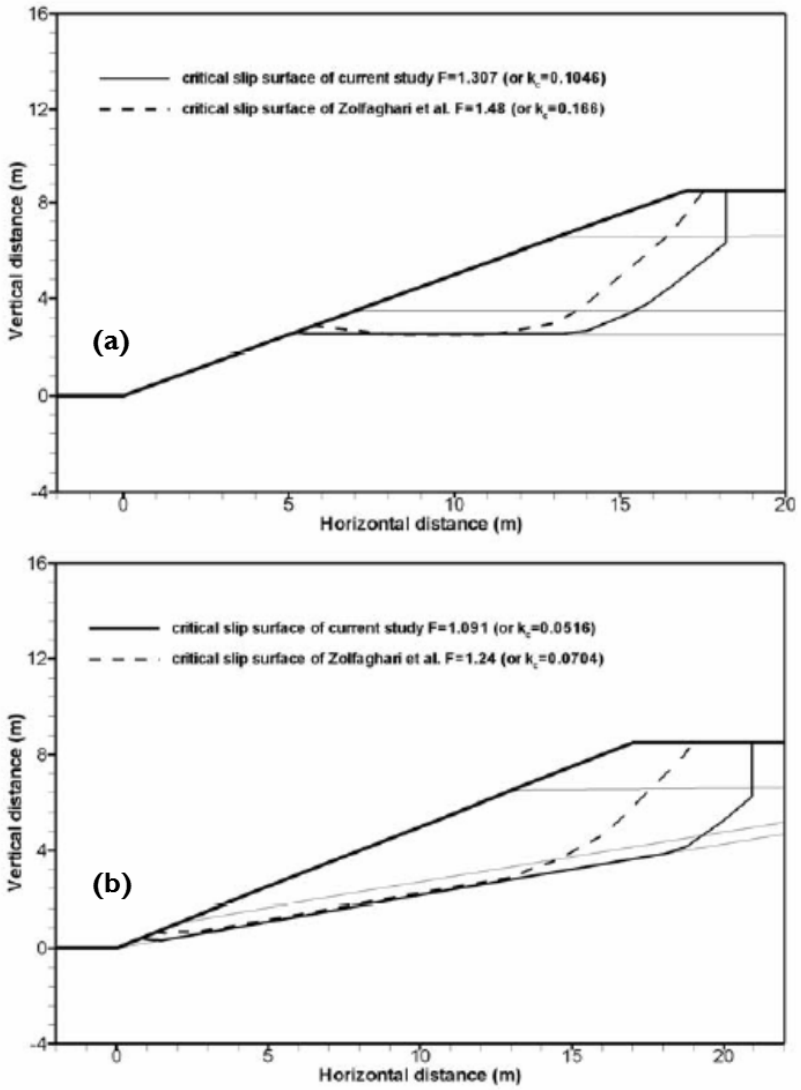

Figure (2- 12): Comparison of slip surfaces of four-layer slope given by the new procedure and that obtained by Zolfaghari et al. (2005) using a genetic algorithm approach for (a) horizontal layers and (b) inclined layers (Ding, 2006)

2.3 Prediction of seismic slope slip

2.3.1 Newmark sliding block analysis

This method was originally proposed by Newmark (1965) and can be used to estimate the amount of movement that a slope will undergo under earthquake shaking. The Newmark sliding block approach provides a better way of investigating the likely hazard imposed to a slope than a pseudo-static analysis for many reasons (Ding, 2006). Firstly, damage assessment in-situ is usually based on measureable induced movement, thus, factor of safety and the yield acceleration cannot be directly measured in-situ – it can only be said that the yield acceleration has been exceeded.

Secondly, the varyiation of the factor of safety below unity during earthquake shaking, especially during strong earthquakes, may not lead to severe displacements with the displacement at the end of the earthquake being extremely small, while the final factor of safety may be above unity. Finally, depending on the nature and requirements of a specific earth-structure, different displacement limits may be regarded as acceptable; and by employing a Newmark sliding block method of analysis, specific tolerances for each particular situation can be employed. Failure and damage can be easily quantified within a model using displacements; such quantities provide a much more comprehensive representation of the real case than does that use of the critical acceleration or factor of safety alone.

The method is based on the concept that the potential failure mass will be accelerated by an unbalanced force if the inertial forces acting on exceed the available resisting force (i.e. FS < 1.0).

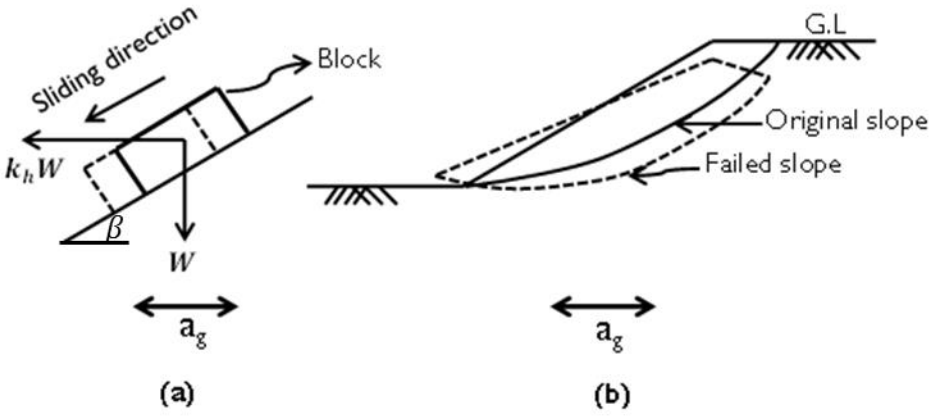

Figure (2- 13): Newmark technique (a) block sliding on inclined plane; (b) real slope sliding

The block shown in Figure (2-13a) is statically stable at a certain inclined plane. Under horizontal acceleration ground motion a_g (neglecting the vertical horizontal acceleration), the horizontal force driving slip will be governed $k_h W$ as shown in Figure (2-13a). The dynamic factor of safety at this case will be:

$$FS = \frac{(\cos\beta - k_h \sin\beta)\tan\varphi}{\sin\beta + k_h \cos\beta} \qquad (2\text{-}18)$$

It can be noticed that with zero k_h coefficient, the factor of safety reduces to that for an infinite slope (slide block) under static conditions (i.e. Equation (2-7)). The yield acceleration is found as in Section 2.2.2 by setting FS = 1.0. For the case of the sliding block, slipping in the downslope direction, this is given by

$$a_y = k_h g = \tan(\varphi - \beta) g \tag{2-19}$$

while for a real slope (e.g. Figure 2-13b) the yield acceleration is calculated using the methods described in Section 2.2.2.2. For idealised homogeneous cases, charts of yield acceleration, such as those by Prater (1979) and Lighrhall, (1979), have been developed, similar to those used to derive the stability charts for the factor of safety. The single block procedure is directly applicable in cases of planar translational failures (using Newmark's formulation) or circular rotational failures (Sarma, 1981).

The slope becomes unstable when the driving forces exceed the resisting forces of the slope mass which results in a net acceleration acting on the slipping mass, causing this mass to slip downhill (Newmark, 1965). The soil mass continues to slip until the inertial forces have been removed or until the net acceleration acting on the mass has slowed it to rest. Further sliding will occur if the ground acceleration exceeds the yield acceleration in subsequent cycles. Newmark slip displacement is determined by double integrating the regions of the input motion record which lie above the yield acceleration, as illustrated in Figure (2-14). Many methods can be used to do this integration, some rigorous and others simplified (e.g. Chang et al., 1984, Makdisi and Seed, 1978, Newmark, 1965).

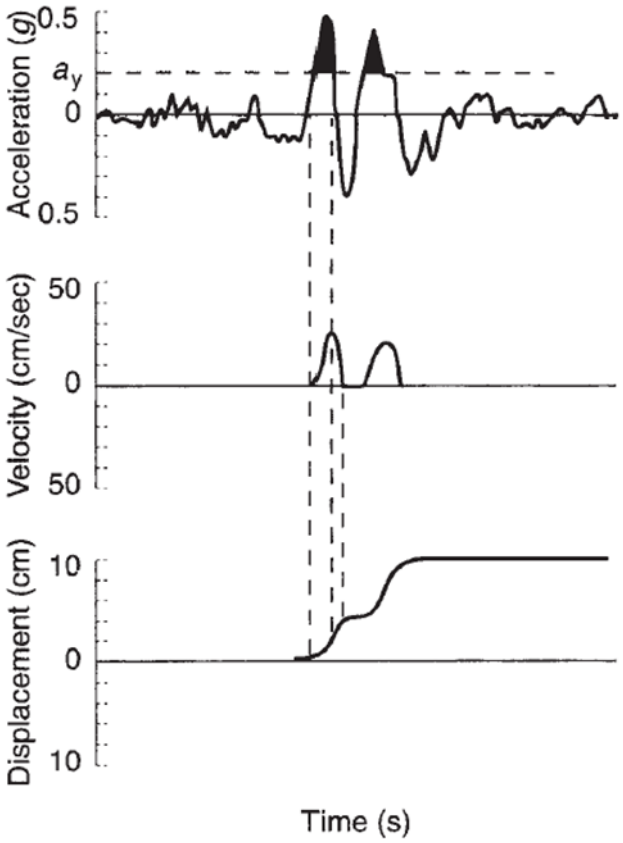

Figure (2- 14): Demonstration of classical Newmark analysis algorithm (Wilson and Keefer, 1983)

The selection of the input ground motion is critically important for two main reasons. Firstly, sensitivity of the earthquake causing slope displacement to the value of the yield acceleration (i.e. small changes in yield acceleration lead to large variation in slope displacement, due to lots of cycles having similar peak accelerations). Secondly, great variation in slope displacements will occur due to any acceleration pulse amplitudes distribution variation between different ground motions and the directionality of the motion (Kramer, 1996). Following the Newmark method, charts have been developed by calculating the cumulative displacement for large sets of earthquake records. These charts include those by Wilson and Keefer, (1983) and Bray and Rathje, (1998).

2.3.2 Effect of soil constitutive properties

In the original development of the sliding block method, (Newmark, 1965), the assumption of a constant shear strength along the slip surface was made, resulting in

the implicit assumption of a constant yield acceleration throughout an earthquake, which may not always be appropriate. Newmark suggested that modification of the method to account for cyclic degradation of the shear strength, i.e. degradation of the yield acceleration, might be justified. However, this suggestion has been largely ignored by the geotechnical communities. Therefore, it is not strange that this procedure is not found in most routine implementations of Newmark analysis.

Matasovic et al. (1997) used a yield acceleration evaluated from residual and large deformation shear strength parameters to account for strength degradation due to shearing. This modification considered a tri-linear model for degradation of yield acceleration as a function of displacement. In this model, shown in Figure (2-15), it was assumed that degradation of the initial value of yield acceleration, k_{y1}, starts when the calculated permanent horizontal displacement coincides with peak shear strength (displacement, δ_1). After reaching the maximum force, the yield acceleration degrades linearly with increasing displacement until the ultimate "residual" yield acceleration, k_{y2} , is reached at a second displacement, δ_2 corresponding to residual strength.

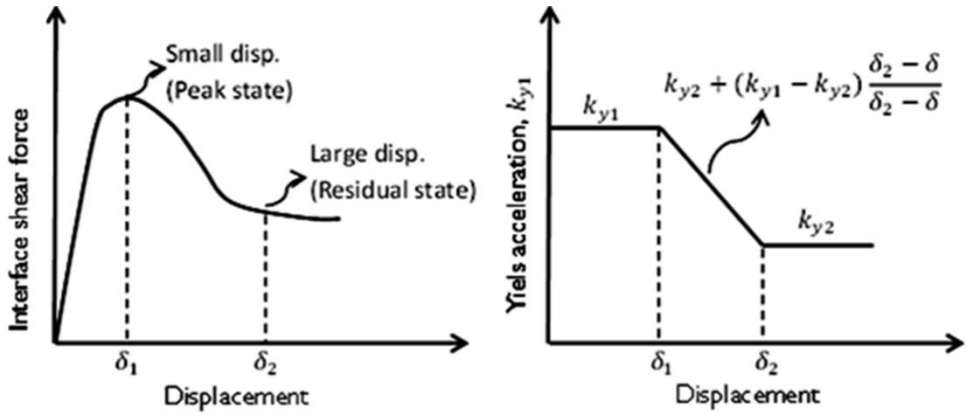

Figure (2- 15): Shear softening behaviour; (a) shear force-displacement; (b) yield acceleration degradation (Matasovic et al., 1997)

Figure (2-16) illustrates how the degrading yield acceleration model shown in Figure (2-15) impacts the results of a Newmark deformation analysis. Analyses performed by Matasovic et al. (1997) support the logical inference that cumulative displacement calculated with the degradation model illustrated in Figure (2-16) is consistently lower

than the cumulative displacement calculated by the classical Newmark procedure with a constant yield acceleration based upon residual strength parameters.

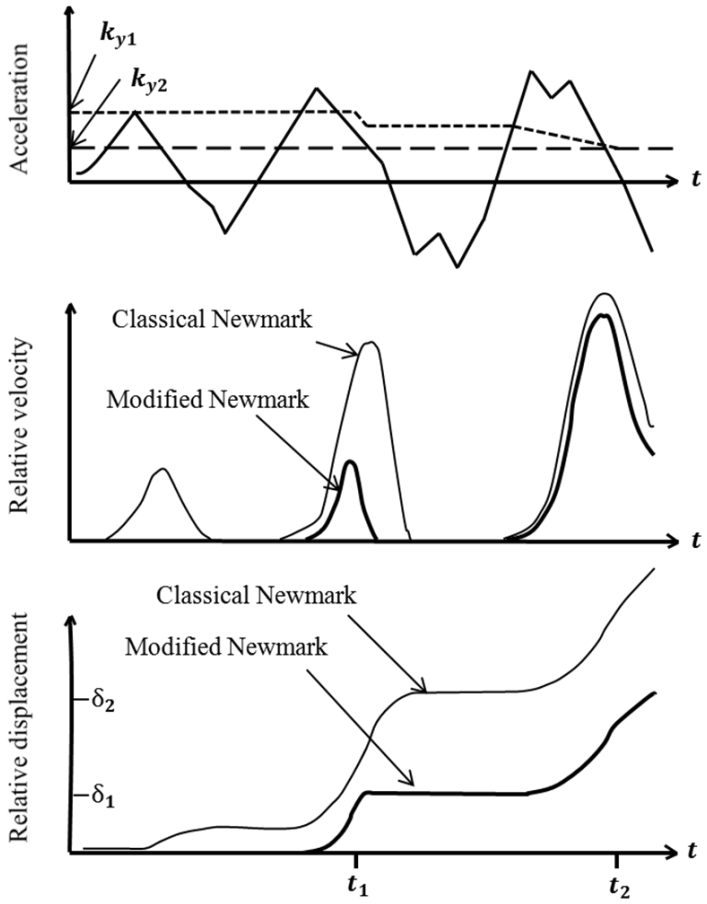

Figure (2- 16): Comparison between classical and modified Newmark's procedure (Matasovic et al., 1997)

2.3.3 Post-earthquake slope deformation

In addition to co-seismic deformation, as described in the previous sections, (Ambraseys and Srbulov, 1995) recognised that in many cases of natural and man-made slopes, slope deformation may be defined by three consequent stages. The first stage relates to the co-seismic slip described previously, where the seismic inertia forces lead to the creation of a failure surface or re-activate an existing slip surface, in either case resulting in permanent displacement of the slope.

In the second stage, which comes directly after the earthquake, the downslope displacement will continue towards the slope toe due to insufficient shear strength on the slip surface to maintain static equilibrium. In this stage, gravity works as the driving force, while the resisting force depends on the strength available on the slip

surface generated during the first stage, the resistance offered by the toe and the rate of strength regain on the slip plane (e.g. due to excess pore pressure dissipation). In the final stage, creep, consolidation and hydrostatic forces may be generated because cracks produced by the earthquake may fill with water, resulting in further movement.

Ambraseys and Srbulov (1995) calculated the displacements in the post-seismic stage, immediately after the earthquake, by employing a two-block sliding model. It simulates the motion of a slide that can be approximated by two planar shear surfaces with minimal internal disruption. In this stage movements will begin with a static factor of safety less than unity, and a section of the slope will move under gravity (but no seismic inertia forces) to a new position of equilibrium. In this procedure, it is assumed that the slope has a finite length and that the mass slips on a surface produced by the earthquake during the first stage. It is also assumed that the slip surface consists of two slip planes: one of length L with a depth h parallel to the slope and inclined to the horizontal at an angle β, and a second plane of initial length b, which is inclined at an angle $\pm\vartheta$ (Figure 2-17). This is a model of two continuous blocks, free to slide on two plane surfaces, separated by an inter-slice plane at an angle β to the horizontal. This model takes into account the internal deformations and uses the concept of mass transfer between blocks.

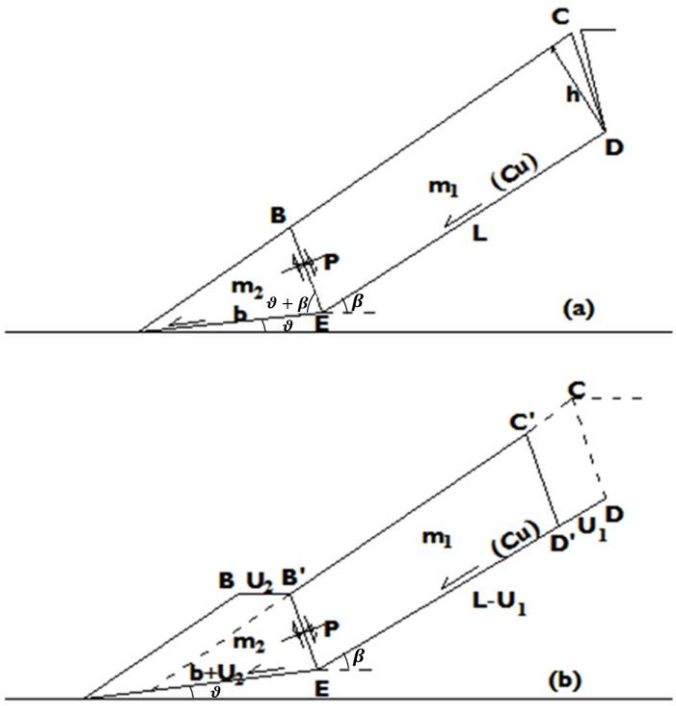

Figure (2- 17): Sliding block model used for the assessment of post-seismic displacements (after Ambraseys and Srbulov, 1995)

Chlimintzas (2003) further developed the method of Ambraseys and Srbulov (1995) by taking into account the seismic sliding of the slope during the earthquake event. The Ambraseys and Srbulov method was limited to two blocks; only the post-seismic movements were analysed, simplified geometry was used to represent the failure mechanism and it does not clearly consider a geometry transformation rule during sliding. Thus, Chlimintzas, (2003) developed a more general multi-block dynamic model which was based on Ambraseys and Srbulov (1995). A failure mechanism must be observed for the application of the multi-block dynamic model and if the slope starts to move, the failure mechanism has to be kinematically acceptable. The main geometry changes that are accommodated by the model are: firstly, the mass is transferring from one slice to another; secondly, it results in changes of the cohesion forces due to variations in inter-slice boundaries. The mass transfer and internal deformation that result from the displacement of the slope can be thought of as constituting a geometry transformation. Figure (2-18) shows the transformation mechanism that is used in the model to produce the deformed geometry.

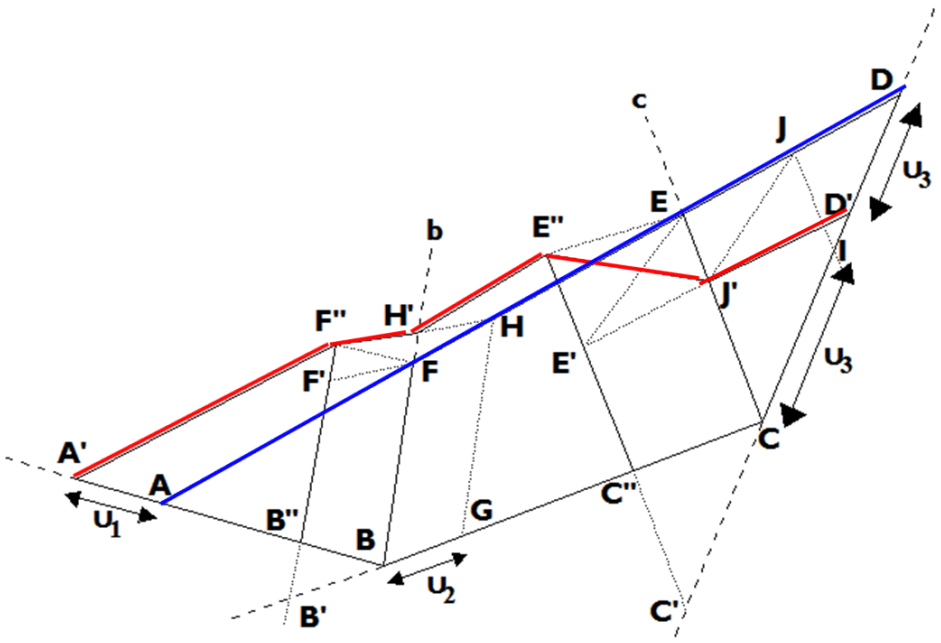

Figure (2- 18): Geometry changes and mass transfer in a three-block system with straight initial ground surface (AD). New ground surface = A'F''H'E''E'J'D' (After Chlimintzas, 2003)

2.5 Pile stabilised slopes

Perry (1989) recommended that the slope must be constructed at a slope angle between (1v:5h – 1v:2h) without any remediation by piles or other techniques. But for steeper slopes, stabilising techniques should be used. Piles are one of the most widely used foundation elements in geotechnical design and widely used by geotechnical engineers to stabilise slopes against environmental effects. Improved slope performance during/after earthquakes is particularly important where the sloping ground is part of an embankment or cutting adjacent to transport infrastructure such as roads and railways.

The main advantage of using deep foundations (piles) in slope stabilisation is to utilise the bending response of the pile to stabilise the sliding mass by making use of the significant resistance available in stronger stable strata, thereby increasing the resistance available, increasing FS and yield acceleration and reducing the downslope movements. These are normally installed as a discretely-spaced pile row running along the slope at a centre-to-centre spacing, *S*, passing through the unstable slipping soil mass to be anchored in the underlying stable soil. Ground movements generate relative soil-pile movement, which in turn leads to lateral soil pressures developing along the piles, inducing bending moment at different depths. If these bending moments are large enough, structural damage and/or failure may occur. As a result the piles must be designed to resist the lateral shear forces and moments due to the soil pressures generated by the lateral ground movements.

In general, there are two main objectives when designing piled slope reinforcement. The first is to find the characteristics and features of the piles such as diameter, length of pile, location, spacing between them and the necessary embedded length in order to achieve the desired slope improvement with the least construction cost. The second is that the internal moments and shear forces (in the seismic case) of the piles within a slope must be determined to design a suitable structural capacity into the piles. The most commonly used approach to achieve these two objectives involves analysing the slope (geotechnically) and the piles (structurally) separately. The piles add an additional resistance force to the slope sliding mass (increasing the factor of safety for the pile-slope system) as demonstrated by Ito et al. (1981); Reese et al. (1992); Hassiotis et al. (1997), amongst others. They additionally provide soil arching in the

slope (increasing the factor of safety due to decreasing of driving stress of the pile-slope system (Liang, 2002).

Wassel Al Bodour (2010) showed a simple schematic model of a pile reinforced slope as shown below:

$$FS = \frac{F_{resistance}}{F_{driving} - (\Delta F_{driving})_{arching}} \tag{2-20}$$

Or

$$FS = \frac{F_{resistance} + (\Delta F_{resistance})_{pile}}{F_{driving}} \tag{2-21}$$

Where:

$F_{resistance}$: Resistance force

$F_{driving}$: Driving force

$(\Delta F_{driving})_{arching}$: Additional driving force due to arching effect

$(\Delta F_{resistance})_{pile}$: Additional resistance forced due to pile resistance

Equations (2-20) and (2-21) above are appropriate to infinite slope procedures, i.e. the slope is assumed to extend to infinity in all directions and sliding is assumed to occur along a plane parallel to the face of the slope (translation failure for cohesionless soils). In rotational failures, the shape of the slip surface is usually circular (or close to it). Thus, it is more appropriate to find the factor of safety using the moment of forces around the point of rotation:

$$FS = \frac{Available\ resistance\ moment}{overturning\ or\ driving\ moment} \tag{2-22}$$

Equation (2-22) is generally applicable for reinforced or unreinforced slopes. Addition of stabilising piles to remediate the slope adds an additional resistance moment obtained from the pile shear force at the pile tip and bending moment in the pile at the depth the sliding surface as shown equation and Figure (2-19).

$$FS = F_i + \Delta F = \frac{M_R}{M_D} + \frac{V_{cr} R\cos\theta - M_{cr} + V_{head} Y_{head}}{M_D} \quad (2\text{-}23)$$

where:

F_i Safety factor of un-stabilised slope.

ΔF Increase in safety factor of slope when reinforced with piles.

M_R Resisting moment

M_D Driving moment.

M_{cr} Bending moment at critical surface.

V_{cr} Shear force at critical surface.

V_{head} Shear force at pile head.

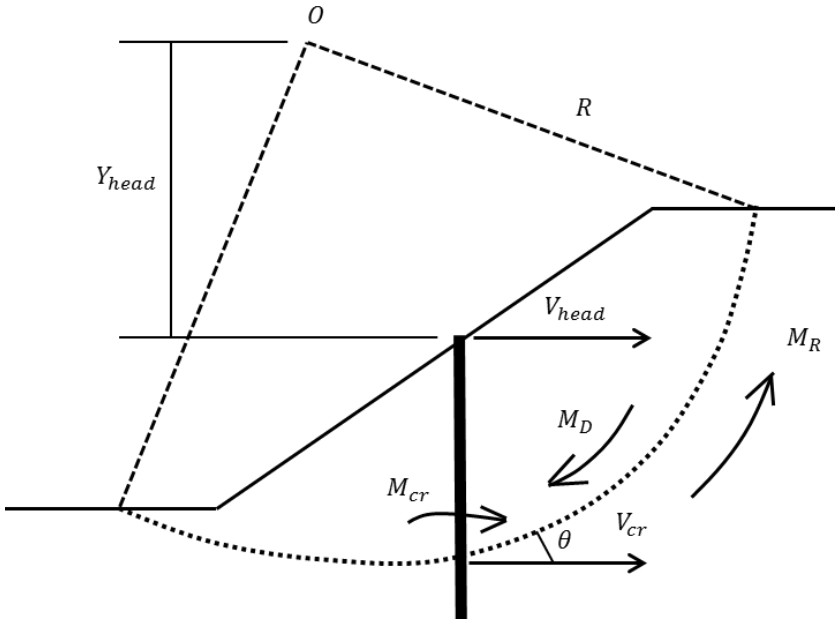

Figure (2- 19): Forces on stabilising piles and slope

2.5.1 Effect of pile row position

Much research has been conducted to investigate the best position of slope stabilising piles within a slope. Actually, this depends on many variables incuding: type of slope soil, failure surface shape and any surcharge loads for any infrastructure located near the cerst of the slope. The earth pressures acting on the piles come from the soil movements and the generated bending moments within the piles will change with position within the slope. Placing piles near the toe of the slope is widely used in case of landslides to cover all of the expected sliding mass. This will not prevent any

failure near the crest of the slope, especially in steeper slopes. While placing of the piles near the crest of the slope will prevent or reduce potential failures at the crest, this could push the failure behined the piles at the crest, leading to damage of any structures near the toe of the slope. From this discussion, it seams that locating the piles between the toe and the crest may be more appropriate to stabilise slopes.

Ausilio et al., (2001) used an upper–bound plasticity method to determine the best place to position piles in a slope (under static conditions). It was found that piles near the toe of the slope gave improved remediation (higher factor of safety). Lee et al., (1995) observed that piles near toe and crest of slope gave optimum results. However, the placement of piles in the middle of the slope has given best stabilisation results in other studies using the finite element method (Wei and Cheng, 2009; Won et al., 2005; Ellis et al., 2010).

Madden (2008) used micro concrete piles modelled in a miniature geotechnical centrifuge to study pile-reinforced slope behaviour of steep cohesive slopes. Different pile spacing and pile positions were used in this study. It was found that when the spacing was reduced between the piles row and moved towards the toe of the slope, the improvement in stability increased especially when the row is installed along the toe of the slope. However, the middle of the slope was found to be almost as effective. Cai and Ugai (2000), used the finite element method to analyse a 10 m high slope to investigate the best position for piles to give the greatest stabilising effect on the slope. Their study showed that the maximum measured factor of safety (by reducing the soil strength parameters until slope failure occurred) was observed when the piles were placed exactly at the middle length of the slope (X/L = 0.5) where X is the distance from the toe to the pile position while L is the total horizontal length of the slope. This finding has been compared with measured factors of safety based on limit equilibrium slope stability analysis principles using Ito and Matsui (1975) as shown in Figure (2-20).

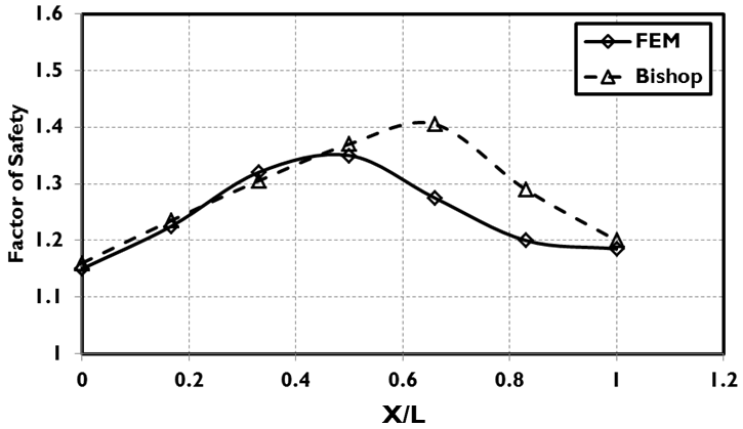

Figure (2- 20): Location of pile in the slope-factor of safety relationship (after Cai and Ugai, 2001)

2.5.2 Effect of pile row spacing

The second design criteria when designing slope-stabilising piles is to determine the maximum pile spacing that can be used to give effective soil arching. For piles at wider spacing, no arching will be developed between piles and flow of soil between piles will occur. If the piles are installed closer together (low S) then the earth pressures from the unstable soil mass will continue to arch between the piles, but below the maximum value, the additional piles will not necessarily provide greater reduction in slope displacements. Many factors affect the maximum pile spacing including: soil properties, type of failure surface and stiffness and diameter of the selected piles. The ultimate bending capacity of the piles is also one of the main important factors in pile-slope system (discussed in greater detail in Section 2.6).

The diameter of piles and the spacing between them must be taken into account in the pile-reinforced slope design in order to minimize the flow of soil between them. Many previous studies have been conducted to better understand the positioning (spacing) of the piles for optimal improvement of a slope's performance. Numerically and analytically, Ito and Matsui, (1975); Ito et al (1982); Wang and Chen 1974 and Bransby and Springman (1999) amongst others investigated the detailed stress conditions and failure mechanisms around a row of piles to understand how the kinematic loading and onset of arching is affected by pile spacing. Most of this existing research suggests that the spacing between piles in a row should not be more than five times the pile diameter as beyond this spacing, interaction between any two adjacent piles is small, and there is no interaction between adjacent piles once the spacing is greater than 8D (Carder, 2009). This has recently been refined by

centrifuge modelling under monotonic loading conditions by Ellis et al. (2010), who proposed a simple means of estimating the maximum spacing for effective reinforcement (i.e. the value beyond which arching would not occur between individual piles):

$$\left[\frac{S}{D}\right]_{\max.} = \frac{K_p^2}{K_p - K_a} \tag{2-24}$$

where S is the pile spacing (centre to centre), d is the pile diameter, K_p is the passive earth pressure coefficient, and K_a is the active earth pressure coefficient.

Hayward et al. (2000) tested a pile-reinforced clayey slope using geotechnical centrifuge modelling. It was noted that at a spacing of 6.3D, the slope failed, while no failure occurred for the other models (spacing = 4.2D and 3.2D).

In terms of using piles to stabilise slopes against seismic actions, Kourkoulis et al. (2011) studied the effect of pile spacing on slope behaviour during earthquakes using the Finite Element Method. This work demonstrated that when the normalised pile spacing, *S/B* (where *B* is the diameter of the pile), was less than 4, soil arching between piles will be generated, while for *S/B* > 5 the piles will behave as single piles (no soil-arching).

2.5.3 Effect of relative soil & pile properties

Martin and Chen, (2005) used a displacement-based method within the FLAC Finite Difference program to evaluate the response of piles in embankment slopes acting in a translational failure mode, induced by a weak soil layer beneath the embankment. The study showed that the maximum shear force developed at the bottom of the weak layer, while the maximum bending moment developed towards the top of the stable layer as shown in Figure (2-21). The study of pile bending stiffness on the quantity and the location of the pile deflection was also investigated. This was done by increasing and decreasing the pile bending stiffness by changing the pile element diameter. When the pile bending stiffness was ten times higher than the primary studied case (i.e. $10E_pI_p$), the pile deflection was larger than the soil movement and this was consistent with what was observed by Polous (1995) (i.e. intermediate mode

failure). In contrast, decreasing of the bending stiffness to ($0.1E_pI_p$) gave pile deflections close to the soil movement (short pile mode). These observations can be attributed to the higher shear forces and bending moment which were observed in the stable layer of the higher bending stiffness model.

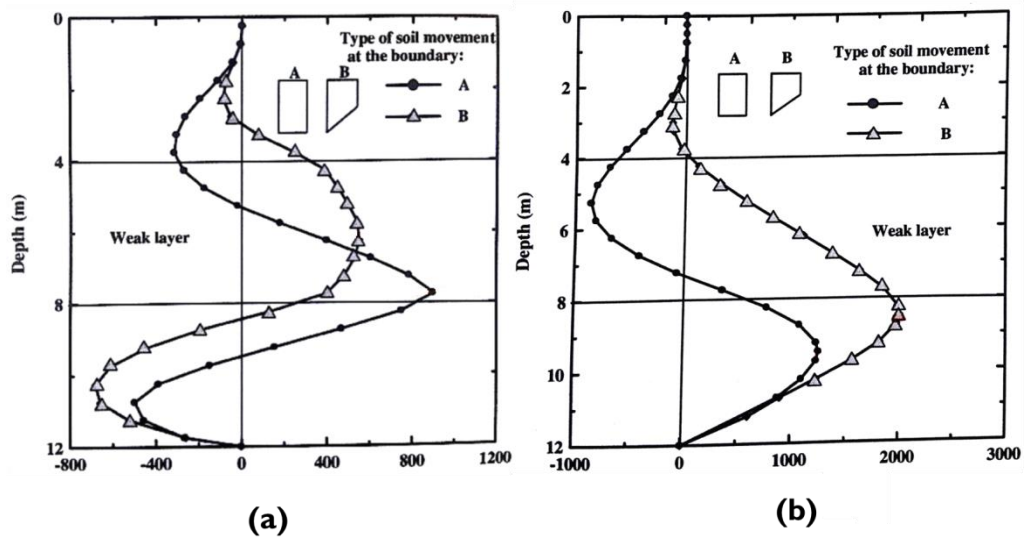

Figure (2- 21): (a) Shear force and (b) bending moment distribution within laterally loaded piles (Martin and Chen, 2005)

2.6 Laterally loaded piles

2.6.1 'Active' and 'passive' piles

Piles which carry lateral loads may be classified as either passive piles (where earth pressure acts along the pile length due to relative soil-pile movement, such as in a pile-reinforced slope) or active piles whereas the piles are pushed into the soil (loaded at the top such as in, for example, a highway bridge). Figure (2-22) shows these two cases of lateral loading of a pile.

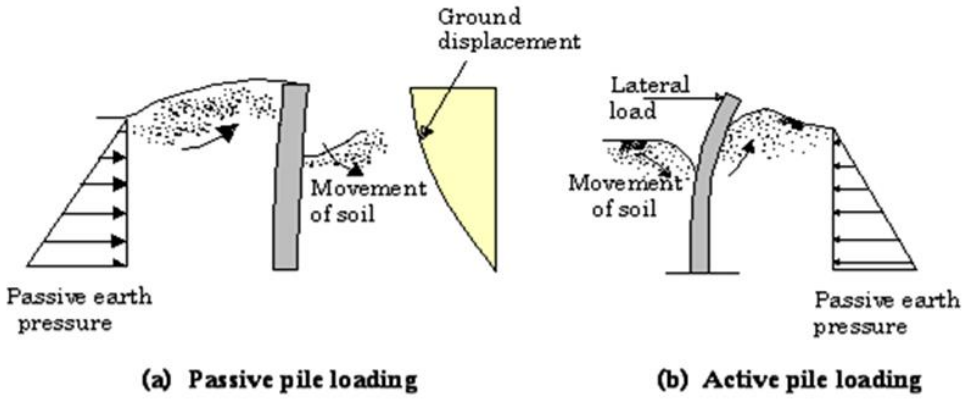

Figure (2- 22): Laterally loaded pile; (a) Passive pile loading; (b) Active pile loading

For passive piles, the relative displacement between any two adjacent piles and the displacement of the pile itself is used to observed the P-δ curve (δ being the relative soil-pile displacement and P is the loading pressure along the pile) while for active piles, the pile displacement itself is used to observed the P-y curve (y is pile displacement). Chen and Martin (2002) showed that the p-δ curves are stiffer from P-y curves and the arching phenomenon is more effective in passively loaded piles (i.e. Figure 2-23).

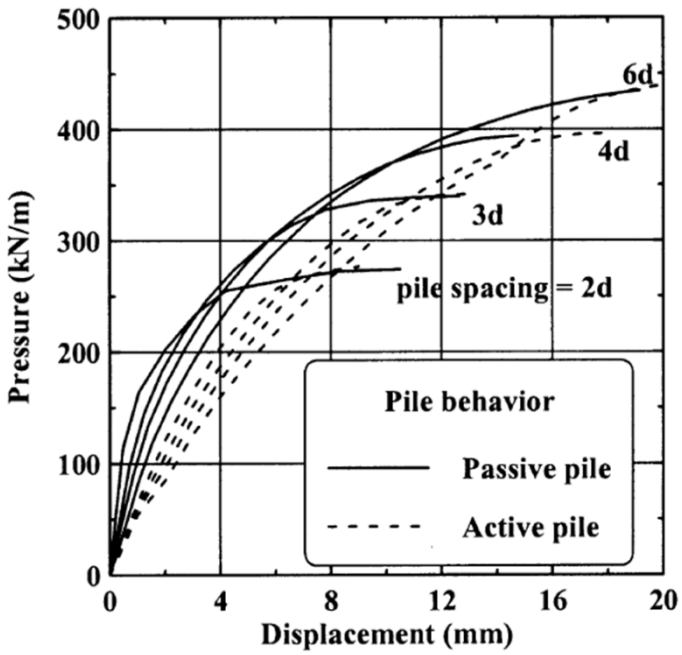

Figure (2- 23): the differences between p-δ and p-y for drained soil strength (After Chen and Martine 2002)

In the case of passive piles, relative soil pile movement generates internal forces in the piles, which depend on many variables including the amount of relative displacement, soil properties, relative soil-pile stiffness and pile spacing. If the piles do not fail, increasing of the movements during an earthquake will lead to increasing of earth pressure acting on each pile to a certain limit, the ultimate soil pressure, beyond which the soil will yield around the pile, and there will be no further increase in internal forces.

2.6.2 Ultimate lateral pressure on individual piles

The maximum lateral pressure induced by mass slope movement that can act along the piles is given by the ultimate pile-soil capacity. After this point, the soil starts to slip plastically between piles. Randolph and Houlsby (1984) showed that this ultimate load for a single pile in cohesive soils at depth, where a flow failure mechanism dominates is given by:

$$P_u = N_p.C_u.d \tag{2-25}$$

where N_p varies between 9.14 for smooth piles to 11.9 for rough piles and d is the pile diameter. The lateral pressure coefficient N_p is suggested to reduce to less than half value (N_p=2.8-4) in the failing zone near the surface of the soil due to a wedge type mechanism forming instead (Viggiani, 1981):

$$N_p = 2.(1+\frac{z}{d}) \leq 9 \tag{2-26}$$

where: z is soil depth and d is the pile diameter.

For cohesionless soil, Broms (1964) assumed that the ultimate lateral resistance is equal to three times the Rankine passive earth pressure. Thus, at any depth below the ground surface, the soil resistance per unit length can be determined from the equation:

$$P_u = 3.b.\sigma_v^{'}.K_p \tag{2-27}$$

where b is the pile width or diameter, K_p is the Rankine passive earth pressure coefficient:

$$K_p = \tan^2(45 + \frac{\varphi}{2}) \tag{2-28}$$

and σ_v' is the overburden pressure at depth *z*. Barton (1982) used centrifuge test results to propose a variation of lateral pressure with depth given by:

$$P_u = K_p{}^2.\sigma_v{}'.d \tag{2-29}$$

Comparing Equations (2-27) and (2-29), $K_p \approx 3$ for most cohesionless soils, so that the two equations would give approximately the same limiting pressure.

2.6.3 Ultimate lateral pressure on piles in a row

Bransby (1996) described the pile-soil displacement under lateral kinematic loading (pile-reinforced slope) as shown in Figure (2-24). Under lateral loads, the pile will be displacing relative to its initial position by (δ_p). The soil in the midway between the two adjacent piles will be displaced by a value of (δ_s). From the equivalent pile-soil displacement (δ_{eq}) for the same swept area (A1 = A2), the total displacement of the system is ($\delta = \delta_{eq} - \delta_p$). Bransby and Springman (1999) subsequently showed that there is a little variation of the ultimate earth pressure acting on the piles over a range of spacing when the piles are in a row in cohesive soil.

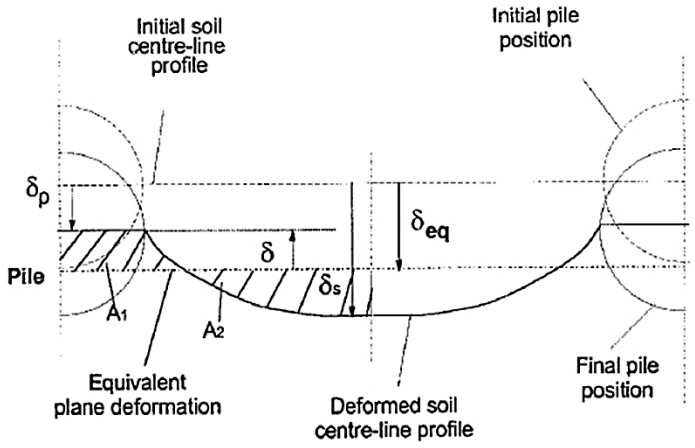

Figure (2- 24): Soil-pile displacement under lateral loading (Bransby, 1996)

Greater variation is observed with spacing in cohesionless soils (Chen and Martin, 2002). Chen and Poulos (1997) studied passively loaded piles in sand and they showed that the ultimate pressure decreases with reducing pile spacing. Similar behaviour was observed by Liang and Zeng (2002) using the Finite Element Method.

Ito and Matsui (1975) considered a general soil strength model (Mohr-Coulomb yield criterion) as shown in Figure (2-25). Assuming that the soil yields around the piles in this way gives the maximum pressures that the piles must be able to carry if they are not to break. Whether this can be provided will depend on the structural capacity of the piles.

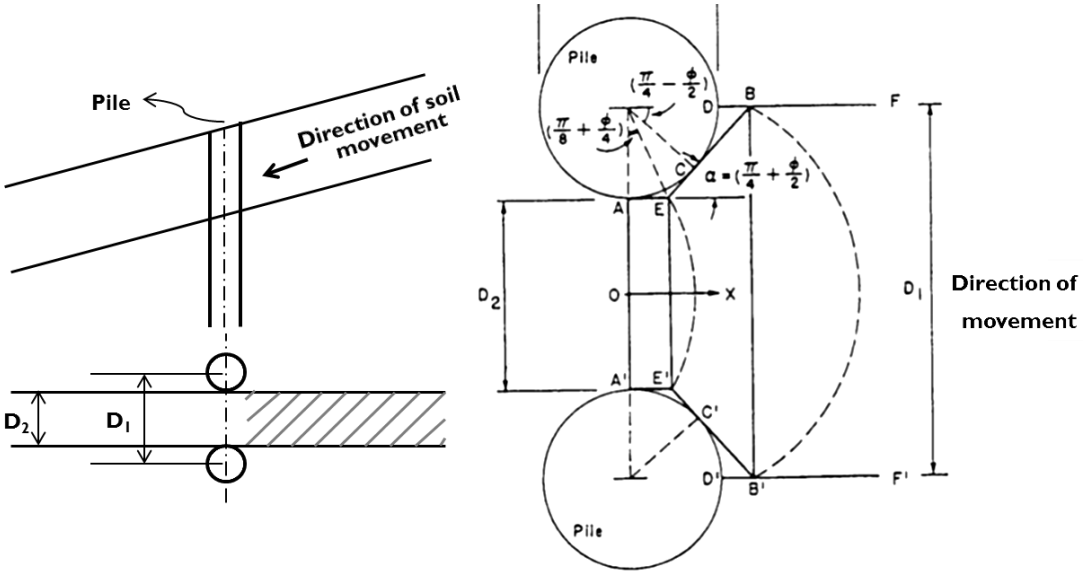

Figure (2- 25): State of plastic deformation in the ground just around piles (Ito and Matsui, 1975)

The planes EB and E'B' in Figure (2-25) are assumed to be principle stress planes (Ito and Matsui, 1975); this assumption is incorrect because the two planes are not perpendicular on another. Thus, De Beer and Carpentier (1977) assumed corrected principal stress directions and resolved the solution to determine the pile loading and they found that there large differences to the Ito and Matsui calculated values especially for drained soils.

2.6.4 Mobilised forces within actively-loaded piles

2.6.4.1. Elastic continuum approach

Laterally loaded piles analysis was started at the beginning of the 1960s using the boundary element methods. Some of the presented solutions for both free-head and fixed-head pile response are presented by Poulos (1974). Some of these solutions are based on constant soil shear modulus with depth, while others based on linear variation in soil modulus with depth (i.e. Banerjee and Davies 1978); these are summarised in Table (2-1) and Figure (2-26).

Table (2- 1): Summary of elastic solutions of laterally loaded piles with constant soil modulus with depth (Poulos, 1971).

Pile response	**Free-head pile**	**Fixed-head pile**
Pile-head displacement (U)	$U = I_{UH}(\frac{H}{E_s L}) + I_{UM}(\frac{M}{E_s L^2})$	$U = I_{UF}(\frac{H}{E_s L})$
Pile-head rotation (θ)	$U = I_{\theta H}(\frac{H}{E_s L}) + I_{\theta M}(\frac{M}{E_s L^2})$	0
Maximum moment $(M_z)_{\max}$ for free-head pile or fixing moment at pile head (M_f) for fixed head pile	From Figure (2-31)	From Figure (2-31)

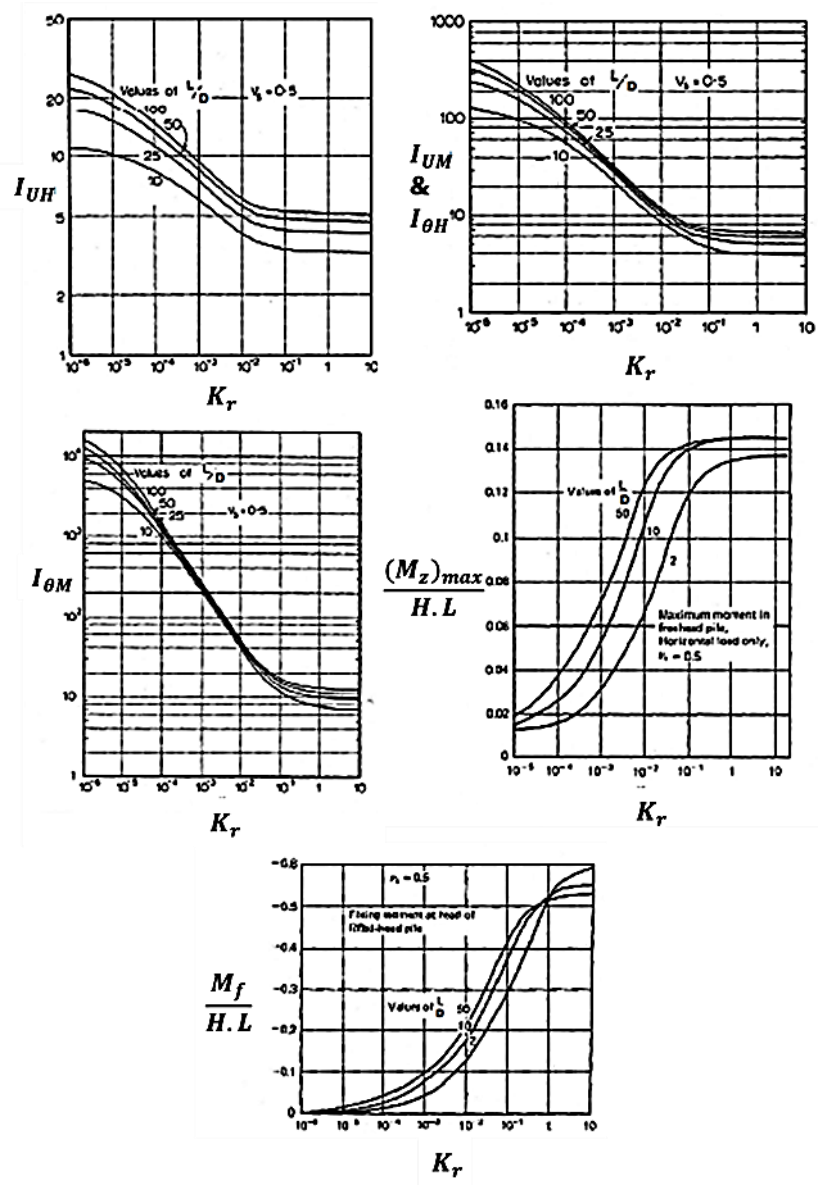

Figure (2- 26): Lateral pile responses influence factors in Case of Constant Soil Modulus (after Poulos, 1971)

In Table (2-1) and Figure (2-28):

$$K_R = \frac{E_p I_p}{E_s L^4} \tag{2-30}$$

where

K_R, the pile flexibility factors.

D is the pile diameter.

E_p is the modulus of elasticity of piles.

Es is soil modulus.

H is the applied horizontal force at ground level.

I_p is moment of inertia of pile.

I_{UH} , I_{UM} , $I_{\theta H}$, $I_{\theta M}$ and I_{UF} are dimensionless influence of factors.

L is the pile length

M is the moment of ground level.

Vs is the Poisson's ratio.

The continuity of the soil is taken into account in the analysis procedure of this method. In determining E_s, Poulos, (1995) provided a simplified lateral pile response analysis in which suggestions of appropriate elastic Young's modulii of the soil were made. It was shown that the lateral piles' response depends significantly on the soil elastic modulus and pile-soil pressure (which depends on the relative stiffness between the piles and the soil). The soil elastic moduli suggested were, for cohesive soil:

$$E_s = \alpha.C_u \tag{2-31}$$

where:

E_s : Soil elastic modulus

α : Rigidity index between 150-400, depending on the relative pile-soil stiffness (Banerjee and Davies, 1978, Decourt, 1991, Poulos and Davis, 1980)

For cohesionless soil:

$$E_s = N_h.z \tag{2-32}$$

where according to (Decourt, 1991):

N_h: 1.5 MPa/m for saturated loose sand
N_h: 5 MPa/m for saturated medium dense sand
N_h : 12.5 MPa/m for saturated dense sand
z : soil depth

The nonlinearity of the soil behaviour, especially under large strains, is not considered in this method. Thus, this method is valid for small strain deformations only due to its simplicity. The elasto-plastic soil behaviour is incorporated into account, the soil yielding, by modified the boundary element method. The lateral pressure along pile is specified and limited for each element and the calculated soil-pile pressure should not exceed these limitations (i.e.Spillers and Stoll, 1964). Poulos (1971) followed some of these principles to investigate the effects of soil yielding on the response of laterally

loaded piles in different soil pressure along the pile-depth. The yield of the soil, variation in soil modulus and layered soil has been widely taken into account in modified boundary element analysis. However, analysis methods that summarised above are suitable for static problems only and they needs a lot of work experimental data to be applicable to work under dynamic loads.

2.6.4.2 Winkler method and P-y method

Winkler (1867) represented a laterally loaded pile as a beam in elastic soil with the soil represented as a series of elastic springs. The idea of this method is illustrated schematically in Figure (2-27).

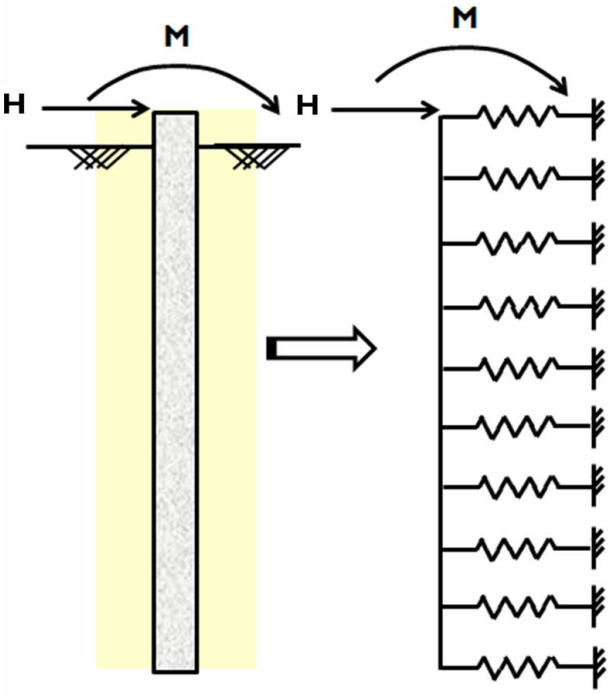

Figure (2- 27): illustration of Winkler spring methods for laterally loaded piles.

The information required for analysing laterally loaded piles using this method are summarised in Table (2-2). The method is also known as the subgrade reaction method. The subgrade reaction term referred to indicates the pressure or soil reaction per unit length of pile, p, induced for unit deflection of the pile, y. The ratio between p and y is called the modulus of subgrade reaction:

$$k = \frac{p}{y} \tag{2-33}$$

Terzaghi (1955) showed that the modulus of subgrade reaction considered being independent of pile diameter while others observed that the soil resistance is significantly effects with increasing of pile diameter. (i.e. Carter, 1984 and Liang, 1988).

Table (2- 2): Definitions and dimensions used in laterally loaded piles analysis

Description	Symbol	Definition	Dimension
Soil resistance per unit length	p		F/L
Pile deflection	y		L
Pile diameter	D		L
Spring spacing	ΔL		L
Spring force	F	$F = p * \Delta L$	F
Soil pressure	P	$\mathrm{P} = p / D$	F/L^2
Modulus of subgrade reaction	K	$K = \frac{p}{y}$	F/L^2
Soil spring stiffness	K_s	$K_s = \frac{F}{y} = K\Delta L$	F/L
Coefficient of subgrade reaction	k	$k = \frac{P}{y} = \frac{K}{D}$	F/L^3

According to this concept, the lateral pile analysis is represented by a fourth-order differential equation:

$$E_p I_p \frac{d^4 y}{dz^4} + ky = 0 \qquad (2\text{-}34)$$

where E_p the modulus of elasticity of the pile, I_p is the moment of inertia of the pile section and z is the depth. By using a constant modulus of subgrade reaction with depth, the analytical solution can be obtained. The finite difference method can be used to solve the problem where the subgrade reaction varies with depth.

Vesic (1961) estimated the modulus of subgrade reaction from the soil shear modulus and pile bending stiffness as:

$$K = \frac{0.65E_s}{1-\nu^2}\left[\frac{E_s D}{E_p I_p}\right]^{1/12} \quad (2\text{-}35)$$

where E_S soil modulus, ν Poisson's ratio of the soil, D pile diameter and $E_p I_p$ the bending stiffness of the pile.

To overcome some of the limitations of the original Winkler model, non-linear springs can be used, with properties that vary with depth. This is widely known as the *p-y* method. Full scale lateral loads tests results conducted at different ranges of pile diameters in-situ have been used to obtain pile deflection-soil resistance relationships, i.e., the P-y curve (e.g. Reese et al., 1974 for sands and Matlock, 1970 for soft clays).

2.6.4.3 p-y curves in sand

Results of in-situ tests of 0.6m embedded piles within the Mustang Island sand and flexible driven embedded piles in submerged dense fine sand of Cox et al. (1974) were used by Reese et al. (1974) to determine P-y curves in sand. He observed that the P-y curve relationship is non-linear and can be approximated by three straight lines covering three regions which can then be connected by a parabolic curve. In this procedure, the initial modulus of subgrade reaction and the ultimate soil resistance are estimated using relative densities (Reese et al., 1974). For small deflection (linear variation of soil modulus, E_s with deflection), the initial line of the curve is governing. Thus, the first portion is observed at a small load level. The ultimate soil resistance can be determined by the wedge failure mechanism theory near the ground surface and flow failure model below the ground surface (as outlined in Section 2.6.2). The wedge failure mechanism is shown schematically in Figure (2-28a) and a typical normalised P-y curve for sand is shown in Figure (2-28b).

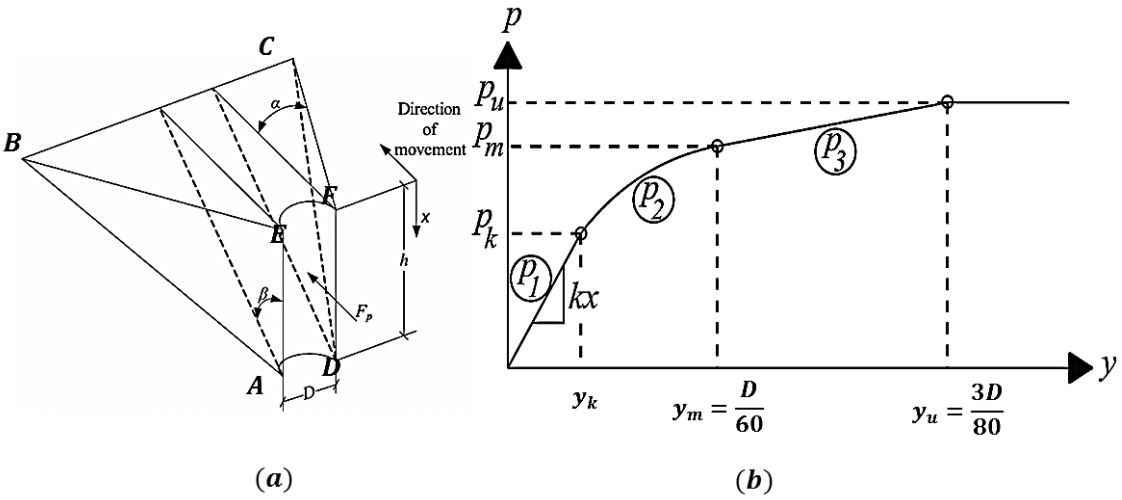

Figure (2- 28): wedge failure mechanism in sand; and (b) P-y curve for sand (After Reese et al., 1974)

where:

$$\alpha = \frac{\phi}{2} \quad \text{and} \quad \beta = 45 + \frac{\phi}{2}$$

The total lateral force can be determined by using the minimum values given by the two equations below:

$$P_{u1} = \gamma z \left[\frac{k_o z \tan\phi \sin\beta}{\tan(\beta-\phi)\cos\alpha} + \frac{\tan\beta}{\tan(\beta-\phi)}(b + z\tan\beta\tan\alpha) + k_o z \tan\beta(\tan\phi\sin\beta - \tan\alpha) - k_a b \right] \tag{2-36}$$

$$p_{u2} = k_a b \gamma z \tan^8(b-1) + k_o b \gamma z \tan\phi \tan^4\beta \tag{2-37}$$

Where

$$K_a = \tan^2(45 - \frac{\phi}{2}) \tag{2-38}$$

And

$$K_o = 0$$

At both $y_u = \frac{3D}{80}$ and $y_m = \frac{D}{60}$, and for static or dynamic problems, p_u and p_m respectively can be calculated using the equations below:

$$p_{u\,cyclic} = A_{cyclic}\, p_u \tag{2-39}$$

$$p_{m\,cyclic} = B_{cyclic}\, p_u \tag{2-40}$$

Where A_{cyclic} and B_{cyclic} are dimensionless parameters to calculated the ultimate soil; resistance and can be determined from Figure (2-29).

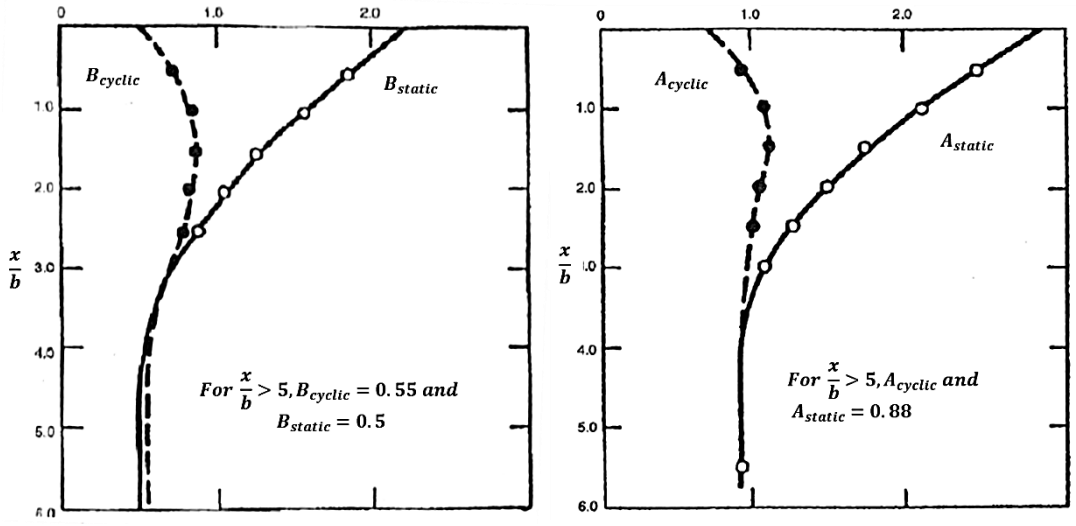

Figure (2- 29): Dimensionless parameters for ultimate soil resistance calculations (Reese et al., 1974)

The initial straight line of the p-y curve in the first portion can be calculated by:

$$p = k_{py} z y \tag{2-41}$$

where k_{py} can be determined from Table (2-3).

Table (2- 3): Initial stiffness for sand (Reese et al., 1974)

State of sand	Loose sand	Medium sand	Dense sand
(based on relative density)	$\phi < 30^o$	$30 \le \phi < 36^o$	$\phi \ge 36^o$
k_{py} above water table (kN/m^3)	6800	24400	61000
k_{py} below water table (kN/m^3)	5400	16300	34000

The parabolic curve to connect the two straight lines at points *m* and *u* can be calculated using the parabolic equation:

$$p = C y^{1/n} \tag{2-42}$$

where $n = \frac{p_m}{m y_m}$, $m = \frac{p_u - p_m}{y_u - y_m}$ and $C = \frac{p_m}{y_m^{1/n}}$

Finally, the point *k* can be determined by the equation:

$$y_k = \frac{C}{k_{py} z} \tag{2-43}$$

O'Neill and Murchison (1983) developed a new set of P-y curves which were later approved by the American Petroleum Institute (API) to estimate the load-deflection relationship (*p-y* curve) in sands. The P-y curve in sandy soil was simplified using a hyperbolic tangent function to represent the shape of the relationship.

$$p = A.p_u.\tanh\left[\frac{k.z}{A.p_u}.y\right] \tag{2-44}$$

where *p* is the soil resistance which is given as the reaction force per unit length acting on the pile, p_u is the ultimate soil resistance which is given as a point of maximum soil resistance, *y* is the lateral relative soil-pile deflection, *A* is a modification factor for cyclic loading (= 0.9), *k* is the initial modulus of subgrade reaction and *z* is the depth of failure zone. The ultimate lateral capacity pu is calculated as the lower of:

$$p_u = (C_1.z + C_2.D).\gamma.z \qquad \text{for shallow depth} \tag{2-45}$$

$$p_u = C_3 D \gamma z \qquad \text{for deep depth} \tag{2-46}$$

where *D* is the pile diameter (width here) and γ is the effective unit weight of soil. The initial subgrade reaction (*k*) can be determined as a function of the angle of friction also from the Figure (2-32a), while coefficients C_1, C_2 and C_3 can also be calculated as a function of the angle of internal friction (API recommended practice, 2000) from Figure (2-30b).

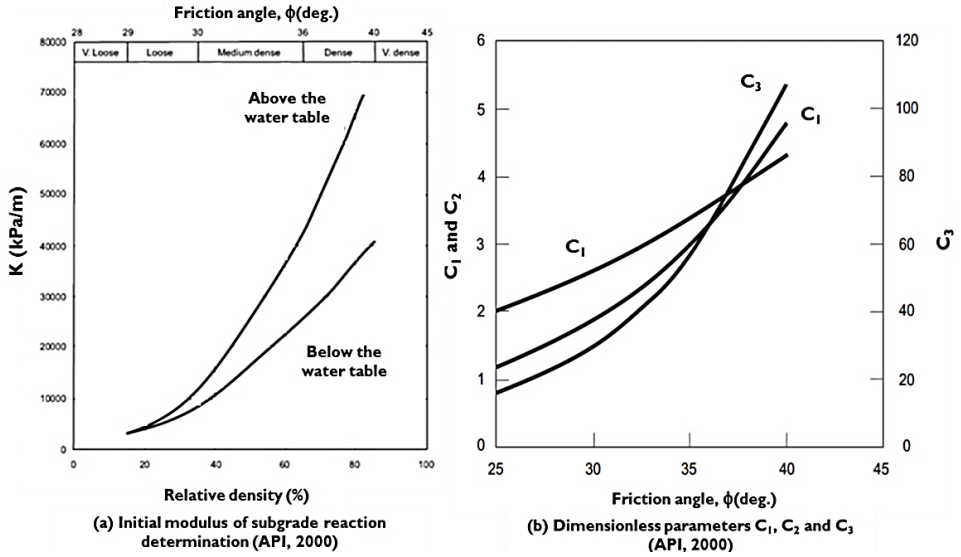

Figure (2- 30): Initial subgrade reaction and dimensioless parameters to determine the ultimate soil resistance (API, 2000)

2.6.5 Mobilised forces within passively-loaded piles

Piles used to remediate slopes will be subjected to lateral load in the direction of the slope due to the relative soil pile movement, as described previously. Two major considerations should be taken into account in the design of laterally loaded piles, namely lateral pile head displacement and the maximum bending moment in the pile (Tandjiria et al 2000).

The slip surface in the slope may be either shallow or deep. Recent studies have shown that the maximum bending moment is generated below the slip surface while the maximum shear force occurs at the slip surface. For these reasons, the piles should be embedded to a suitable depth below the slip surface to prevent or reduce the overall sliding of the pile through the soil mass and to make the pile as a restrained element against the movement. Figure (2-31) shows the failure mode for different slip depth-pile length ratios (Poulos, 1995).

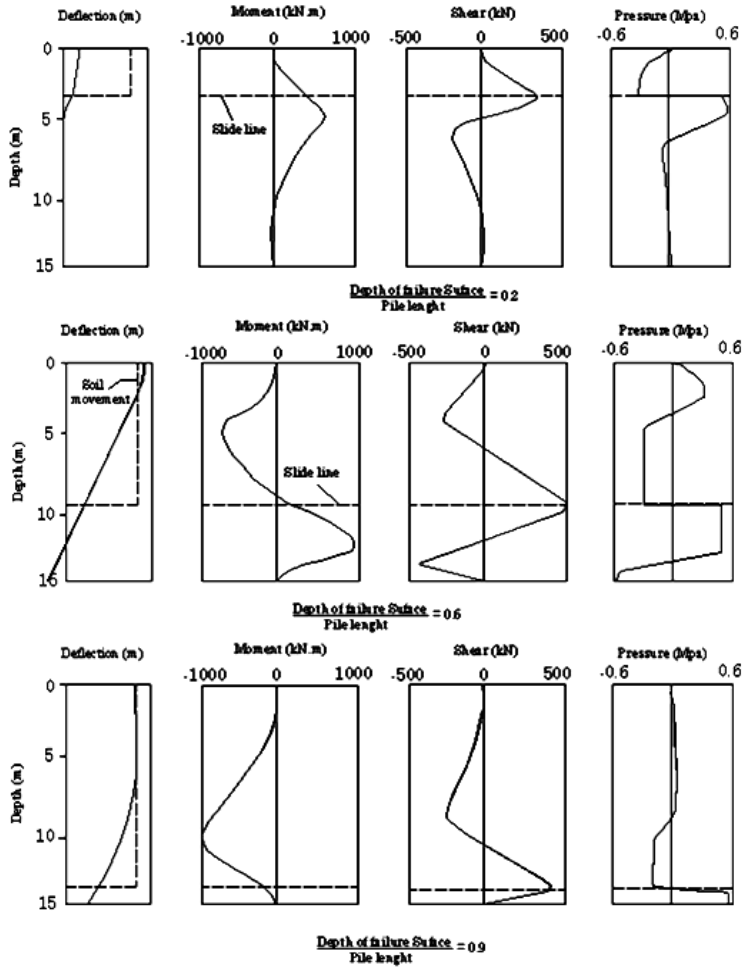

Figure (2- 31): Typical failure mechanisms observed for piles with different embedded lengths (Poulos, 1995)

The mobilised soil pressures also depend on the relative soil-pile stiffness. The piles which stabilise a sliding slope may be idealised as rigid or flexible. (Viggiani, 1981). The term 'rigid' refers to a pile which is very stiff compared to the soil and generally having a moment of resistance much bigger than the maximum bending moment induced. The term 'flexible' refers to piles which are likely to bend appreciably as the soil deforms and which have a moment of resistance near the value of maximum bending moment induced within the pile. Models of failure and induced forces and bending moments for rigid and flexible piles are shown in Figure (2-32).

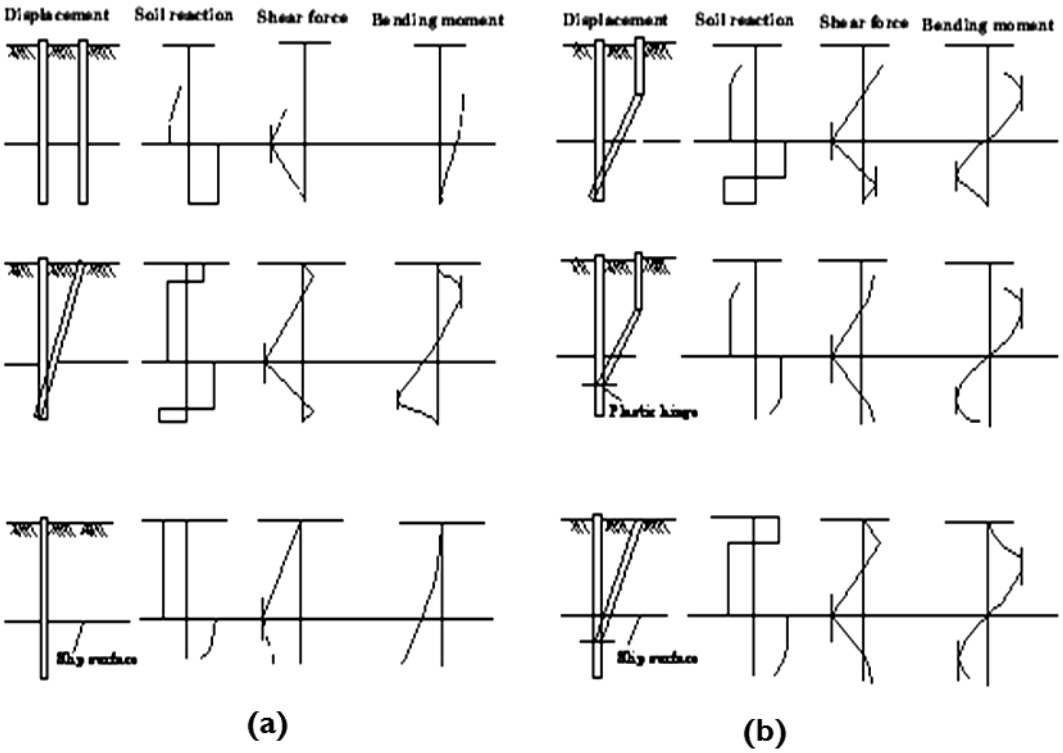

Figure (2- 32): Failure models for: (a) rigid piles, (b) with plastic hinges (Viggiani, 1981)

It is generally assumed for laterally loaded piles that there is no bending moment along the piles before soil movement due to slope failure, with the initial distribution of stresses assumed to be uniform around pile (Figure 2-33a). As the soil starts to move due to slope failure, a soil pressure on the upslope face of pile is induced and the distribution of this pressure will be just on upslope face along the pile (Figure 2-33b). The soil pressures acting on the pile can be determined using the *p-y* method where the *p-y* curves have soil displacements included within the moving soil as part of the relative displacement. Once the soil reactions have been determined, the shear force distribution can be obtained by integration of the soil reactions along the length of the piles; further integration can then give the bending moments, rotations and displacements.

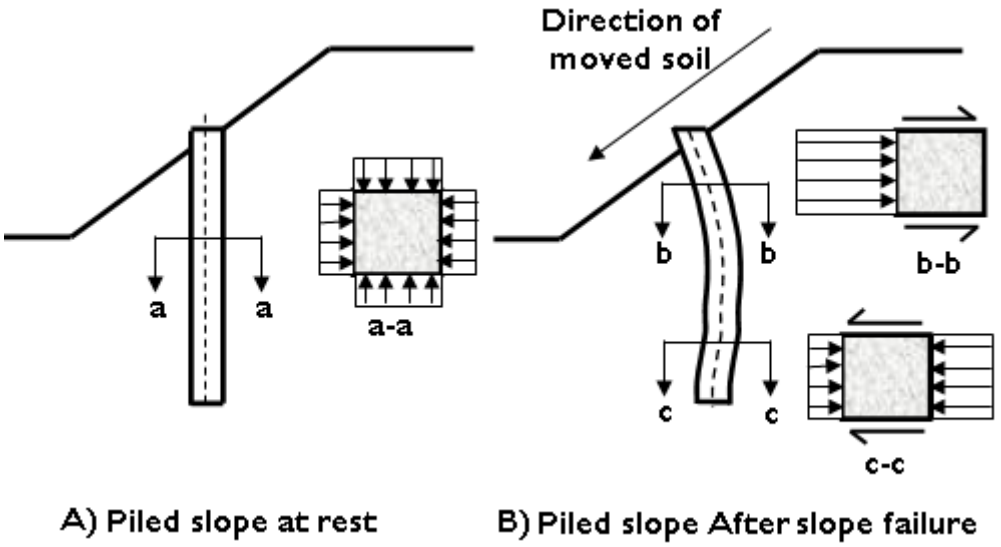

Figure (2- 33): schematic conceptual of load-deflection definition

2.7 Arching in pile-reinforced slopes

According to the published ASCE Glossary of terms and definitions in soil mechanics in 1958, arching refers to the transfer of stresses from yielding regions of the soil mass to an adjacent less yielding or restrained region of the soil mass. Many variables effect this phenomenon including: soil strength, elastic modulus and displacement.

Much previous research has been conducted for different types of soil and circumstances to investigate and observe the arching mechanism within piled slope systems. Adachi et al. (1989) used circular and square cross sectional pile models made from aluminium, distributed in a horizontal arrangement in a loose sandy slope with 30^{o} angle of friction as shown in Figure (2-34). A moving plate at one end of the model was used to provide soil movement. Strain gauges were glued along the piles to measure the load during soil movement Different pile spacing were used in this study. They found that the arching shape between piles was observed to be approximately semi-triangular in the plane of movement as shown in Figure (2-34). The loading acting on the piles was also observed to increase with increased pile spacing and this effect was 15% larger for square piles compared with circular piles as shown in Figure (2-35).

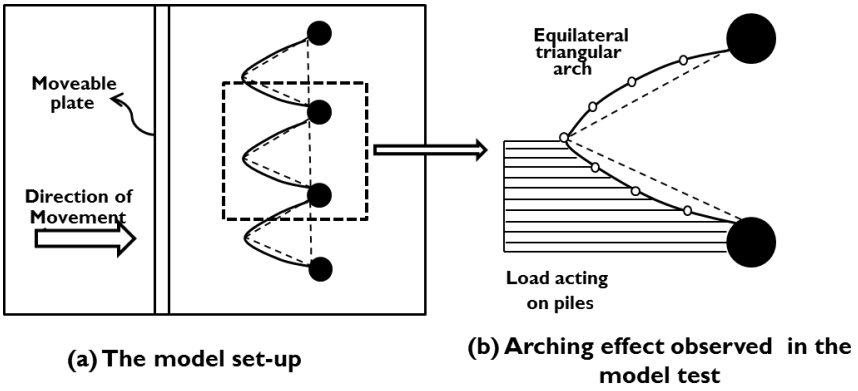

Figure (2- 34): Arching effects observed (after Adachi et al., 1989)

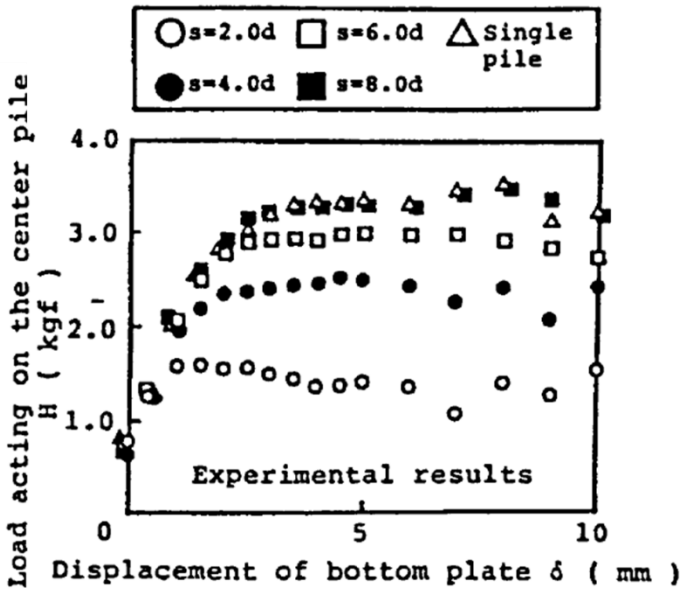

Figure (2- 35): Load-displacement curves for the piles at different spacing (after Adachi et al., 1989)

Kaolin model slopes stabilised by piles at different pile spacing ratios (3, 4 and 6 times the pile diameter) were tested using centrifuge modelling by Hayward et al. (2000) as shown in Figure (2-36). Strain gauges were glued along the piles to measure bending moment while two cameras were installed, one observing the glass side face of the soil container and the other mounted above the slope, both for displacement tracking. Hayward et al. (2000) observed that about 2m of the length of pile (measured from the top) was loaded uniformly due to downslope movement. The distribution of the pressure along the loaded portion was calculated by differentiating the measure bending moment. It was also observed that the calculated pressure was less than the limitations suggested by Broms (1964) and Fleming (2009); this was

attributed to the absence of a stiff strata underling the slope body leading to slope-pile movement towards the toe of the slope. The effect of pile spacing on the pressures on the piles is shown in Figure (2-37).

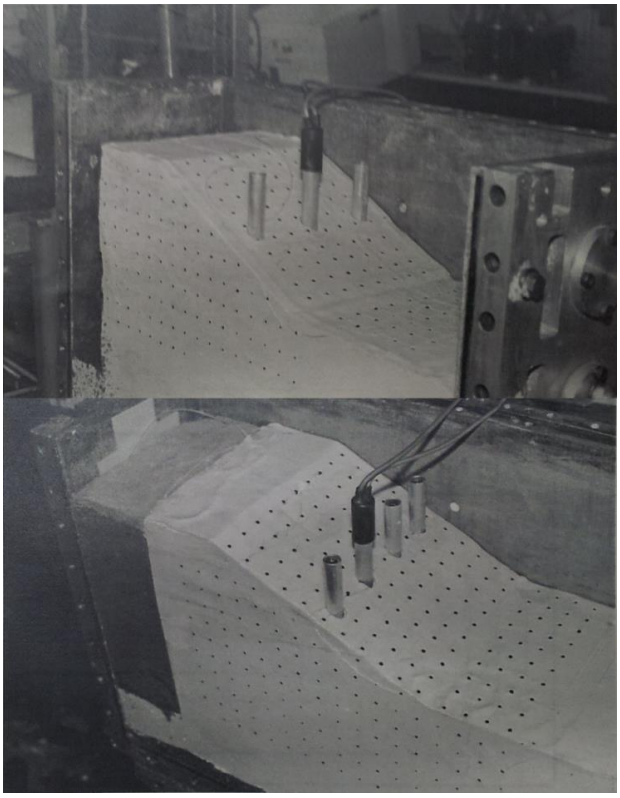

Figure (2- 36): Model kaolin slope (after Hayward et al, 2000)

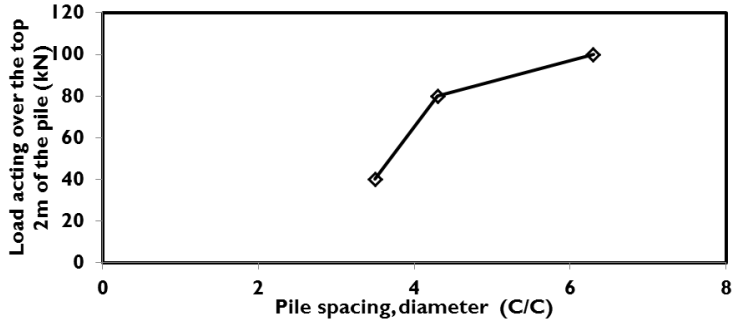

Figure (2- 37): Effects of pile spacing on pile-head loads acting on the top 2 m of pile in prototype scale (after Hayward et al, 2000)

Many numerical models have also previously been implemented to investigate the arching mechanism. Liang and Zeng (2002) used the experiments of Bosscher and Gray (1986) and Adachi et al (1989) and by using two dimensional Finite Element

principles to study this behaviour as shown in Figure (2-38). Elastic-perfectly plastic soil behaviour was modelled and the piles were assumed to be rigid. A triangular prescribed displacement was applied between the two piles to simulate the soil arching. The results are summarised in Figure (2-39). They also concluded that the square pile gives more effective of arching compared to the circular section.

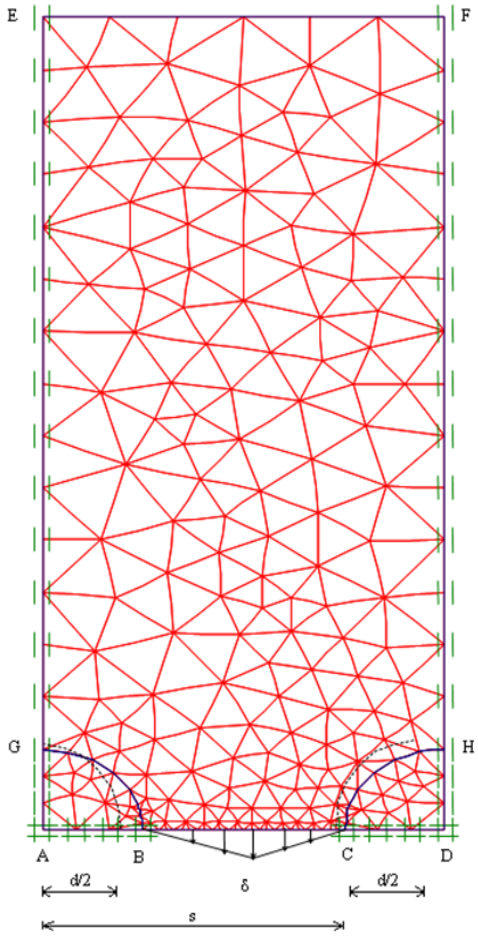

Figure (2- 38): Finite element model of slope-pile system (After Liang and Zeng, 2002)

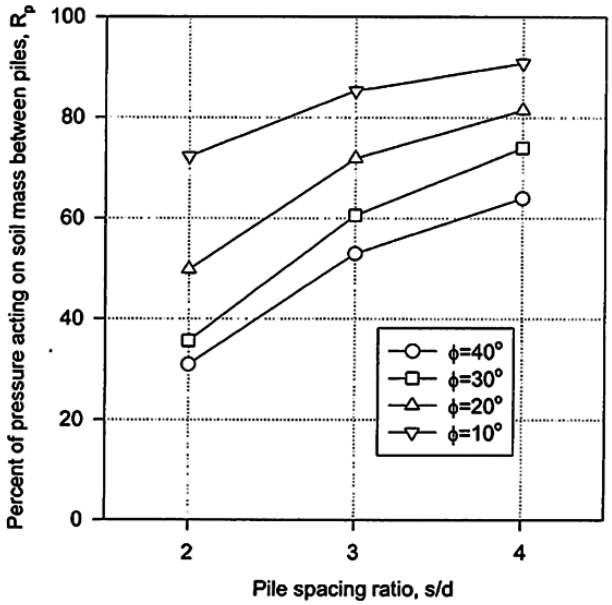

Figure (2- 39): Pile spacing effect on generated loads on between piles (After Liang and Zeng, 2002)

Chen and Martin (2002) used the Finite difference method to study the arching behaviour within pile-slope systems as shown in Figure (2-40). A fixed displacement at opposite boundaries of the models and the piles remain fixed in position (In contrast of Liang and Zeng, 2002 model). A semi-circular shape for the arching effect is indicated upslope of the piles based on the rotation of the principal stresses as shown in Figure (2-41).

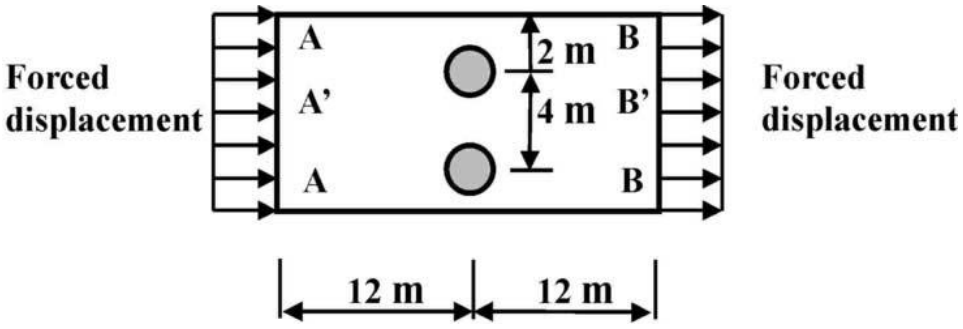

Figure (2- 40): Configuration finite difference model (Chen and Martin, 2002)

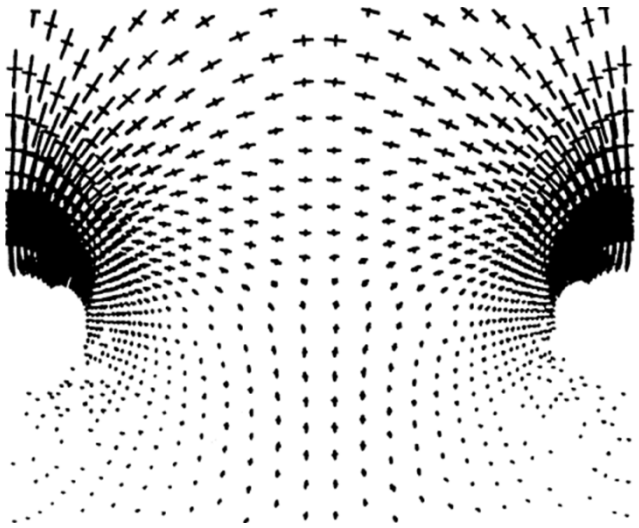

Figure (2- 41): Rotations of principal stress direction in granular soil between piles (Chen and Martin, 2002)

Wang and Yen (1974) studied the behaviour of an infinite slope stabilised by circular piles and sliding above a strong underlying stratum, with the piles at different pile spacing. As shown in Figure (2-42a), the shear bands were assumed to be generated either side of the piles and these shear bands transfer the stresses from the yielded soil between the piles to the un-yielded soil adjacent to it and then to the piles themselves. Figure (2-43) shows the effect of pile spacing on calculated loads along the first four meters of the piles' length.

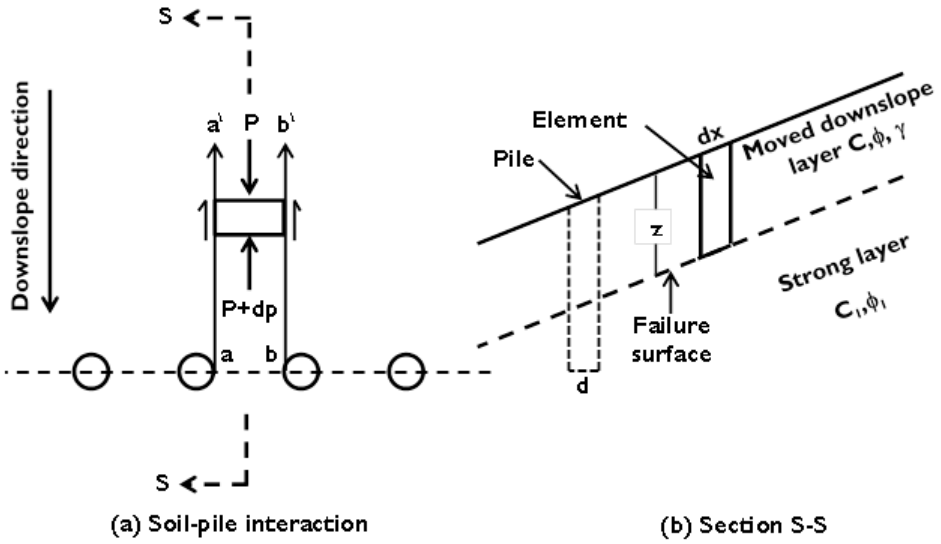

Figure (2- 42): Soil-pile configuration for Wang and Yen, 1974

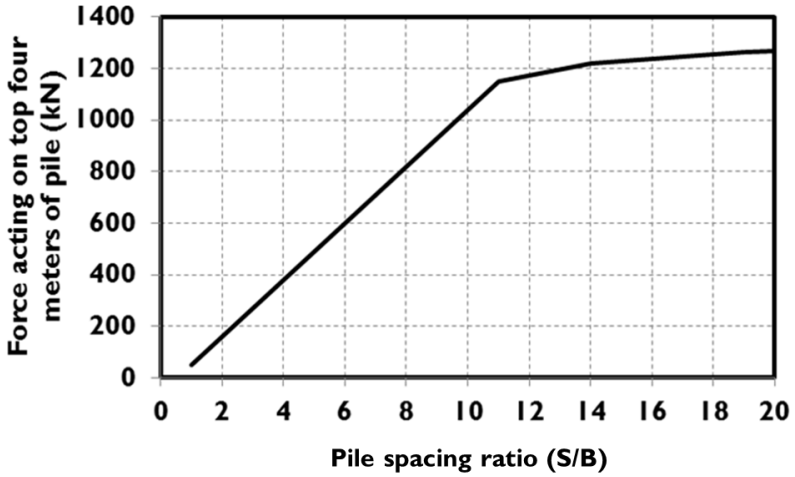

Figure (2- 43): Pile spacing-head pile load relationship
(after Wang and Yen, 1974)

As it seen in Figure (2-43), pile-spacing up to 11 times the diameter gives some soil arching.

2.8 Dynamic soil behaviour

2.8.1 Overview

The dynamic seismic response of cohesionless soils has been widely studied in previous research, both to understand the mechanism of cyclic loading under earthquakes and to develop analytical procedures for evaluating the response of soil deposits and structures under these seismic loads. In general, the seismic response of soil can be described by the shear modulus (G) and damping (D) characteristics for the soil deposits under cyclic loading conditions. This can be done by using the equivalent linear analysis method in which the shear modus and damping ratio are dependent on the magnitude of the shear strain developed in the soil deposits.

The maximum shear modulus can be determined using the general formula proposed by a lot of researchers (i.e. Hardin and Drnevich, 1972; Iwasaki et al., 1976; Ishibashi, 1993) amongst others:

$$G = K(\gamma).f(e).\sigma_o^{'m} \qquad (2\text{-}47)$$

where $K(\gamma)$ is a decreasing function of the cyclic shear strain amplitude, γ , being unity at very small strain (for G_{max} calculations); $\sigma_o^{'}$ isotropic effective stress and *m*: exponent of isotropic effective stress. Hardin and Black (1968) presented a relationship to calculate the initial shear modulus (G_o) at zero shear strain level (Maximum shear modulus) and the degradation of this shear modulus (G) with increasing of the strain level as a ratio from the Max shear modulus (G/G_o) using the equation:

$$G_{\max} = 6908\frac{(2.17-e)^2}{1+e}.\sqrt{\sigma_o^{'}} \tag{2-48}$$

Where: G_{max} is in kPa; e is void ratio and σ_v' is the principles affective stress in kPa.

The equation above is more applicable for sand with round-grained particles. For angular grained sand particles is more applicable to use the equation:

$$G_{\max} = 3230\frac{(2.97-e)^2}{1+e}.\sqrt{\sigma_o^{'}} \tag{2-49}$$

The shear modulus as a function of strain can then be calculated from the relationship:

$$G = \frac{G_{\max}}{1+\frac{\gamma}{\gamma_r}} \tag{2-50}$$

where, γ_r the reference strain is given by:

$$\gamma_r = \frac{\tau_{\max}}{G_{\max}} \tag{2-51}$$

and

$$\tau_{\max} = \sqrt{[(\frac{1+K_o}{2}.\sigma_v^{'}.\sin\varphi^{'} + c^{'}.\cos\varphi^{'})^2 - (\frac{1-K_o}{2}.\sigma_v^{'})^2]} \tag{2-52}$$

where:

K_o: coefficient of lateral earth pressure.

$\sigma_o^{'}$: vertical effective stress.

$c^{'}$, $\varphi^{'}$: static strength parameters in term of effective stress.

The damping ratio can be also calculated as a function of the strain by:

$$D(\%) = \frac{D_{\max} \frac{\gamma}{\gamma_r}}{1 + \frac{\gamma}{\gamma_r}} \tag{2-53}$$

Where $D_{\max}$ is the maximum damping ratio (at very large strain) and can be estimated by:

$$D_{\max} = B - 1.5 \log_{10} N \tag{2-54}$$

Where B a factor is equal to 33 for dry sand and 28 for saturated sand, and N is the number of cycles of loading.

2.8.2 Factors influencing shear modulus for sand

Hardin and Drnevich (1972) showed that there are many factors affecting the shear modulus during seismic loading, including confining pressure, shear strain amplitude, void ratio and relative density. Seed and Idriss (1970) proposed a convenient relationship between the shear modulus and confining pressure:

$$G = 218.82.k.\sqrt{\sigma_o'} \tag{2-55}$$

where k is the shear modulus coefficient, having a maximum value at very low shear strain levels (10^{-4}). They also plotted the measured shear modulus at any shear strain level, G normalised by the maximum shear modulus, G_0 with the shear strain as shown in Figure (2-44).

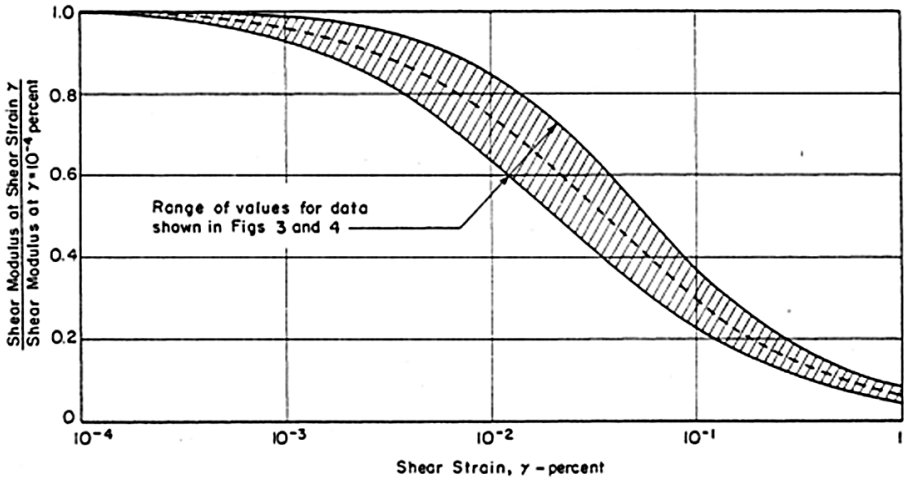

Figure (2- 44): Variation of normalised shear modulus with shear strain for sand (after Seed and Idress, 1970)

Figure (2-45) shows how the shear strength parameter φ', effective vertical stress σ_v', and lateral earth pressure K_o affect the shear modulus coefficient, k, based on the equations proposed by Hardin and Drnevich (1972). From Figure (2-47), three important points can be summarised:

1- At high shear strain level ($\gamma > 10^{-3}$), shear modulus coefficient is slightly influenced by the vertical stress, but not affected by lateral pressure K_o, strength parameter φ' and void ratio *e*.

2- For intermediate shear strain ($10^{-5} < \gamma < 10^{-3}$), there are slight influences on shear modulus coefficient, k, from vertical stress, effective angle of friction, φ' and lateral earth pressure, K_o, but it is strongly influenced by void ratio *e*.

3- At low shear strain ($\gamma < 10^{-5}$), the shear modulus coefficient is influenced strongly by void ratio.

These points suggest that the shear modulus coefficient is in general strongly influenced by the void ratio (i.e. relative density) and the shear strain level.

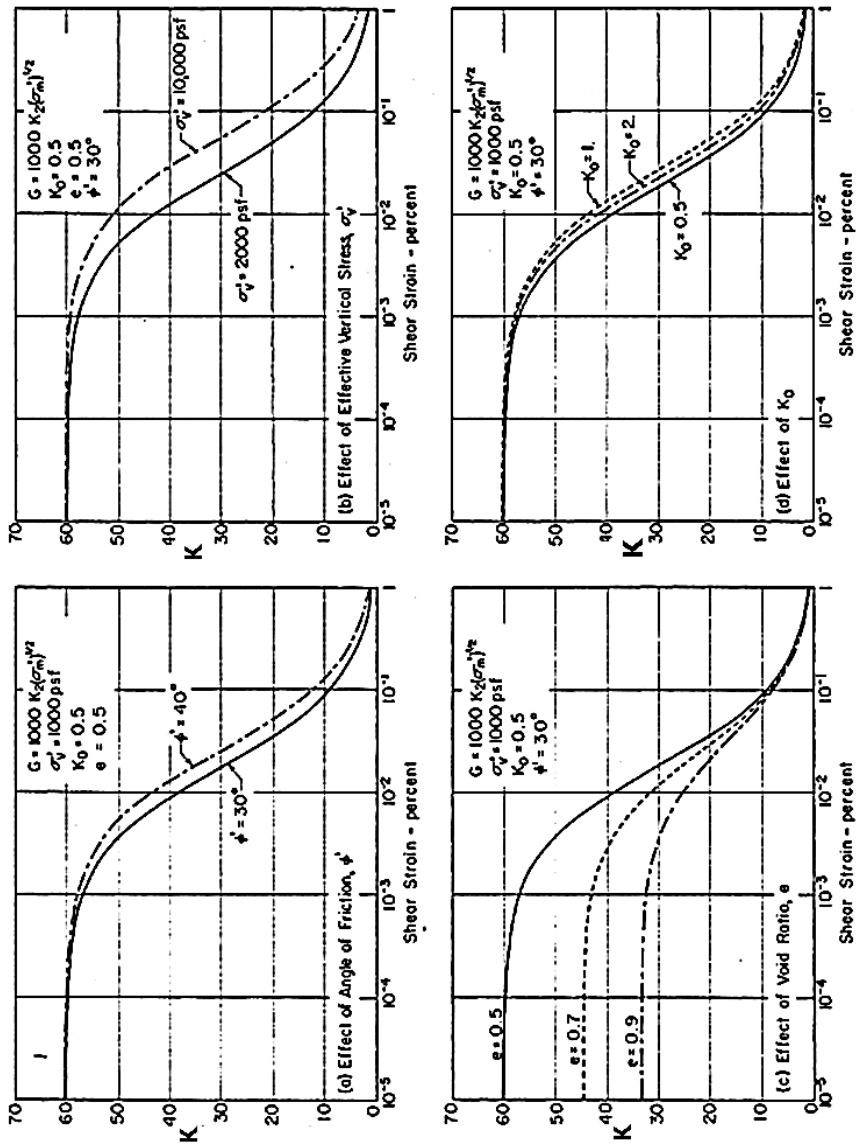

Figure (2- 45): Shear moduli of sand at many various factors (based on Hardin and Drnevich, 1972 equations)

Iwasaki et al. (1976) provided support for the results of Hardin and Drnevich (1972) in that the normalised shear modulus of sand is influenced slightly by the confining pressure. This is shown in Figures (2-46).

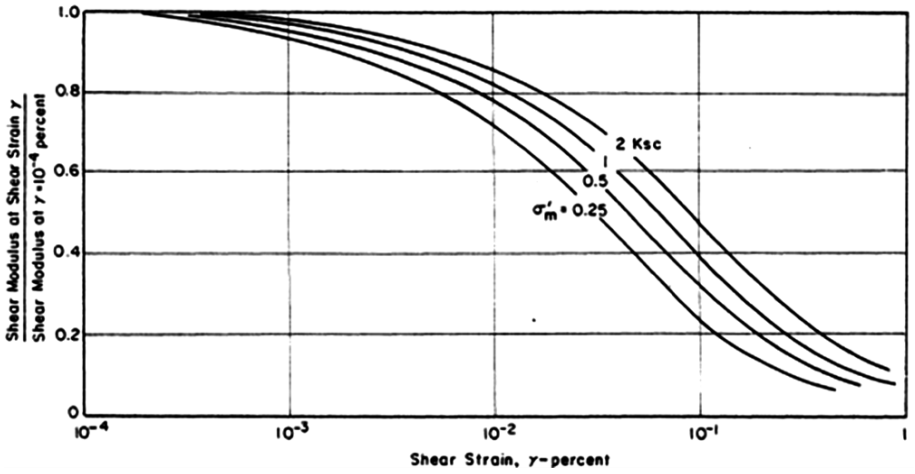

Figure (2- 46): Variation of normalised shear modulus with shear strain for sand (after Iwasaki et al., 1976)

2.8.3 Factors influencing damping ratio for sands

As for shear modulus, Hardin and Drnevich (1972) also concluded that the damping ratio of sand is influenced strongly by shear strain, γ and effective mean principal stress, $\sigma_v^{'}$, while slightly influenced by lateral earth pressure, K_o, void ration, e, angle of friction, $\varphi^{'}$ and degree of saturation, S. They concluded also that the number of cycles does not significantly affect damping by determining the damping for the first 5 cycles and then the number of cycles from 5 to 30. Figure (2-47) show the effects of various factors on the damping ratio for sand.

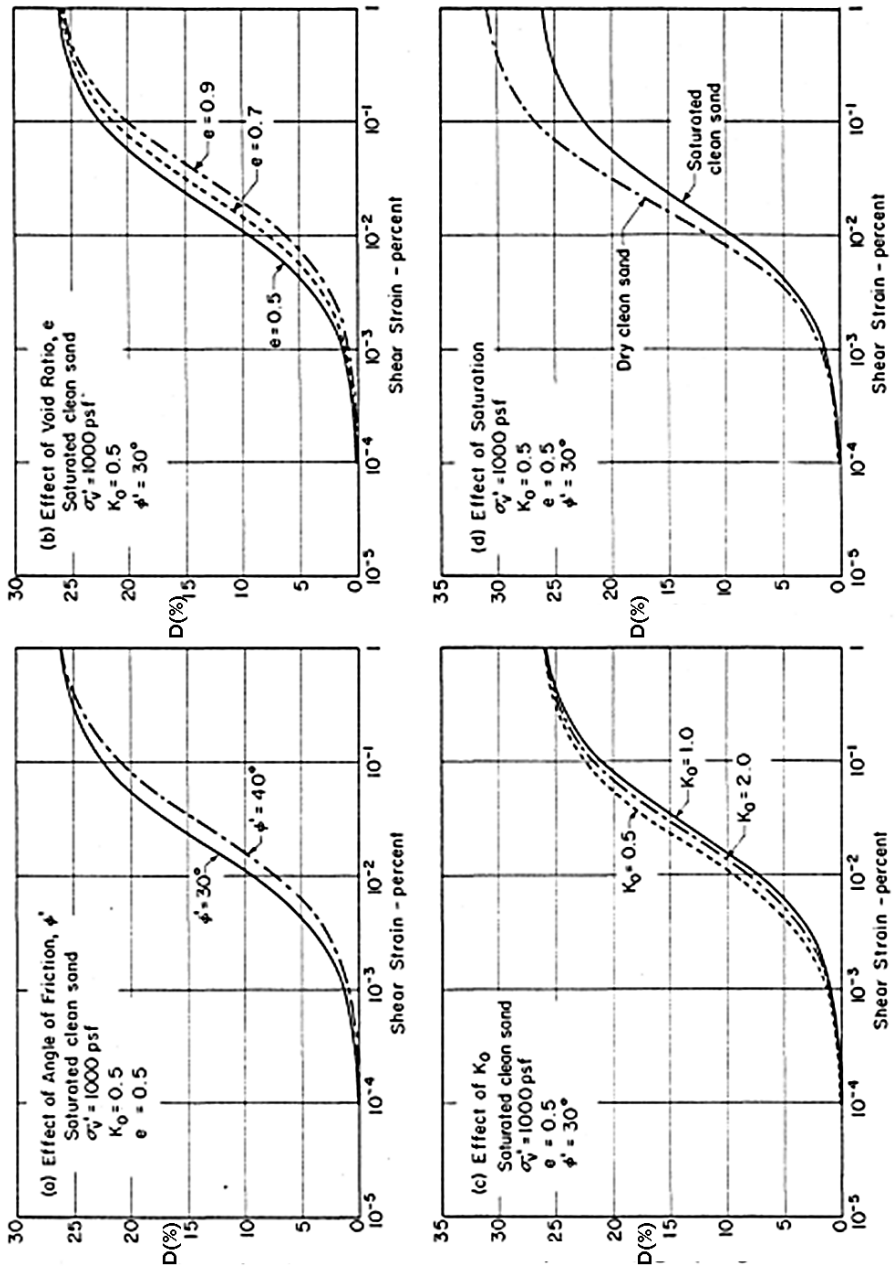

Figure (2- 47): Damping ratio of sand at many various factors (after Hardin and Drnevich, 1972 equations)

It can be seen from Figure (2-48) that the main factor affecting the damping ratio is the vertical confining stress $\sigma_v^{'}$ for both saturated and dry sand. The damping ratio is strongly influenced by the confining pressure especially at shallow depth (low stress) in dry sand (scattered points data in Figure (2-48b)) while the average line for all the test data (solid line) can be consider convenient for many practical purpose.

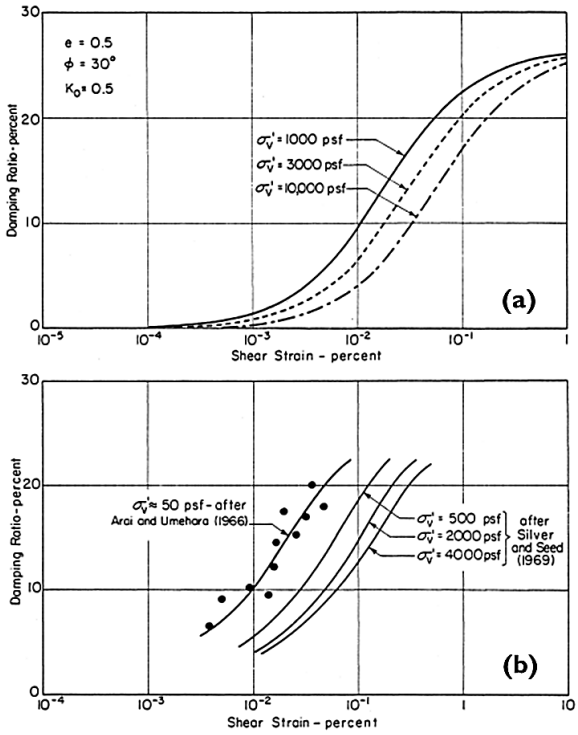

Figure (2- 48): confining pressure effects on damping ratio for (a) saturated sand and (b) dry sand. (after Hardin and Drnevich, 1972)

Figure (2-49) shows many calculated sets of damping data from many studies for sand. For practical purposes, if the damping ratio is calculated at shear strain level between 0.1 to 0.5, then the values of damping for other strain levels can be approximately determined by plotting a line through the data parallel to the solid line in Figure (2-49).

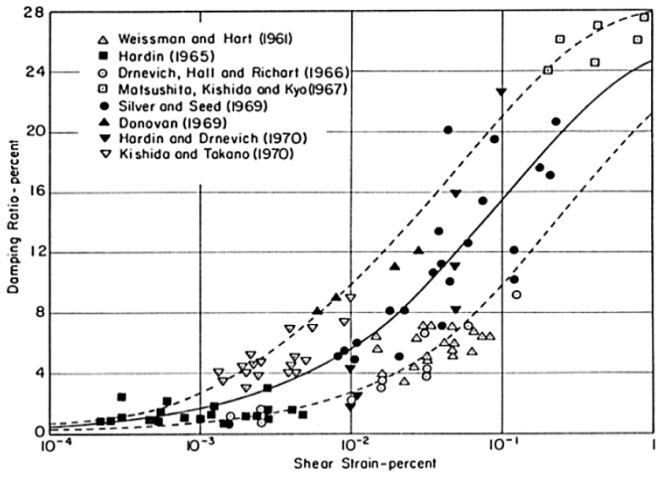

Figure (2- 49): Damping ratio for sand (Seed et al., 1984)

2.9 Dynamic response amplification in slopes

One of the main reasons of damage close to slopes due to earthquakes is the amplification of the soil response at the crest of the slopes. Dynamic amplification can be defined simply as the ratio between the response acceleration at any position in the slope and the input ground acceleration. Often, the term dynamic amplification is used to refer to the effect in level ground (at the ground surface), with an additional term, topographic amplification, being used to describe the amplification due to the slope geometry (i.e. the response at the slope crest divided by the ground surface response in the free-field). Many studies have been conducted on different kinds of soil slopes to investigate dynamic amplification within the slope. These studies were either using principles of physical modelling (e.g. Yu-yuzhen et al., 2008; Yu-yuzhen et al., 2010; Brennan and Madabhushi, 2009) or by using finite elements and numerical simulation (i.e. Kourkoulis et al., 2011; Paolucci et al., 1999; Bouckonalas and Papadimitriou, 2005). In most of the previous studies, the response of the soil at the crest of the slope is larger than at any other position within the slope. Yu et al., 2004 showed that the amplification tendency is consistent with the physical results from Ng et al, 2004 by testing sandy slope using centrifuge technique.

Yu-yuzhen et al (2008) investigated the dynamic performance of a 37^{o} dry sandy slope using a series of geotechnical centrifuge models excited by historically recorded earthquake motions (El-Centro earthquake). They observed that the different frequency contents of the input motions (A1 in Figure 2-50) were amplified to different degrees. It can be seen also that the acceleration response was amplified by approximately 1.6 (A1 = 0.25g at the substrata of the model and A7 = 0.7g near the slope) while this ratio arrived to about 2 comparing with the A8 = 0.35g at the same height in the model away from the slope.

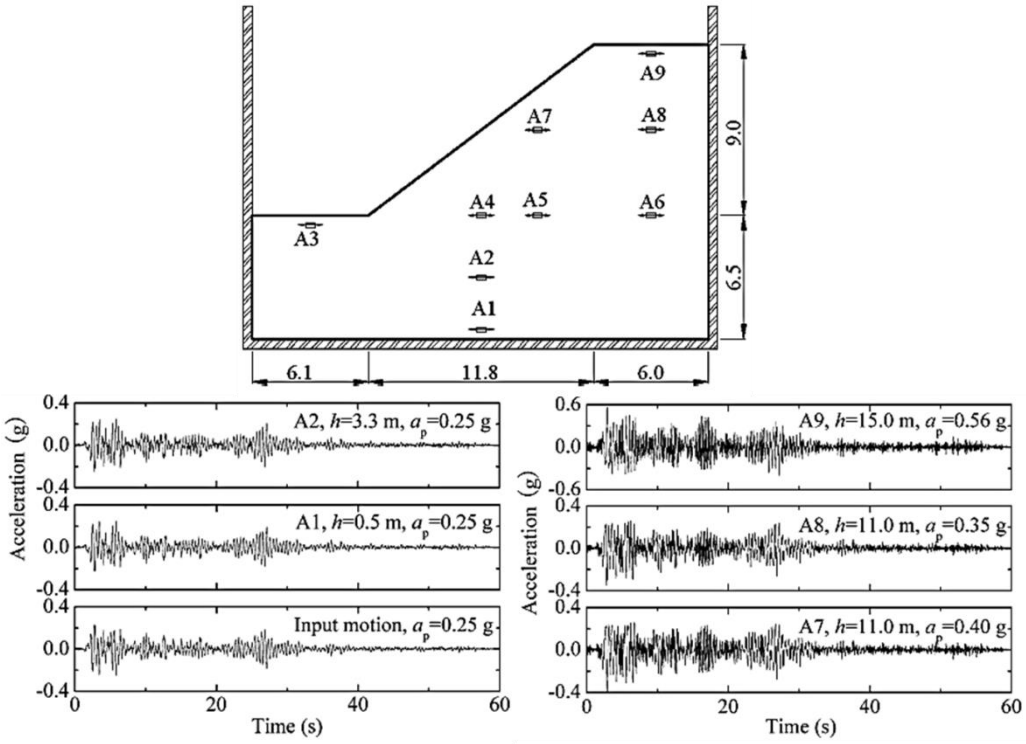

Figure (2- 50): Amplification of the input motion at different position within the slope (Yu-yuzhen et al., 2008)

Yu-yuzhen et al., 2010 observed the dynamic response for pile-reinforced slopes with a similar configuration as the slope described above, but with a small difference in the slope angle (38.5^{o}) under the same previous earthquake motion (smaller peak acc., 0.18g). They observed (Figure 2-51) that the amplification were reduced to approximately 1.2 (A1 = 0.18g at the model substrata and A7 = 0.21g) and they attributed this to the stabilising effect that the piles had in restraining the response of the soil surrounding the piles.

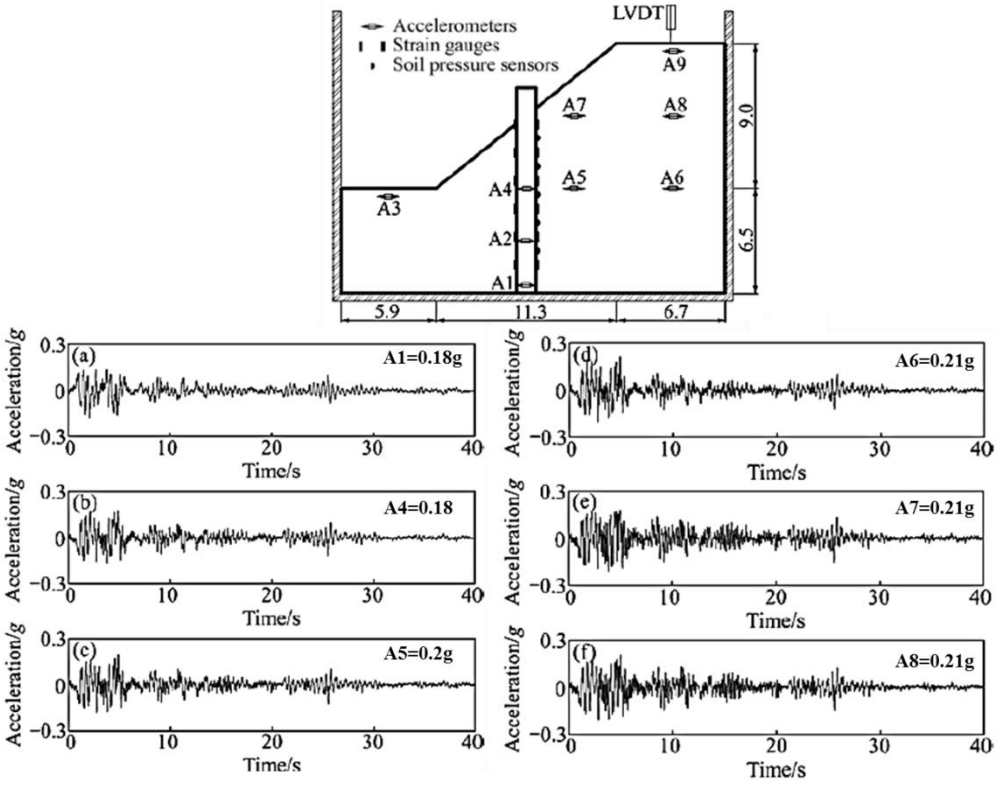

Figure (2- 51): Amplification of the input motion at different positions within a pile reinforced slope (Yu-yuzhen et al., 2010)

Davis and West (1973) investigated the topographical effect on the amplification of the transmitted seismic waves from the base to the top of mountains by studying three different mountains. He found also that the movements at the crest of the mountains were amplified significantly compared to any other parts of the mountains. Havenith et al. (2003) pointed out that the amplification in the wave in the dynamic soil response analysis is the main reasons of the gravitational movement during the earthquake in the north-eastern Tien Shan Mountain and they observed that a strong amplification was occurred at the top of the slope.

Paollucci et al. (1999) used a numerical simulation of the seismic response of Mt. Ushibara mountain site using a 3D digital evaluation model. These results were compared with analysis results from the records of several moderate earthquakes at the Matsuzaki local array, operated by the Public Works Research Institute (PWRI) of Japan, using five of the accelerograph stations which are located near Mt. Ushibara hill. Theoretical predictions of topographic amplification of ground motion using a

homogeneous 3D model underestimated the observed amplification by about 50% whereas the amplification at the top of the hill reached to 30-40%.

Bouckovalas and Papadimitriou (2005) explored the effect of the slope geometry, predominant excitation frequency and duration, as well as of the dynamic soil properties on the seismic response of the slope by using numerical analysis based on the finite difference method. Among the main conclusions of this study is that the amplification at the crest of the slope and de-amplification near the toe have been observed. The peak values of topographic aggravation factors for horizontal ground accelerations behind the crest were found to vary between (1.2-1.5).

Meen and Hsien, (2009) used a finite difference programme, FLAC^{2D} for modelling non-linear systems to investigate the seismic response of the Renyitan Dam in Taiwan and by using time-acceleration histories of the Chi-Chi earthquake as an input motion. The dam dimension and typical boundary condition used in FLAC programme are shown in Figure (2-52).

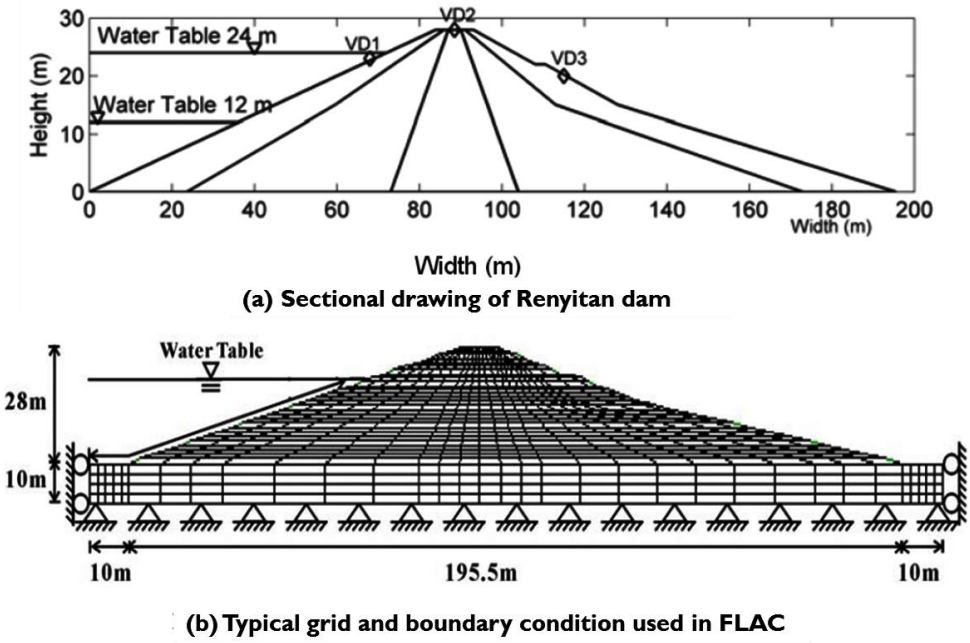

Figure (2- 52): Dimension of the studied dam and; (b) the typical boundary condition (After Meen and Hsien, 2009)

They found that during the earthquake shaking, the acceleration at the base of the dam foot was magnified approximately 2.13 when the wave reached to the top of the crest. The relationship between the computed magnification (amplification) factors at three depths of the core of the dam and the height of the dam for two diierent water table

level are shown in Figure (2-53). In general, the level of the storage water tables did not have any influences in the magnification factor of the core of the dam.

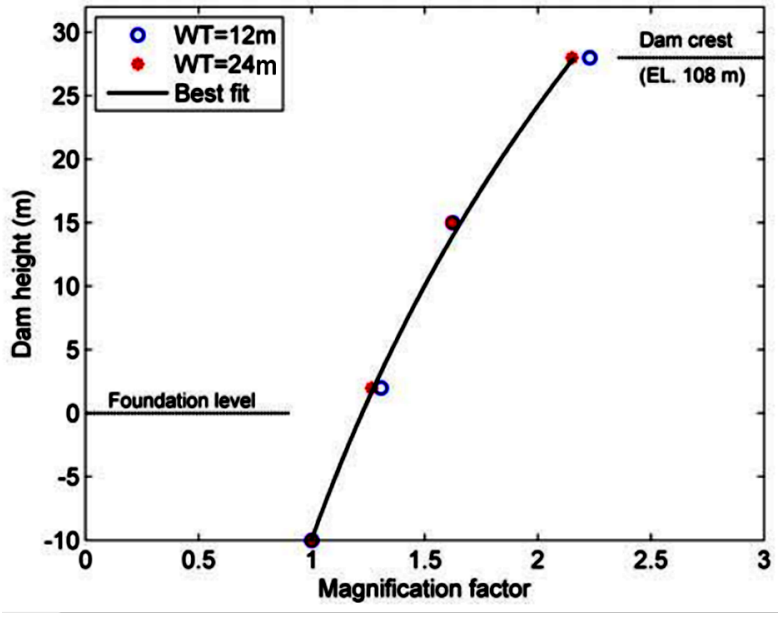

Figure (2- 53): Dynamic magnification factor (After Meen and Hsien, 2009)

2.10 Summary

The review of the literature has revealed the following points:

1- The slope failure mechanism for cohesionless slopes, both under static and seismic conditions appears to be well understood.
2- The Newmark sliding block method, combined with a suitably determined yield acceleration, appears to be very useful for predicting seismic slip and quantifying seismic damage.
3- Pile-reinforced slopes have been widely used and researched under static and dynamic conditions, whereas a little centrifuge tests have been done to investigate how pile elements behave to stabilise slopes under dynamic loads (earthquakes).
4- Many methods have been presented to analyse (passive) laterally loaded piles for static problems and under seismic loads, but there is still much uncertainty regarding piles behaviour under kinematic seismic loads.

The subsequent chapters of this thesis report a series of dynamic centrifuge tests to overcome the issues described above, supported by appropriate numerical and analytical modelling to develop practically useful design and analysis techniques. The investigation includes determining how pile spacing affects the dynamic geotechnical performance of a slope, and the confirmation of appropriate maximum normalised spacing for optimum reinforcing effect. Secondly, there are potential economic benefits of being able to use appropriately reinforced precast concrete sections over (more conventional) steel tubular piles. If the piles designed to not exceed yield, pile behaviour could justifiably be assumed to be elastic; however it is not clear whether a potentially damageable concrete section with more complex dynamic behaviour can be treated in the same way. Finally, existing Newmark methods will be developed based on the centrifuge test results to provide an easy-to-use design tool for quantifying seismic damage to slopes, and assessing the improvement provided by pile reinforcement.

Chapter Three
Physical modelling methodology

3.1 Introduction

Geotechnical centrifuges are more widely used than before in the world, especially in the UK, United States, and Japan to study the static and dynamic performance of civil engineering infrastructures. Due to the nonlinear mechanical behaviour of soil (stress-strain dependency), use of a geotechnical centrifuge allows the gravitational acceleration (and therefore effective stresses) within the model to be increased by the same factor as the stresses are reduced by using a small scale model. The result is that the stresses within a small scale model in the centrifuge are identical to those at corresponding points within the full-scale prototype.

This chapter will introduce the principles of centrifuge modelling, and describe the modelling procedures used in the subsequent chapters of this thesis. This includes the development and detailed characterisation of novel model reinforced concrete piles that are realistically damageable.

3.2 Principles of centrifuge testing

Model tests in geotechnical engineering problems are usually conducted at a scale of (1:N) where N is the scaling factor. The use of small scale (1-g) models is usually limiting in geotechnical engineering as the behaviour of soil depends on effective stress and these are N times smaller in a 1:N scale model Wood, 2004). To retain the correct prototype behaviour of soils (i.e. the model's stress and strain conditions are the same), a centrifuge can be used to increase the strength of the g-field (by a factor N) to offset the reductions in stress due to the reduced size. Figure (3-1) shows a full-size block of soil (in-situ case) and a 1:N scale model of the same soil mass under enhanced gravity (*Ng*). In the in-situ/full-scale case (Figure 3-1a), the calculated vertical (total) stress, σ, at the bottom of the soil mass and vertical strain, ε, across the soil mass are:

$$\sigma = \frac{M.g}{L.B} \tag{3-1}$$

and

$$\varepsilon = \frac{\Delta L}{L} \tag{3-2}$$

In a centrifuge (Figure 3-1b) applying *Ng* to a model with all dimensions reduced by *N* (and therefore having mass reduced by N^3), the stresses and strains are:

$$\sigma = \frac{\frac{M}{N^3} * N * g}{\frac{L}{N} * \frac{B}{N}} = \frac{M * g}{L * B} \tag{3-3}$$

$$\varepsilon = \frac{\frac{\Delta L}{N}}{\frac{L}{N}} = \frac{\Delta L}{L} \tag{3-4}$$

Thus, the stress and strain in the centrifuge is equivalent to that in the full scale prototype.

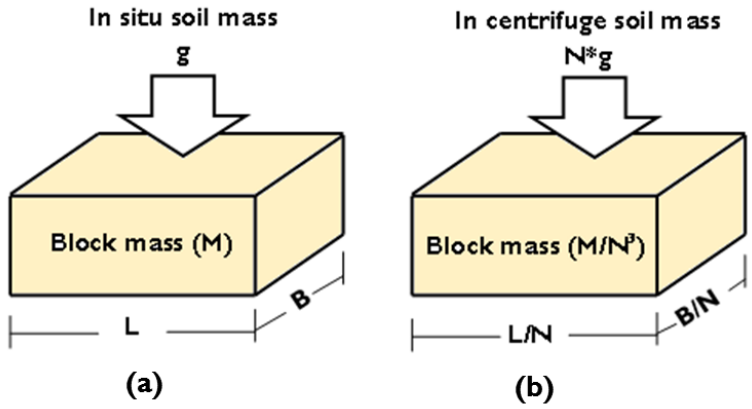

Figure (3- 1): Basic principal of centrifuge testing of reduced scale models

In centrifuge testing, enhanced acceleration is applied to the soil model by spinning the model in the centrifuge in a horizontal plane at a prescribed angular velocity at a centrifuge radius (*r*). The acceleration a model experiences in the radial direction is then:

$$a^* = r.\omega^2 \tag{3-5}$$

where ω is the angular velocity of the centrifuge. However, there is additionally a component of acceleration acting vertically towards the ground (Earth's gravity). As such, the resultant acceleration acting on the model is:

$$a = \sqrt{(\omega^2 r^2)^2 + g^2} \tag{3-6}$$

For a 1:N scale model, the angular velocity is selected such that:

$$a = N.g \tag{3-7}$$

Once this acceleration field has been achieved, the model represents an equivalent full-scale prototype, and its model scale properties can be related to the equivalent prototype scale values via well-established scaling laws. Typical scaling laws between parameters in the model and equivalent prototype (full-scale parameters) are tabulated in Table (3-1).

Table (3- 1): Scaling laws for centrifuge testing (Schofield, 1981 and Kutter, 1994)

Parameter	**Scaling law: Model/Prototype**	**Dimensions**
General Scaling Laws		
Length	1/N	L
Area	$1/N^2$	L^2
Volume	$1/N^3$	L^3
Density	1	M/L^3
Mass	$1/N^3$	M
Stress	1	M/LT^2
Strain	1	-
Force	$1/N^2$	ML/T^2
Bending Moment	$1/N^3$	ML^2/T^2
Seepage velocity	1/N	L/T
Time (Consolidation)	$1/N^2$	T
For dynamic events		
Time (Dynamic)	1/N	T
Time (Seepage)	$1/N^2$	T
Frequency	N	1/T
Displacement	1/N	L
Velocity	1	L/T
Acceleration	N	L/T^2

3.3 Beam centrifuge and earthquake simulator (EQS)

The centrifuge modelling described in the subsequent chapters was conducted using the geotechnical centrifuge at University of Dundee. The centrifuge is a C67-2 machine, built by Actidyn, France. The machine consists of a 7m diameter rotating arm equipped with a swinging platform/basket that can carry a payload of up to 1500 kg with platform dimension of 0.8m x 1m x 1m to a maximum acceleration of 100g with a speed range of 38 – 208rpm.

The beam centrifuge operates with a balanced counterweight at the other end of the arm to the swinging platform. Centrifuge models are usually prepared outside of the centrifuge basket, and then transferred carefully to the platform using a crane. The model instruments are monitored using a 64-channel data acquisition system with continuous in-flight surface observation provided by a digital video camera. The instruments are logged locally onto on-board PC mounted at the centre of the arm; this and the video streams are networked over a 10/100 Ethernet LAN (using PCI Network cards) via a 1GBit Fibre-optic communications slip ring to allows control and monitoring from a separate room.

Horizontal ground motion ('shaking') of the model container during flight is applied to models using a servo-hydraulic earthquake simulator, also built by Actidyn, that can carry a 400 kg model (including container) with exterior dimensions of 0.8 m × 0.4 m × 0.6 m. The frequency response of this system covers the range 40-400 Hz. This EQS allows users to select the earthquake frequency, magnitude and duration if harmonic motions are to be used. The EQS can also simulate recorded earthquake time histories once they have been band-pass filtered to ensure frequency content (at model scale) in the range of 40-300 Hz. Figure (3-2) shows the Dundee geotechnical centrifuge with the EQS attached, while Figure (3-3) shows the shaker in greater detail. Further information on the EQS capabilities and performance can be found in Brennan et al. (2014).

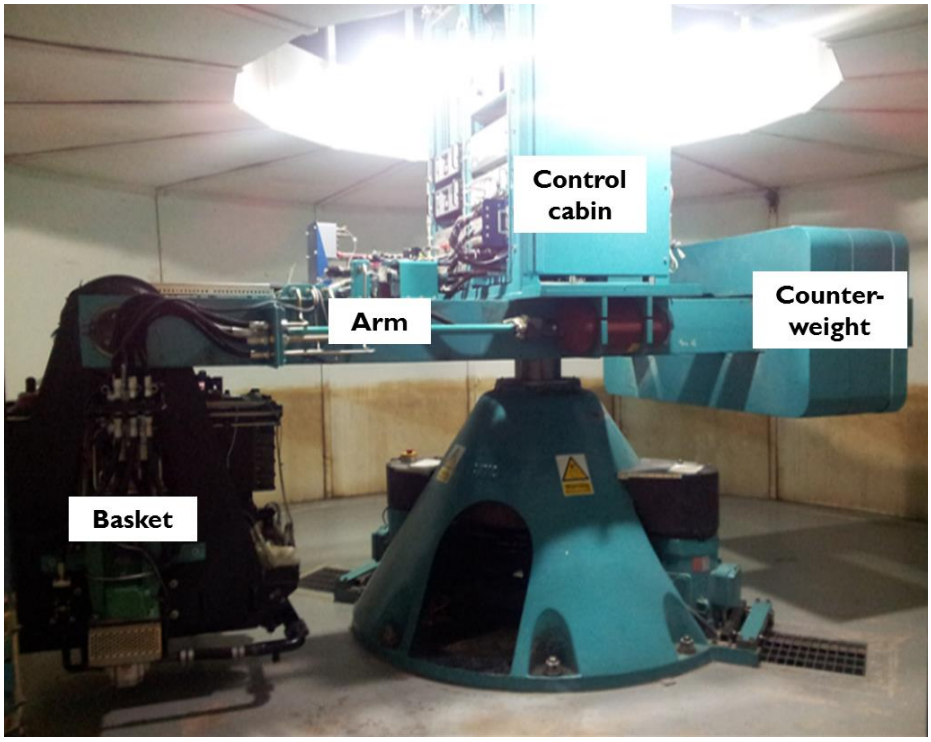

Figure (3- 2): University of Dundee geotechnical centrifuge.

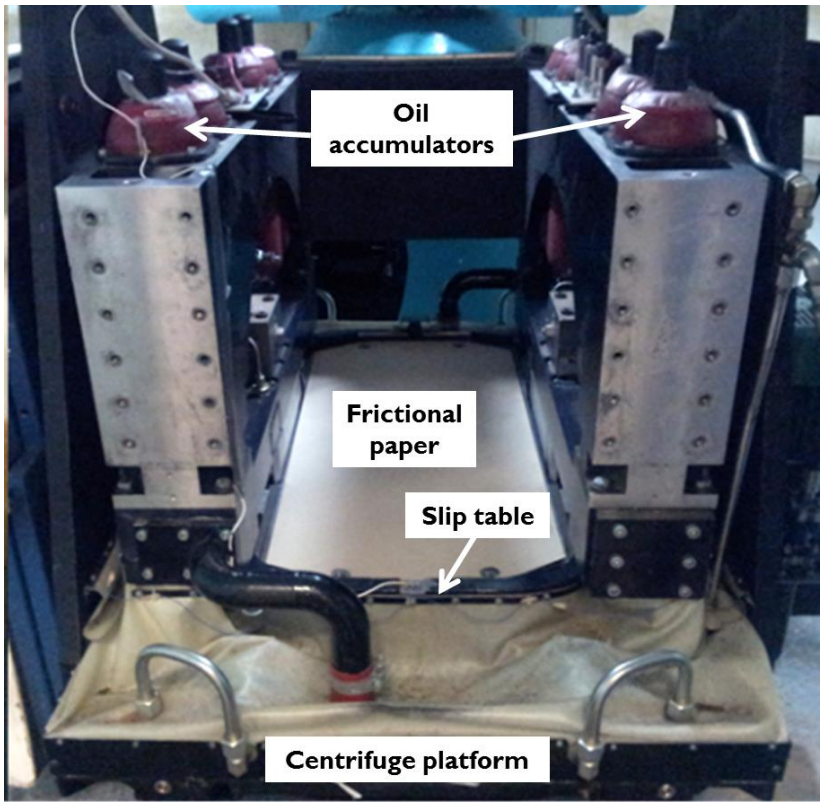

Figure (3- 3): EQS.

3.4 Centrifuge modelling considerations

3.4.1 Particle size

The most basic requirement when selecting soils for centrifuge testing is that there are a sufficient number of particles across the dimensions of a model so that the soil can be considered as a continuum. It is not reasonable to scale down the particle size of soil according to the scaling law for length because the reduction of the soil particle size leads to a change in the mechanical properties of soil. For example, the silica sand which is used in this study (see Section 3.5.1) has a mean particle size D_{50} = 0.12 mm – this would be modelled by very fine particles soil (D_{50} = 0.0024 at 1:50 scale and 50g) which are within the range for clays. Ovensen (1979) studied the effects of particle size on circular footings using dry sand in a series of geotechnical centrifuge tests. It was observed that the size effect could be ignored when the footing radius was > 15D_{50}. For piles in the same study, the minimum diameter of the pile was found to be between 20-40D_{50}. In this study, square piles of size 10 × 10 mm at model scale are used within a 1:50 scale model, which is more than 83 times D_{50}. Therefore, there should be no undesirable size effects due to particle size.

3.4.2 Radial distortion

Because the gravitational acceleration (g) in prototype scale is effectively constant at any point in soil strata (due to the ratio of soil depth to radius of the Earth being small), thus, vertical stress varies linearly with depth (z) throughout the soil strata according to the equation:

$$\sigma_v = \gamma z = \rho g z \tag{3-8}$$

In a centrifuge model, the variation in the vertical stress across the model is nonlinear as the change in radius to the centre of rotation is significant compared to the radius of the arm. Stewart (1989) showed that the vertical stress variation depends on the differences of the square between the radius (measured from the centre of the centrifuge axis to the top of the model) and the radius to any point (z) in the model according to the equation:

$$\sigma_v = \rho\omega^2 = \int_{r_1}^{r_2} r dr = \frac{1}{2}\rho\omega^2(r_2^2 - r_1^2) \tag{3-9}$$

Where r_1 is the radius from the axis of rotation of the centrifuge to the top of the model while r_2 is measured to the depth *z* in model (i.e. Figure 3-4). Knappett (2010) shows that this effect can be minimised by keeping the model height small relative to the radius of centrifuge (model height < R/10), where R is the radius measured to the base of the container. In the centrifuge testing described herein, the largest model depth used was 280 mm which satisfies this requirement in the Dundee centrifuge where R = 3.5 m.

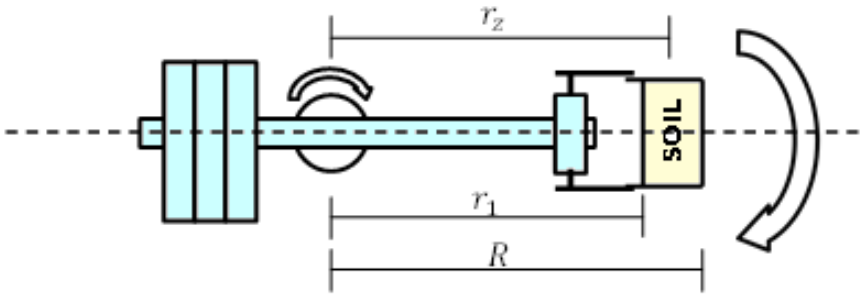

Figure (3- 4): Definition of radii for determining radial distortion of stress field.

3.4.3 Angular distortion

In situ, points of constant vertical stress (same depth under the ground surface) lie on horizontal planes and they have approximately the same distance to the centre of the Earth's rotation. In the centrifuge, this is not true due to the finite radius of the spinning (Knappett, 2010). To keep the studied problem as rectilinear in prototype scale, the surface of the model needs to have circular loci (concave up surface). The angle between the horizontal plain and to the end point in which the effective radius is the same (see figure 3-6) called angular distortion. This angular distortion should not reaches to the maximum value of:

$$\theta = \frac{b}{2.r} \tag{3-10}$$

where *b*, container width here while *r*, effective radius of centrifuge. In this thesis, the angular distortion is ignored due to its small value (2.4^o).

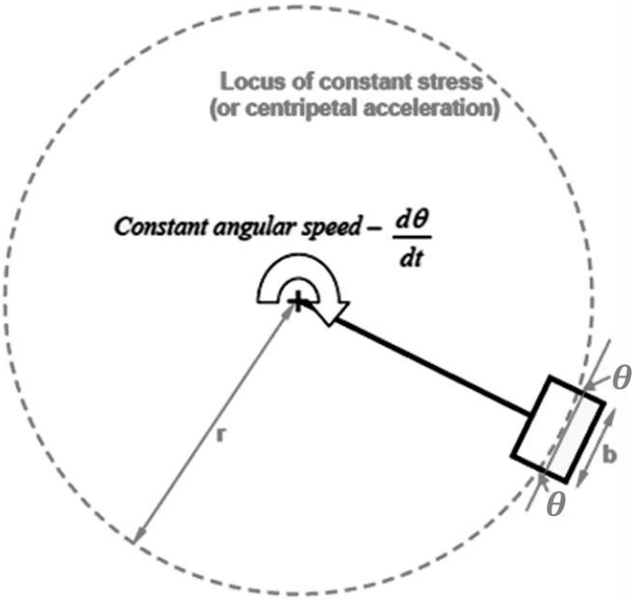

Figure (3- 5): Definition of angular distortion (Knappett, 2010)

3.4.4 Gravitational distortion

Gravitational distortion can occur if the model is rotates in flight so that its surface is held exactly perpendicular to the arm. Under these circumstances, the resultant acceleration (Equation 3-6) is not perpendicular to the surface of the model. This is termed gravitational distortion. However, for centrifuges with a free-swinging platform such as that at the University of Dundee, the model will automatically take up a position in flight such that the resultant acceleration is normal to the model surface, and hence there is no gravitational distortion.

3.5 Soil properties and preparation

3.5.1 Soil (HST95 sand)

HST95 Congleton silica sand will be used in the centrifuge tests with properties shown in table (3-2). This sand has been used by earlier researchers to study structural settlement due to liquefaction phenomena. Lauder (2011) determined the minimum and maximum void ratio of this sand in accordance with (BS, 1990). These minimum and maximum void ratio values for sand are very important in calculation of relative density. This sand is very fine and uniformly graded as shown by the particle size

distribution (PSD) in Figure (3-6) and was used in a medium state in all centrifuge models.

Soil properties in shear are presented in detail in Section 3.8.

Table (3- 2): Physical properties of HST95 silica sand

The physical property	**The value**
Specific Gravity (G_s)	2.63
Shape	Rounded
D_{10}	0.09
D_{30}	0.12
D_{60}	0.17
C_u	1.9
C_z	1.06
Optimum dry density (kN/m^3)	15.35
Maximum dry density (kN/m^3)	17.58
Minimum dry density (kN/m^3)	14.59
Maximum void ratio (e_{max})	0.769
Minimum void ratio (e_{min})	0.467

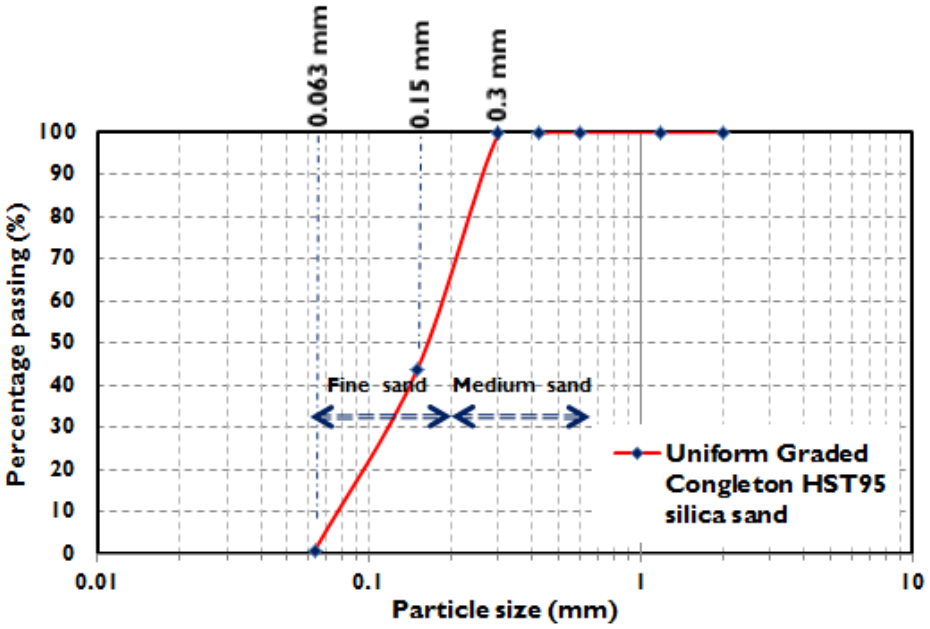

Figure (3- 6): Particle size distribution for HST95 silica sand

3.5.2 Soil preparation techniques

All centrifuge models described in this thesis were air pluviated to 55% nominal relative density (this value is chosen for seeing bigger slope failure under earthquakes but not loose as many aftershocks would be conducted). A slot pluviator was used to prepare all the centrifuge models as shown in Figure (3-7). This pluviator has been widely used by many geotechnical researchers at Univerity of Dundee (e.g. Lauder, 2011; Bertalot, 2013). The width of the pluviator was 540 mm along the slot and this was so enough to cover the full width of the container during the pluviation process. The hopper rests on a linear guide frame by four wheels which allow it to be moved by hand along the length of the model container as an approximately constant speed (height kept constant as it gave best uniform density for slope). The slot width can be changed to vary the relative density by moving the two plates shown in Figure (3-7, inset) up or down the inclined sides of the container. It is very difficult to control relative density exactly by pluviation, so calibration tests were conducted in a known volume box to determine the flow rate (slot width) and drop height required to achieve satisfactory results. From Figure (3-8) it can be seen that approximately 3mm slot width gives a density around 55% with no further change in relative density for any slot width greater than this.

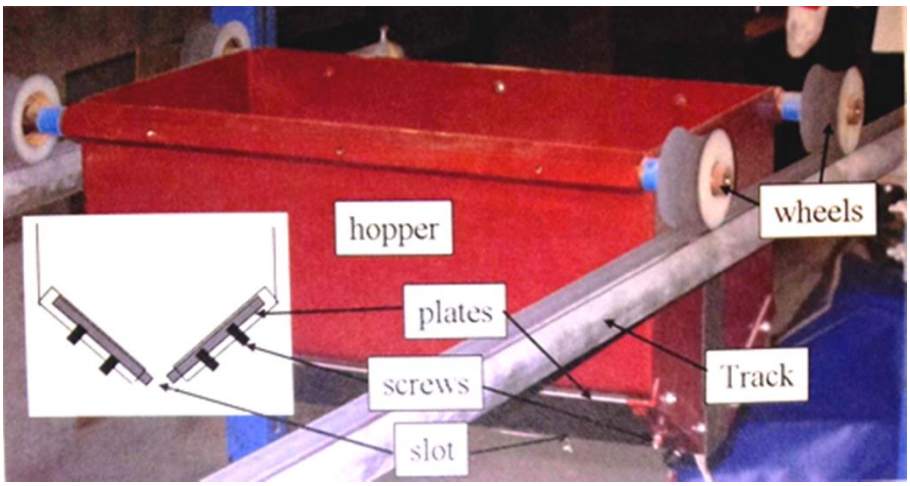

Figure (3- 7): Slot pluviator with cross section (inset) for preparing all centrifuge models (image: Lauder, 2011)

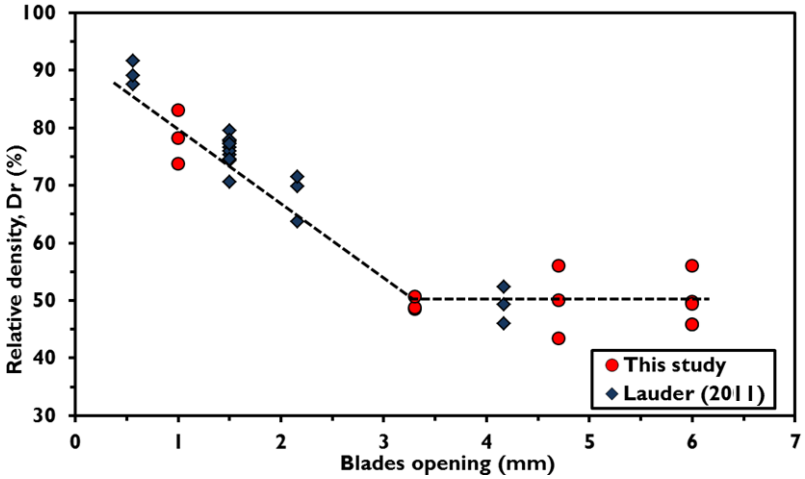

Figure (3- 8): Relationship between slot width and relative density

Figure (3-9) shows the relationship between the relative density and soil dry density. It can be seen that the 55% relative density is corresponding to approximately 16 kN/m^3 dry density. This value was a reference for all centrifuge tests.

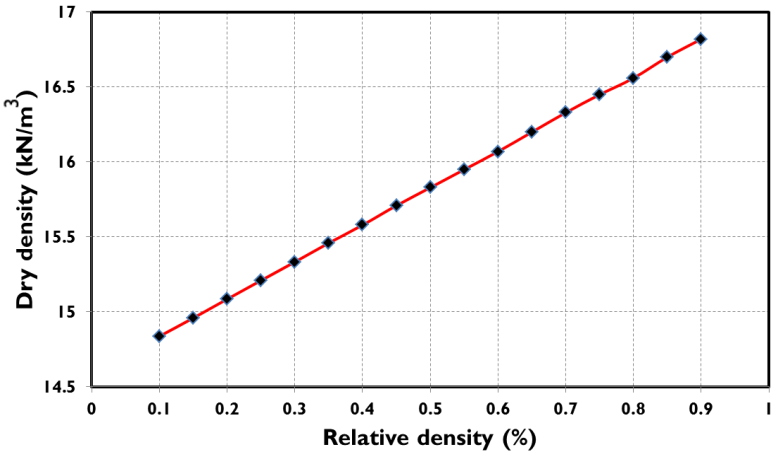

Figure (3- 9): Dry density-relative density relationship (after Lauder, 2011)

3.5.3 Equivalent Shear Beam (ESB) container

An ESB (Equivalent Shear Beam) container exists at the University of Dundee which is fabricated from aluminium alloy in six rings with sandwich rubber layers to give the equivalent dynamic shear stiffness as the adjacent soil and satisfy the other key boundary conditions described by Schofield and Zeng (1992).

The design of this container is described in Bertalote, 2013. The container has internal dimensions of 669 mm (length), 279 mm (width) and 338 mm (height). The container is shown in Figure (3-10).

Uniform slope conditions were modelled across the slope width within the container. Taylor (1994) and Khoo et al. (1994) observed that plane strain models should be wide enough to minimise the effect of side friction from the container walls on the deformation behaviour of the slope. This can be achieved through a minimum container width to model height ratio. Davies (1981) suggested that this value should ideally be around 1.0; in the used container in this study, the ratio between the container width to the slope height was approximately 0.86 which is very close to 1.0. Properties of both frames and rubber layers were used to compute the lateral deflection (bulging) due to gravitational or static forces is also computed. It was approximately 0.89 and this value consistent with the measured maximum value for saturated losses sand, 0.4mm (Betalote, 2013).

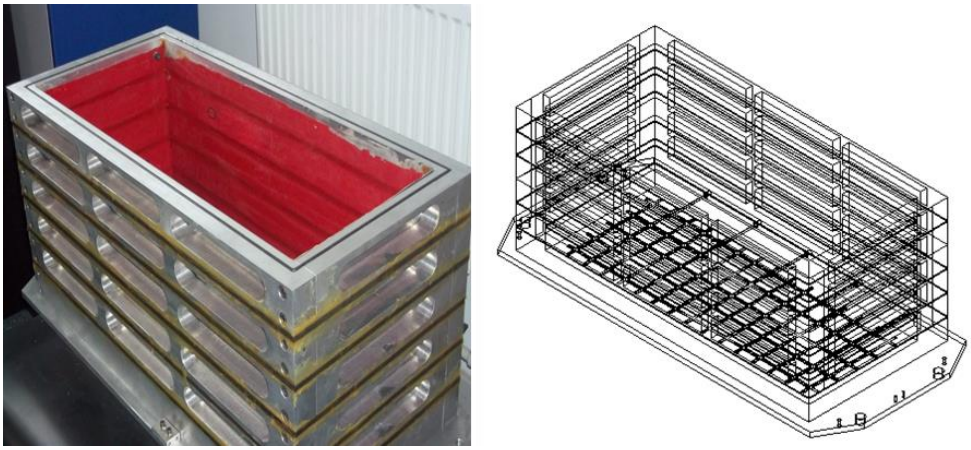

Figure (3- 10): ESB container used in the tests (Bertalot, 2013)

3.6 Instrumentation

3.6.1 MEMS Accelerometers

Miniature iMEMS (ADXL78) accelerometers manufactured by Analog devices Inc. were used to measure accelerations within the centrifuge models. This product is a single-axis accelerometer and can measure both dynamic acceleration (vibration) and static acceleration (gravity). The instrument measures acceleration with a full scale range of $\pm 70g$ with sensitivity between (25 – 28) mV/g and has dimensions of 5 × 5 ×

2.5 mm. A typical transducer and geometry are shown in Figure (3-11). The accelerometers were calibrated relative to gravity by measuring the output voltage when aligned in opposite directions parallel to the gravitational acceleration of the earth (-1g and +1g). The average of the two orientations gave the calibration factor. Because the ADXL78 accelerometer is very small and delicate, they were attached using cyanoacrylate adhesive ('super glue') to a 20mm diameter circular PVC disk and then coated by a plastic-dip flexible emulsion. The purpose of the disk was to keep the transducer in a horizontal plan during placement within the soil models, increase the movement sensitivity during earthquake shaking through better coupling with the surrounding soil, and to make them waterproof with neutral buoyancy for use in saturated (liquefaction tests).

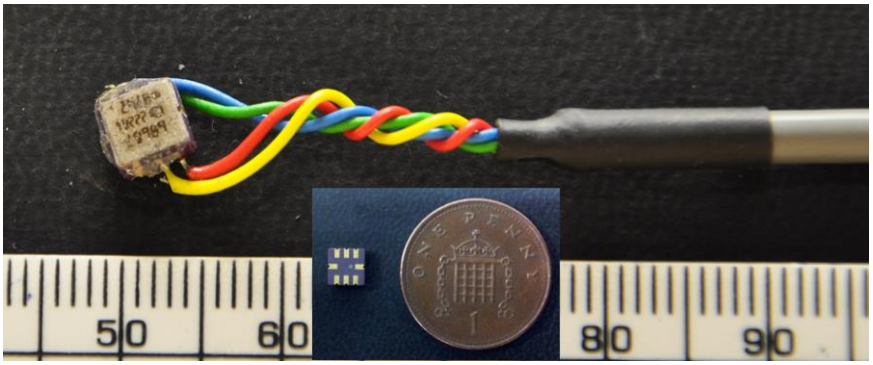

Figure (3- 11): iMEMS accelerometer

3.6.2 Strain gauges

FLA- strain gauges manufactured by Tokyo Sokki Kenkyujo Co. (Japan), having a gauge resistance of 120 ± 0.3 Ohm were used to instrument some of the model piles (discussed further in Section 3.8). The gauge length and width of these instruments were 1 mm and 1.3 mm respectively while the backing length and width were 5 mm and 2.5 mm respectively. The strain gauges were fixed along 6063-T6 Aluminium alloy piles using cyanoacrylate adhesive (type CN). The time required to bond these gauges is extremely short and handling is very easy – the curing time under normal conditions is 20 – 60 s. They were then coated by Neoprene rubber N-1 type protective coating material which also made them waterproof. The strain gauges and its accessories are shown in Figure (3-12).

All of the strain gauges were wired in pairs to constitute half-bridges so as to measure bending moment along piles during and after seismic shaking. The strain gauges were calibrated by testing the instrumented pile as a cantilever beam under known applied bending loads and measuring the output voltage. The gauges were interfaced to the centrifuge PC running a LabVIEW script for data logging via a special junction box which multiplexes the information from the different channels. A solid copper wire manufactured by Vishay Precision Group was used for wiring the strain gauges together and connecting them to the junction box. A linear relationship was obtained (Figure 3-13) between known moment in Nm at model scale and measured output voltage for each strain gauge pair.

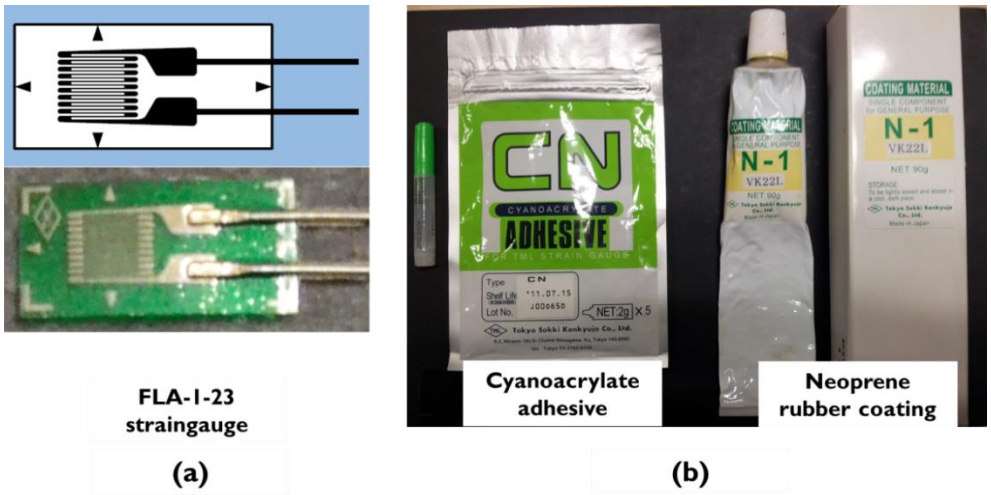

Figure (3- 12): (a) TML strain gauge, (b) adhesive and coating

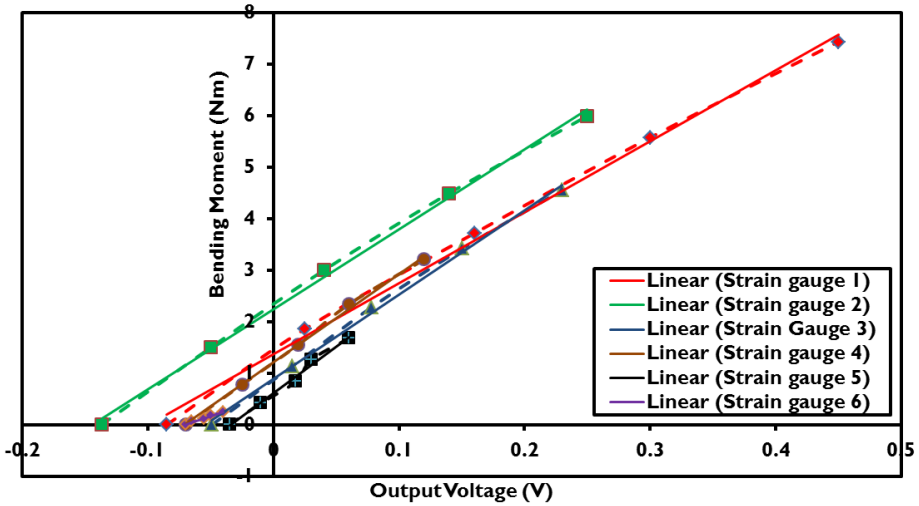

Figure (3- 13): Calibration of strain gauge pairs

3.6.3 Linear Variable Differential Transformers (LVDTs)

LVDTs fabricated by RDP electronics Ltd. (Series DC to DC) have been obtained with lowest range ±12.5 and linearity ±0.1. These LVDTs were calibrated by applying known downward and upward movements in increments of 5 mm and measuring the corresponding output voltage. The slope of the relationship between the displacement and the corresponding output voltage provides the calibration factor. Figure (3-14) shows this type of LVDT while Figure (3-15) shows a typical voltage-displacement relationship obtained from the calibration.

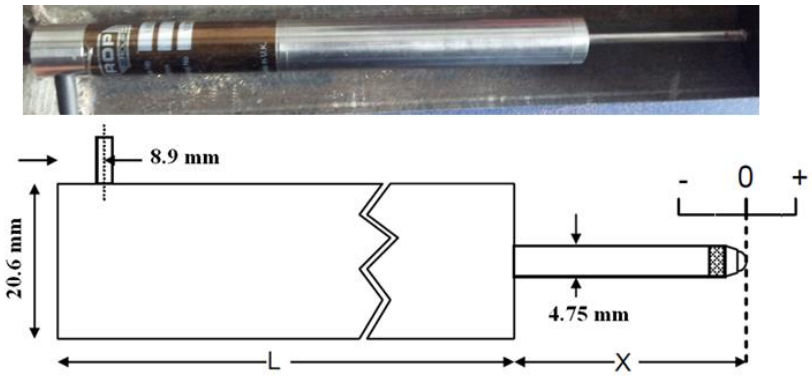

Figure (3- 14): Linear variable differential transformers (LVDT)

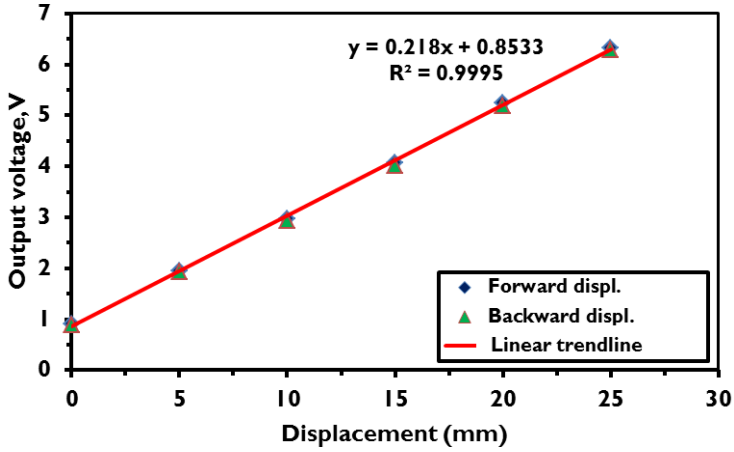

Figure (3- 15): Displacement-output voltage relationship for LVDT

3.6.4 Data acquisition

The data acquisition system consisted of a number of components which are shown in Figure (3-16). A power supply unit (1) steps-down the on-board centrifuge power supply to provide 5V or 10V DC supply as required. This power is sent to the junction boxes (2) where it is distributed across the various channels to the

instruments. Output voltages are collected from the signal lines and routed to a bank of signal conditioners which can apply individually controllable gains to each channel. Once processed, the signals are sent the on-board PC via four 16 channel PCI data acquisition cards. This "Host PC" has 3 PCI slots for installation of these cards with one serial port, one parallel port and two USB ports which can be used for data transfer. The logging is performed by means of four Adlink NuDAQ 2204 high frequency data acquisition board, A/C conversion (Bertalote, 2013). These are accessed using a LabVIEW routine originally developed by Bertalot (2013), which monitors the data, applies user-defined calibration factors and saves the data locally to a solid-state hard disk as both calibrated and un-calibrated (raw voltage) data.

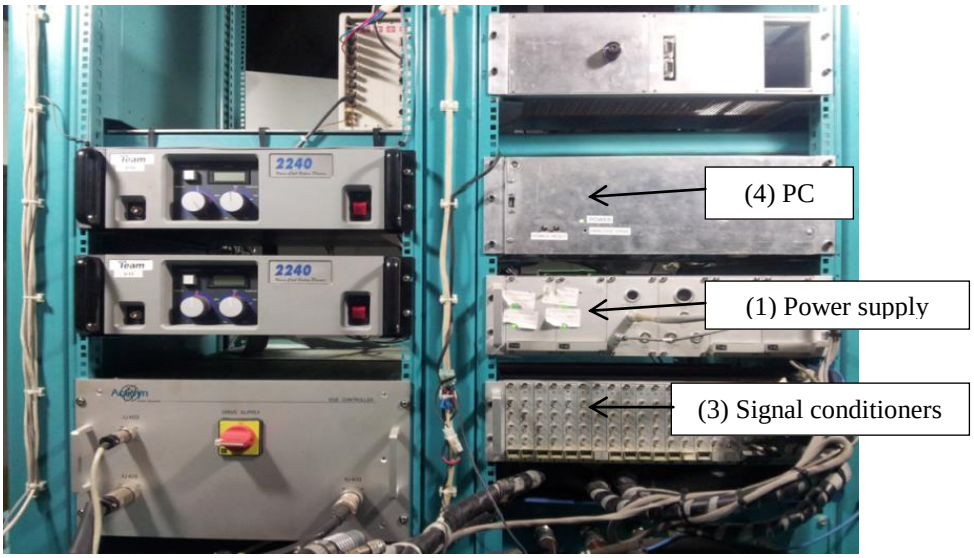

(a)

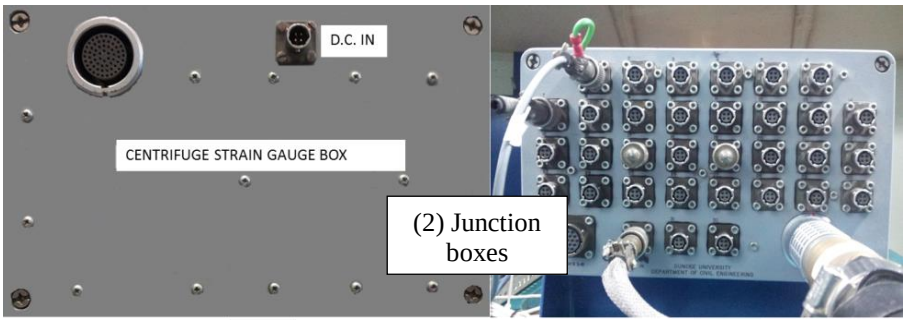

(b)

Figure (3- 16): (a) Data acquisition system and shaker controller; (b) Strain gauge junction box (left) and general purpose (voltage) junction box (right)

The LabVIEW routine incorporates a manual trigger which is activated immediately prior to firing the earthquake. This records 10 s of data at a sampling frequency of 2 kHz. As the earthquake motions used in this work were no longer than 1 s in model scale, the pre- and post-earthquake data outside the earthquake was deleted via a post-processing routine. Once the 10 s of data had been collected, it was automatically displayed on the screen of a PC within the centrifuge control room in calibrated units allowing for immediate review and decision making about the application of further earthquakes. A typical output following and earthquake event is shown in Figure (3-17).

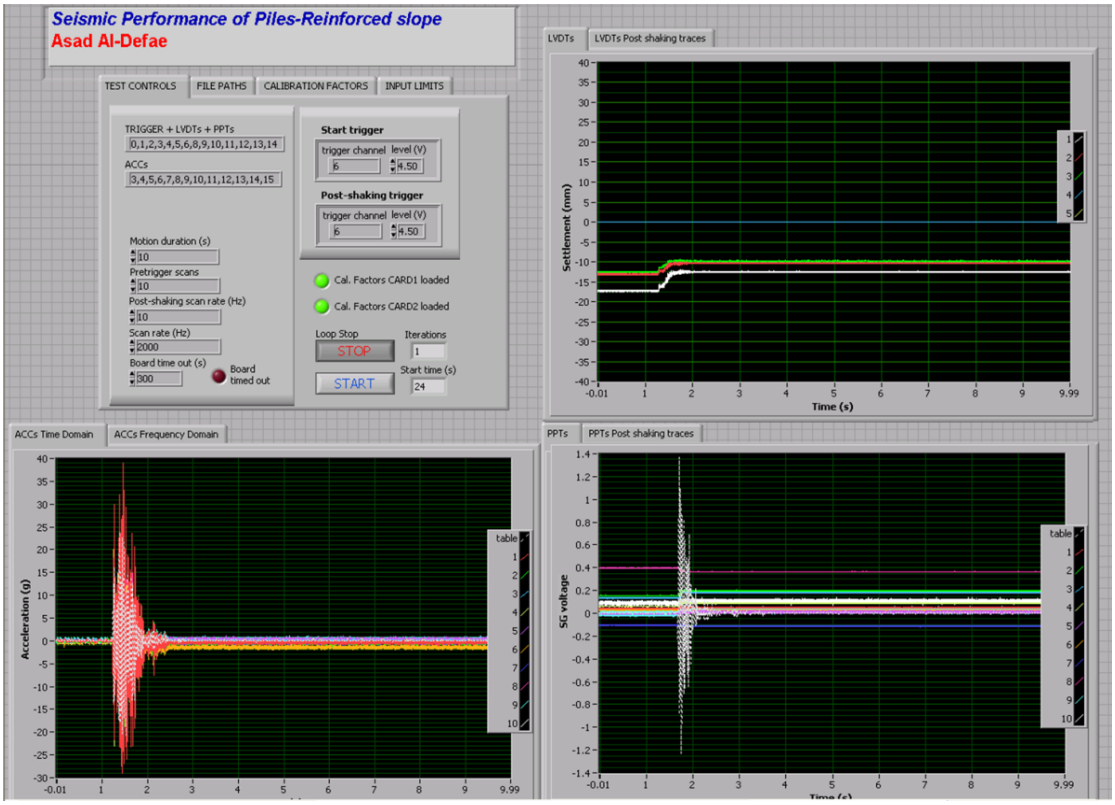

Figure (3- 17): Data acquisition programme, showing results from a typical test

3.7 Model reinforced concrete piles

3.7.1 Introduction to pile modelling approach

Two types of pile models were used in this study. The first model ('RC pile') was made from a recently developed set of materials and procedures for producing a reinforced micro-concrete which can replicate damage realistically. The second type

of pile was fabricated from aluminium alloy and strain gauged and is hereafter termed 'elastic pile'. This type was used to measure the bending moment mobilised along the pile due to slope mass movement. The RC piles were designed (and tested) first, such that the elastic pile models could be designed to have (as closely as possible) the same bending stiffness, *EI* to give similar soil-pile interaction during the tests, prior to yield. In this way, the two pile models would be considered to be nominally the same within the elastic range. However, due to their construction, the RC piles are able to realistically simulate damage (i.e. they have similar shear and moment capacities at prototype scale as real reinforced concrete), and can also sustain changes in residual mechanical properties due to fatigue effects. The former characteristic has been demonstrated for generic reinforced concrete elements at highly reduced scale by Knappett et al. (2011). The work described herein represents the first use of this novel 'micro reinforced concrete' within a full boundary value problem in the centrifuge. The remainder of Section 3.7 details the development, construction and characterisation of the RC piles; the elastic piles will be described in Section 3.8.

3.7.2 Micro-concrete

The capacity and the bending stiffness of a model reinforced concrete pile is affected by scaling of the quasi-brittle fracturing process which affects the tensile strength of the concrete component, resulting in a scale effect (Litle and Paparoni, 1966). According to this concept, the model piles should be fabricated from a carefully selected brittle material for the concrete component to give the same elastic bending strength at prototype scale as full scale reinforced concrete material (Knappett et al., 2011). Higgins (2007), Gilhooly (2008), Mcdonnel (2008) and Madden (2008) developed new cementitious mortars based on casting and surgical plaster, mixed with sand and water, to create a micro-concrete mix which replicates conventional concrete at typical centrifuge scaling factors. This micro-concrete mix consists of a surgical plaster (as a binder instead of cement), HST95 Congleton silica sand (representing scaled coarse aggregate at prototype scale – see Figure 3.18) and water. The use of a geometrically scaled aggregate component is important as crack size and propagation are strongly correlated to the particle size of the aggregate (Madden, 2008). The component materials are mixed together in the same percentage by mass (1:1:1) following a procedure defined by Higgins (2007). O'Reilly (2009) measured the compressive strength of various micro-concrete mixtures using a set of standard 100 ×

100 mm cube tests. It was found that the compressive strength of 'Mix 1' concrete, which was used in the work presented in this thesis, could reach up to 30 MPa using casting plaster in the ratios given above, which represents similar compressive strength as typical grades of concrete commonly used in piles (this is essential, considering the scaling laws on stress in Table 3-1). To check these compressive strength values, Five further 100 x 100 mm cubes have been cast as part of this work and a further set of four 150 x 300 mm cylinders cast for the same purpose. All of the samples were left for 28 days of air curing (laboratory temperature between 20 – 30 C^o). The compressive strength results were correlated to 150 x 150 mm cubic strength ($f_{c_{150}}$) and cylinder strength (f_c') using the relationships presented by (Mansur and Islam, 2001):

$$f_{c_{150}} = 0.91 f_{c_{100}} + 3.69 \tag{3-11}$$

$$f_c' = 0.9\, f_{c_{100}} - 6.26 \tag{3-12}$$

These results showed that the average compressive strength was approximately 25 MPa. Table (3-3) presents the test results in detail. The estimated cylinder strengths evaluated from the cube test data by Equation (3-12) are compared with the direct cylinder tests in Table (3-3) where only small differences were observed, demonstrating consistency across the different types of test.

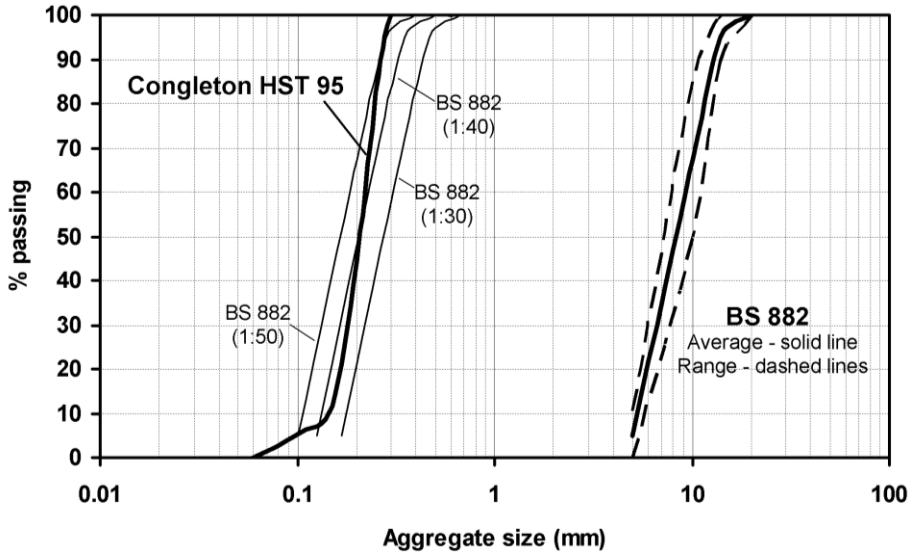

Figure (3- 18): Use of HST95 sand as a geometrically scaled coarse aggregate (Knappett et al. 2011)

Table (3- 3): Compression test results for micro concrete (all results in MPa).

Test No.	$f_{c_{100}}$	$f_{c_{150}}$	f_c'	f_c' **(Cylinder test)**
1	21.4	23.1	13.0	16.0
2	25.4	26.7	16.6	15.2
3	23.3	24.8	14.7	14.9
4	22.6	24.2	14.1	15.4
5	24.5	25.9	15.8	-
Mean	**23.5**	**25.0**	**14.9**	**15.4**

3.7.3 Micro reinforcing steel

Stainless steel wire from Ormiston Ltd. in UK was used as model scale reinforcing steel. Wire 0.6 mm in diameter was used in the pile model as longitudinal reinforcement, representing a bar of 30 mm diameter at prototype scale (1:50). Smaller 0.25 mm diameter model reinforcement was used to model shear reinforcement (representing 12.5 mm bar at prototype scale). The ultimate tensile stress and yield stress of the wires were provided by the supplier (Ormiston Ltd); however, these values were verified by tensile tests conducted in the geotechnical laboratory using the Instron 1196 loading frame, due to their importance in defining the moment capacity of the model pile.

Test results for the longitudinal and shear model reinforcement are shown in Figures (3-19) and (3-20), respectively. It was noted that the stress-strain relationship and wire strength are similar to the properties of full scale reinforcing bars at prototype scale. Knappett et al., (2011) defined the yield strength (f_y) at 0.2% permanent strain. The average yield strength so calculated was 461 MPa for longitudinal model reinforcement and 455 MPa for shear model reinforcement. Table (3-4) shows the summarised results of the wire strength tests. Higgins (2007) and others explained the importance of roughness of the wires for good mechanical bond between the steel wire and micro-concrete mix, mimicking the ribbing on full scale reinforcing steel. Because of the small size of the model wires, ribbing is not practical, so very fast drying epoxy resin mixed with HST95 silica sand was used to give a rough coat to achieve very good bonding (Knappett et al., 2011).

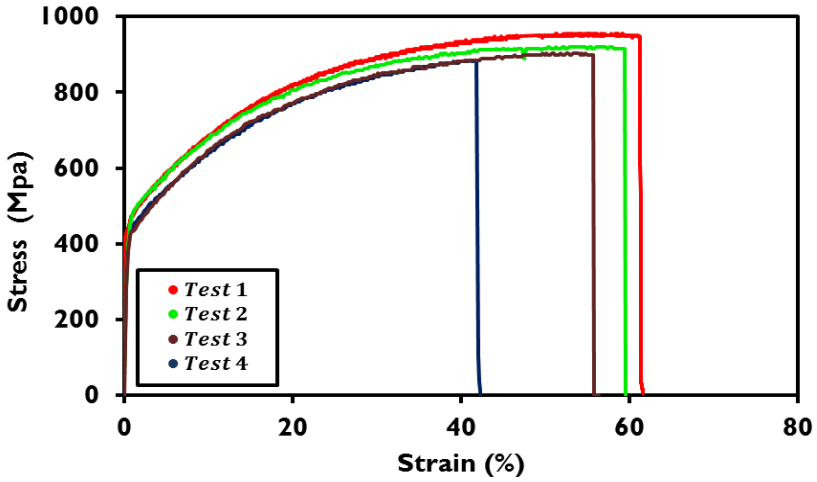

Figure (3- 19): Stress-strain relationship for model longitudinal reinforcement

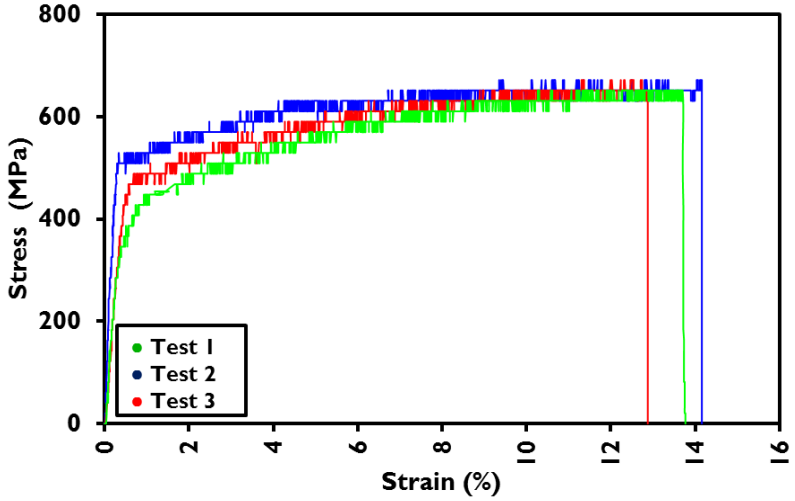

Figure (3- 20): Stress-strain relationship for model shear reinforcement

Table (3- 4): Strength and stiffness properties of model reinforcement.

Longitudinal Model Reinforcement			
Test No.	**Yield Strength (MPa)**	**Ultimate Strength (MPa)**	**Young's Modulus (GPa)**
1	473	951	197
2	451	885	187
3	459	920	191
4	460	916	192
Mean	**461**	**918**	**192**
Shear Model Reinforcement			
Test No.	**Yield Strength (MPa)**	**Ultimate Strength (MPa)**	**Young's Modulus (GPa)**
1	529	611	212
2	429	651	170
3	407	638	195
Mean	**455**	**631**	**190**

3.7.4 Design and construction of RC piles

The piles were designed to represent a 0.5 × 0.5 m square cross section pile of 10 m length (dimensions at prototype scale). The square cross section dimensions of the model piles (at a scaling factor of 1:50) are therefore 10 × 10 mm and 200mm in length. An aluminium alloy formwork was designed and fabricated for casting the piles, including holding the reinforcement in place. Only square piles are used in this thesis. The same procedure that was developed by Knappett et al. (2011) was used to mix the micro-concrete and cast the piles as shown in Figure (3-21). In addition to the reinforced pile models, some unreinforced beams were also cast for determination of the modulus of rupture (tensile strength in bending).

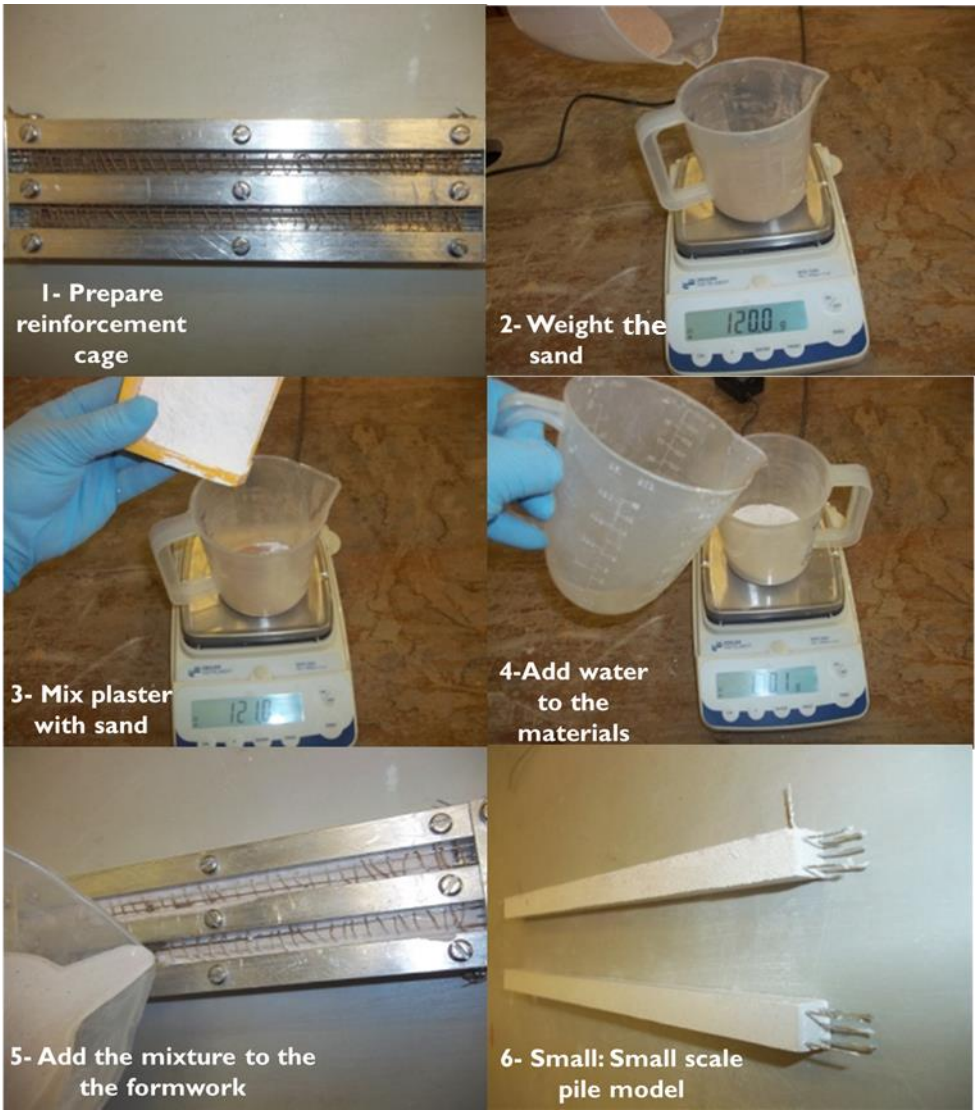

Figure (3- 21): Piles casting procedures

Figure (3-22) shows the reinforcement and cross sectional details for the RC pile model. This consisted of three roughened steel wires on the upslope side of the pile to carry the tensile stresses induced by downslope soil movement and two smooth steel wires on the downslope side with low pull-out capacities, which were used principally in fixing the shear reinforcement. The section can thus be considered to behave as a singly-reinforced concrete beam.

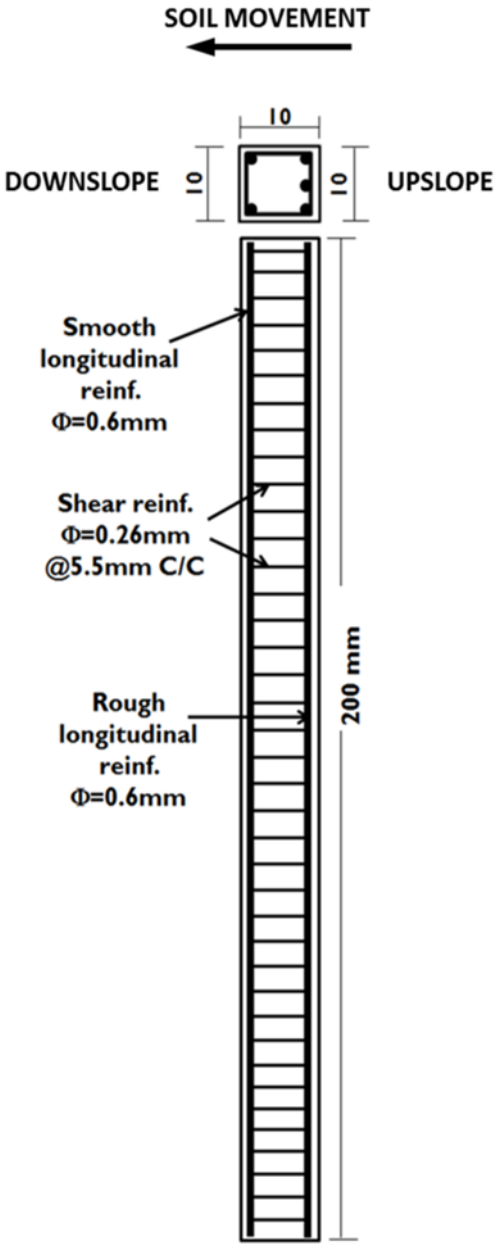

Figure (3- 22): Model RC pile section (all dimensions shown at model scale).

3.7.5 Bending tests of RC piles

3.7.5.1 Procedures

After casting of the model piles, they were left for 28 days to cure before standard four-point bending tests were conducted. Unreinforced models (consisting of just the micro-concrete) were tested to determine the rupture modulus for the model concrete. Many further model piles were tested having a maximum singly-reinforced section can be used (A_s/A_c = 0.85%, where A_s is the cross-sectional area of the steel and A_c the cross-sectional area of the concrete) and different reinforcing wire distributions in the pile section (changing of the spacing between model bars). Flexural shear strength and bending moment can be determined by conducting standard four-point bending tests on specimens as shown in Figure (3-23).

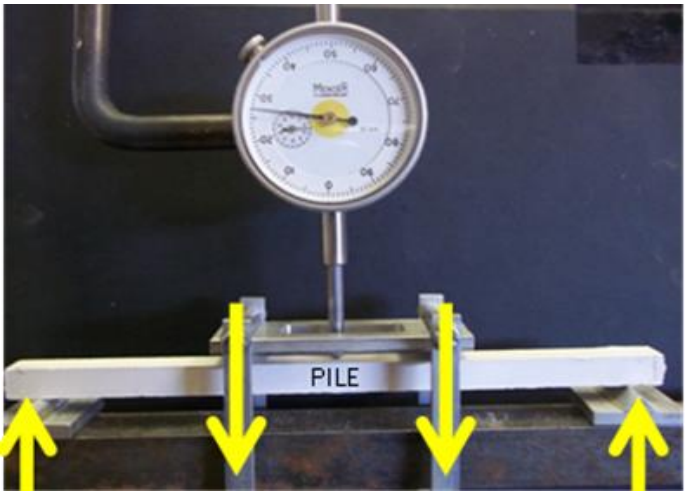

Figure (3- 23): Four-point bending test

Six specimens of the model RC piles used in the centrifuge tests were tested in four-point bending, three in which the transverse shear forces were applied in the downslope direction, and three with the forces applied in the upslope direction. This allowed the bending behaviour to be fully constructed for bi-directional loading of the reinforced section. The resulting average moment curvature behaviour is shown in Figure (3-24). In this figure, positive bending moment denotes that the upslope reinforcement is in tension (i.e. the case when the soil is moving downslope). By testing some additional piles without shear reinforcement, it was possible to show that

the shear reinforcement was essential for obtaining bending failure rather than flexural shear failure (Figure 3-25).

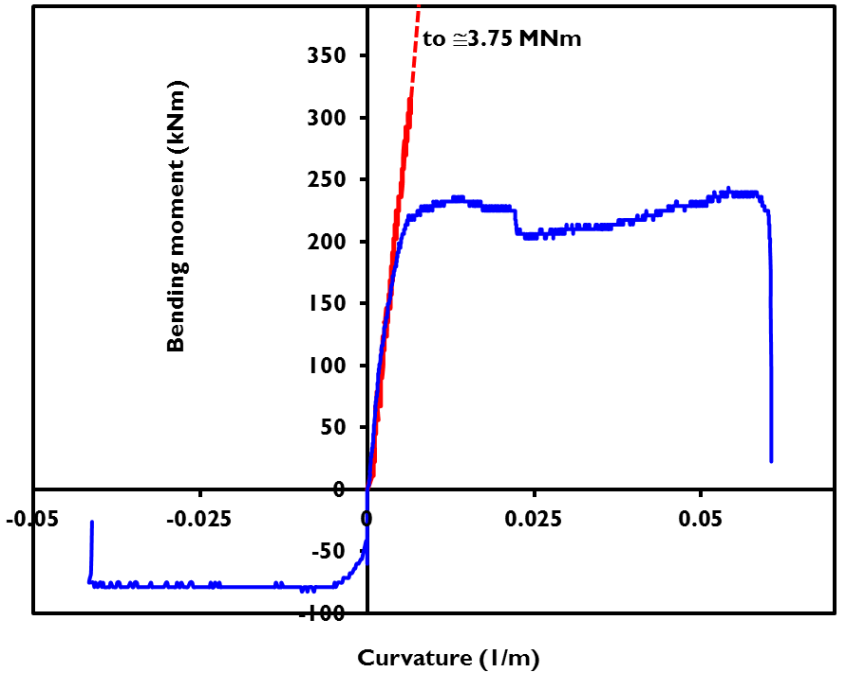

Figure (3- 24): Moment-curvature relationships for model pile sections

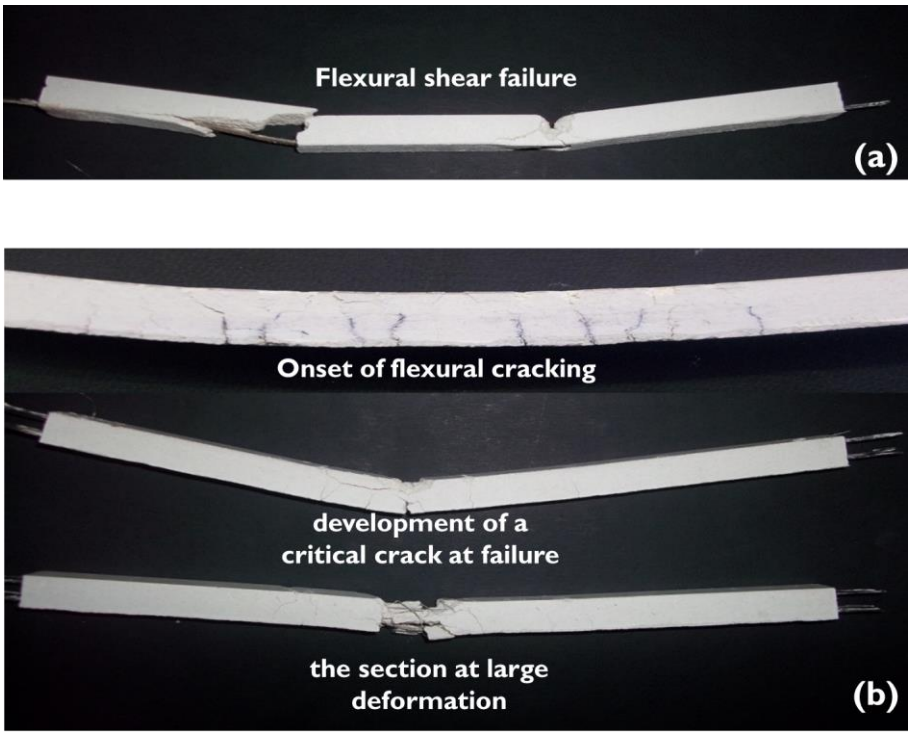

Figure (3- 25): Figure (3-25): (a) Shear and (b) bending failures observed during model

3.7.5.2 Bending stiffness, EI

The initial gradient of the moment-curvature relationship in Figure (3-24) gave the bending stiffness (EI = 50 MNm^2 at prototype scale). These results can be compared with the bending properties at prototype scale from a theoretical transformed cracked section, as described below (see Figure 3-26).

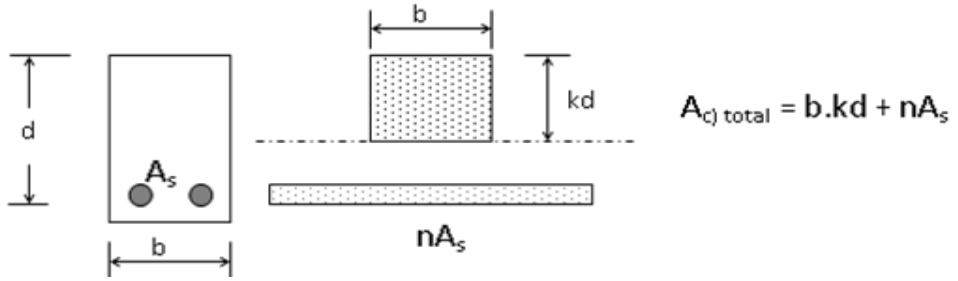

Figure (3- 26): Transformed section method

The basic concept of transformed section theory is that the section of steel and concrete is transformed into a homogenous section of concrete by replacing the actual steel area by an equivalent concrete area. Two conditions must be satisfied: the first is compatibility (ε_c=ε_s) where ε_c and ε_s are the longitudinal strains in the concrete and steel respectively; the second condition is equilibrium (i.e. the force in transformed concrete section = force in actual steel section) leading to the equivalent area of steel $A_c = \eta.A_s$, where $\eta = E_s/E_c$ (called the modular ratio) and E_s and E_c are the Young's modulii for steel and concrete, respectively. Concrete Young's modulus E_c was estimated after Kong and Evans (1987) as 25 GPa (for concrete of f_{c100} = 30 MPa). The bending stiffness of the transformed cracked section is then determined using:

$$EI = E_c\{\frac{b.(kd)^2}{3} + \eta.A_s.(d - kd^2)\} \qquad (3\text{-}13)$$

Additional tests were conducted for two different bar spacing (small and large) having the same A_s to check the best spacing for the reinforcement in the pile models for the centrifuge testing. Further tests were also conducted with and without coating the shear reinforcement with the epoxy/sand mixture to determine the effect of this roughness on the beam behaviour. Results of four-point bending tests were compared with the value resulting from the Equation (3-13) which gave EI = 47.7 MNm^2. All the results are shown in Table (3-5).

3.7.5.3 Capacity

The theoretical ultimate moment capacity (i.e. bending failure) can be determined using a similar cracked-section theory (i.e. by summation of ultimate moment contributions from the steel and concrete). Bazant and Yu (2005), determined the flexural shear capacity of singly–reinforced beams by considering a large database of tests, resulting in Equation (3-14):

$$V_{ult} = 1.104.(\frac{A_s}{A_c})^{3/8}.(1+\frac{d}{a}).(\sqrt{\frac{f_c^{'}}{1+\frac{d}{d_o}}} \quad (3\text{-}14)$$

where

d: the effective depth to the reinforcement of section

a: the shear span

$f_c^{'}$: the cylinder concrete crushing strength

d_o: empirical constant based on concrete strength and determined by equation 3-15:

$$d_o = 3036(f_c^{'})^{2/3} \quad (3\text{-}15)$$

3.7.5.4 Ductility

Ductility is a term that refers to the ability of a material to deform permanently in a stable/ductile way at yield. Brittle materials, such as the model concrete, lack ductility, and fracture rather easily. By adding reinforcing steel the beam can be made reasonably ductile.

In general, the displacement ductility can be defined as the ratio of the deflection of the beam in the middle under a four-point bending test when the load has dropped to 85% of the ultimate value ($\Delta_{\max\, at failure}$) to the deflection of the beam in the middle at yield (Δ_y), (Pam et al., 2001):

$$\mu = \frac{\Delta_{max.at\ failure}}{\Delta_y} \quad (3\text{-}16)$$

Due to difficulties in determining the yield point directly, the method used to estimate the yield displacement in this study is shown schematically in Figure (3-27). This may

occur for many reasons such as nonlinear behaviour of the material or the longitudinal bars being at different depths in a reinforced concrete section and therefore reaching yield at different deformations (Park, 1988). The deflection at yield and maximum deflection can be determined from elastic stiffness taken as a secant stiffness at 75% of the ultimate load from the load –deflection curve; the intersection of this line with the maximum load horizontal line gives the yield deflection (Δ_y) as shown both in Figure (3-27), and as applied to an example test from this research (Figure 3-28).

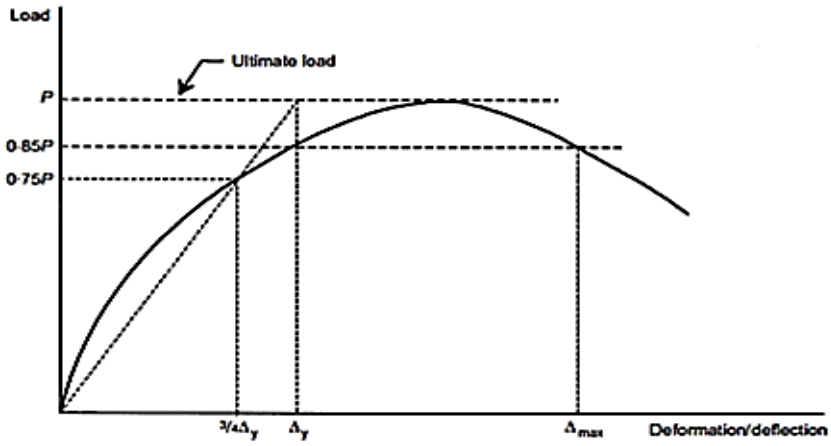

Figure (3- 27): Definitions of Δ_y and $\Delta_{max.at\ failure}$ (After Pam et al. 2001)

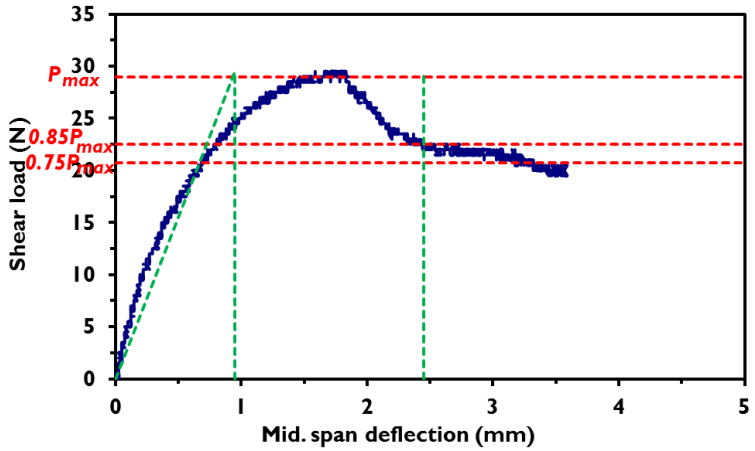

Figure (3- 28): Example of determination of yield and ultimate deformations

Values have been calculated for all tests showing ductile behaviour using the method described above and these values are compared with theoretical values for equivalent full scale concrete beams of the same design using the curvature ductility relationship presented by Maghsoudi and Sharifi (2009):

$$\mu = \frac{\alpha.\beta_1 f_c^{'} \varepsilon_c E_s}{f_y^{\,2}(\rho - \rho^{'})}.(1-K) \tag{3-17}$$

$$K = [\eta^2(\rho + \rho^{'}) + 2\eta(\rho + \frac{\rho^{'} d^{'}}{d})^{0.5} - \eta(\rho + \rho^{'}) \tag{3-18}$$

Where: $\rho^{'} = 0$ (singly reinforced section)

$\rho = \frac{A_s}{bd}$ (reinforcement ratio)

$\alpha = 1$ (stress block depth coefficient)

$\beta_1 = 1$ (coefficient defining the average stress of the equivalent rectangular stress block and it is defined as the ratio between the height of the stress block and neutral axes at ultimate state)

ε_c assumed = 0.003 (Knappett et al., 2011)

The results showed good agreement between theoretical and experimental values, with a theoretical value of ductility for this section of $\mu = 2.07$.

3.7.5.5 Modulus of rupture

For determining the modulus of rupture for the model concrete from four-point bending tests of unreinforced, Knappett et. al (2011) state that:

$$f_r = \frac{2V_{ult}L}{bh^2} \tag{3-19}$$

where V_{ult} is the shear load at which rupture (failure) occurs.

3.7.5.6 Summary of results

Table (3-5) shows all four-bending tests results for all different reinforced models. Based on these results, it was observed that bar spacing and shear reinforcement roughness had a significant effect on moment capacity, and so roughened shear reinforcement and large bar spacing were used in the centrifuge model piles. A summary of the model pile properties is given in Table (3-6).

Table (3- 5): Four-point bending test results.

Group (details)	Test No.	Ultimate Moment (kN.m)	Load at shear failure (kN)	Ductility	Bending Stiffness MNm^2
No shear reinforcement (small bar space)	1	160	53	5.3	60
	2	168	56.25	-	41
No shear reinforcement (large bar space)	1	176.5	58.75	2.7	54
	2	173	57.5	-	61
	3	157	52.5	-	52
With smooth shear reinforcement (small bar space)	1	210	70	3	54
	2	195	65	-	53
With rough shear reinforcement (small bar space)	1	221	73.75	2.05	55.5
	2	218	72.5	-	62
With rough shear reinforcement (large bar space)	1	225	75	-	59
	2	237	76.25	4.8	56
Theoretical values		256	79.4	2.07	47.7

Table (3- 6): Properties of RC model piles.

Parameter	Symbol	Value (model)	Value (prototype)
Pile size (square)	B	10 mm	0.5 m
Longitudinal bar diameter	D_d	0.6 mm	30 mm
Reinforcement ratio	$\frac{A_s}{A_c}$	0.85 %	0.85 %
Steel yield strength (0.2% proof strain)	f_y	341 MPa	341 MPa
Steel Young's Modulud	E_s	179 GPa	179 GPa
Concrete compressive strength	f_{cu}	24.95 MPa	24.95 MPa
Concrete rupture modulus	f_r	2.54 MPa	2.54 MPa
Concrete elastic Modulus	E_c	9.4 GPa	9.4 GPa
Pile bending stiffness	EI	7.8 $N.m^2$	49 $MN.m^2$
Pile moment capacity	M_{ult}	1.86 N.m	233 kN.m
Shear load at failure	V_{ult}	30.5 N	76.25 kN

3.8 Model 'elastic' (instrumented) piles

As explained at the start of Section 3.7, an 'elastic' analogue of the model RC piles was also created, which was designed to mimic the elastic behaviour of the RC piles, but (i) be stronger, (ii) have more truly linear behaviour in the elastic range and (iii) be instrumented to measure pile bending moments.

The 'elastic' piles were modelled using 6063-T6 Aluminium-alloy with E = 68 GPa and this was machined to give a central plate with dimensions of 5.2 mm in the direction of slope movement and 10 mm perpendicular to this, as shown in Figure (3-29). The purpose of these dimensions was to achieve a bending stiffness, EI, equivalent to the bending stiffness of the RC piles (Table 3-6). However, as the section was much stronger than the model concrete piles, strain gauges could be attached to these piles. The strain gauges were fixed along the length of the pile in pairs to measure bending strains within the pile at six locations, as shown in Figure (3-29). The strain gauges are distributed over the pile length so that the first is at 10mm from the pile head, below the inclined slope surface, and the rest of the strain gauges are evenly spaced over the pile embedded length. The preparation of these instruments is described in Section 3.6.2.

Once instrumented, silicon was used to protect the gauges and to 'fill-out' the pile to exterior dimensions of 10 × 10 mm, without having a significant effect on increasing EI. The piles were subsequently coated in HST95 sand using epoxy resin to give a similar rough (soil-soil) interface to that of the RC-soil interface (Knappett et al., 2011). It should be noted that at the bottom of the pile, the aluminium-alloy covers the whole cross-section of the pile to act as a driving shoe, protecting the composite construction during pile installation.

At prototype scale, the concrete piles have a relatively rough surface, and so to simulate this (and therefore the soil-pile interaction) in the elastic piles they were covered by a thin aluminium sleeve before being coated by a mixture of epoxy resin and HST95 sand.

In addition to two instrumented piles, six further non-instrumented 'dummy' piles were made having the same construction as described above. This was necessary as at the closest pile spacing considered in the centrifuge tests, eight piles were required to

cover the whole slope. Figures (3-30) and (3-31) summarise the construction process of the elastic piles described in this section.

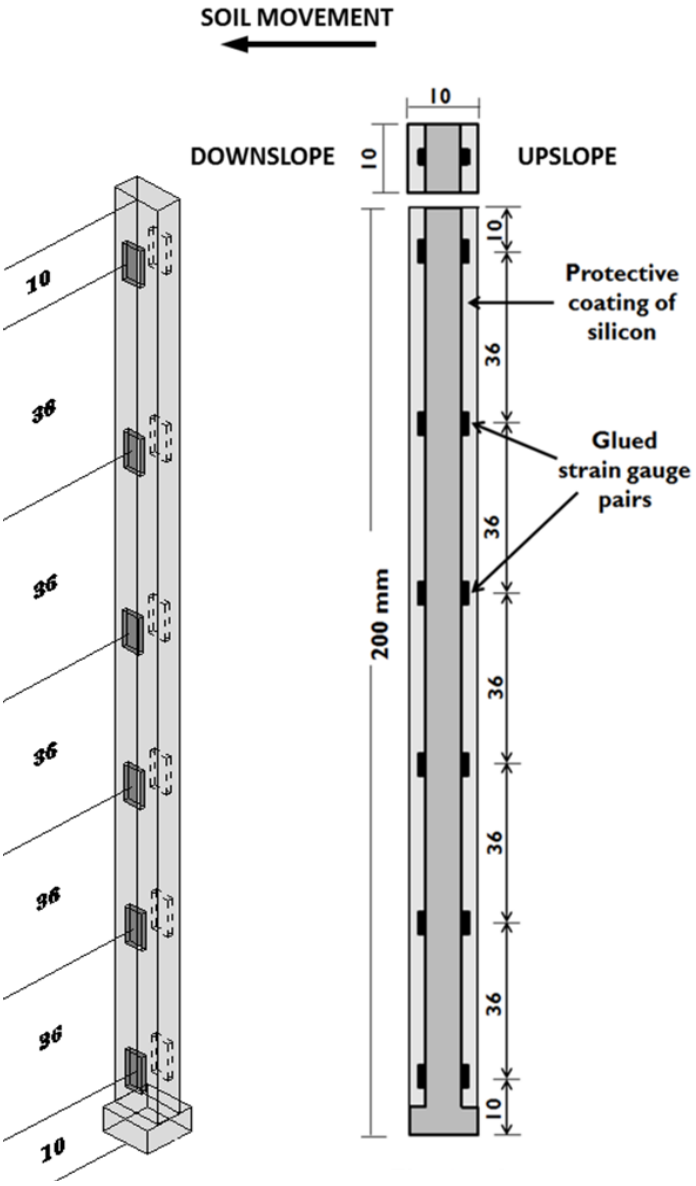

Figure (3- 29): Elastic pile, showing instrumentation

(a) Aluminium Pile

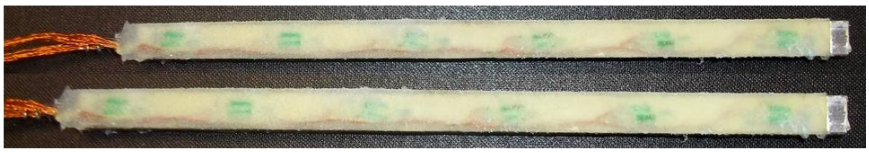

(b) With strain gauge and protective coating

(c) With epoxy resin-sand mixture

Figure (3- 30): Instrumented elastic piles

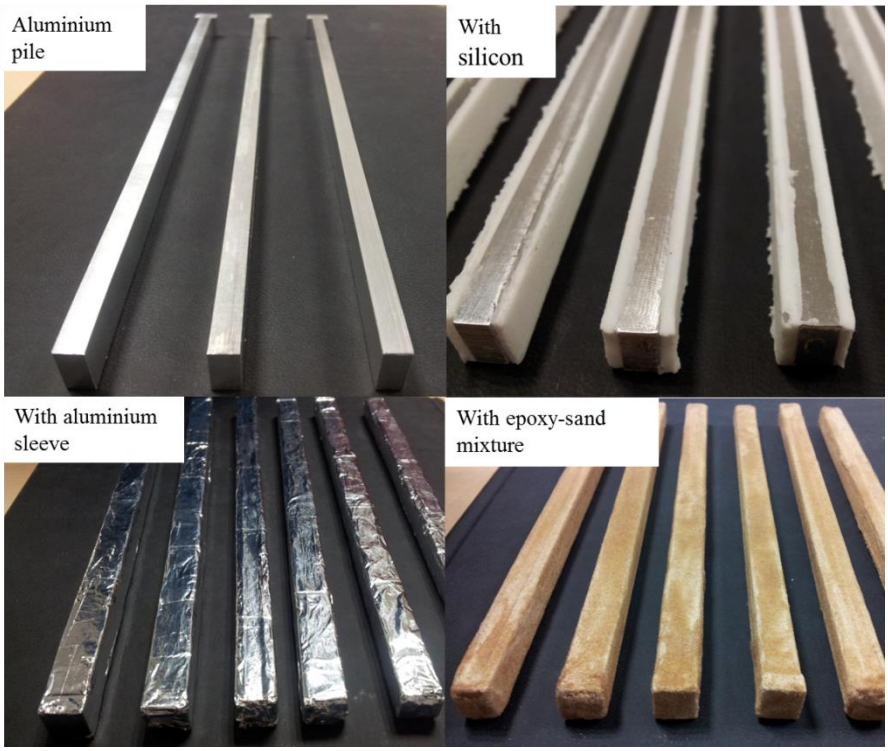

Figure (3- 31): Non-instrumented ('dummy') aluminium piles

The elastic model pile was tested as a cantilever to determine the bending stiffness, yield and ultimate bending moment as shown in Figure (3-32). A typical bending moment-curvature relationship is shown in Figure (3-33) which shows a good match to the stiffness (*EI*) of the model RC piles from Table (3-6).

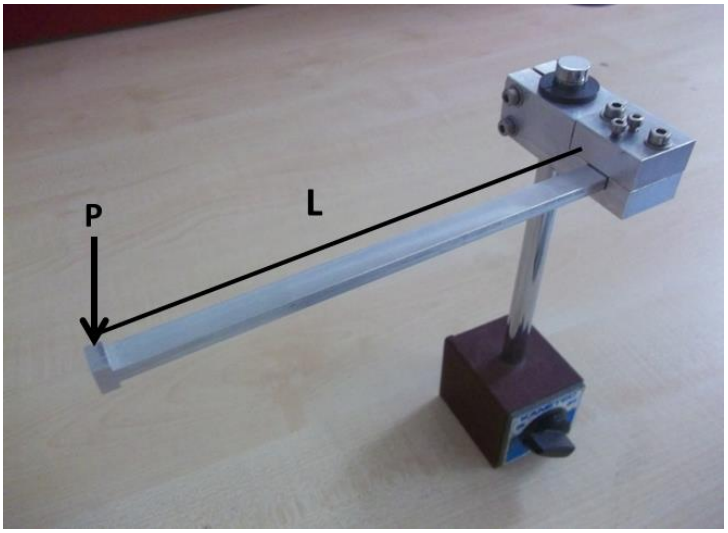

Figure (3- 32): model pile bending test (as a cantilever)

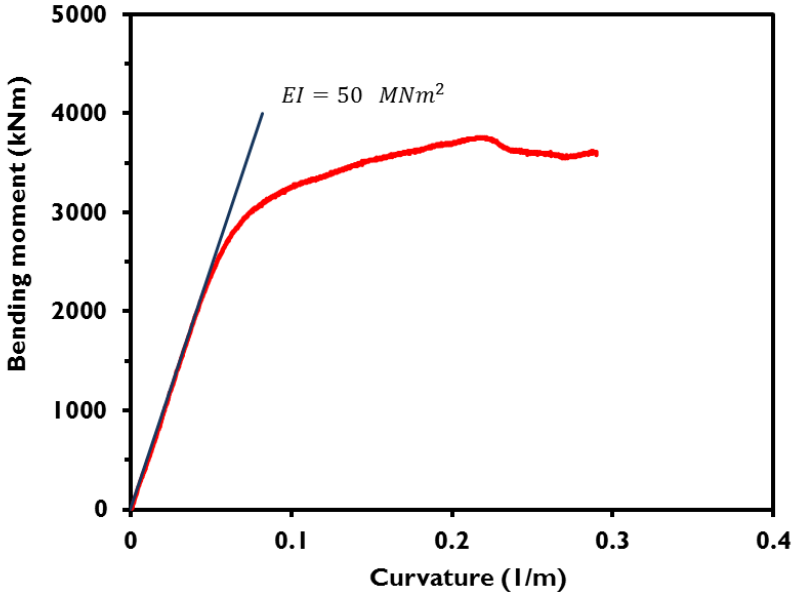

Figure (3- 33): Typical bending moment-curvature relationship for the 'elastic' model pile

3.9 Model 'weak RC' pile

Other RC model piles were made for use in further centrifuge tests (see section 6-7). The same overall cross sectional model was used as discussed in section 3-7, but only nominal longitudinal smooth steel wires (at the corners of the section) were used instead of the roughened (well-bonded) wire explained before. The idea of using this section (hereafter referred to as 'damageable section') is to investigate how the

detailing requirements for laterally loaded piles (slope stabilising piles here) are important to provide adequate resistance to the moving soil due to slope failure (details of this will come later in chapter 6). These models were made after observations of the results of the designed section after the seventeenth centrifuge test (test AA17 – no damage was observed after all these centrifuge tests). Two additional models were created to observe the stabilised slope performance with damaged piles and to inspect the failure model after earthquake (i.e. AA18 and AA19).

3.10 Soil and interface shear properties

Direct shear box tests are widely used in geotechnical engineering to determine the shear characteristics of soil. In this thesis, a standard 60 × 60 mm direct shear apparatus was used to determine the peak and critical state shear strength of the soil used in the centrifuge testing, as well as the interface shear strength between the sandy soil and the pile materials (Figure 3-34a and b, respectively). All testing was conducted at low and high normal stress levels (between 2.77 kPa to 200 kPa) for both soil-soil and soil-pile interface characteristics. The low confining stresses were used as the slope used in all of the testing was expected to fail as a shallow translational slip. Data at conventional low stress levels was already available from previous studies (summarised in Al-Defae et al., 2013). With the exception of the low stress levels, all of the tests were otherwise performed in accordance with (ASTMD3080-72Standard, 2000). Medium dense sand, at 55% relative density, was pluviated into the shear box using the same pluviator used in centrifuge model preparation, before the shear box was then transferred to the testing frame.

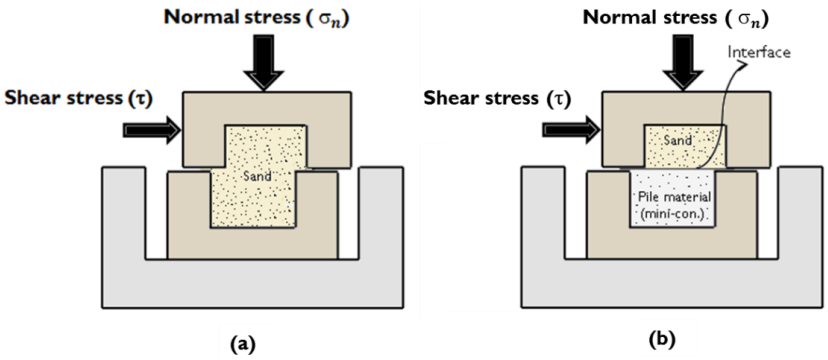

Figure (3- 34): Shear box schematic, (a) soil-soil testing; and (b) soil-pile interface properties

To verify the interface properties of the reinforced concrete (RC) piles model, interface shear testing was conducted, where the bottom half of the apparatus contained a slab of the model micro-concrete cast within a formwork having a similar surface roughness to that used in casting the model piles (Figure 3-34b). The Mohr-Coulomb strength envelope for this data is shown in Figure 3-35, along with soil-soil shear data calculated using the same apparatus and reported elsewhere (Al-Defae et al., 2013). The peak and the residual or critical angles of internal friction were approximately 38° and 32° respectively HST95 sand at 55% relative density. The peak and critical interface friction angles between the soil and the micro concrete are 33° and 27° respectively. It can be seen that the properties of the model concrete – soil interface can be summarised as $\delta'/\varphi' \approx 0.85$ at both peak and critical state, where δ' is the interface friction angle and φ' is the soil friction angle. This suggests that the model concrete is close to being rough (the elastic piles are fully rough, $\delta'/\varphi' \approx 1.00$, as the interface is sand-sand).

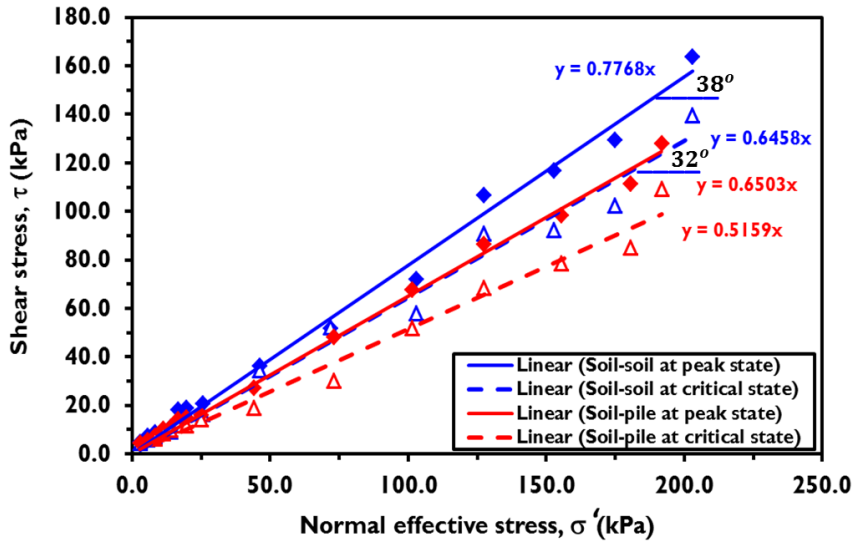

Figure (3- 35): Shear strength envelopes.

Figure (3-36) shows the shear stress mobilisation with slip displacement for both soil-soil and soil-pile interface tests at low normal stress levels, respectively, while Figure (3-37) shows the vertical -horizontal displacement relationships for soil-soil interface only, demonstrating that the soil has a very dilative response at the low stress levels tested, and that this is gradually suppressed with increasing confining effective stress.

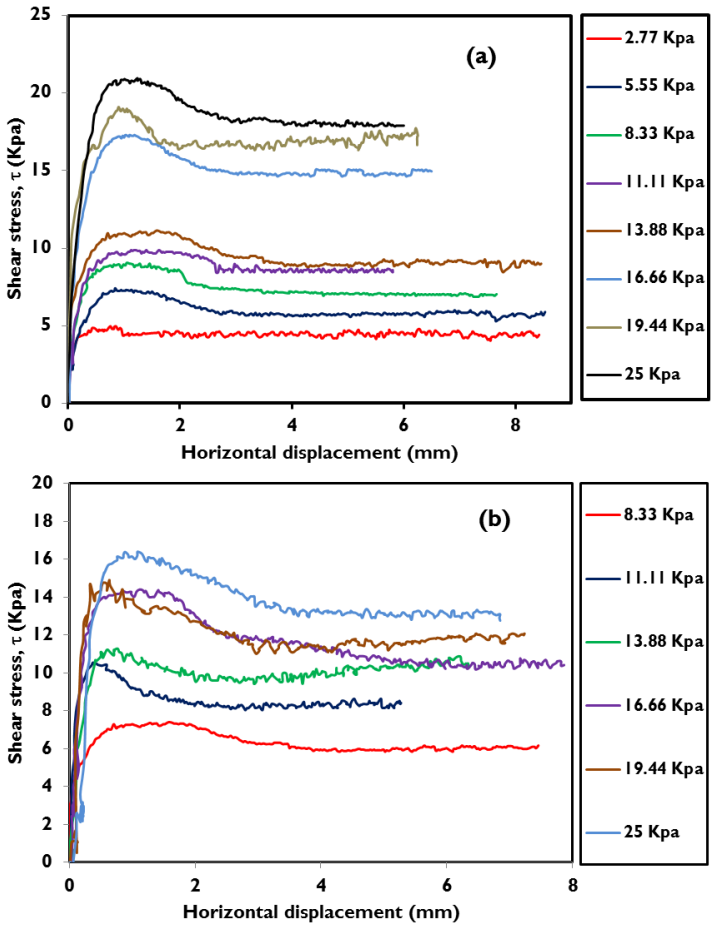

Figure (3- 36): Shear stress-normal stress relationship for (a) soil-soil; and (b) soil-pile interface

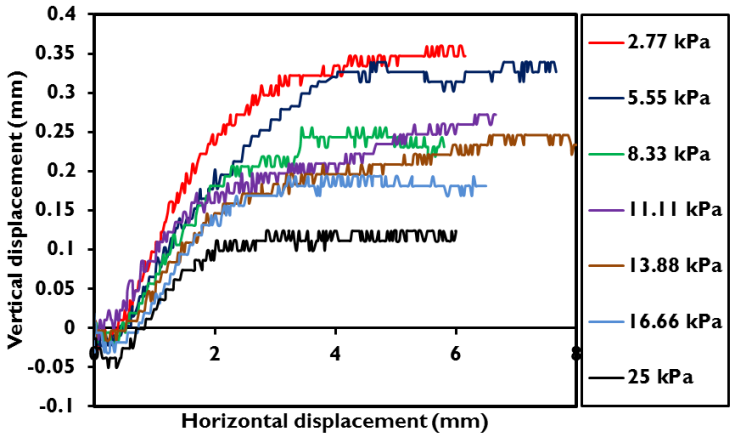

Figure (3- 37): Vertical displacement-Horizontal displacement for HST95 silica sand at medium state (D_r = 55%)

3.11 Pile installation

In order to install the piles at a regular spacing (so as not to bias failure away from the centreline of the box where the measurements were made) and to maintain verticality, a pair of perforated wooden jigs were fabricated as shown in Figure (3-38), for each pile spacing configuration tested. These were placed across the ESB container as shown and the piles were pushed through these by hand once the model had been loaded onto the EQS. The holes were of dimensions 12 × 12 mm (i.e. 1 mm from each side bigger than the pile size) to prevent any damage or wedging of the piles during installation.

Figure (3- 38): Perforated wooden jigs and resulting installed piles (s = 4.67B shown)

3.12 Input ground motions

Earthquake ground motions recorded in previous events were downloaded from the PEER (Pacific Earthquake Engineering Research) NGA database. Most of the models were subjected to a horizontal strong ground motion recorded during the M_w = 7.6 Chi-Chi Earthquake in 1999 (Station TCU072, PGA = 0.41-g), while in some models, a second motion was used which was recorded at the Nishi-Akashi recording station in the M_w = 6.9 Kobe earthquake in 1995 (PGA = 0.43-g). These motions had approximately the same peak acceleration, but different characteristics in the time and frequency domains as shown in Figure (3-39a and b) and Figure (3-40a and b). Both records were recorded in ground with V_s > 450 m/s, representing shaking from stiffer layers beneath the soil profile tested, such that any site amplification occurs solely due to the soil layer tested in the model. The former motion was used as the Chi-Chi earthquake caused a particularly high number of slope failures (Khazai and Sitar, 2004) and is strongly directional (in these tests, the stronger shaking was directed in the downslope direction which is represented by positive values of acceleration). The latter motion is well known to be particularly destructive to civil engineering infrastructure having a broad frequency band below 3 Hz. The demand motions were band-pass filtered between 0.8 – 8 Hz (40 – 400 Hz at model scale) using a zero phase-shift digital filter to remove components of the signal which were out-with the range that could be accurately controlled by the EQS.

In one centrifuge test (AA03) a stepped sine burst, having a predominant frequency of 1 Hz was used to induce an harmonic response within the slope. The time- and frequency-domain characteristics of this motion are shown in Figures (3-39c) and (3-40 c), from which it can be seen that higher harmonic components are kept to a minimum, giving a very good replication of a purely sinusoidal motion. The burst was ‘stepped’ in terms of its peak magnitude, having a number of cycles at an initial magnitude approximately equal to the historical motions described above; after this, additional cycles were input at a much stronger level (0.7g) to verify how the behaviour of the slope (e.g. topographic amplification) would change under extreme shaking (where the induced stress-strain response would be different).

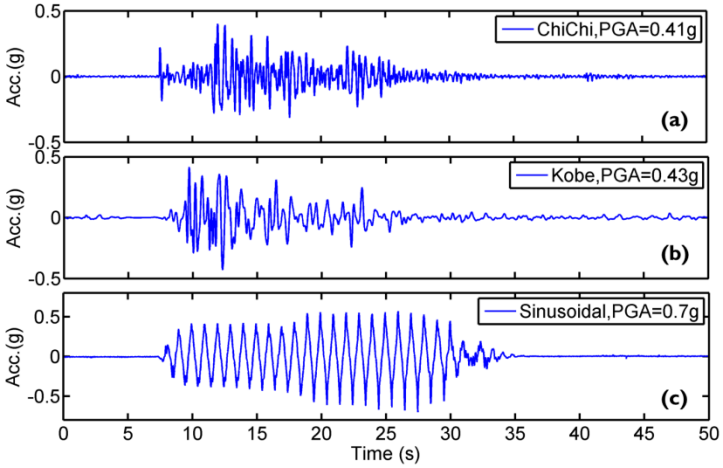

Figure (3- 39): Input ground motions in the time domain: (a) Chi-Chi; (b) Kobe; (c) stepped sine burst.

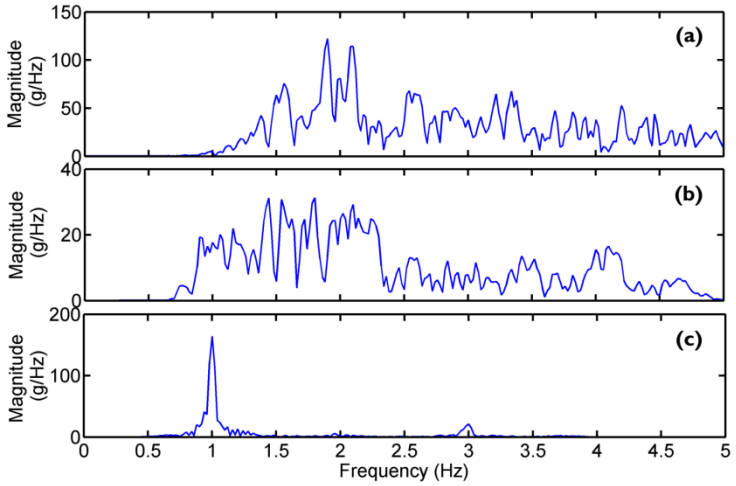

Figure (3- 40): Input ground motions in the frequency domain: (a) Chi-Chi; (b) Kobe; (c) stepped sine burst.

3.13 Centrifuge testing programme

A total of nineteen centrifuge tests were conducted on a 28^{o} (≈ 1:2) cohesionless slope without and with stabilisation by one of two kinds of pile model. The centrifuge tests were classified to five groups. The first group contained four non-reinforced slopes under three input motions (Chi-Chi, Kobe and stepped sine burst). These tests are described in detail in Chapter 4 and the results are discussed in Chapters 4 and 5. Sinusoidal wave is used once during this study (only for unreinforced slope in group one) only to compare the dynamic response of the slope under both wide range of frequencies (real motion) and single frequency (sinusoidal) whereas Chi-Chi motion

is used in all reinforced slopes at different pile spacing and some tests were conducted under Kobe motion to verify the results and to investigate how the frequencies characteristic effect on dynamic response and also to calculate the acceleration response spectra. The second group consisted of four models reinforced with RC piles under a single Chi-Chi earthquake while the third group was the same as the second group, but was subjected to four Chi-Chi motions in succession (e.g. an initial strong earthquake, followed by strong aftershocks). The fourth group consisted of five tests containing 'elastic' instrumented piles and subjected to multiple successive strong earthquakes. The first four tests used four Chi-Chi motions, while the last test used twelve Kobe motions. Finally, the last group contained two tests, both of them reinforced by a weak section RC pile, with one subjected to a single Chi-Chi motion while the other was identical but subjected to four Chi-Chi motions. Figure (3-41) shows the centrifuge test programme schematically. The last four groups of tests are described in detail in Chapter 6. The elastic pile test (group four) data are also discussed in Chapter 7.

In the case of the RC piles, the mechanical (bending) properties of the piles were determined following testing and careful exhumation. This was to determine whether there was any degradation in properties due to shaking in both a single string motion, and after a series of strong motions (e.g. an earthquake 'storm'). The data from these post-shaking tests is presented in Chapter 6.

3.14 Summary

In this chapter, the model materials, procedures and equipment used in the centrifuge testing programme have been described and characterised. It has also been shown that it was possible to develop two model piles having the same or very similar principal elastic soil-pile interaction properties (same exterior dimensions, bending stiffness, and interface friction) but with different strength characteristics (one a damageable RC section and the other an elastic section which would be unlikely to fail in the centrifuge tests due to its high moment capacity). This means that the (instrumented) elastic piles can be used to investigate the detailed seismic soil-pile interaction, while the RC piles demonstrate whether a purely elastic response is likely

to be achieved when the material model is more representative of the behaviour of reinforced concrete.

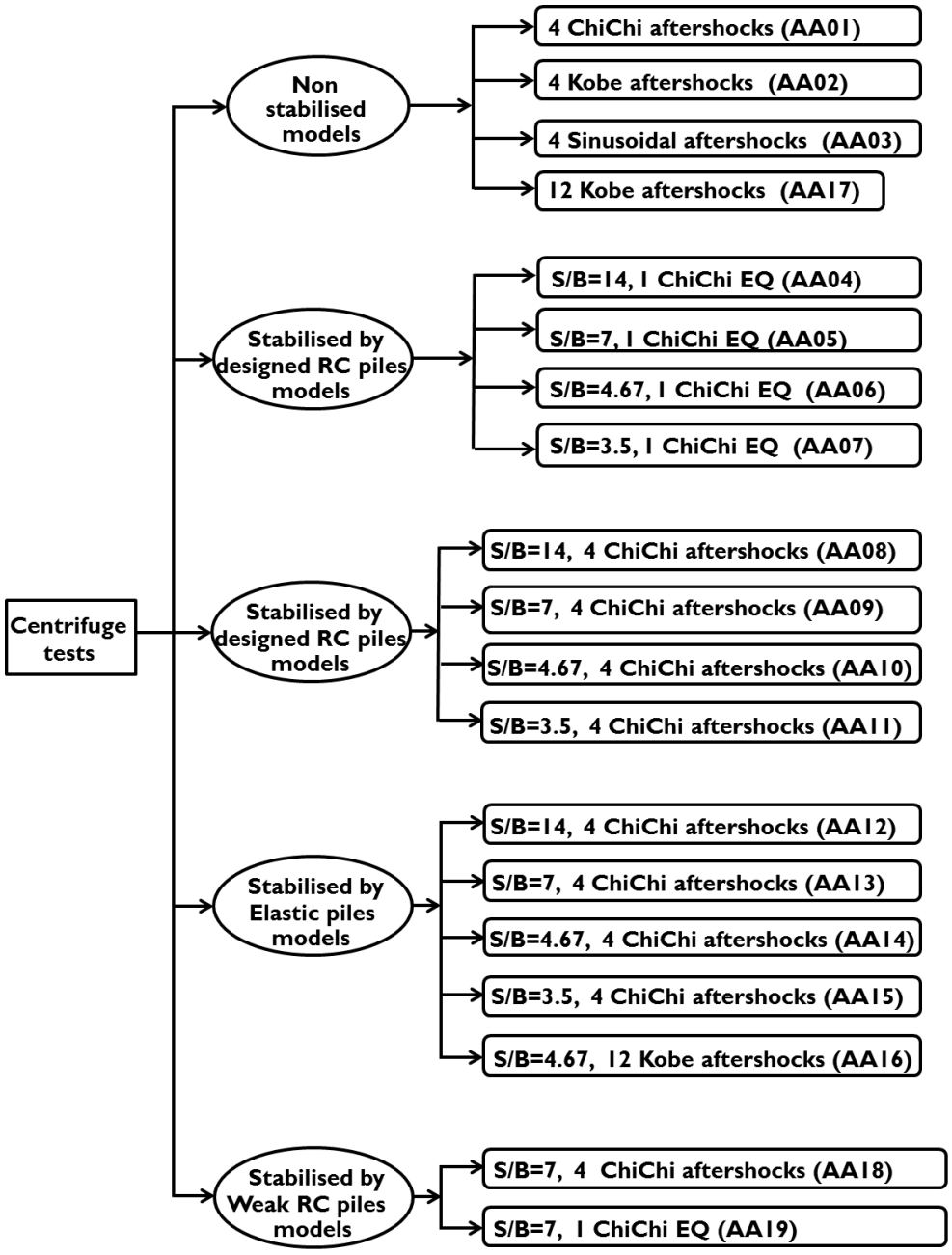

Figure (3- 41): Centrifuge testing programme.

Chapter four
Development of analytical tools for determining seismic performance of unreinforced slopes

Contents of this chapter have been published as:

Al-Defae, A.H., Caucis, K. and Knappett, J.A. (2013). Aftershocks and the whole-life performance of granular slopes. Géotechnique .63(14): 1230-1244.

4.1 Introduction

Shallow embankment slopes are commonly used to support elements of transport infrastructure in seismic regions to allow changes in gradient and damage to this type of infrastructure could inhibit the movement of emergency services and rebuilding in the aftermath of an earthquake. While the infrastructure generally supported on such constructions is relatively light (low bearing pressure) and flexible, significant damage can be caused due to large permanent seismic slip within the slope. Recent periods of seismic activity in Japan and New Zealand (2011-2012) have additionally demonstrated that civil engineering infrastructure may be subjected to a number of successive strong ground motions within a short period ('short' here meaning that there has been insufficient time to complete remediation or reinstatement of damage caused by earlier ground shaking). This means that there is a need to understand the behaviour of seismically-damaged infrastructure under further ground shaking. This feature is not currently incorporated into existing sliding-block methods.

In this Chapter, the seismic performance of such slopes in non-liquefiable granular soils is considered, focussing on permanent movements and dynamic motion at the crest, which would form key inputs into the aseismic design of supported infrastructure. In contrast to previous studies, the evolution of this behaviour under multiple sequential strong ground motions is studied through dynamic centrifuge modelling, and an improved sliding-block ('Newmark') approach is developed for estimating permanent deformations during preliminary design phases. In this improved method, the formulation of the yield acceleration is fully strain-dependent,

incorporating the effects of both material hardening/softening and geometric hardening (re-grading). It is shown that this new model considerably outperforms existing state-of-the art models (Newmark, 1965; Matasovic and Kavasanjian, 1997) which do not incorporate the geometric changes for the case of an earthquake on a virgin slope.

The ability of the new model to fully incorporate the seismic strain history of the soil (seismic memory) within the formulation, means that they may also be used to determine the whole-life performance of a slope under a suite of representative ground motions that the slope may see during its design life, and therefore, potentially allow improved estimates of the seismic performance of slopes beyond their design life. The simplicity of the sliding-block model, which requires no specialist software, means that it can be used to undertake rapid parametric analyses (such as may be necessary during the early stages of design or in the immediate aftermath of an earthquake) or used within a probabilistic Performance-Based Earthquake Engineering framework (PBEE) if desired.

Chapter five will extend this work by detailing the development of numerical (Finite Element) models which can additionally predict the settlement profile at the crest of the slope and also the dynamic ground motions at this point, for detailed seismic design stages.

4.2 Development of an improved sliding block method

The horizontal yield acceleration of a shallow translational (infinite) slip can be determined using standard limit equilibrium techniques, incorporating a pseudo static acceleration component representing the seismic ground motion (Figure 4-1). For a slip plane at depth z beneath the slope surface, the applied downslope shear stress is

$$\tau_{applied} = \gamma z \sin\beta \cos\beta + k_h \gamma z \cos^2\beta \qquad (4\text{-}1)$$

where the first term relates to the static shear stress due to the ground slope, and the second term relates to the additional peak dynamic shear stress induced by the

earthquake. The shear strength of the soil along the slip plane, assuming that the soil can be idealised as a Tresca material at failure, is given by:

$$\begin{aligned}\tau_{ult} &= c' + \sigma' \tan\phi' \\ &= c' + \left(\gamma z \cos^2\beta - k_h \gamma z \sin\beta\cos\beta - u\right)\tan\phi'\end{aligned} \tag{4-2}$$

The soil yields when $\tau_{applied} = \tau_{ult}$. The value of k_{hy} at which this occurs (the yield acceleration, k_{hy}) can be determined from Equations (4-1) and (4-2) as:

$$k_{hy} = \frac{c' + \left(\gamma z \cos^2\beta - u\right)\tan\phi' - \gamma z \sin\beta\cos\beta}{\gamma z \cos^2\beta + \gamma z \sin\beta\cos\beta\tan\phi'} \tag{4-3}$$

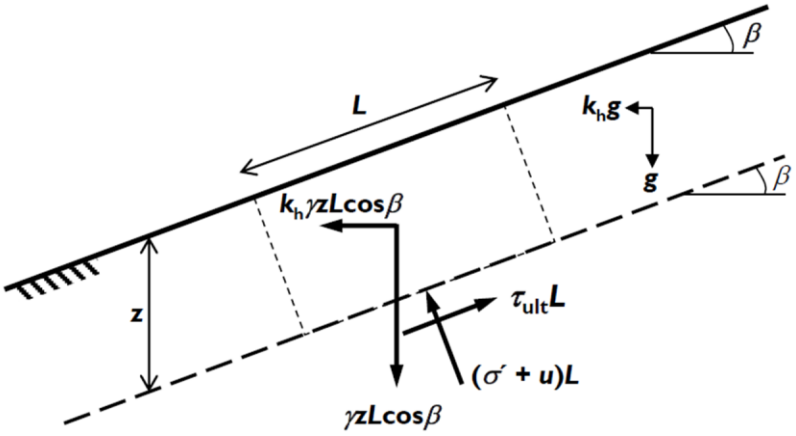

Figure (4- 1): Forces acting within an infinite slope

In a standard Newmark analysis, when the horizontal component of the ground acceleration (*a)* exceeds k_{hy} in the downslope direction, the slope will start to accelerate under the slip acceleration $a_{slip} = a - k_{hy}$. This acceleration is numerically integrated with respect to time to obtain slip velocity, which is then itself integrated to obtain slip displacement. Once a < k_{hy}, the sliding block will begin to decelerate (as $a_{slip} < 0$) until the slip velocity reaches zero, at which point the block comes to rest until a_{slip} is again positive. This procedure has been described in greater detail in Chapter two.

In a dry cohesionless soil, $c' = 0$, $u = 0$ and γz cancels in Equation (4-3), i.e. k_{hy} is independent of the depth of the slip plane (so long as it continues to be parallel to the slope surface). Equation (4-3) therefore simplifies to:

$$k_{hy} = \frac{\cos\beta\tan\phi' - \sin\beta}{\cos\beta + \sin\beta\tan\phi'} \tag{4-4}$$

The equation (4-4) is to calculate the yield acceleration in the downslope direction. By checking the yield acceleration at the opposite direction (i.e. upslope direction by changing the additional peak dynamic shear stress induced by the earthquake to the opposite direction) to investigate whether measured yield acceleration in upslope direction is affected by negative acceleration of the seismic ground motion. Equation (4-5) shows the yield acceleration in opposite direction.

$$k_{hy} = \frac{\cos\beta\tan\phi' + \sin\beta}{\cos\beta - \sin\beta\tan\phi'} \tag{4-5}$$

The yield accelerationin upslope direction was measured in case of critical state of soil strength (around 1.73g) and this suggest there is no movement for the soil in upslope direction due to negative acceleration as the PGA values of the input motions does not reach to the measured yield acceleration.

In both Equation (4-4) and (4-5) the only parameters affecting k_{hy} are the slope angle β (geometric) and the soil friction angle φ' (constitutive). In a standard analysis, both β and φ' are constant. In reality, however, the soil may be strain softening, in which case φ' will depend on the magnitude of the shear strain (ε_s) on the slip plane and the density of the soil, reducing from the peak value (φ'_{peak}) to the critical state value (φ'_{cr}) which is applicable at large shear strain. Matasovic *et al*. (1997) presented a simplified model for this which was described in Chapter two. Figure (4-2) shows this strain softening behaviour. If $\varphi'_{peak} = \varphi'_{cr}$, the model reduces to the standard case of a strain softening material. To incorporate this behaviour into an analysis, the value of k_{hy} at a particular time step is calculated based on the current permanent downslope displacement, computed in the previous time step, divided by the thickness of the shear plane to obtain an estimate of the shear strain. For small to moderate earthquakes whose peak ground acceleration magnitude is close to k_{hy} (and which will

therefore have only a limited amount of slip), strain softening behaviour can have a dramatic effect on computed slope displacements, with k_{hy} potentially changing continuously throughout the earthquake as φ' changes. In larger earthquakes, where a single large cycle causes sufficient slip/strain to reach critical state conditions, then the strain softening model is likely to predict only a marginally smaller slip compared to a standard (strain-hardening) analysis using a constant $\varphi' = \varphi'_{cr}$.

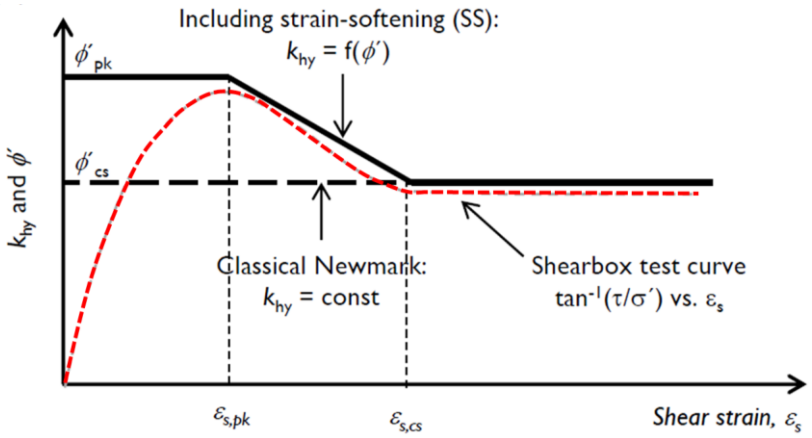

Figure (4- 2): Newmark sliding block procedure, incorporating strain-softening

The slope angle β will also change during an analysis, as slip will cause settlement at the crest and accumulation of material at the toe, i.e. the slope will become shallower (re-grading). A simplified model for this geometric effect is developed in this chapter and is shown in Figure (4-3). Figure (4-3a) shows the kinematically admissible failure mechanism assumed for an increment of sliding; in which infinite sliding is the predominant component. This leads to settlement of the material at the slope crest and a translation of the position of the toe. Provided that β is relatively small (such that the slope is long compared to its height), the equilibrium of this mechanism will be well approximated by infinite slope theory (i.e. Equations (4-3) or (4-4) will adequately describe k_{hy}). It is assumed that any volumetric change in the material in the sliding block is negligible to simplify the analysis (the settlement are important as it may causes change in geometry). From Figure (4-3b), the instantaneous slope angle β_{i+1} can be determined from:

$$\beta_{i+1} = \tan^{-1}\left(\frac{H_i - d_i \sin\beta_i}{H_i \cot\beta_i + d_i \cos\beta_i}\right) \tag{4-6}$$

where H_i is the height of the slope at the previous time step. For the initial time step, $d_o = 0$, $H_i = H$ and $\beta_i = \beta_o$.

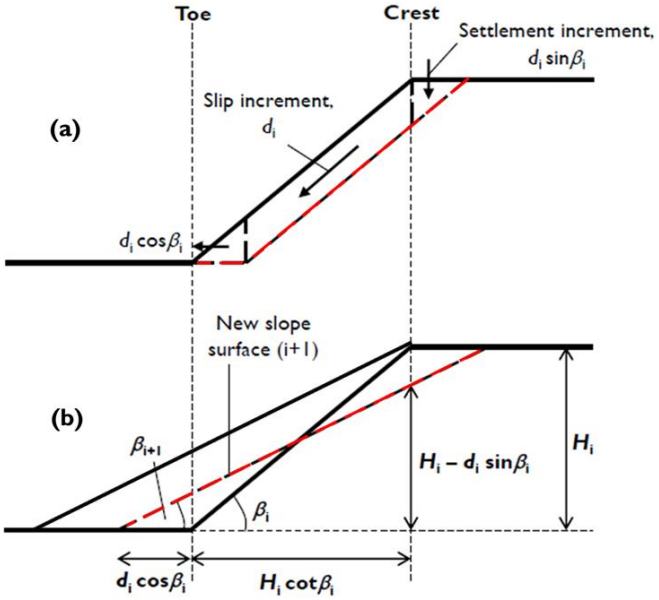

Figure (4- 3): New incremental slope re-grading mechanism

It should be noted that the deformations in Figure (4-3b) are shown at exaggerated scale for clarity. The slope angle can therefore be recalculated at each time step to account for the re-grading of the slope based on the increment of slip occurring in the previous time step, as φ' was previously to account for strain-softening. The yield acceleration will thus be fully strain-dependent. This method assumes that once the slope has been deformed to a new, smaller value of β, the failure mechanism will continue to be of the infinite type, with a new slip surface forming parallel to the new slope surface. It also assumes that the strain-dependent effects on β and φ' are independent to simplify the calculations – in reality, this latter assumption may not be true as the changing angle of a softened slip plane (i.e. with $\varphi' = \phi'_{cs}$) may push at least part of it into previously undisturbed soil. If this effect and the effects of strain softening are significant, it is expected that the model will overestimate movements; however, this would be conservative for use in analysis and design. It should also be

noted that the model as formulated can be used even for the case of large total slope movements (such as may accrue during a series of strong aftershocks) as the displacement increment in each individual time step will remain small, and therefore the instantaneous failure mechanism will be represented by Figure (4-3a) for small displacements.

From the form of Equation (4-5) it is clear that β can only ever reduce during an earthquake, resulting in an increase of k_{hy} from Equation (4-3) or (4-4), i.e. the slope will geometrically harden during an earthquake, and the slip in a subsequent (identical) earthquake will be less than that occurring in the original. The behaviour of a seismically damaged slope during a subsequent earthquake can therefore be determined by starting from the initial conditions (amount of slip, accumulated strain, re-graded slope angle and current friction angle) obtained at the end of the previous ground motion.

4.3 Centrifuge modelling

4.3.1 Modelling details

To validate the improved yield acceleration and sliding block model developed in the previous section, dynamic centrifuge testing was conducted using the 3.5 m diameter beam centrifuge and servo-hydraulic earthquake simulator at the University of Dundee, which was described in chapter three. Three models were flown representing identical 1:2 slopes ($\beta_o \approx 28°$) at 1:50 scale in dry sand (HST95 silica sand, also described in Chapter 3) at 50-g. A 1:2 slope was selected to ensure that the soil was statically stable, but with a sufficiently low factor of safety (and therefore low k_{hy}) to ensure that large slip displacements would be generated during strong ground motion such that the analytical model could be validated to large displacements. All subsequent dimensions and properties are given at prototype scale at 50-g, unless otherwise stated.

The arrangement and instrumentation of the slope models is shown in Figure (4-4). The slopes were prepared at a relative density of $D_r = 55 – 60\%$ (the range accounts for the accuracy in being able to measure and replicate D_r), 8 m tall from toe to crest and were underlain by a further 6 m of sand at the same relative density. Details of

the basic soil properties, instrumentation and container were described previously in Chapter 3.

A check of the static stability of this slope was conducted using Equations (4-1) and (4-2), with $k_h = 0$ with the result expressed as a factor of safety (*FS*).

$$FS = \frac{\tau_{ult}}{\tau_{applied}} = \frac{\tan\phi'}{\tan\beta} \tag{4-7}$$

This was also verified using the Discontinuity Layout Optimisation (DLO) technique (Smith and Gilbert, 2007), with the calculations carried out using LimitState: GEO, V2.0. It is a general purpose software program which is designed to rapidly analyse the ultimate limit state (or 'collapse state') for a wide variety of geotechnical problems. The factors of safety were determined for both peak (40°) and critical state (32°) friction angles (see Section 4.5), and the results are summarised in Table (4-1).

Table (4- 1): Static slope stability data

	Static stability parameters	
Soil strength	*F* (Eq. 4-6)	*F* (DLO)
$\varphi' = 32°$	1.17	1.20
$\varphi' = 40°$	1.56	1.61

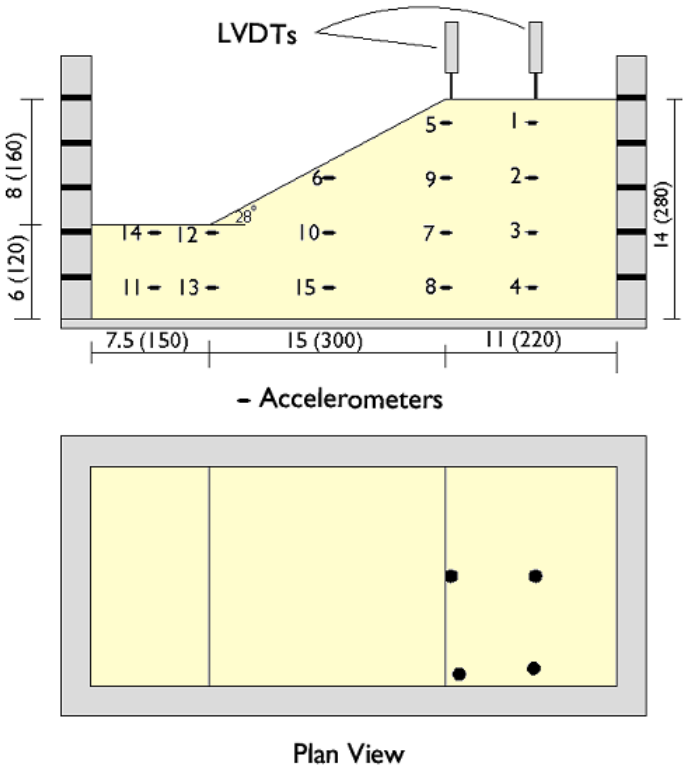

Figure (4- 4): Centrifuge test layout, 1:2 slope; dimensions in m at prototype scale (values in brackets in mm at model scale)

4.3.2 Summary of testing programme

Details of the model tests are summarised in Table (4-2). All ground motions were initially calibrated on a dummy model identical to that shown in Figure (4-4), but without instrumentation, to train the programmable logic controller within the earthquake simulator to achieve a faithful and repeatable replication of the demand motions. As a result, the ground motions applied in each successive earthquake are felt to be as close to identical as could realistically be achieved in practice.

Table (4- 2): Summary of centrifuge models tested

Test ID	β (°)	D_r (%)	Input motion (no.)	Peak input acceleration (g)
AA01	28	56	Chi-Chi, 1999 (4)	0.41
AA02	28	59	Kobe, 1995 (4)	0.43
AA03	28	57	Stepped sine (1)	0.4/0.7

4.4 Determination of seismic slip mechanism of tested slope

To confirm that the infinite slip mechanism assumed in the analytical model is valid for the slopes tested in the centrifuge, DLO was also used to obtain a minimum upper-bound mechanism for the actual limited geometry of the centrifuge model under earthquake shaking. DLO calculations were carried out using LimitState:GEO, v2.0. Seismic loadings may be modelled in this software using the pseudo-static method by specifying horizontal and vertical accelerations. Figure (4-5) shows the failure mechanism for the cohesionless centrifuge test slope using the same soil strength properties for HST95 silica sand as used in the determination of *FS* in Section. 4.3.1.

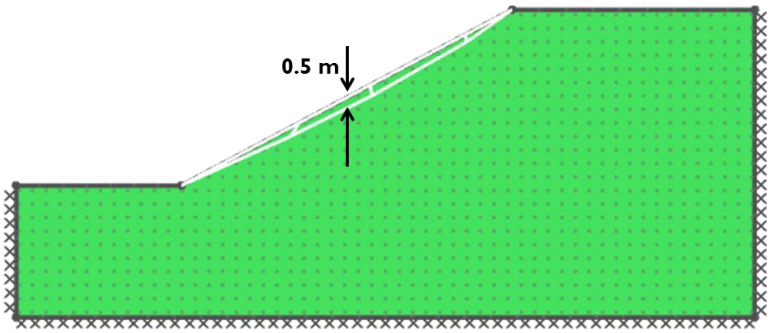

Figure (4- 5): Failure mechanism for 1:2 slope computed from DLO for seismic case

The yield acceleration was also determined using Equation (4-4). All of the calculations were conducted for friction angles of 32° and 40°as before, representing the critical state and peak friction angles of the sand at the approximate depth of the shear plane, respectively (see following section). The results are summarised in Table (4-3).

Table (4- 3): Dynamic slope stability data

		Dynamic stability parameters	
Soil strength	k_{hy} (Eq. 4-4)	k_{hy} (Eq. 4-4)	k_{hy} (DLO) in downslope direction
$\varphi' = 32°$	0.07g	1.73	0.07g
$\varphi' = 40°$	0.21g	2.46	0.22g

4.5 Validation of sliding-block model

Visual observations from the centrifuge tests (by using colour sand columns) suggested that the 1:2 slopes tested failed in a shallow translational mechanism consistent with that shown in Figure (4-6).

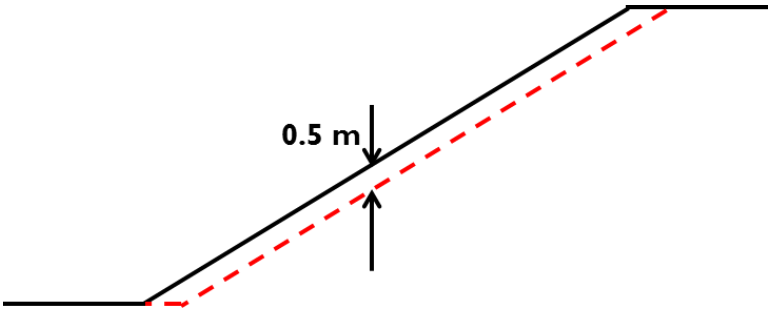

Figure (4- 6): Failure mechanism for 1:2 slope computed from DLO for seismic case

Before predictions could be made of the displacement observed in the centrifuge tests, shear box testing was conducted on samples of dry sand prepared to the same relative density as in the centrifuge tests using a standard 60 × 60 mm direct shear apparatus (DSA) to obtain φ'pk and φ'cs. These tests were conducted at a range of effective confining stresses representing those within the top 1 m of the soil, as the shear plane depth was predicted to be at approximately 0.5 m depth from Figure (4-5) via the DLO technique and from Figure (4-6) from the centrifuge test results. The test data is shown in Figure (4-7), from which φ'pk = 40°, φ'cs = 32°, εs,pk = 3.5% and εs,cs = 7.5%. The shear band thickness (required for converting slip displacement in the sliding-block model into an approximate shear strain) was estimated at t = 16D50 = 2.4 mm based on a range of previous studies (Muhlhaus and Vardoulakis, 1987; Oda and Kazama, 1998; Muir Wood, 2002, amongst others). The calculations were conducted at prototype scale and so the shear strain was estimated using 50t = 120 mm to model the correct ratio between the slope geometry and the grain size within the model. For application to a true field case where the grains are smaller compared to the overall size of the slope, the true shear band thickness should be used instead. For the tests presented herein, changing the shear band thickness from 120 mm to 2.4 mm resulted in less than 1% change in crest settlement (the actual value varied slightly with the input motion considered) confirming that the grain size scaling effect is negligible and that centrifuge modelling is therefore an appropriate technique for modelling slope failure problems in coarse-grained soil. A similar conclusion was

reached by Anastasopoulos et al. (2007) for fault rupture (shear band) propagation through the same sand.

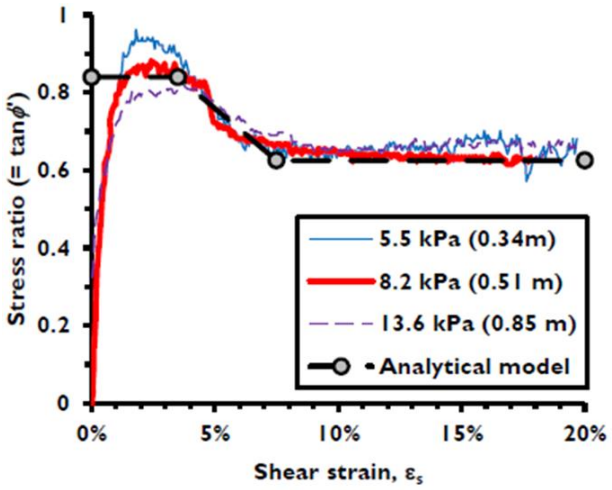

Figure (4- 7): Soil test data from direct shear apparatus (DSA)

Using these constitutive parameters, sliding-block analyses were conducted for each of the centrifuge tests (for all four earthquakes in the cases of tests AA01 and AA02). Simulations were conducted using the 'bedrock' input motion, this being taken from the bottom-most accelerometer in the models – instrument 8 in Figure (4-4) – so that the motion was that actually seen by the slope after any losses due to the shear transfer through the shaking table and into the model container. In slopes with deep rotational failure surfaces, e.g. in municipal solid waste or steep cohesive slopes, the dynamic behaviour of the material within the sliding block may be significant (e.g. Rathje and Bray, 1999); this was not the case for the extremely shallow translational slips which occurred within the cohesionless slopes tested herein. Figure (4-8) shows the effect of the geometric re-grading (change in β) using the first earthquake of test AA01 as an example. Only the positive (downslope) accelerations have been shown for clarity (i.e no possibility for upslope movement due to negative acceleration). No downslope slip occurs until the ground motion exceeds the yield acceleration based on the peak strength. Once the ground motion exceeds this value however, and the slope begins to slip, the shear strain rapidly accrues resulting in softening to critical state conditions after the first large pulse. Motion of the slope also causes re-grading (geometric hardening) and the yield acceleration can subsequently be seen to increase non-linearly throughout the remainder of the earthquake, leading to reduced slip

velocities (and hence reduced permanent slip) compared to the case with no geometric hardening.

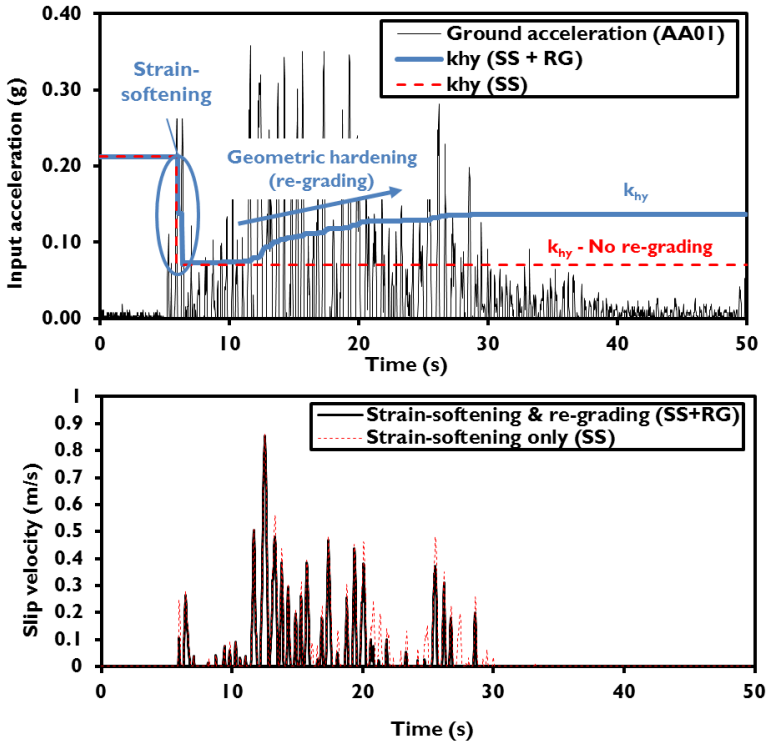

Figure (4- 8): Application of new sliding block model showing key features (Chi-Chi EQ1, test AA01)

Figure (4-9) shows the re-grading mechanism for the harmonic motion (test AA03). Because most of acceleration cycles values are above the yield acceleration of the slope, thus, the re-grading mechanism is very clear and the yield acceleration was increased sharply (above even the original peak value) due to slope re-grading.

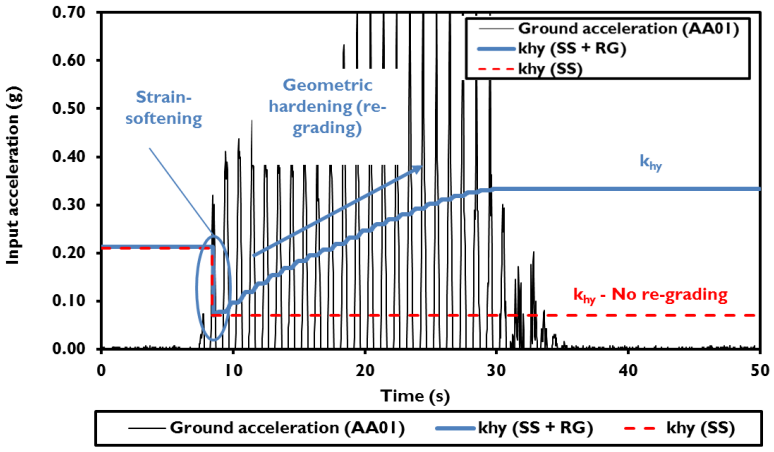

Figure (4- 9): Application of new sliding block model showing key features (Sine burst motion, test AA03)

Figures (4-10) and (4-11) show the results of simulations of cumulative crest displacement both with (SS + RG) and without (SS) re-grading with the centrifuge test data, for tests AA01 and AA02 respectively. It can be seen that in each case, the improved model presented in this chapter (SS + RG) tracks the settlement at the crest of the slope much more closely than the model which only incorporates the constitutive effect (SS). These latter models increasingly diverge from the measured values with further strong shaking, as they always start with the initial (steeper) slope geometry and therefore over-predict the slip. If the input motions were identical, the slip in each subsequent earthquake would be identical for the case of no re-grading (though the movements in the first earthquake may be slightly smaller due to the strain-softening effect). Figure (4-12) shows the instantaneous slip occurring in each earthquake for tests AA01 and AA02, both as measured, and as predicted using sliding-block models. From these figures, it can be seen that the motions were not identical in each test as the SS models show differing amounts of slip; however, it is clear that without re-grading, the sliding block model cannot capture the decay in slope movement as the slope geometrically hardens. Also shown in this figure are the results of simulations conducted with re-grading but without strain-softening (RG only). In these simulations, a constant value of $\varphi' = \varphi'_{cs}$ was used.

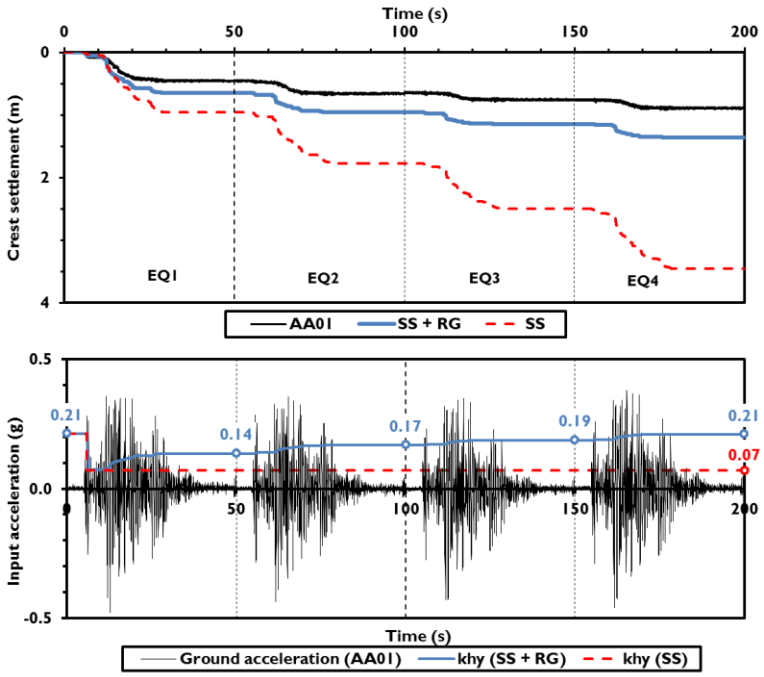

Figure (4- 10): Comparison of predicted cumulative crest settlements (with and without re-grading) with centrifuge test measurements: test AA01 (Chi-Chi)

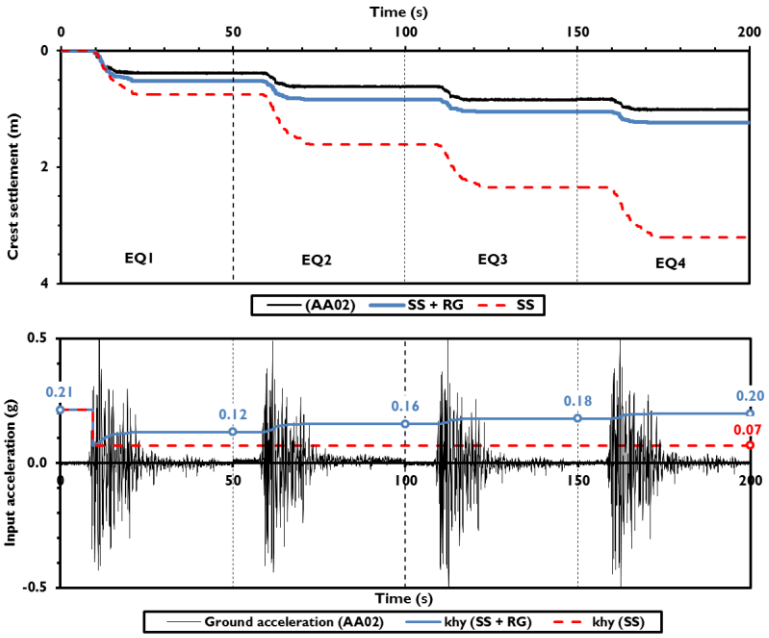

Figure (4- 11): Comparison of predicted cumulative crest settlements (with and without re-grading) with centrifuge test measurements: test AA02 (Kobe)

Figure (4-12) suggests that for large earthquake motions such as those reported here, the strain-dependency of β, rather than φ' is of greatest importance for the accurate prediction of permanent slip. It should be noted that the improved models are not perfect and in each case over-predict the measured movements, as suggested earlier; however, this would be conservative in design. As the slope re-grades, the new position of the slip plane may cause it to pass at least partially through undisturbed soil, thereby leading to an enhanced average friction angle along the slip-plane. As this is not accounted for in the analytical model, this may explain the over prediction.

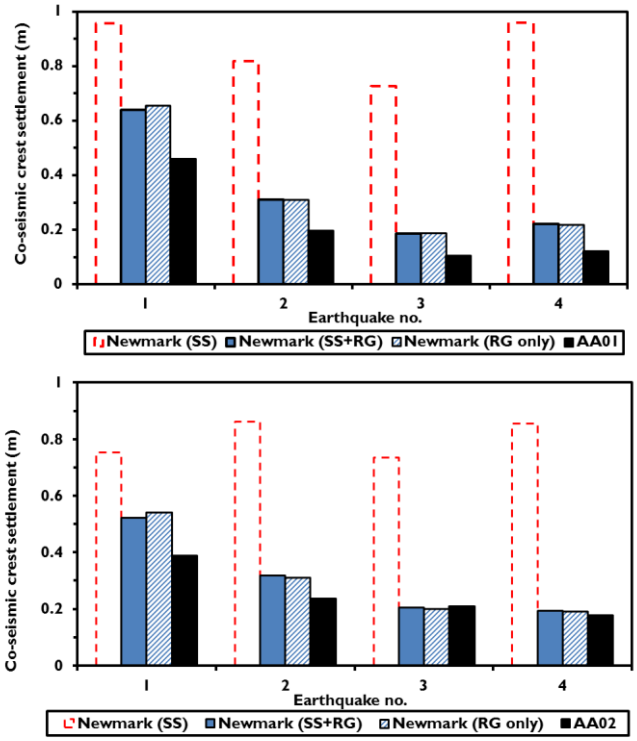

Figure (4- 12): Instantaneous settlement measurements and predictions, showing reduced displacement with increasing strong shaking due to geometric hardening (re-grading)

The sliding-block models are compared to the centrifuge test data for the harmonic excitation (test AA03) in Figure (4-13). As with tests AA01 and AA02, including the geometric hardening effects produces a better prediction than the method which only incorporates strain-softening. However, comparing Figure (4-13) with Figures (4-10) and (4-11) shows that the predictions for harmonic shaking are much poorer (225% over-prediction for test AA03, compared to 139% in test AA01 (EQ1) and 134% in test AA02 (EQ1)). The reasons for this are not clear, but it suggests that in this case, the predicted yield acceleration was too low, suggesting a change in mechanism.

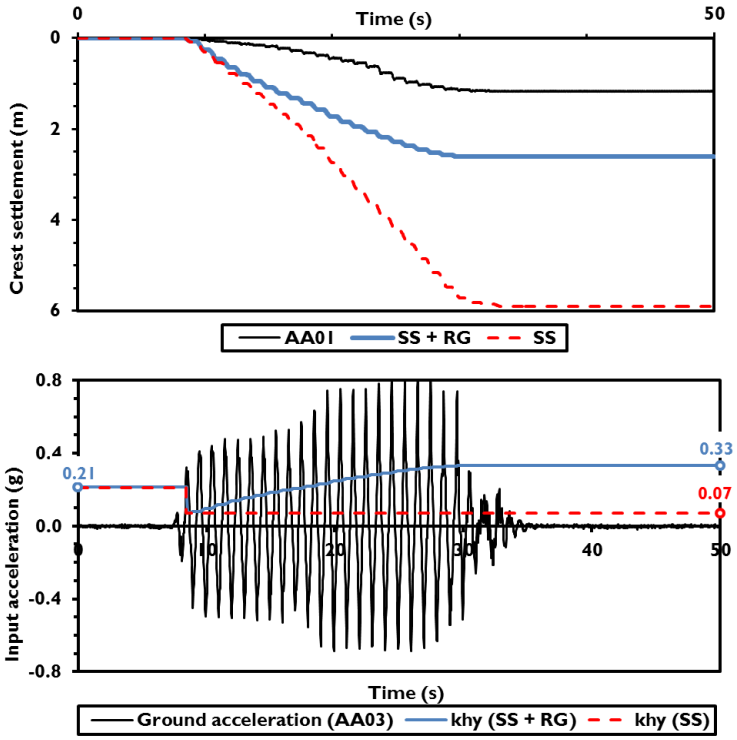

Figure (4- 13): Comparison of predicted crest settlements (with and without re-grading) with centrifuge test measurements: test AA03 (stepped sine burst)

4.6 Performance during earthquake 'storms' (many aftershocks)

A fourth centrifuge test (AA17) was subsequently conducted on the same cohesionless slope under 12 successive Kobe motions to observe whether the new method could be used to continue to predict the slope slip over a much more extreme seismic history, which may represent a 'storm' of strong earthquakes occurring in rapid succession (as occurred in the 2011 Tohoku earthquake). As can be seen in Figure (4-14), the measured crest settlement from the centrifuge test was extremely close to the predicted crest settlement from the modified procedure after the fourth earthquake. This congruence in the two values continues to the end of the eighth quake, and the performance continues to be good even to the twelfth earthquake. In contrast, the calculated crest settlement using the strain softening (SS) model (existing state-of-the-art) gives excessive over-prediction which only gets worse with successive earthquakes. The rate of increase of the yield acceleration also decreases with further shaking due to slope re-grading after each earthquake.

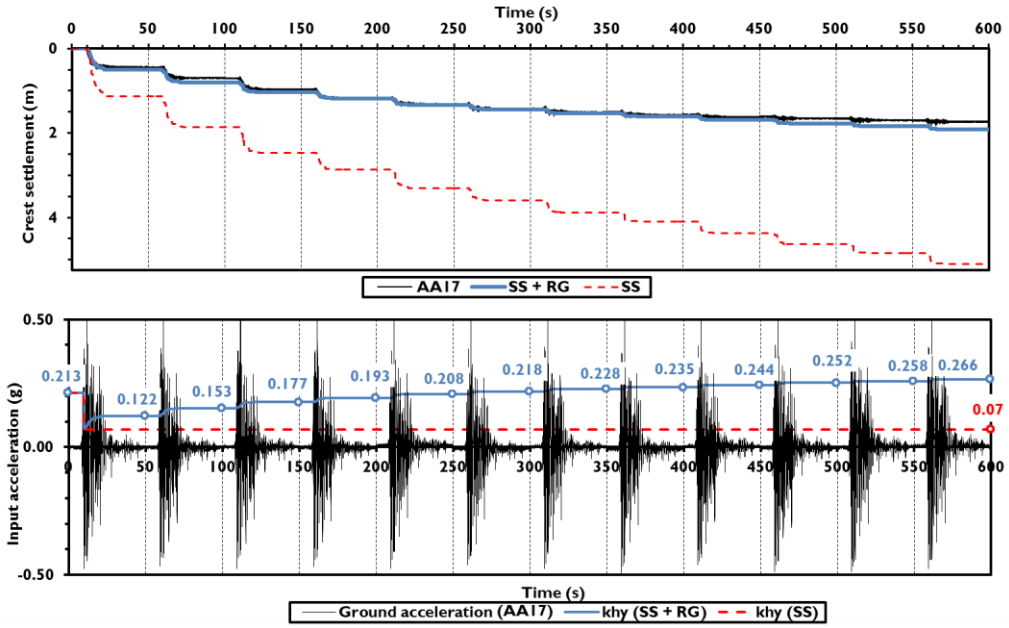

Figure (4- 14): Comparison of predicted cumulative crest settlements (with and without re-grading) with centrifuge test measurements: test AA17 (Kobe)

It can be seen in Figure (4-15) from the instantaneous settlements that there is some degradation in slip for the standard SS model, suggesting that the later earthquakes were not replicated quite as strongly over such a long sequence. However, they consistently over-predict the movements in each case and only the new model, including re-grading, is able to predict the hardening correctly.

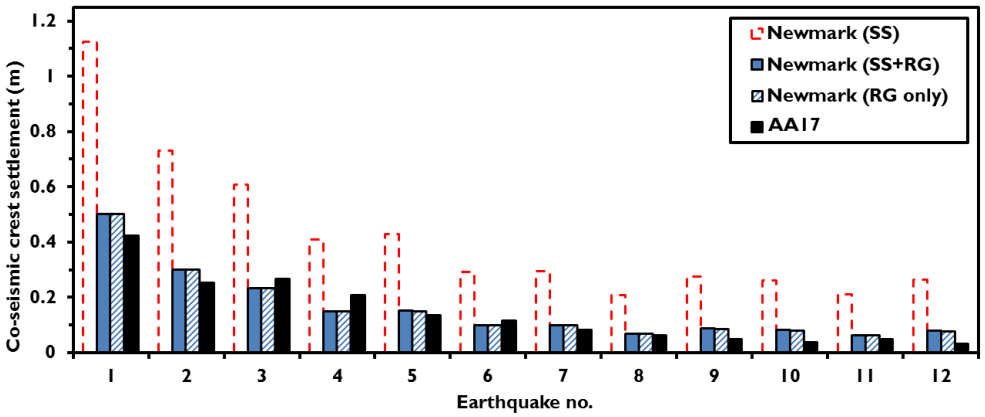

Figure (4- 15): Instantaneous settlement measurements and predictions, showing reduced displacement with increasing strong shaking due to geometric hardening (AA17)

4.7 Arias intensity and yield acceleration

As explained before, the strain softening and re-grading leads to a significant increase in the yield acceleration of the slope after each aftershock. It can be seen from figure (4-16) how the yield accelerations were changed after each earthquake. The yield acceleration for the studied slope before the earthquakes was calculated as mentioned before and it was (0.213g). For test AA01 (Chi-Chi model), the yield acceleration reduced during the earthquake after development of strain softening to 0.07g for Chi-Chi and was increased to 0.137g at the end of EQ1 due to geometric hardening or re-grading. In test AA02 (Kobe model), the yield acceleration dropped to the same values 0.07g (same strain-softening characteristics) while it was increased to 0.124g which is less than of AA01 model. The same ratio between motions in tests AA01 and AA02 were observed after second, third and the last earthquake as shown in figure (4-16).

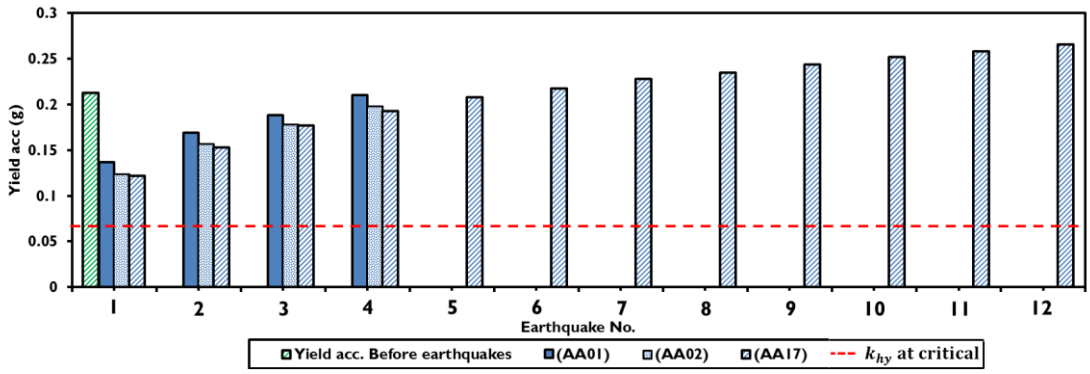

Figure (4- 16): (a) Yield acceleration variation with earthquake No.

It is well known that the stability of the slopes and the seismic displacement due to earthquakes are not dependent only on the time-acceleration histories, but the duration, mode shape and frequencies of the accelerations (Seed, 1979). Thus, a better way of characterising the earthquake motion may be by measuring the intensity of shaking through the Arias Intensity. It has been previously felt to be strongly reliable to describe earthquake shaking particularly for the case of landslides and slope failures. It is defined as the time-integral of the square of the ground acceleration as shown in equation (4-8):

$$I_A = \frac{\pi}{2g}\int_0^{t_o} a^2(t).dt \qquad (4\text{-}8)$$

where a is the acceleration in (m/sec^2), g is the round acceleration (9.81 m/s^2). The Arias intensity has been calculated for all unreinforced tests (AA01, AA02 and AA17). In figure (4-17), the calculated yield acceleration reduction factors at the end of each earthquake were plotted for AA01, AA02 and AA17 against the accumulated calculated arias intensity. It should be noted that the yield acceleration for the slope is return to the original value (before earthquake) at the end of the fourth earthquake.

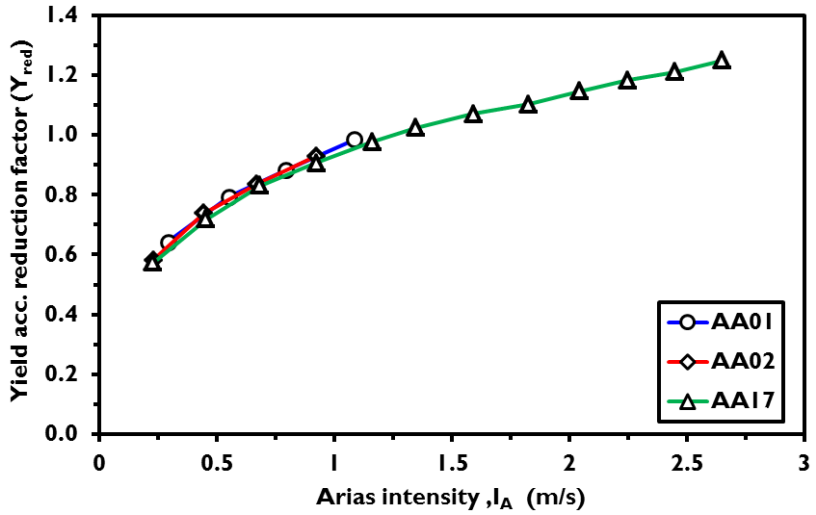

Figure (4- 17): Yield acceleration reduction as a function of Arias Intensity

The yield acceleration factor is the ratio between the yield acceleration after each earthquake to the original (pre-softened) yield acceleration for the slope. Maximum reduction in the yield accelerations was observed after the first earthquake (64% for AA01 and 58 % for AA02 respectively) due to strain softening in the first earthquake. It is particularly noticeable that the behaviour appears to be independent of the input motion (so long as this is described by Arias Intensity), suggesting that it is a unique function of the slope geometry and soil properties.

4.8 Implications of findings for a seismic design

The development of a fully strain-dependent model for the yield acceleration (i.e. where all of the parameters in Equation (4-4) are a function of strain) means that k_{hy} has a seismic memory as it incorporates strain history for a given slope. This has two clear benefits for aseismic design. Firstly, improved probabilistic predictions of damage and economic loss within a PBEE design framework (Kramer, 2008) can be made. At present, such models determine the performance of an engineered system under a design basis earthquake (DBE) which is statistically described based on local seismological data and modelling. It is clear from the centrifuge test observations presented earlier that seismic history has an important effect on performance – a slope which does not see the DBE until late in its design life, after being subjected to a significant number of smaller-moderate strength earthquakes will have a reduced response under the DBE, compared to the same slope which sees the DBE as its first event. Use of the new fully strain-dependent k_{hy} model is numerically only marginally less efficient than existing sliding-block techniques, and so could straightforwardly be incorporated into PBEE utilising Monte-Carlo simulation to produce probabilistic estimates of whole-life damage and loss under predicted suites of future earthquake motions over the design life of the slope.

The second major benefit is that once the slope has been constructed, the effects of any earthquakes which occur can be simulated based on locally-recorded ground motions. Having initially conducted analyses under the DBE when designing the slope, the performance under the DBE can then be re-evaluated after any smaller event ('pre-shock') to produce an improved prediction. The predicted displacements under the small events can also be validated against measured response (e.g. from topographic surveying to determine slip in the pre-shocks) to back-calculate and empirically improve the values of the parameters in the model, further improving the subsequent prediction under the DBE. This information may be useful for re-evaluating insurance premiums to ensure that sufficient funds will be available to repair seismic damage. The use of a sliding block analysis with seismic memory in this way means that as the slope ages, predictions of its subsequent performance and damage susceptibility improve and mean that the potential continued use of the

structure at the end of its design life can be more reliably determined based on the existing condition of the slope, incorporating its seismic history until that point.

Clearly the sliding-block techniques developed herein are limited in their ability to fully describe the seismic hazard posed to slopes which may support infrastructure at the crest. For structures located at the slope crest it is important to also understand the amplification or attenuation of ground motion within the slope such that the dynamic response can be determined (either via time-history or spectral methods). However, transport infrastructure, such as roads or railways, is likely to be more affected by the distribution of settlement back from the crest (and the associated angular distortion). Chapter 5 will develop Finite Element modelling procedures, validated against the centrifuge test results, which can be used to estimate the permanent and dynamic response at all points within the slope. Nonetheless, the simple siding block technique developed in this paper will be useful in preliminary design for comparative evaluation and screening of different design options in terms of the magnitude of the permanent movements at the slope crest (within a PBEE framework if desired). More sophisticated (and computationally less-efficient) FE modelling can then be applied for a more detailed analysis of the final design options selected.

4.9 Summary

Development of an analytical procedure to investigate the seismic displacement of slopes under strong earthquakes and many aftershocks has been presented in this chapter. The modified analytical procedure's results have been compared with centrifuge tests results for 1:2 cohesionless slopes and existing procedures. The summary of what has been observed in this chapter is explained below:

1. The yield acceleration of the 1:2 cohesionless slopes is independent of the depth of the slip surface but dependent on both angle of internal friction and the angle of the slope variation during the earthquake time.
2. As the slope starts slipping due to an earthquake event (the ground motion acceleration exceeds the yield acceleration of the slope), the soil strength reduces from the peak state to the critical state due to strain softening behaviour. The results shows that the subsequent seismic slope displacements

are not significantly influenced by the strain softening in large earthquakes while it is strongly influenced by geometric hardening (re-grading), which has been added in the new model.

3. The modified Newmark's procedure to calculate the seismic displacement of the cohesionless slope (with hardening or re-grading) showed a much improved match to centrifuge results while the models without re-grading showed very poor predictive ability.

Chapter five
Development of FEM-based tools for determining seismic performance of unreinforced slopes

Contents of this chapter have been published as:

Al-Defae, A.H., Caucis, K. and Knappett, J.A. (2013). Aftershocks and the whole-life performance of granular slopes. Géotechnique .63(14): 1230-1244.

5.1 Introduction

In chapter four, improved analytical tools, based on the Newmark sliding block method, were developed for predicting the seismic slip and resultant crest settlement in shallow granular slopes. By incorporating the changes in slope geometry as a function of slip, a fully-strain-dependent yield acceleration was determined. By incorporating strain history ('seismic memory') in this way, the model was shown to be accurate to large displacements through validation against dynamic centrifuge test data, allowing the effects of aftershocks or other sequences of multiple seismic events to be modelled (e.g. to determine the whole-life performance of the slope). While such analytical tools are useful for parametric/comparative study, particularly in preliminary design, they are not able to predict the dynamic ground motions or settlement distribution (angular distortion) behind the slope crest, both of which will have a controlling influence on the design of any infrastructure supported at the top of the slope.

In this paper, fully-dynamic numerical modelling using the Finite Element Method (FEM) will be applied to the problem, with the aim of producing a single analysis in the time domain which captures both the dynamic vibration effects and the permanent slope deformations. PLAXIS 2D v9.0 is the software used for conducting the analyses. The cross-section utilised for the numerical model, dynamic input motions, and material parameters are the same as those used in the centrifuge models. These Finite Element models are validated against the centrifuge test data from the tests described in Chapter four, with particular attention paid to the specification of the

model parameters using routine site investigation data. Existing non-linear soil constitutive models will be used which encapsulate the strain history ('seismic memory') of the soil. Emphasis will be placed on the efficient parameterisation of such a model, using previously published correlations based on databases of element test data (which require only relative density as an input), and through the use of routine laboratory test data to produce improved soil-specific calibrations. The ability to realistically model soil response, without requiring an excessive number of empirical parameters derived from non-standard tests, will allow the FEM procedures developed to be used in routine geotechnical practice for conducting detailed analyses of candidate slope designs arising from use of the analytical models from Chapter four.

5.2 Constitutive modelling

5.2.1 Overview

An elasto-plastic soil model with isotropic hardening (Shanz et al 1999) is used, in which the elastic behaviour incorporates strain-dependent stiffness variation following the model proposed by Hardin and Drnevich (1972), as modified by Santos and Correia (2001):

$$\frac{G}{G_0} = \frac{1}{1 + 0.385\left|\frac{\varepsilon_s}{\varepsilon_{s,0.7}}\right|} \tag{5-1}$$

Plastic failure is modelled using a cap-type yield surface combined with the Mohr-Coulomb failure criterion. This model is included in the PLAXIS finite element suite as the 'Hardening Soil model with small-strain stiffness'. While this model captures only strain-hardening (and not strain softening behaviour), it was shown in Chapter 4 that the effect of strain softening on slope movement is small when the earthquake is strong enough to induce significant slip, as in the motions used in the centrifuge testing. The selection of appropriate soil strength (peak or critical state friction angles) will be further discussed later in this section.

The model requires thirteen input parameters: unit weights under saturated and dry conditions; three measureable effective stress strength parameters φ'_{pk}, c' and ψ' (angle

of dilation) for use in the Mohr-Coulomb failure criterion; six measurable stiffness parameters (which are stress-dependent) describing (i) the response to deviatoric loading (E_{50}), (ii) compressive loading (E_{oed}), (iii and iv) unload/reload cycles (E_{ur}, ν_{ur}), (v) small strain stiffness (G_0) and (vi) a shear strain for describing the shape of the G-ε_s relationship ($\varepsilon_{s,0.7}$, i.e. the shear strain at which G/G_0 is 70%); finally, two empirical parameters R_f and m, the former of which controls the deviatoric stress at failure and the latter the variation of the stiffness parameters with effective confining stress:

$$E^*(\sigma_3') = E_{50}^{*ref}\left(\frac{c'\cos\varphi' - \sigma_3'\sin\varphi'}{c'\cos\varphi' + P_{ref}\sin\varphi'}\right)^m \tag{5-2}$$

$$E_{oed}(\sigma_3') = E_{oed}^{ref}\left(\frac{c'\cos\varphi' - \frac{\sigma_3'}{K_o}\sin\varphi'}{c'\cos\varphi' + P_{ref}\sin\varphi'}\right)^m \tag{5-3}$$

where E^* may be either E_{50}, E_{ur} or G_0, E^{ref} is the value of the parameter at a reference stress of p_{ref} and K_0 = 1 - sinφ'. A reference pressure of p_{ref} = 100 kPa is used throughout the remainder of this chapter. Although the model has a number of input parameters, it should be noted that all except R_f and m can be measured in some form through routine laboratory testing.

In the first set of FEM simulations which will be described in the subsequent sections, the correlations between the input parameters and relative density for coarse-grained soils presented by Brinkgreve et al. (2010) were used. Use of these parameters required no additional soil testing and all of the constitutive parameters can be defined using relative density, I_D, alone (which was uniform for the centrifuge model slopes). Use of this model represented the case in practice where no detailed laboratory test data is available, but where relative density can be determined from SPT tests or a CPT profile (e.g. as outlined in Knappett and Craig, 2012).

A second set of simulations was then conducted in which the key strength and stiffness parameters were calibrated for the soil used in the centrifuge tests using laboratory test data, the stiffness parameters being important in modelling the dynamic effects, shear-wave propagation and the strength properties controlling the permanent deformations. This model is termed 'HST95'. A large amount of shear box test data had already been published in a range of previous studies for the HST95 sand used (Lauder 2011; Bransby et al., 2012) and others have been conducted as part

of this research (Figure 5-1); this data was used to derive soil-specific strength parameters, supplemented with oedometer tests to determine soil-specific stiffness parameters. In practice, it would only be necessary to undertake tests appropriate for the in-situ soil states (e.g. density in this case); however, in this chapter a range of test data were collated/obtained for reconstituted samples covering the full range of relative densities such that a more complete model could be developed for use in future simulations of physical test results at the University of Dundee.

5.2.2 Strength parameters

Figure (5-1) shows a summary of shear box data from a total of 38 tests conducted over a range of confining normal effective stresses between 5 – 200 kPa, as summarised in Table (5-1). Figure (5-1a) shows shear stress measurements at critical state (when volumetric change had stopped), indicating that the critical state friction angle is $\varphi'_{cs} = 32°$. Figure (5-1b) shows the secant peak friction angles measured over the stress ranges considered. Stress-independent values were determined by straight line fits to the peak strength data, as φ'_{pk} is stress-independent within the constitutive model. Focussing on the datapoints below $I_D = 80\%$ gave:

$$\varphi'_{pk} = 20I_D + 29 \qquad \text{(degree)} \qquad (5\text{-}4)$$

Dilation angles are also shown in this figure; the straight-line fit for this data was found to be:

$$\psi' = 25I_D - 4 \qquad \text{(degree)} \qquad (5\text{-}5)$$

These simple linear fits to φ'_{pk} and ψ' satisfy the dilatancy relationship given by Bolton (1986) and predict the value of $\varphi'_{cs} = 32$ with an error of < 1% either using this relationship, or that by Rowe (1962) which is incorporated within the constitutive model formulation.

While the strength properties given by Equations (5-4) and (5-5) match the element test data well, their use within a strain-hardening model would imply that the peak strength is appropriate to the analysis. It has been demonstrated in Chapter 4 that for large strain slope problems, the permanent deformations are governed by the critical

state strength. Hence in modelling the centrifuge tests, $\varphi'_{pk} = \varphi'_{cs} = 32°$ and $\psi' = 0°$ were used.

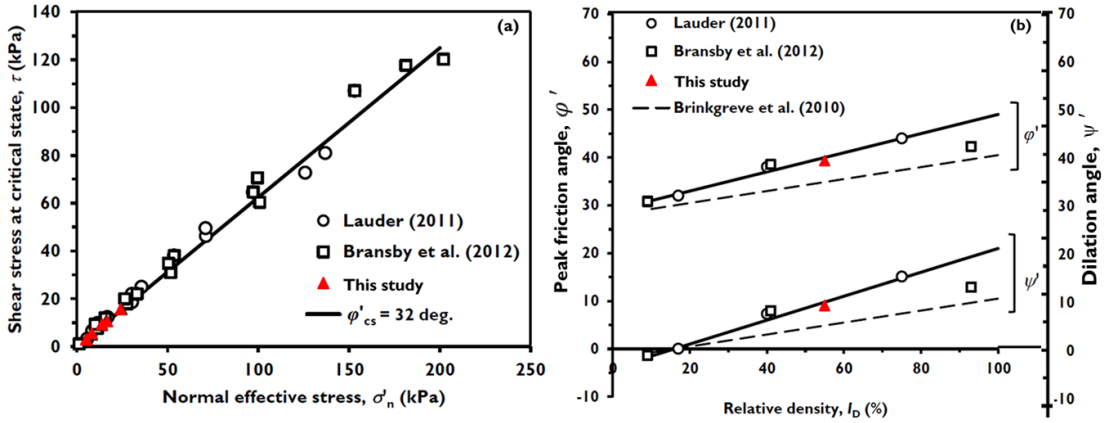

Figure (5- 1): DSA (shear box) test data used in the soil-specific calibration of the constitutive model: (a) φ'_{cs}; (b) φ'_{pk} and ψ'

Table (5- 1): DSA test data for HST95 silica sand

Source	I_D (%)	No. of tests	Effective normal stresses (kPa)
Lauder (2011)	17	8	5, 8, 11, 16, 30, 35, 70, 125
	40	6	16, 30, 55, 100, 135, 150
	75	4	11, 16, 30, 70
Bransby et al. (2012)	9	5	10, 25, 50, 100, 200
	41	5	15, 35, 55, 100, 150
	93	5	10, 25, 50, 100, 180
This study	55	5	5, 8, 13, 16, 25

5.2.3 Stiffness parameters

Oedometer test data for dry HST 95 sand were reported by Caucis (2012). These were conducted on dry samples of sand prepared by air pluviation within a Clockhouse Engineering Ltd J550 oedometer (sample height = 19 mm; sample diameter = 76 mm) at a range of relative densities between I_D = 5 – 83%. The tests were conducted up to an effective stress of 600 kPa and included 3 unload-reload cycles (200 – 100 – 200; 400 – 200 – 400; 600 – 400 – 600 kPa) to ensure that E_{ur} was well calibrated (this parameter is likely to important during cyclic (seismic) loading. The model parameters for PLAXIS were determined from virtual oedometer tests,

also by Caucis (2012), starting with the parameters suggested by Brinkgreve et al (2010) and modifying them as necessary to achieve a reasonable fit to the data. Figure (5-2) shows the axisymmetric model geometry and boundary conditions employed. To develop a complete density-dependent model (i.e.to capture both densification and loosening of the soil) in this chapter, calibrated parameters were determined for loose and dense samples from which linear interpolations were made as a function of relative density as presented by Brinkgreve et al. (2010). The interpolated parameters were subsequently checked against further tests at intermediate densities.

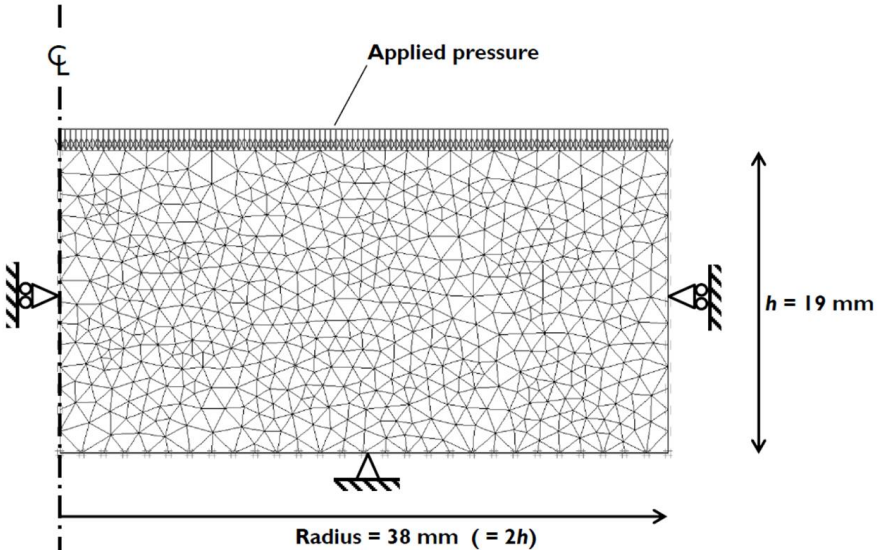

Figure (5- 2): FE mesh used in simulating oedometer tests, showing boundary conditions (after Caucis, 2012)

Figure (5-3a) shows a comparison of some results for the Brinkgreve *et al*. (2010) model which under-predict stiffness in dense sand and dramatically over-predict stiffness in loose sand. Figure (5-3b) shows the markedly improved results using fitted values of E_{oed}, E_{50}, E_{ur} and m. To reduce the number of independent parameters $E_{50} = 1.25E_{oed}$ and $E_{ur} = 3E_{oed}$ was assumed, so that E_{oed} could be used to simulate the strain magnitude correctly, and m used to control the shape of the stress-strain curve. $E_{50} = E_{oed}$ was proposed by Brinkgreve *et al.* (2010), but this is not exactly true from comparison of Equations (5-2) and (5-3); the value of 1.25 ensured that there were no unrealistic values of K_o implied in denser soils, and the analyses appeared to be

relatively insensitive to this assumption at lower densities. Following iteration, the best-fit stiffness parameters were determined to be:

$$E_{oed}^{ref} = 25I_D + 20.22 \qquad \text{(Mpa)} \qquad (5\text{-}6)$$

$$m = 0.6 - 0.1I_D \qquad (5\text{-}7)$$

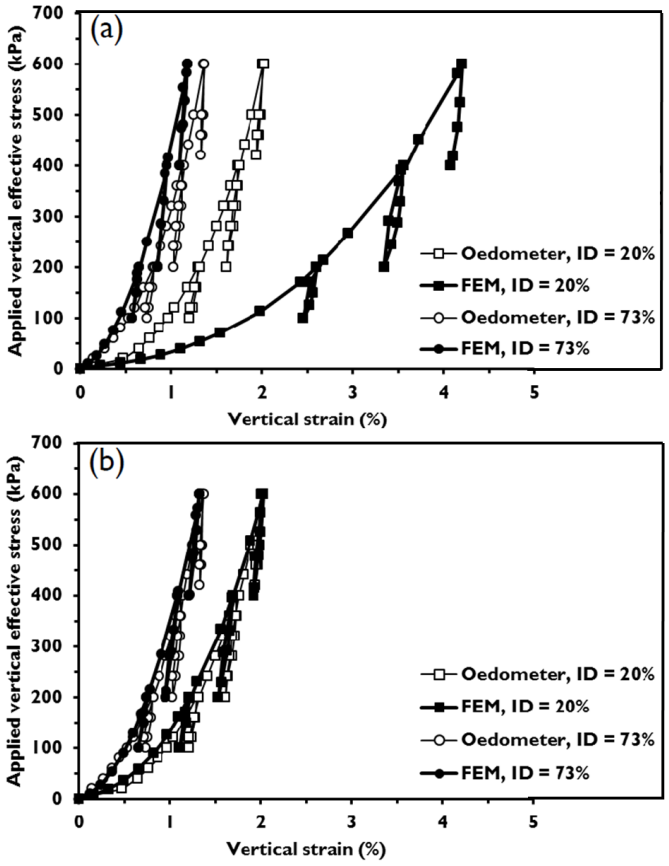

Figure (5- 3): Comparison of one-dimensional compression curves for loose and dense samples: (a) using Brinkgreve et al. (2010) parameters; (b) using HST95 (soil-specific) parameters. (Data from Caucis 2012).

It should be noted that the proposed calibration for *m* (Equation 5-7) gives a power-law exponent for stress-dependency which is between 0.5 – 0.6 at all densities. This is consistent with previous studies, e.g. Lo Presti *et al*., (1998), while maintaining the negative correlation between the two parameters noted by Brinkgreve *et al*. (2010).

As neither of the aforementioned tests measure small strain parameters, G_o was estimated using the relationship based on void ratio (*e*) proposed by Hardin and Drnevich (1972):

$$G_o^{ref} = 33\frac{(2.97-e)^2}{1+e}\sqrt{\sigma'_v} \quad \text{(Mpa)} \qquad (5\text{-}8)$$

for p_{ref} = 100 kPa. Equation (5-8) can be linearised ignoring terms of order e^2 and above; expressing e in terms of relative density with the values of e_{max} and e_{min} in chapter four then gives:

$$G_o^{ref} = 50I_D + 88.80 \quad \text{(Mpa)} \qquad (5\text{-}9)$$

as shown in Figure (5-4). The shear strain parameter $\varepsilon_{s,0.7}$ was assumed to increase linearly from 0.01% at I_D = 20% to 0.02% at I_D = 80%, i.e.

$$\varepsilon_{s,0.7} = 1.7I_D + 0.67 \quad (x10^{-4}) \qquad (5\text{-}10)$$

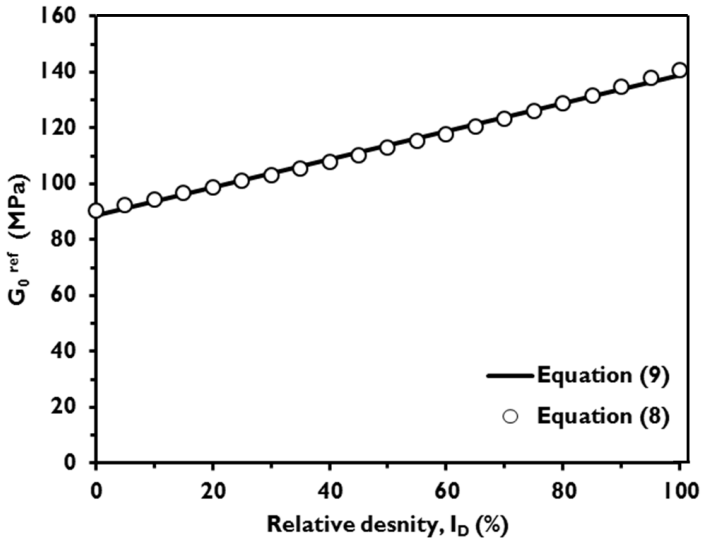

Figure (5- 4): Small strain stiffness (G_o) as a function of relative density

5.2.4 Other parameters and comments

Of the remaining parameters, the default value of R_f = 0.9 was used and the unit weight parameters were determined from standard relationships as a function of relative density and linearised, giving:

$$\gamma_{dry} = 3I_D + 14.5 \quad (kN/m^3) \tag{5-11}$$

$$\gamma_{sat} = 1.8I_D + 18.8 \quad (kN/m^3) \tag{5-12}$$

The particular choice of DSA and oedometer tests for determining the parameters as described was guided by available test data. Triaxial test data could equally be used to determine both strength and stiffness data by simulating triaxial compression on a virtual test sample using FEM in a similar way to that described for the oedometer tests. For the nominal relative density of I_D = 55% used in the centrifuge tests, values of the parameters for both the Brinkgreve et al. method (requiring only relative density) and HST95 models (utilising routine laboratory test data) are summarised in Table (5-2). Damping will be discussed later in the chapter.

Table (5- 2): Summary of constitutive parameters for nominal relative density of ID = 55%

Parameter	Brinkgreve et al. (2010)	HST95 (this chapter)
φ'_{pk}	34.9°	32° [1]
ψ'	4.9°	0° [2]
c'	0.3 kPa	0.3 kPa
E_{oed}^{ref}	33 MPa	34 MPa
E_{50}^{ref}	33 MPa	42.5 MPa
E_{ur}^{ref}	99 MPa	102 MPa
ν_{ur}	0.2	0.2
m	0.53	0.55
G_o^{ref}	97.4 MPa	116.3 MPa
$\varepsilon_{s,0.7}$	0.015%	0.016%
γ_{dry}	17.2 kN/m^3	16.2 kN/m^3
R_f	0.93	0.9

[1] 40° from Equation (5-4)
[2] 9.8° from Equation (5-5)

5.3 Validation against centrifuge test data

5.3.1 Modelling considerations

The 1:2 slopes tested in chapter 4 were modelled in plane strain with the mesh and boundary conditions shown in Figure (5-5). Figure (5-5a) shows the model layout in the centrifuge tests (Figure (4-4) in Chapter four, repeated here for ease of reference). In the FEM, the dimensions of the model domain were extended laterally and combined with non-reflecting boundary elements to better represent the semi-infinite soil conditions, i.e. boundary deformations at the location of the centrifuge container wall which are controlled by the dynamic deformation of the adjacent soil. This boundary condition can also be modelled by horizontal node-to-node ties between the two vertical boundaries in case of a symmetrical model including the width of the soil tested in the centrifuge. Compared to this alternative, the method used has a higher element requirement for the same mesh density, but allows information to subsequently be collected for points far from the crest and toe of the slope (though these are not reported here). A dynamic ground displacement was applied along the bottom-edge of the FE model, shown by the repeating arrows in Figure (5-5b). For validating the constitutive model described previously for seismic analysis, the input motion applied to the model was that measured at instrument 8 in the centrifuge model, i.e. the motion that the slope in the centrifuge actually saw, accounting for any losses between the shaking table, container and soil. The motions were input as ground displacements, determined by high-pass filtering and integration of the accelerometer records; filtering before integration to obtain velocity, and again, before integrating velocity to obtain displacement ensures that there is no permanent 'wander' due to any offset in the accelerometer recordings or integration of random noise within the signal. Displacement data was extracted from the FE models at the locations of the instruments in the centrifuge tests shown in Figure (5-5a). At points 1 – 15, accelerations were subsequently determined from double-differentiation of the displacements. For ease of reference, details of the centrifuge models and the seismic motions applied are provided in Table (5-3) (data from Chapter four).

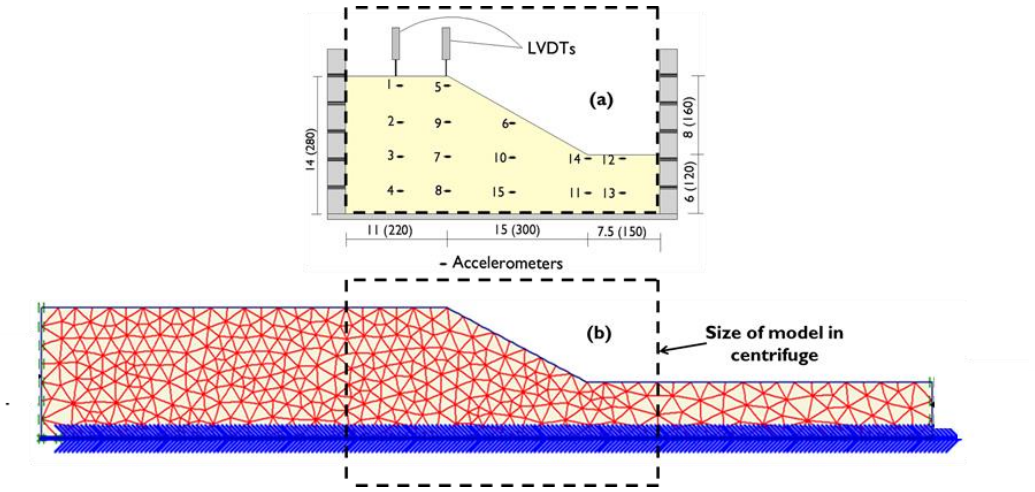

Figure (5- 5): Simulation of centrifuge tests: (a) centrifuge model layout and location of 'virtual' instruments in numerical models; (b) FE mesh, showing boundary conditions

Table (5- 3): Summary of centrifuge configurations

Test ID	β (°)	I_D (%)	Input motion (no.)
AA01	28.2	56	Chi-Chi, 1999 (4)
AA02	28.2	59	Kobe, 1995 (4)
AA03	28.2	57	Stepped sine (1)

5.3.2 Prediction of soil accelerations

Figure (5-6) shows a comparison of the measured and simulated acceleration at the toe of the slope (instrument 14) and at the mid-height of the slope (instrument 6) in the first earthquake of test AA01 (Chi-Chi motion) in both the time and frequency domains. In this figure (and subsequent figures in this section) three cases are considered: (i) Use of Brinkgreve et al. (2010) constitutive parameters; (ii) use of HST95 parameters and (iii) use of HST95 parameters with additional Rayleigh damping. The constitutive model implicitly includes material hysteretic damping within its formulation; however, these models generally over-predicted accelerations. The Rayleigh damping formulation allows additional mass and/or stiffness proportional (modal, frequency dependent) damping (ς_{add}) to be included:

$$\zeta = \alpha(\frac{1}{4\pi f_n}) + \beta(\pi f_n) \quad (5\text{-}13)$$

where ς_{add} is the additional equivalent viscous damping ratio, and f_n is the natural frequency of modes within the soil. Many models with different Rayleigh damping parameters were conducted for use in case (iii), but the best results were found using values of α = 0.0005 and β = 0.005 were selected, and the justification for these will be explained later.

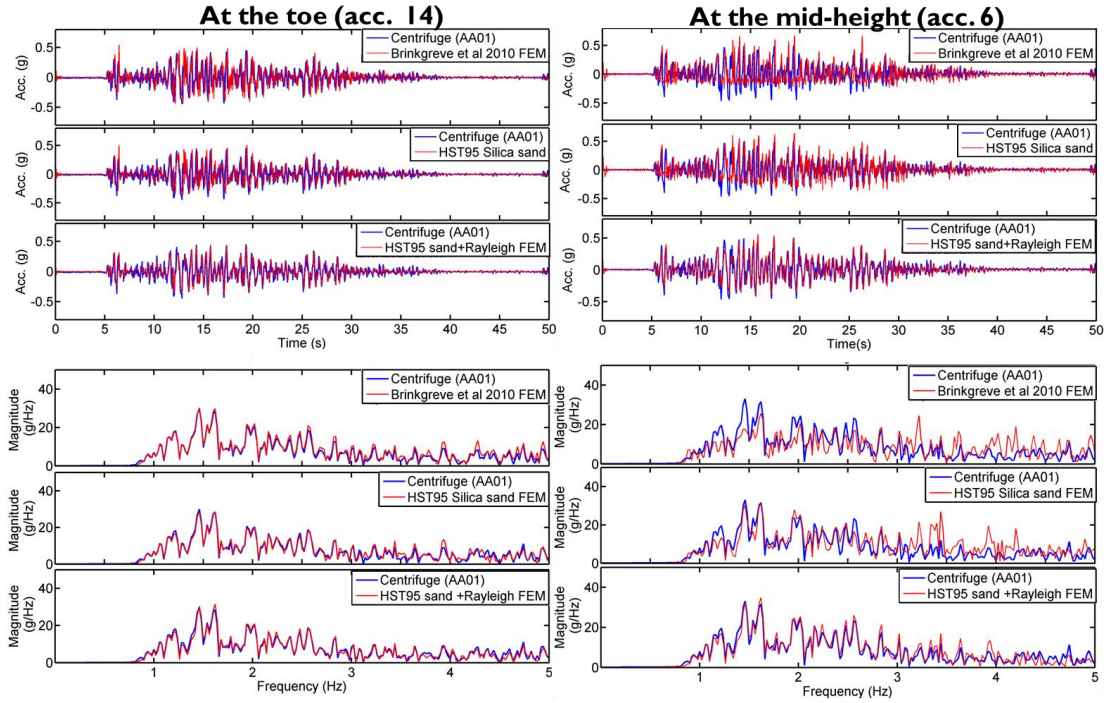

Figure (5- 6): Comparison of measured and predicted accelerations at slope toe and mid-height during test AA01: time domain (top) and frequency domain (bottom).

At point 14 or at the toe of the slope (Figure 5-6), the match between the centrifuge test and FEM is good for all models considered, both in the time and frequency domains, though the models without the additional Rayleigh damping slightly over-predict the peak acceleration values in some of the cycles. At point 6, very good results were obtained for case (iii) where the additional Rayleigh damping reduced the frequencies above (3 Hz) compared to cases (i) and (ii), bringing them closer to those measured in the centrifuge.

Figure (5-7) shows similar plots at the crest of the slope (instrument 5) and behind the crest of the slope (instrumented 1), representing a more stringent test of the capabilities of the numerical model. This would be of significant interest for being

able to determine the input motion to any (infra-) structure located at the crest of the slope. For both cases (i) and (ii) without any additional damping, significant over-prediction of acceleration is observed. From Figure (5-7), it is clear that this arises due to increased amplification of the higher frequency components (above 3 Hz). The Rayleigh damping parameters reported earlier give damping that is predominantly stiffness-proportional, such that the motions at higher frequencies would be more significantly damped, without over-damping the lower frequencies where the match was good. Case (iii) in Figure (5-7) shows a markedly improved prediction of the acceleration time history at this point, due to reduced contribution of the higher frequency modes.

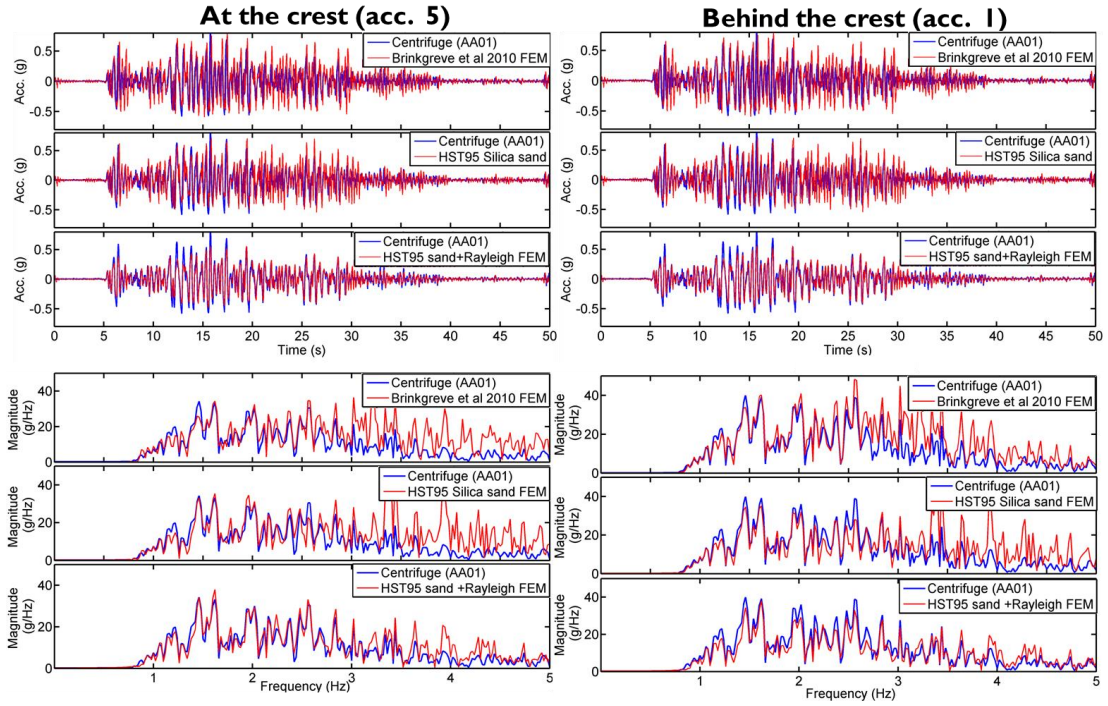

Figure (5- 7): Comparison of measured and predicted accelerations at and behind slope crest during test AA01: time domain (top) and frequency domain (bottom).

A similar result was found for simulations of test AA02 (Kobe motion) as shown in Figure (5-8) and Figure (5-9). As can be seen, the selected Rayleigh damping parameters (α and β) again damped the frequencies above (3 Hz) for the points near the slope surface and amplified the frequencies below this value near the base of the slope. The match at the base is not surprising given that the shear wave has only propagated a short distance at this point, and has not yet interacted with the slope. By

comparing Figures (5-6) – (5-9), the constitutive model appears to work well independent of the input motion.

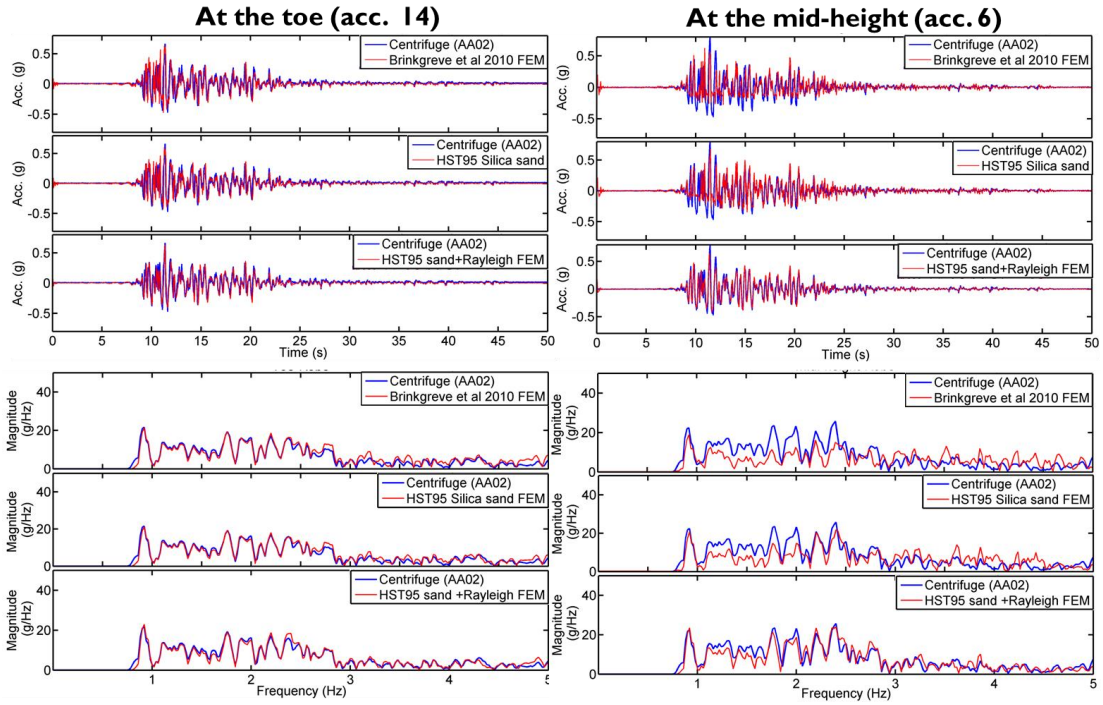

Figure (5- 8): Comparison of measured and predicted accelerations at slope toe and mid-height during test AA02: time domain (top) and frequency domain (bottom).

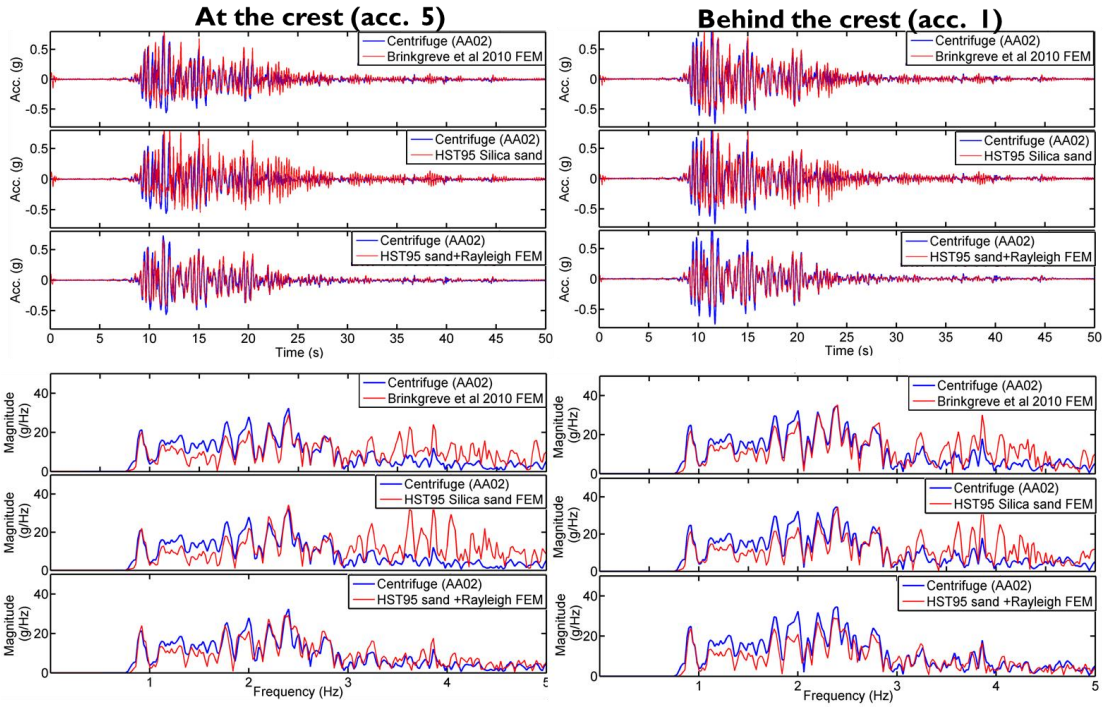

Figure (5- 9): Comparison of measured and predicted accelerations at slope toe and mid-height during test AA02: time domain (top) and frequency domain (bottom).

The harmonic motion from test AA03 was also used as an input motion. The comparison with the centrifuge data for all of the previously mentioned points (at the toe of the slope, at the mid-height of the slope, at the crest of the slope and behind the crest of the slope) are shown in Figure (5-10) and Figure (5-11) respectively. It can be seen from these two figures how the Rayleigh damping is again important especially for the points near the crest of the slope (where larger amplification is expected).

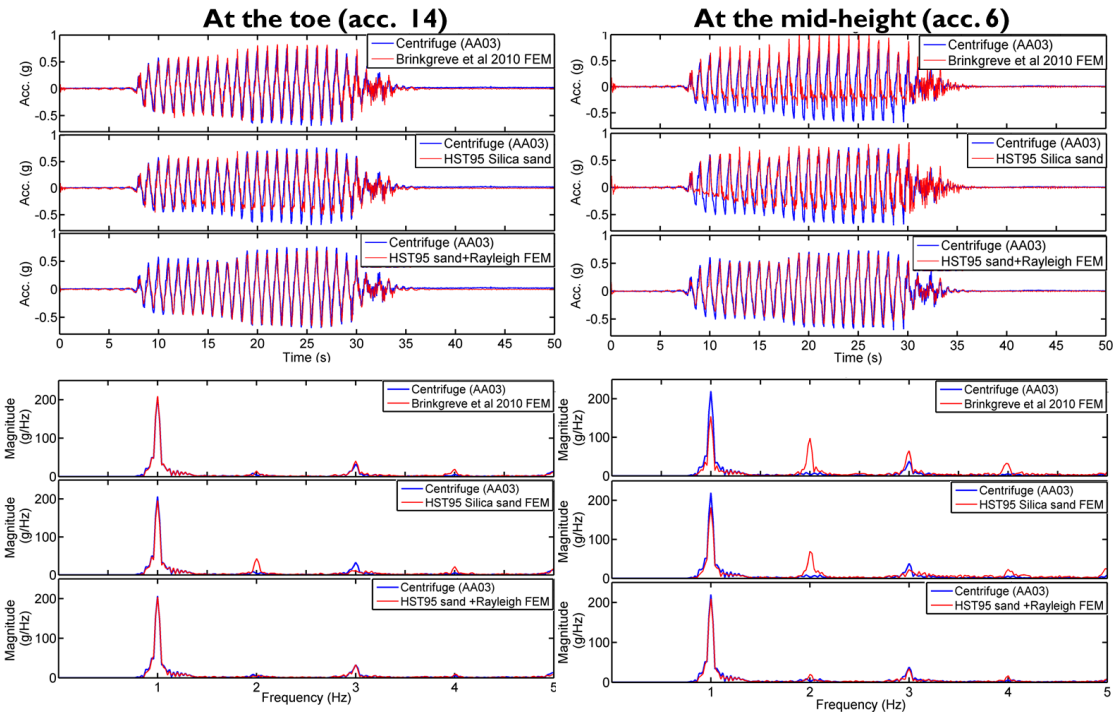

Figure (5- 10): Comparison of measured and predicted accelerations at slope toe and mid-height during test AA03: time domain (top) and frequency domain (bottom).

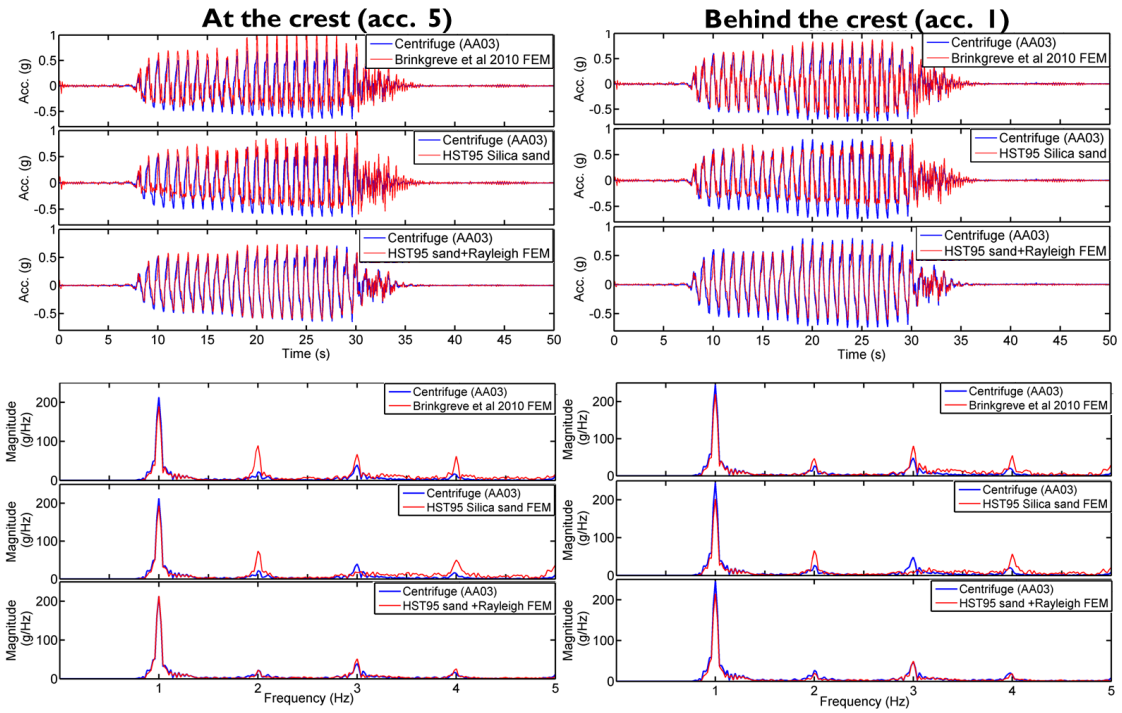

Figure (5- 11): Comparison of measured and predicted accelerations at and behind the slope crest during test AA03: time domain (top) and frequency domain (bottom).

Topographic amplification factors are often used to quantify the effects of the slope on the propagation of the ground motion. Figure 5-12 shows the amplification factors on peak acceleration at the crest of the slope (instrument 5), i.e. the ratio of crest peak acceleration to the peak value of the input motion for both AA01 and AA02. This amplification factor clearly contains two distinct effects: the site effect (in essence a material property effect, due to the dynamic properties of the soil) and a topographic effect (a geometric effect due to the ground surface profile). Because the boundaries of the centrifuge model are too close to assume free field conditions are reached, thus only finite model is used to derive the topographic amplification factor, dividing the acceleration at the crest with the one far from it, at the free field. Also shown in Figure (5-12) are recommended values from Eurocode 8, Part 5 (EC8:5; BSI, 2005b). In EC8:5, the ground motion at the surface (e.g. for use in constructing response spectra) is calculated using:

$$PGA = S.S_T.a_g \qquad (5\text{-}14)$$

where a_g is the peak acceleration in the underlying bedrock (input motion in the centrifuge tests), S is the 'soil factor' describing the site effect (= 1.4 for the soil in this study, classified as Ground type E using Eurocode 8, Part 1 (EC8:1; BSI, 2005a)) and S_T is the topographic amplification factor (≥ 1.2 for shallow slopes). The overall amplification factor is then = PGA/a_g . Based on EC8, the overall amplification within the centrifuge test would be predicted to be between 1.2 – 1.7, which would be conservative when compared to the centrifuge observations (overall amplification ≈ 1.3) for the two motions considered. Ashford et al. (1997) and Bouckovalas and Papadimitiou (2005) have conducted detailed numerical studies based on harmonic ground shaking and have demonstrated that the topographic amplification is dependent on the ratio of slope height to wavelength and position from the crest. In light of this, the centrifuge tests of Brennan and Madabhushi (2009) are a useful comparison to the test data in this chapter, as they considered a slope of similar (though not identical) height, slope angle and sand. Their results support the value of 1.3 measured in tests AA01 and AA02.

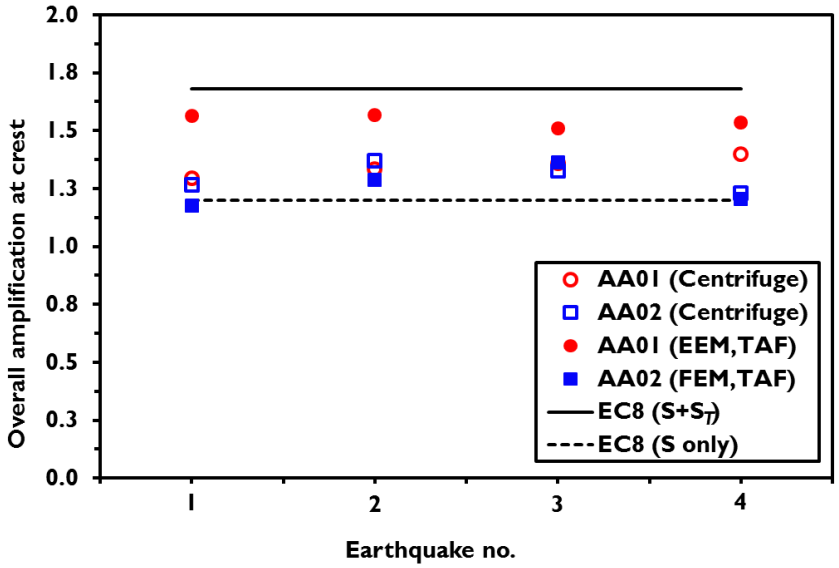

Figure (5- 12): Comparison of measured dynamic amplification with Eurocode 8 recommendations

Figure (5-12) shows that the Eurocode recommendations give an excellent prediction of PGA when both the site and topographic effects are taken into account. It further shows that this parameter appears to be insensitive to the effects of multiple strong earthquakes (i.e. this parameter does not evolve as the slope progressively deforms).

5.3.3 Acceleration response spectra at crest

The hazard posed to infrastructure at the crest is more usefully represented by a response spectra, rather than a topographic amplification factor, which represents the spectral response at a period T = 0 s only. Figure (5-13) shows a comparison of predicted crest spectra for 5% nominal structural damping from FEM and measured data from the centrifuge tests, including also design spectra based on EC8 for context. Spectra determined from the recorded accelerations in the centrifuge at instrument 5 are shown for both Kobe and Chi-Chi motions for the first (EQ1) and last (EQ4) earthquakes. Figure (5-14) confirms the result from Figure (5-12) in that the spectral magnitudes appear to be relatively insensitive to repeated strong earthquake shaking. Figure (5-13) also suggests that there is a range of natural period (approximately between 0.4 to 1.0 s) over which the FEM may substantially under-predict the response compared to the centrifuge data (this is particularly noticeable for test AA02). This range could be used as a simple screening tool to identify key pieces of infrastructure atop slopes which may be more vulnerable to seismic damage than FEM would suggest, and to which extra consideration should be paid in design. Figure (5-12) and (5-13), when considered together, also suggest that the topographic amplification factor S_T in EC8 may not be independent of natural period as assumed in the code, but increases from a value of $S_T = 1.2$ at low periods to $S_T \approx 2.1$ by 0.3 s, reducing back to 1.2 beyond 0.6 s.

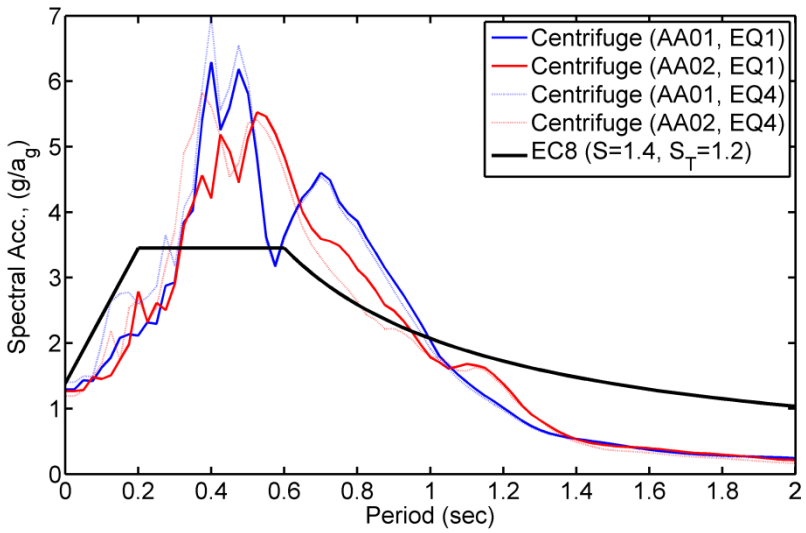

Figure (5- 13): Effect of repeated strong shaking on acceleration response spectra at the top of the slope (spectra are plotted for typical 5% structural damping)

Figure (5-14) also shows a comparison of predicted crest spectra from FEM, recommended curves from EC8 and measured data from the centrifuge tests for both tests AA01 and AA02. For the cases including Rayleigh damping (HST95, case iii), a very good match to the centrifuge data are obtained, though there is a tendency for the response to be slightly under-predicted for periods above 0.5 s. Use of the other constitutive models results in a much more significant under-prediction of response above 0.5 s, and over-prediction below this. It is clear that care should be taken in interpreting the hazard to supported infrastructure from analyses using FEM, and that this will be significantly dependent on the natural period of the supported structure.

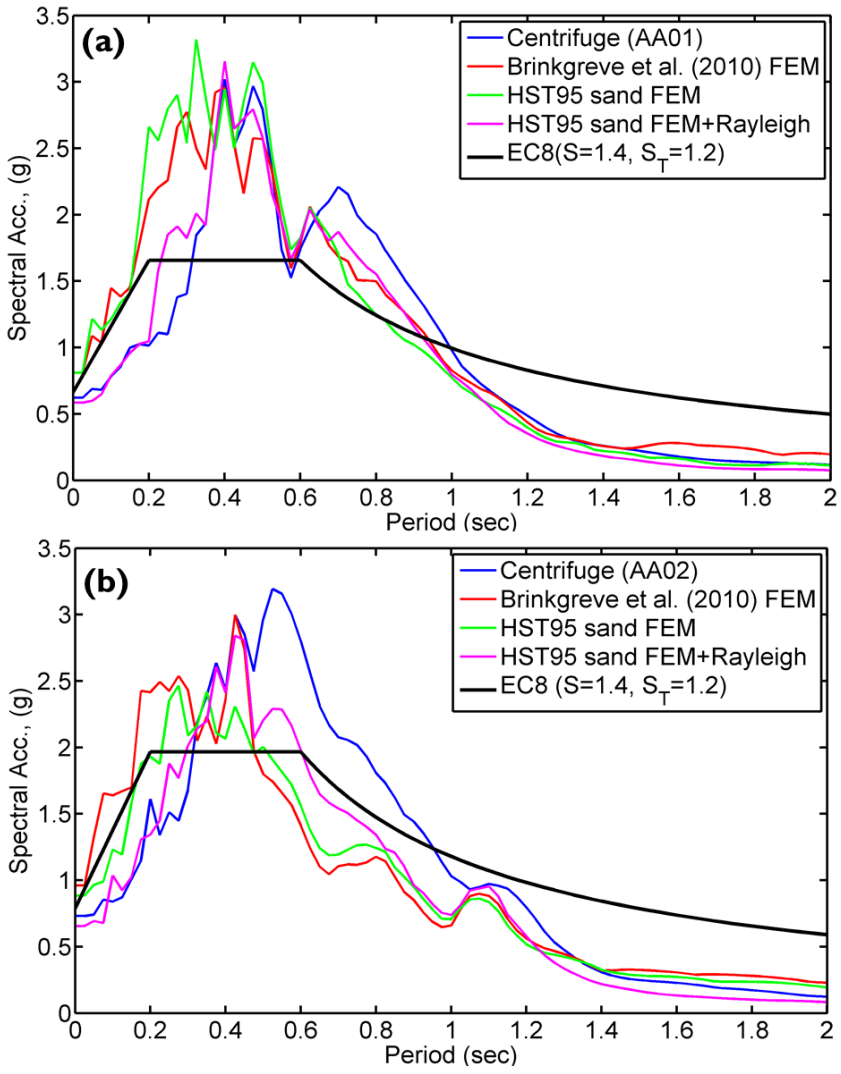

Figure (5- 14): Measured (centrifuge), predicted (FEM) and design (EC8) response spectra at the top of the slope (instrument 5) for 5% structural damping (a) Chi-Chi (AA01); (b) Kobe (AA02)

5.3.4 Replication of dynamic soil behaviour

Sections 5.3.2 and 5.3.3 have suggested that the inherent hysteretic damping within the constitutive model may be too low. In this section, shear modulus degradation and damping ratio will be compared as observed in both the centrifuge tests and FE models.

The dynamic shear modulus, *G*, can be calculated as a secant line to the maximum values of a stress-strain hysteretic loop, as shown schematically in Figure (5-15), while damping is proportional to the area inside the hysteretic loop. Thus, shear modulus and damping ratio are dependent on the variation of the shear strain in the soil deposit during dynamic loading.

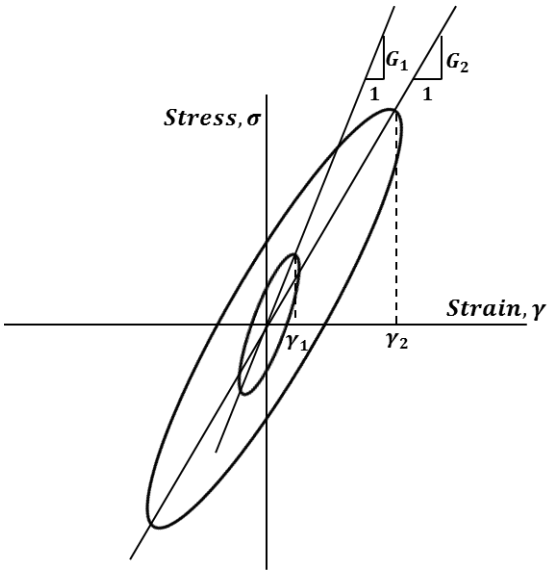

Figure (5- 15): Hysteretic shear stress-shear strain relationship

The degradation curve (shear modulus-shear strain relationship) and viscous damping ratio (damping-shear strain relationship) were determined based on the data from centrifuge tests AA01 and AA02. The recorded data from the accelerometers within the slope (those in the column below the crest of the slope) were used to calculate the shear modulus (*G*) and viscous damping (*D*). The FE data at the homologous points was similarly analysed.

The shear stress and shear strain were calculated from the accelerometers column below the crest of the slope using a second-order estimate (three accelerometers) following the method outlined by Brennan et al. (2006). The resulting values

represent the soil response at the mid-depth of the accelerometers. The shear stresses in this method are determined following Zeghal and Elgamal (1994):

$$\tau_z = \frac{1}{2}\rho \frac{a_1 z_3^{\,2} - 2a_2(z_1 z_3) + a_3 z_3^{\,2}(z - 2z_1)}{(z_3 - z_1)} \tag{5-15}$$

where τ_z is the shear stress at depth z, $z_1 - z_3$ are the depths of the accelerometers, $a_1 - a_3$ are the corresponding accelerations and ρ is the soil density.

The shear strain was calculated from the displacement data which were obtained from double integration of the recorded time-acceleration histories using a band-pass filter in MATLAB before integrating each time. Thus, the computed shear strain is more reasonable at the mid.-point between the accelerometers:

$$\gamma = \frac{[(d_3 - d_2)\frac{(z_2 - z_1)}{(z_3 - z_2)} + (d_2 - d_1)\frac{(z_3 - z_2)}{(z_2 - z_1)}]}{(z_3 - z_1)} \tag{5-16}$$

Where $d_1 - d_3$ are the displacements at the three accelerometer locations.

As mentioned before, the shear modulus represents the secant line of the maximum and minimum shear stress and the maximum and minimum shear strain loop. So, after calculation of the dynamic shear stress and shear strain time histories, the shear modulus was calculated as a ratio between the difference of the maximum and the minimum shear stress to the difference of the maximum and minimum shear strain. This value is represented as a dashed line in figure (5-16) below.

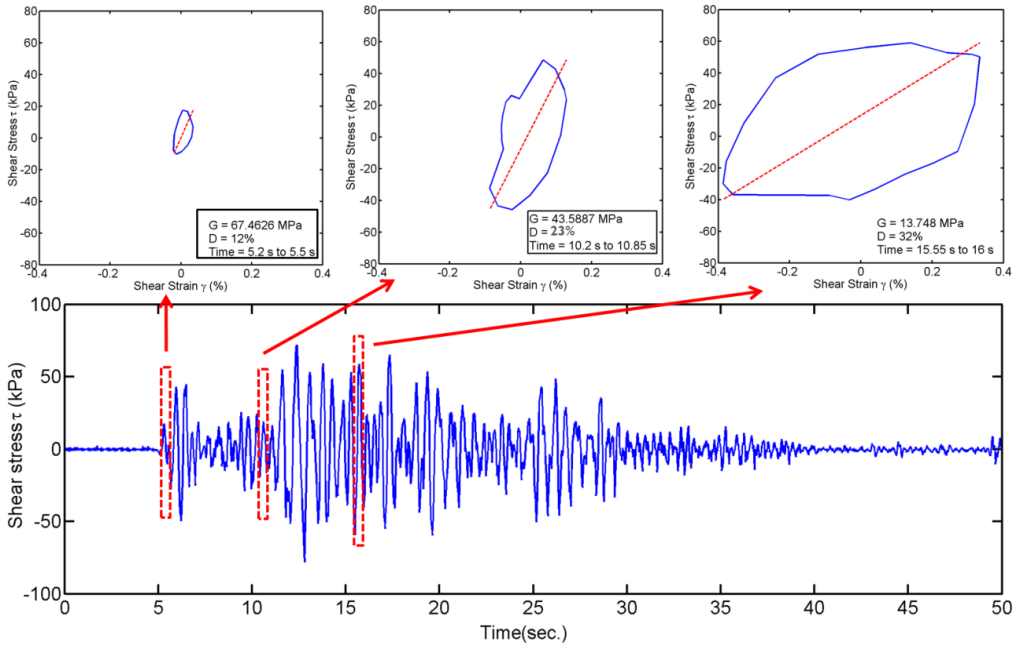

Figure (5- 16): Determination of shear modulus at different points during the earthquake – centrifuge data, test (AA01).

Figure (5-16) demonstrates reducing shear modulus (lower gradient) as the cyclic shear strain range increases. Figure (5-17) shows similar behaviour over much larger windows of the data, demonstrating that scatter is to be expected in the determined response.

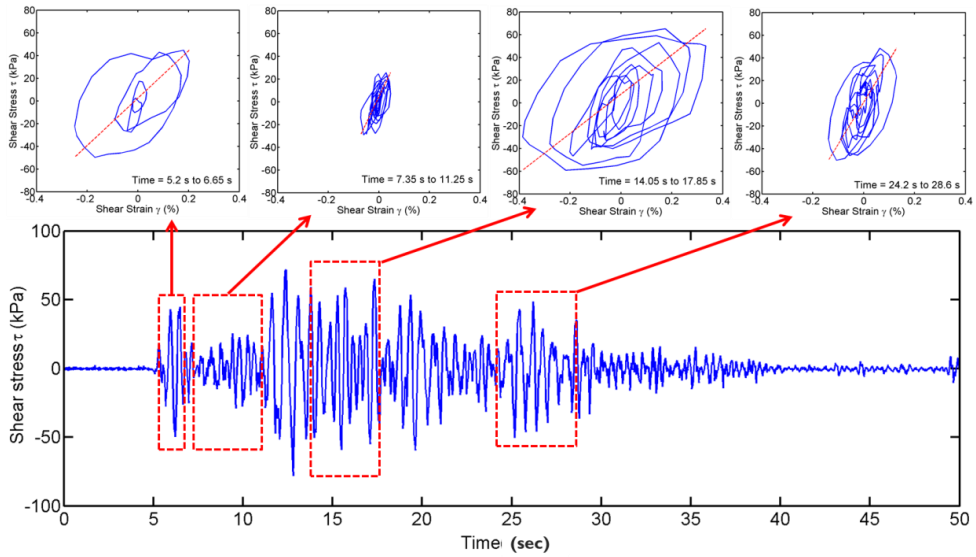

Figure (5- 17): Scatter in dynamic soil response loops (AA01).

Having determined shear modulus values from the centrifuge and FEM data, the shear modulus ratio (G/G_0) was calculated according to the estimated initial shear modulus by the empirical equation given by Hardin and Drnevich (1972), previously given as Equation (5-8). These values were then plotted against the cyclic shear strain amplitude. This data, along with previously suggested design degradation curves are shown in Figures (5-18) and (5-19). The shear modulus degradation curves from the centrifuge data were higher than for the FE data for both Chi-Chi and Kobe motions. However, both methods generally give a reasonable comparison with Hardin and Drenvich (1972), Ishibashi and Zhang, (1993) and Santos and Correia, (2001).

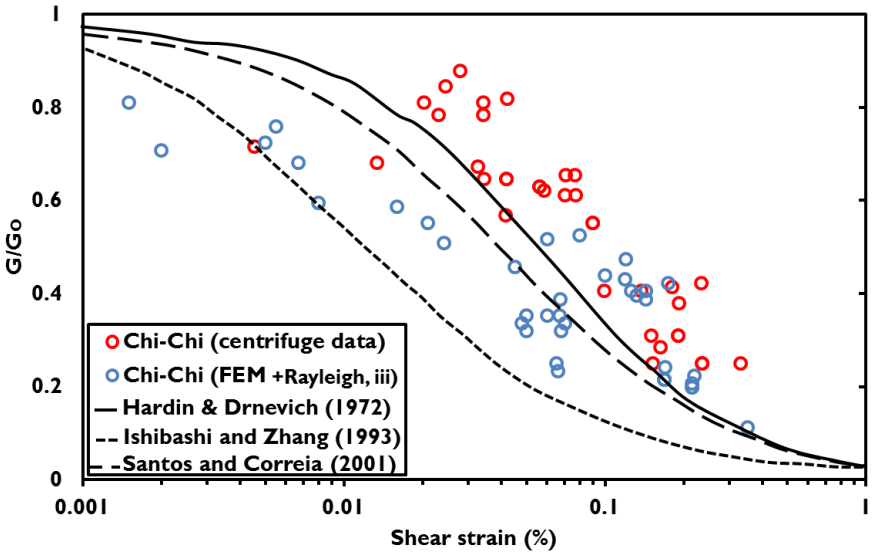

Figure (5- 18): Degradation curve based on Chi-Chi earthquake data

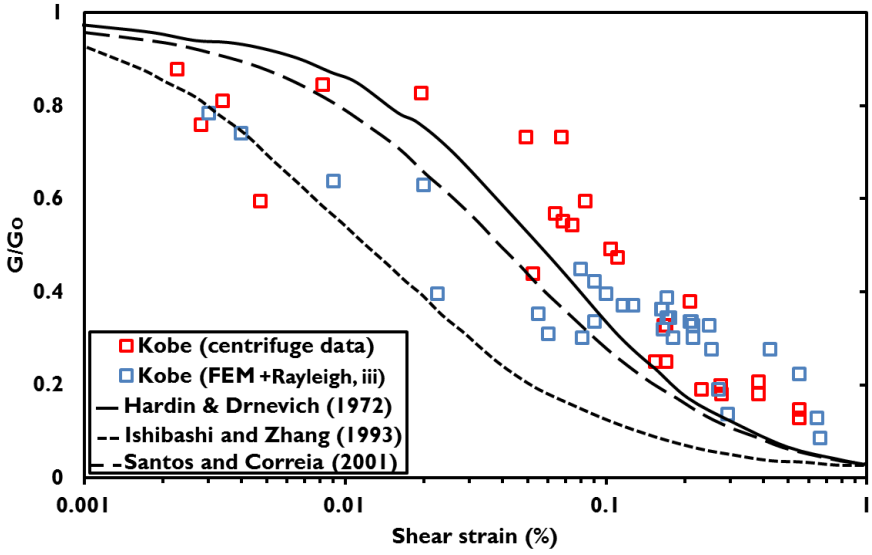

Figure (5- 19): Degradation curve based on Kobe earthquake data

The damping ratio was estimated from the calculation of the area inside the stress-strain loop after Brennan *et al*., (2006):

$$D(\%) = \frac{W}{2\pi W_{elastic}} = \frac{\int \tau . d_y}{2\pi(0.25\Delta\tau\Delta\gamma)} \tag{5-17}$$

Figures (5-20) and (5-21) show the damping–shear strain relationship for case (ii) properties (i.e. no additional Rayleigh damping). It can be seen from these two figures that the implicit hysteretic damping in the constitutive model is lower than that observed in the centrifuge tests. This explains why additional Rayleigh damping was required to fully match the dynamic response within the soil.

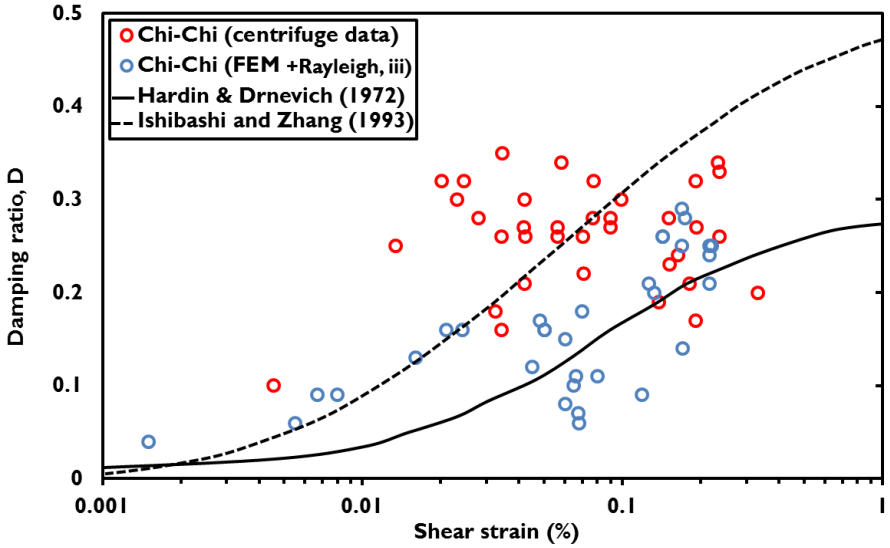

Figure (5- 20): Damping ratio for Chi-Chi earthquake data

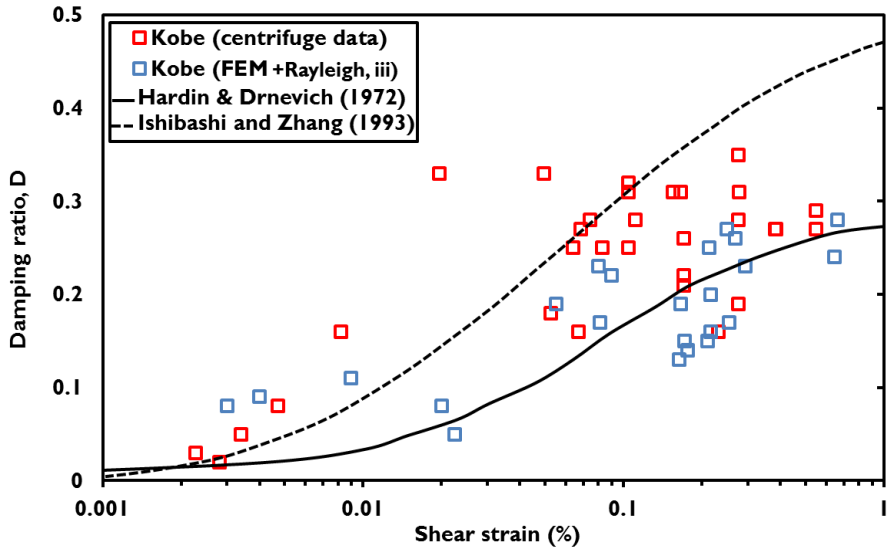

Figure (5- 21): Damping ratio for Kobe earthquake data

5.3.5 Prediction of permanent deformations

Figure (5-22) shows the permanent crest settlements across the four earthquakes as predicted by FEM (all three cases are shown) and as measured in the centrifuge. It is clear that for both suites of earthquake motions, use of the Brinkgreve *et al*. (2010) parameters hugely over-predicts settlement at the crest. This would lead to significant over-prediction of the risk posed to the slope and hence, potentially, uneconomic design. In contrast, use of the HST95 parameters (either case) give a much better prediction, though it should be noted that inclusion of the additional damping, which was beneficial for modelling the dynamic behaviour accurately, results in an under-prediction of permanent deformation (which is unsafe). The Brinkgreve *et al*. (2010) parameters were initially expected to be useful for cases where there is extremely limited site investigation data – however the implication of Figure (5-22) is that it is always important to obtain high-quality laboratory (or in-situ) test data to achieve an accurate prediction of movement. It is likely that the additional cost of this additional investigation would be significantly offset if a lower amount of remediation/repair would be required. When considered alongside the dynamic performance discussed in the previous sections, it is clear that neither case (ii) or case (iii) can give consistently better performance of both dynamic and permanent movements simultaneously; this would appear to suggest that the additional Rayleigh damping may not be a material characteristic, but may be masking an effect of the sloping ground geometry in which wave reflection at the sloping ground surface is not modelled correctly within the FE model.

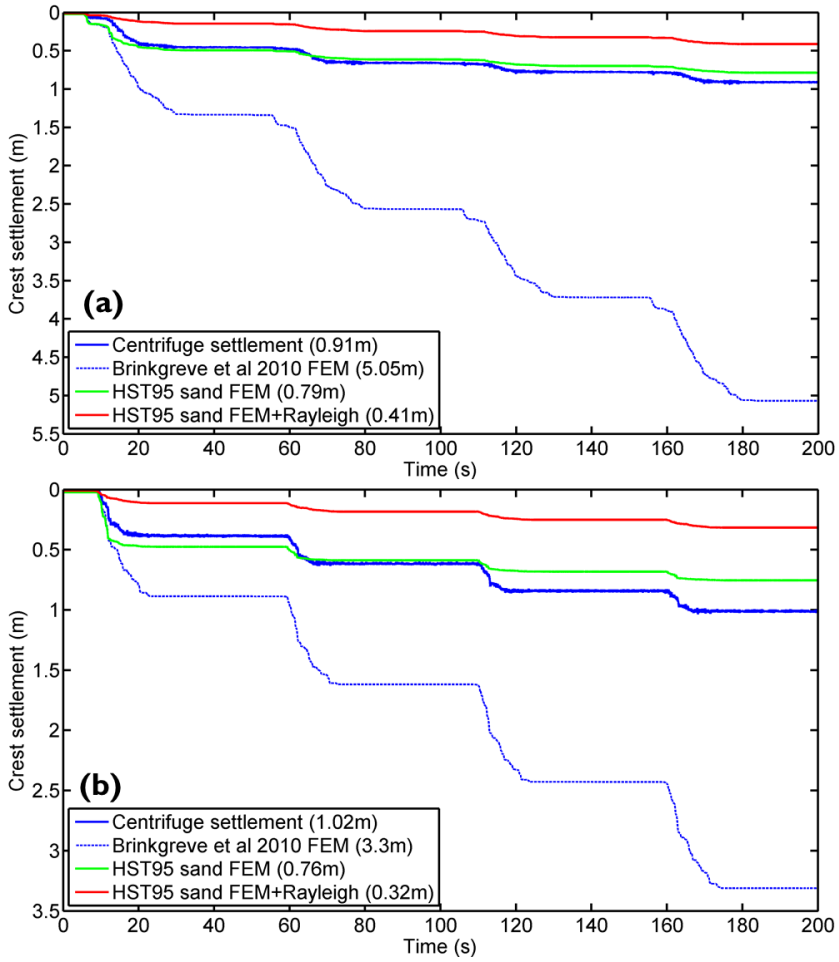

Figure (5- 22): Comparison of permanent crest settlements from FEM and centrifuge modelling: (a) test AA01; (b) test AA02.

Figure (5-23) shows a comparison (drawn to scale) of the ground surface profile measured at the end of the centrifuge test (a negligible amount of movement was recorded during spin-down), and as predicted at the end of the last earthquake (EQ4) from the FE model (case ii) for test AA01. It can be seen that the numerical model captures the deformed shape of the slope well, particularly the angular distortion at the crest which is likely to be of greatest significance for supported infrastructure. A similar result was obtained for test AA02.

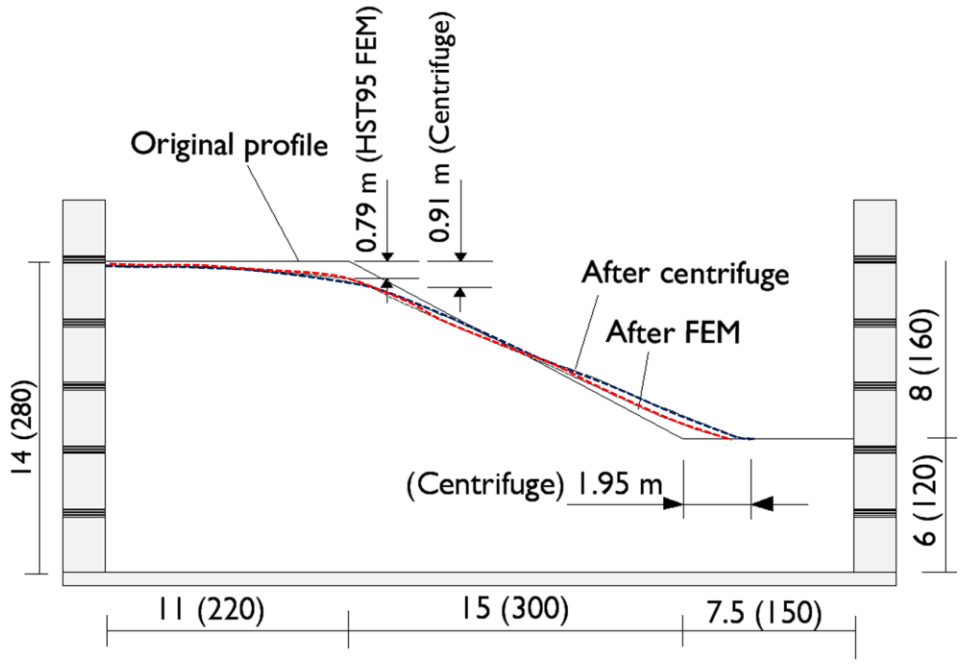

Figure (5- 23): Comparison of slope profile after EQ4 as predicted by FEM and as measured in the centrifuge, test AA01.

5.4 Comparison of FEM with sliding block models

In chapter four, an improved sliding block model was developed for estimating the magnitude of crest settlement. These predictions are compared to those from the FEM (case ii) reported in this chapter in Figure (5-24). In all cases the FEM gives a lower prediction than the sliding block model. The FEM predictions are closer to the centrifuge observations for test AA01 (Figure 5-24a), but do not appear to capture the gradual reduction in movement after the first earthquake as well in the case of test AA02 (Figure 5-24b). Figure (5-25) shows a plot of the accumulated shear strain within the FE simulation of test AA01 (case ii) at the end of EQ4, overlaid onto which are the estimated shear band locations under the initial conditions and for the re-graded slope angle at the end of EQ4 form the sliding block model. These suggest that the failure mechanism in both types of analysis are similar (shallow translational sliding), though there is a much deeper zone of distributed shear strain within the FE model. This allows for the prediction of the settlement profile back from the crest that was shown in Figure (5-23). Although the sliding block model outperforms the FE model in terms of the overall magnitude of the settlements, the real advantage of the FEM is that it is able to also estimate the settlement profile (angular distortion) at the

crest and quantify the dynamic motions within the soil, which the sliding block model cannot do.

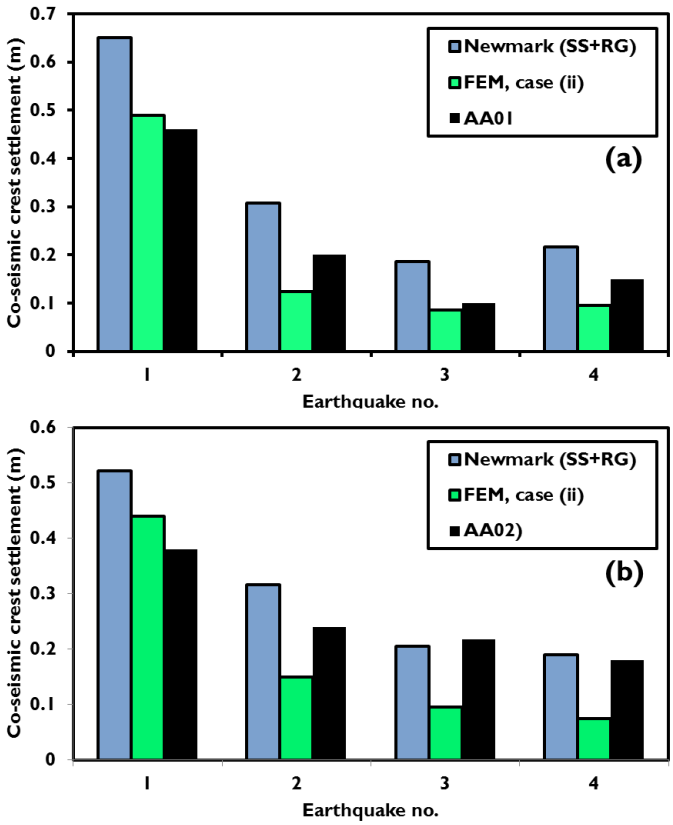

Figure (5- 24): Comparison of FEM and sliding-block crest settlement predictions with centrifuge observations (a) test AA01; (b) test AA02

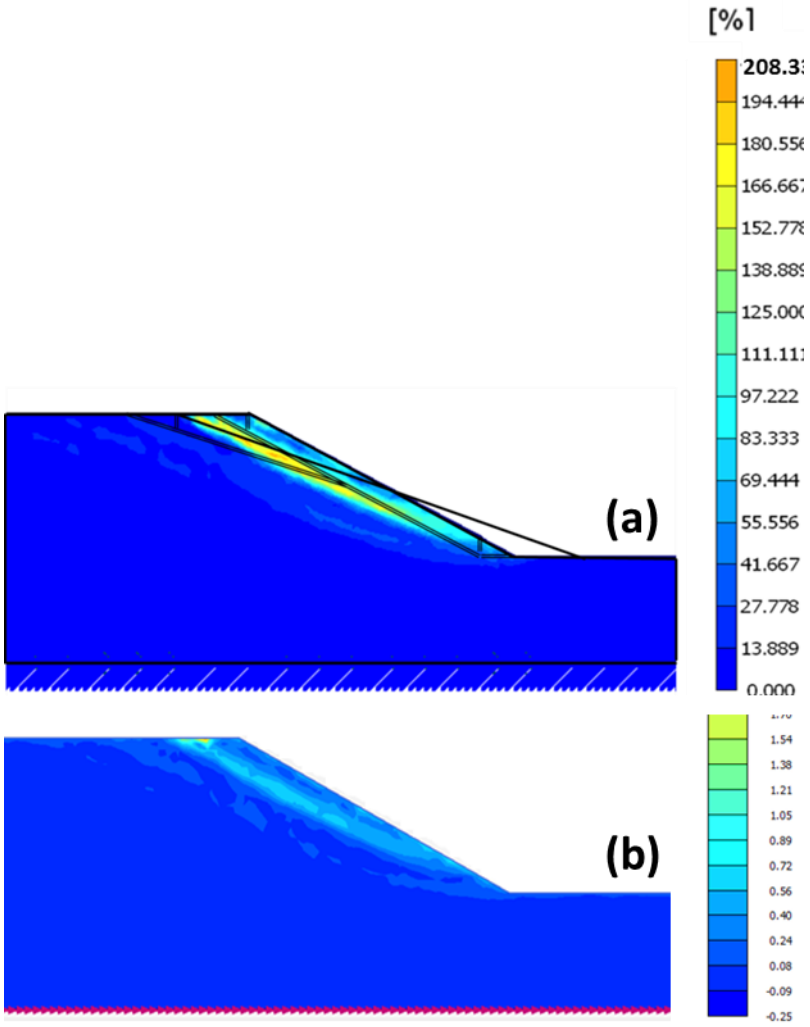

Figure (5- 25): Comparison of accumulated shear strain at the end of EQ4 (test AA01) with failure mechanism assumed in analytical model; (b) total volumetric strain.

Figure (5-26) presents a summary of the predictive ability of the FEM methods described in this part and the sliding block models reported in Chapter four for determining permanent settlements due to earthquake shaking. These have been grouped into 'existing' models, representing the current state-of-the-art, namely sliding block with strain-softening and FEM using the previously-published parameters of Brinkgreve et al. (2010); and 'improved' models, consisting of the fully strain-dependent sliding block model developed in Chapter four (strain-softening and geometric hardening) and the laboratory-test calibrated FEM developed in this chapter. While the improved models are not perfect, they give a better prediction of the response under the initial earthquake on virgin soil and are subsequently able to give a reasonable prediction of behaviour even after a number of previous strong earthquakes during which significant deformation has accrued. Both existing models

over-predict settlements in the first earthquake and then get progressively worse with further shaking, as they are unable to correctly capture the effect of the previous seismic history on the slope. In the case of the sliding block model this is associated with incorrect description of the deformed slope geometry (see Chapter 4); in the case of the FEM, the existing (Brinkgreve) constitutive parameters do not appear to correctly capture the strain history or mechanical response.

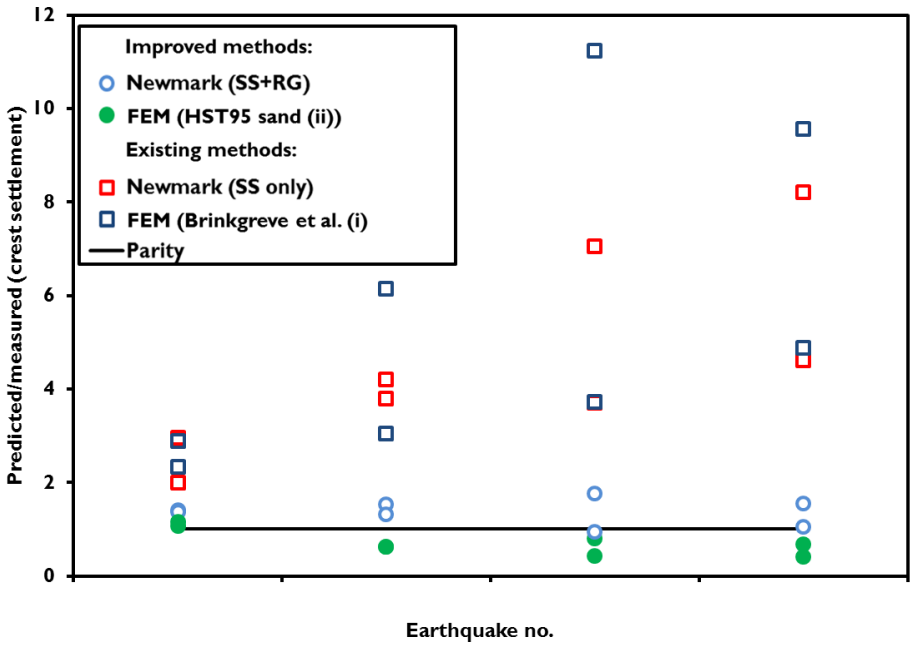

Figure (5- 26): Accuracy of 'existing' models, compared to those proposed in Chapters four and five ('improved' models) for predicting permanent crest settlement.

The development of the 'improved' analytical tools in Chapters four and five, provide a means of quantifying the response of shallow cohesionless slopes under multiple successive earthquakes. These tools will allow civil engineers to obtain a better estimate of the hazard associated with aftershocks and lead to new approaches to seismic design and asset management in which whole-life performance can be considered (as outlined in Chapter four).

5.5 Summary

Centrifuge and finite element models for the seismic performance of 1:2 cohesionless slopes under dynamic loads have been presented in this Chapter. The significant results are summarised below:

1. Seismic displacement results from plane-strain finite element models (using Plaxis 2D) using the input parameters presented by Brinkgreve et al., (2010) based on relative density were over predicted compared to results from centrifuge tests for both real earthquake motions (AA01 and AA02) whereas better results were observed for sinusoidal wave model (AA03).
2. Using soil-specific parameters derived from routine laboratory test data gives a significant improvement of permanent seismic displacements. In terms of the dynamic motions, these model parameters showed amplification for all frequencies below 3 Hz and these were identical with centrifuge tests. These parameters significantly outperform existing correlations. This highlights the importance of specifying a suitably detailed site investigation.
3. Additional Rayleigh damping was required to attenuate response above 3 Hz and provide an extremely close replication of the dynamic motions within the soil.
4. Shear modulus and damping at a wide range of engineering shear strain were calculated for both centrifuge and finite element models. By using the HST95 model, the shear modulus was well replicated while the damping results especially at a medium shear strain range were lower than those of the centrifuge tests.
5. The developed constitutive model does not capture soil softening during successive earthquakes. This didn't let surprising as the computed settlement in chapter 4 is slightly influenced by strain softening in large earthquake events.

The FE models, which are more computationally complex than the sliding block models of Chapter four, are complimentary to these, being useful in the later stages of detailed design.

Chapter Six
Centrifuge modelling of the seismic performance of pile-reinforced slopes

Contents of this chapter have been submitted for review as:

Al-Defae, A.H. and Knappett, J.A. (2013). Centrifuge modelling of the seismic performance of pile-reinforced slopes. J. Geoetech. and Geonv. Engng. (Accepted).

Al-Defae, A.H. and Knappett, J.A. (2014). Stiffness matching of model reinforced concrete for centrifuge modelling of soil-structure interaction. 8th Inter Conf. of Phys. Model. In Geot. (8th ICPMG 2014). (accepted).

6.1 Introduction

In this chapter, an extensive programme of geotechnical centrifuge testing is described to investigate the performance of pile-reinforced cohesionless slopes during earthquakes. This will build on the tests on unreinforced slopes described in Chapter 4 and will use these previous tests as unreinforced benchmarks. Elastic pile models will firstly be used to investigate the fundamental behaviour in terms of the permanent post-earthquake and co-seismic dynamic motions within the slope. The effects of pile spacing on this performance and the performance in strong aftershocks will also be investigated.

Model reinforced concrete piles, described in Chapter 3 are then used to demonstrate how the performance of the slope changes when the piles are no longer linearly elastic, and will also highlight the importance of appropriately detailing the reinforcement to resist the downslope kinematic loads, rather than relying on a nominally reinforced pile.

6.2 Model preparation and test procedures

A total of fifteen 1:50 scale centrifuge model slopes were tested during the main programme of work reported in this chapter. The dimensions of the slope in each model were identical to those described in Chapter 4, which were 8 m tall from toe to crest, having a slope angle of 28° (≈ 1:2) and were underlain by a further 6 m of sand

prepared to the same state, as shown schematically in Figure (6-1). One of the tests from Chapter 4 (test AA01) is used as an unreinforced benchmark in this chapter.

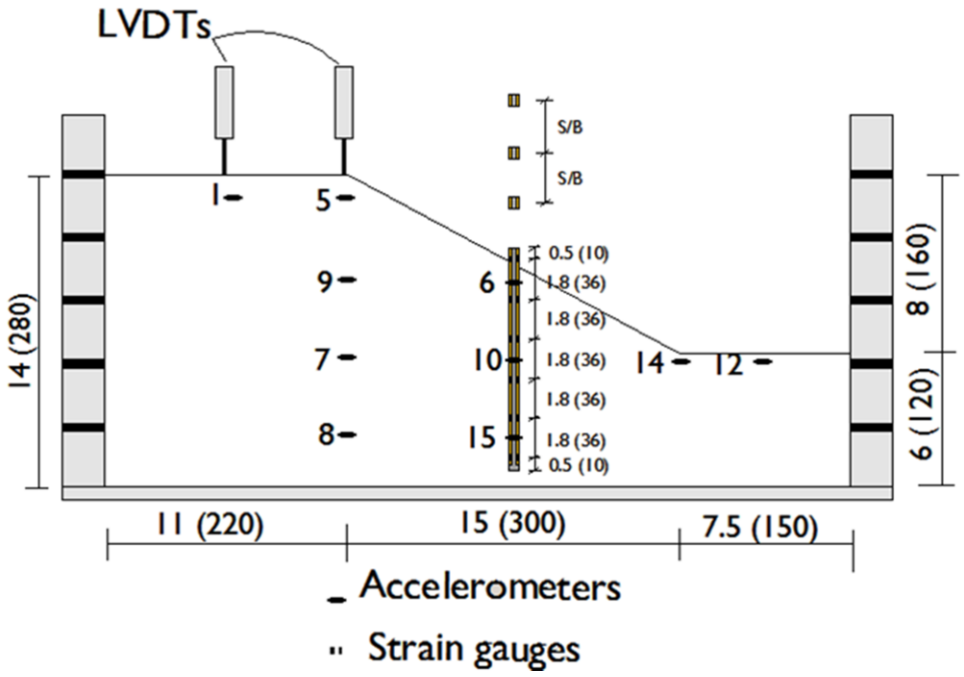

Figure (6- 1): Centrifuge model layout, with instrumented elastic piles shown, dimensions in m prototype scale (mm model scale in brackets).

During pluviation, the soil was instrumented with ten accelerometers within the slope and two external Linear Variable Differential Transformers (LVDT's) measuring settlement at and behind the crest of the slope along the centreline of the model. This instrumentation is shown in Figure (6-1).

After preparation of the model slopes, the ESB container was installed onto the centrifuge and model piles, representing a B × B square cross-section (B = 500 mm at prototype scale), were pushed vertically into the model at 1-g in a discretely-spaced row midway between the toe and crest of the slope. Guide frames, as described in Chapter 3, were used to do this which ensured that the piles remained vertical and the pile centre-to-centre spacing (*S*) was accurate. Initially, two different types of model piles were tested, namely (i) an 'elastic' model (Two of these piles were instrumented with strain gauge pairs to measure bending response as described in chapter three) and (ii) a damageable model reinforced concrete model (hereafter denoted 'RC' pile) using the new micro reinforced concrete described in Chapter 3. The properties and

construction of these model piles are fully described in detail in Chapter 3. Figure (6-2) shows both the RC pile and elastic pile models after model preparation and loading onto the centrifuge.

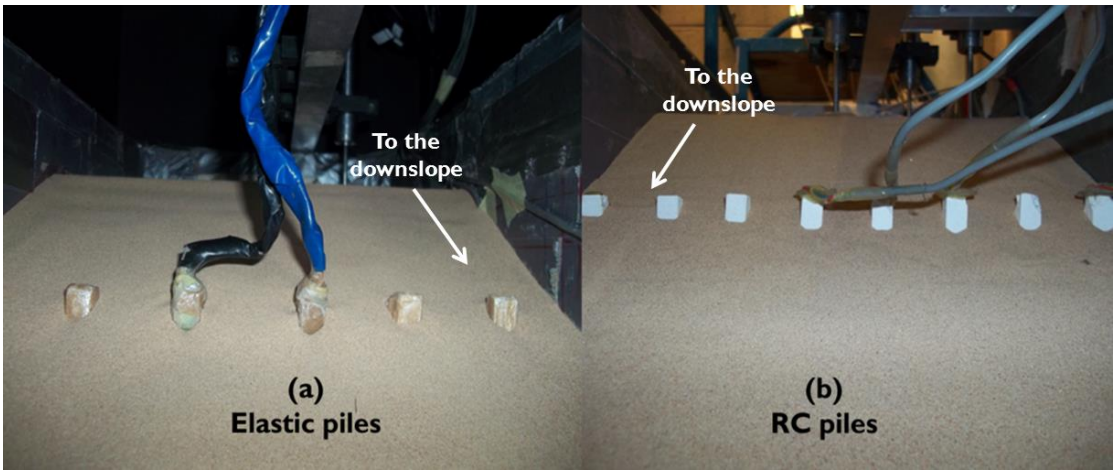

Figure (6- 2): Elastic and RC piles.

Table (6-1) lists the pile types and normalised pile spacing (*S/B*) used in each model. The closest spacing tested was *S/B* = 3.5 as it proved impossible to push the RC piles in at closer spacing without damaging them (due to the stress enhancement within the soil from installation of the adjacent piles, coupled with the high dilation within the soil at low effective stress).

Table (6- 1): Summary of centrifuge models tested

Test ID	I_D (%)	Pile type	*S/B*	No. of earthquakes
AA01	56	Unreinforced	-	4
AA17*	57	Unreinforced	-	12
AA12	58	Elastic	14.0	4
AA13	60	Elastic	7.0	4
AA14	57	Elastic	4.7	4
AA15	59	Elastic	3.5	4
AA16*	58	Elastic	4.7	12
AA04	56	RC	14.0	1
AA05	57	RC	7.0	1
AA06	60	RC	4.7	1
AA07	57	RC	3.5	1
AA08	56	RC	14.0	4
AA09	59	RC	7.0	4
AA10	57	RC	4.7	4
AA11	55	RC	3.5	4

*Kobe input motion for this test

Most models were subjected to four nominally identical earthquakes. The same input motions which were earlier described in Chapter 4 were used for all models. All models except AA16 and AA17 were subjected to the M_w = 7.6 Chi-Chi Earthquake in 1999. The M_w = 6.7 Kobe earthquake from 1995 was used for models AA16 and AA17. By using successive earthquakes the behaviour of the models under strong aftershocks could be observed, as in Chapter 4. Four of the models with RC piles (AA04 – AA07) were subjected to just a single motion, so that changes to the residual properties of the RC piles post-shaking could be determined after both a single earthquake and multiple earthquakes.

6.3 Performance of slopes reinforced with elastic piles

In this section, the behaviour of the elastic pile tests (AA12 – AA16) will be considered to investigate seismic soil-pile interaction and the resulting improvements to seismic slope performance through the inclusion of a discretely spaced row of vertical piles. These can be considered an example of the case where the piles have been suitably designed structurally so as not to become damaged in any way. The validity of this assumption, for the case where the piles have properties which are more representative of real concrete piles, will be considered in Section 6.4. The key indicators of slope performance considered herein are the crest settlement and angular distortion between the two LVDTs (these two parameters would be indicative of the damage induced in infrastructure such as railway lines or highways sitting at the crest of the slope) and the peak ground accelerations and response spectra at instrument 5 in Figure 6-1 (the latter being indicative of the dynamic response of structures located at the crest of the slope).

Figures 6-3 to 6-7 show the crest settlement (throughout this chapter, this term refers to the LVDT closest to the crest in Figure 6-1) and angular distortion developed in all cases of the pile spacing tested (starting from S/B = 14 to S/B = 3.5), compared to values at the same locations in the unreinforced test (AA01 or AA02). The maximum bending moment and input motion (at instrument 8) are also shown in each of these Figures.

6.3.1 Permanent slope deformations

S/B = 14 (AA12)

The maximum pile spacing was used in this test (Figure 6-3). As observed in Chapter 4 for unreinforced slopes, the pile reinforced slope appears to harden as it deforms, with subsequent earthquakes of equal magnitude resulting in smaller deformations. This may be attributed to the geometrical hardening effect noted in Chapter 3 as the slope re-grades itself to be less steep as it deforms.

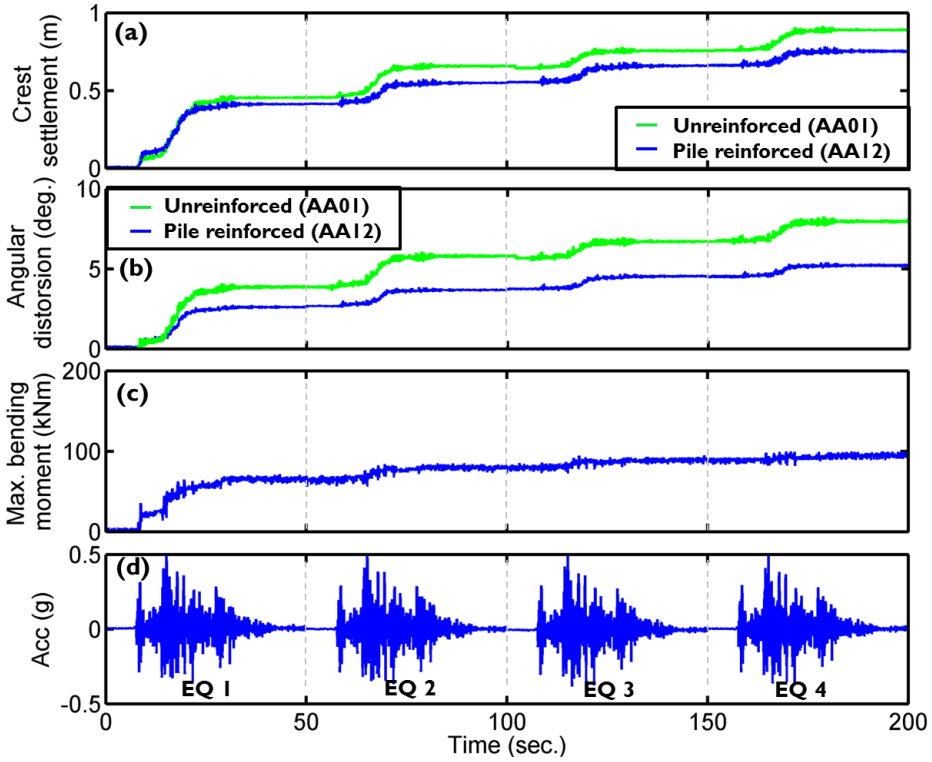

Figure (6- 3): Slope performance at *S/B* = 14 compared to unreinforced case: (a) crest settlements; (b) angular distortion at crest; (c) maximum pile bending moments (at 3.5 m below ground surface); (d) input motion at instrument 8.

At *S/B* = 14, very little improvement in the crest settlement is observed, and in the first earthquake, this may be considered negligible. As shown in Figure (6-3c), the variation in the maximum bending moment appears to be proportional to the crest settlement characteristics of the slope. Thus, the bending movement is increasing rapidly with increasing of soil displacement of the slope during shaking and then remains constant once shaking has stopped. Subsequent earthquakes only increase the bending moment by a small amount. This can be attributed to the soil yielding around

the piles at the end of the first earthquake so that there is subsequently continuing slope movement with a negligible increase in bending moments along piles The measured maximum bending moment at this pile spacing was approximately 94 kNm (approximately 41% of the static capacity).

S/B = 7 (AA13)

As the pile spacing decreases, significant reductions in permanent slope movements and angular distortion compared to the unreinforced case (and with *S/B* = 14) are observed, particularly in subsequent strong shaking (e.g. strong aftershocks) as shown in Figure (6-4).

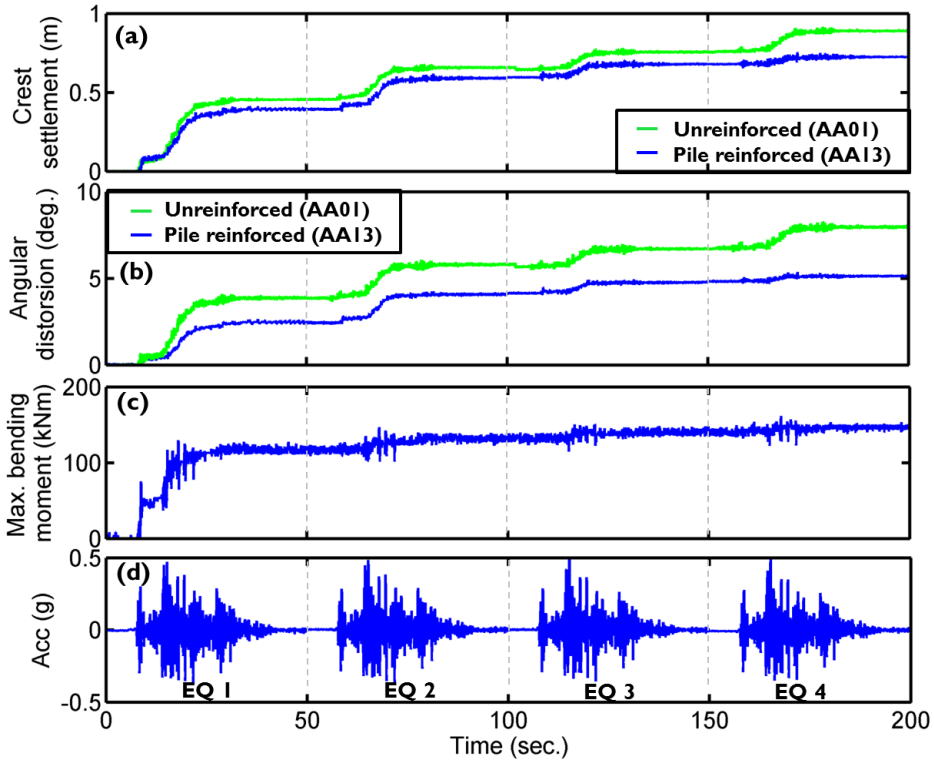

Figure (6- 4): Slope performance at *S/B* = 7 compared to unreinforced case: (a) crest settlements; (b) angular distortion at crest; (c) maximum pile bending moments (at 3.5 m below ground surface); (d) input motion at instrument 8.

The maximum induced bending moment across all of tests was observed at this pile spacing. This can be attributed to the increasing of soil pressure along piles during the earthquake, perhaps due to a change in mechanism from local soil flow around the piles, to one in which the soil arches across the gap between piles. In the first

earthquake (EQ1), the reduction in permanent deformation can again be correlated with the mobilisation of soil-pile interaction as the piles bend in response to the kinematic loading.

S/B = 4. 7 (AA14)

Further reduction of pile spacing leads to more significant reduction in crest settlement and angular distortion, as shown in Figure (6-5). Compared to *S/B* = 7, a small reduction of the maximum induced bending moment is observed (from 147 kNm at *S/B* = 7 to 137 kNm at this pile spacing). This reduction in bending moment actually is likely due to a reduction of soil pressure on the piles as they become closer together and individually support less of the soil mass (i.e. increase in the overlap between wedge type mechanism mobilised behind the upslope face of the piles). The induced bending moments increase very little with subsequent aftershocks, again implying that the soil-pile reaction had reached a maximum following EQ1.

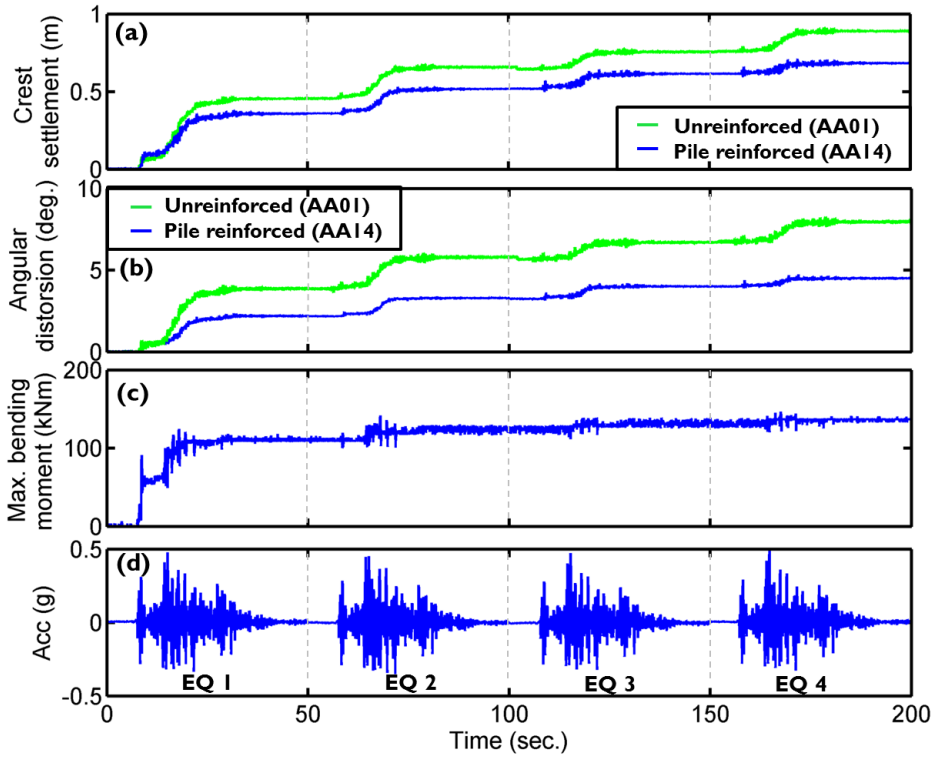

Figure (6- 5): Slope performance at *S/B* = 4.67 compared to unreinforced case: (a) crest settlements; (b) angular distortion at crest; (c) maximum pile bending moments (at 3.5 m below ground surface); (d) input motion at instrument 8.

Similar results were observed for the other test at *S/B* = 4.67 (test AA16 using the Kobe input motion), which are shown in Figure 6-6. Comparing the performance to

that during the Chi-Chi earthquake, the induced bending moments are slightly smaller following EQ1, but subsequently reach similar values by the end of EQ4. This is consistent with the permanent bending moments being principally due to the permanent slip, which is similar in the two pile-reinforced cases.

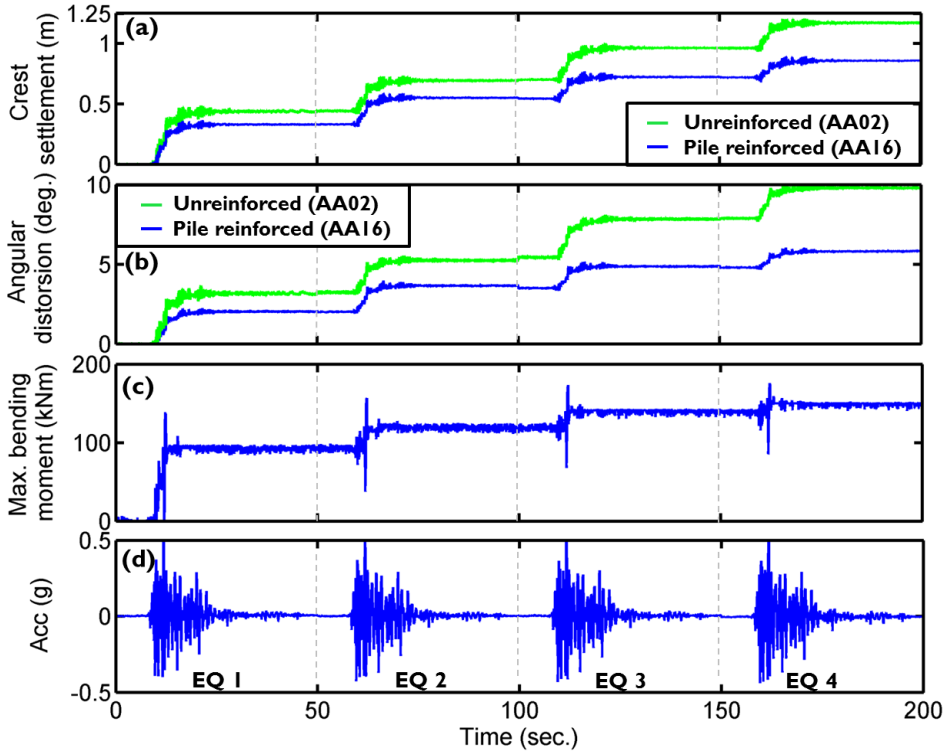

Figure (6- 6): Slope performance at *S/B* = 4.67 (Kobe) compared to unreinforced case: (a) crest settlements; (b) angular distortion at crest; (c) maximum pile bending moments (at 3.5 m below ground surface); (d) input motion at instrument 8.

S/B = 3.5 (AA15)

The minimum pile spacing used in this thesis is *S/B* = 3.5. As the pile spacing decreased, more significant reductions in permanent slope movements and angular distortion were observed, particularly in subsequent strong shaking (e.g. strong aftershocks) as shown in Figure (6-7a). At this spacing the maximum improvement to the deformation of the slope was observed, and the bending moments carried by the piles continued to reduce as a smaller amount of soil was supported by each pile.

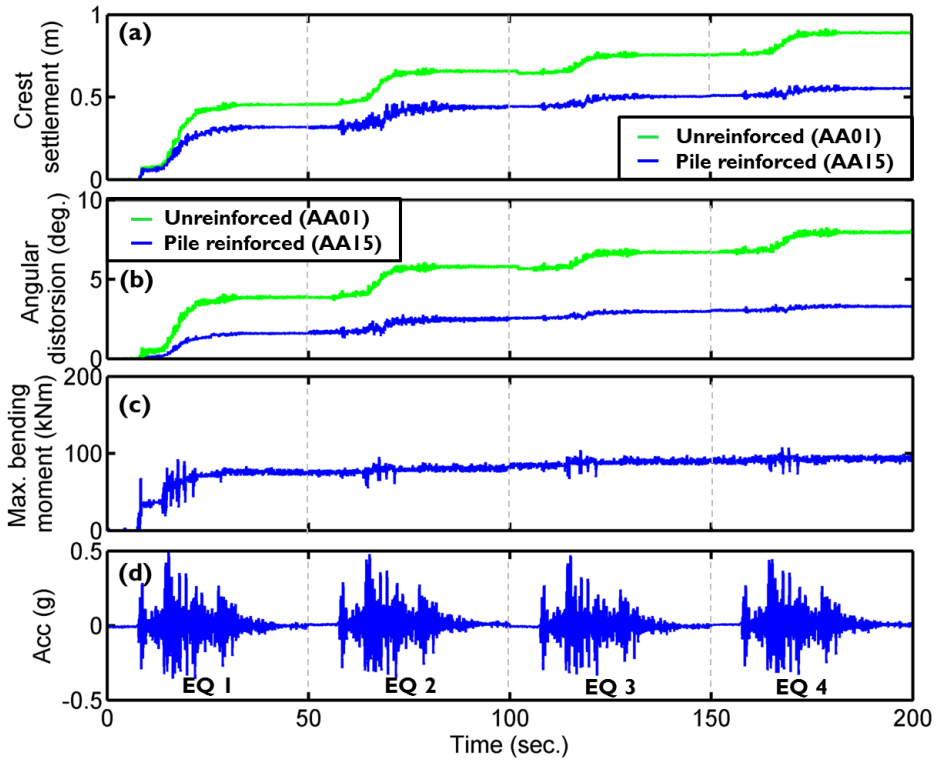

Figure (6- 7): Slope performance at *S/B* = 3.5 compared to unreinforced case: (a) crest settlements; (b) angular distortion at crest; (c) maximum pile bending moments (at 3.5 m below ground surface); (d) input motion at instrument 8.

6.3.2 Effect of pile spacing on induced pile bending moments

Although the principal consideration in designing a pile-reinforcement scheme for a slope should always be the improvement to the slope's performance, it is also necessary to consider the bending moments which are induced in the pile, to ensure that they are appropriately detailed. Points of measured maximum bending moments were connected using smooth curves lines. Figure (6-8) shows the post-earthquake bending moments along the length of the instrumented piles after each earthquake in each of the elastic tests.

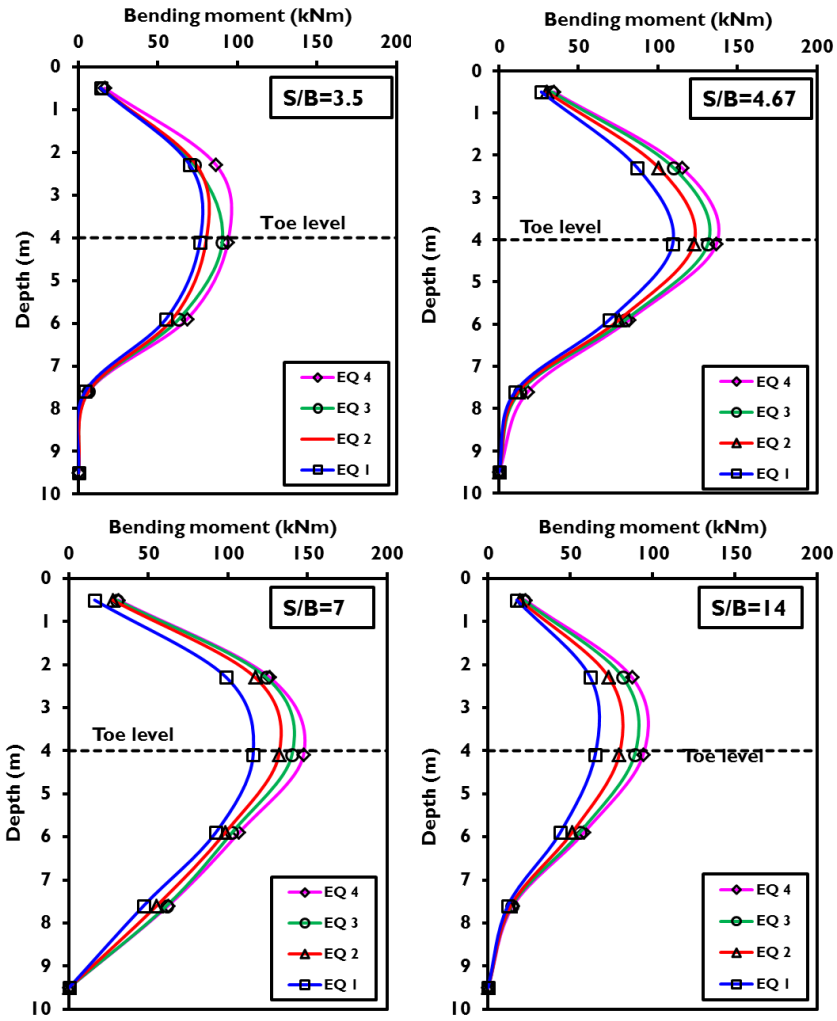

Figure (6- 8): Post-earthquake permanent bending moments along the instrumented pile in the elastic pile tests.

The following behaviour can be observed from Figure (6-8):

1. In all four tests the maximum bending moment occurs at between 3 – 4 m below the ground surface;
2. This maximum bending moment is mainly induced by the initial earthquake; further shaking at the same magnitude does not change the shape of the bending moment distribution and only increases their magnitude by a small amount;
3. As the pile spacing increases from *S/B* = 3.5, the piles carry increasing amounts of moment despite their effect on slope performance reducing (Figures 6-3 – 6-7). This suggests that they are still having some combined effect on restraining the soil mass, but that the configuration is suboptimal; By *S/B* = 14.0, the piles are carrying less moment than at *S/B* = 7.0, presumably as

any load transfer/arching effects have completely broken down and the moments are induced due to a local flow-around mechanism.

4. Pile fixity depth is increasing with increasing pile spacing.

Figure (6-8) also suggests that when used in a discretely spaced row, the moment capacity (i.e. the amount of longitudinal reinforcement) could be reduced towards the top and bottom of the piles, potentially saving material within the pile.

Figure (6-9) compares tests AA16 and AA14, having the same *S/B* = 4.7, but subject to different input motions. Approximately 80% of the measured bending moment at the end of the last earthquake for AA14 (Chi-Chi model) was after the first earthquake (110 kNm after the first earthquake and 138 kNm after the last earthquake). In test AA16 (Kobe model), approximately 62% of the total induced bending moment at the end of all aftershocks was after the first earthquake (92 kNm after the first earthquake and 149 kNm after the last earthquake). However, despite the differences in magnitude and the different characteristics of the two input motions, the shapes of the bending moment distributions are similar.

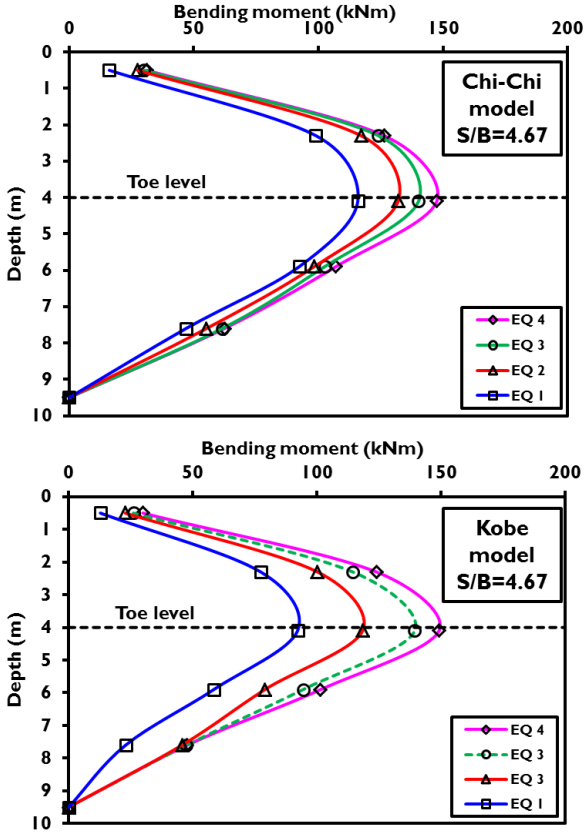

Figure (6- 9): Post-earthquake permanent bending moments along the instrumented for *S/B*=4.67 (AA14 and AA16)

6.3.3 Dynamic response

In addition to reducing permanent movements (e.g. settlement and angular distortion) pile-reinforcement may also reduce the seismic shaking demand on any structures located at the crest. Spectral accelerations for 5% nominal structural damping ratio were therefore determined at the crest of the slope (i.e. ccc. No.5 data in figure 6.1) for the elastic pile tests (AA12-AA16) for comparison with those for an unreinforced slope, and are shown in Figure (6-10). These acceleration response spectra (ARS) have here been normalised by the peak ground acceleration at the bedrock of the slope (accelerometer 8 in Figure 6-1).

As seen from Figure (6-10), the stabilising piles reduced the response spectral acceleration at the crest of the slope in all cases and attenuated the motion across the entire frequency range. It can clearly be seen that the amount of attenuation increases as the piles are brought closer together. The attenuation was also more pronounced in the later earthquakes (aftershocks).

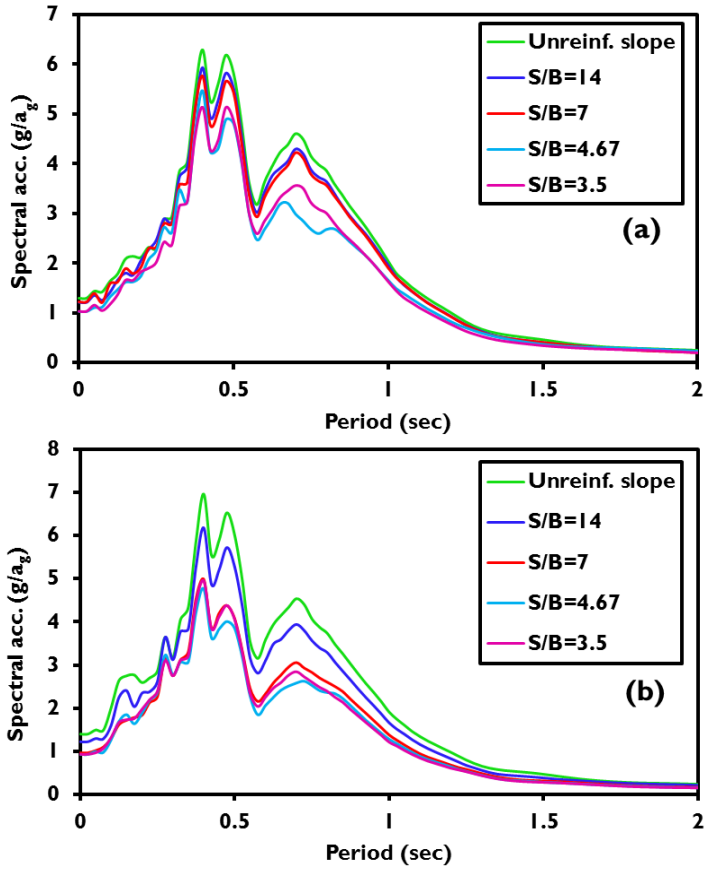

Figure (6- 10): Spectral acceleration for elastic models; (a) after EQ1; (b) after EQ 4.

6.3.4 Summary of slope performance improvements

Figure (6-11) summarises the effects of the elastic piles on the seismic slope performance in terms of the post-earthquake permanent movements (settlements and angular distortions) and the magnitude of the dynamic motions (i.e. S_{red}), all at the slope crest. The effect on accelerations has also been plotted as a ratio of peak accelerations at instrument 5 (A_{red}) to that input, for comparison with the values of S_{red} (the ratio between the normalised ARS at any *S/B* to the normalised ARS of unreinforced case). As expected, the improvement offered by the piles increases as the piles are spaced closer together. At *S/B* = 3.5, the permanent movements are reduced by approximately 35%, while the dynamic motions are reduced in magnitude by approximately 20%. It is not surprising that the permanent movements are reduced to a larger degree – considering the slope deformations in a Newmarkian way, the piles would be expected both to increase the yield acceleration and reduce the induced accelerations by S_{red}.

Maximum *S/B* ratios recommended for piled slopes to ensure that arching is taking place between piles have been recommended by Ellis et al. (2010) for static conditions and Kourkoulis et al. (2011) for dynamic conditions. The latter suggests $S/B \leq 4$ based on finite element modelling, while the former suggests the following simple expression, based only on the soil friction angle (via coefficients of active and passive lateral earth pressure, K_a and K_p respectively):

$$\frac{S}{B} \leq \frac{K_p^2}{K_p - K_a} \tag{6-1}$$

Based on the data shown in Figure (4-7) the friction angle of the soil will be between 32^o – 38^o depending on whether the soil strains are large (critical state) or small (peak state). To be certain that the pile reinforcement will be as effective as possible it would be prudent to use the lower critical state friction angle, resulting in $S/B \leq 3.6$. This is approximately the same as the closest spacing reported herein at which the maximum improvement was observed. If arching is then acting fully at this point, it would suggest that there would be no further benefit of bringing the piles closer together; however, it was not possible to confirm this during the testing due to the practical difficulties in installing the piles closer than *S/B* = 3.5. It is therefore provisionally suggested that Equation (6-1) may be useful in specifying the required

spacing between piles to achieve the maximum improvement in slope performance at the minimum cost.

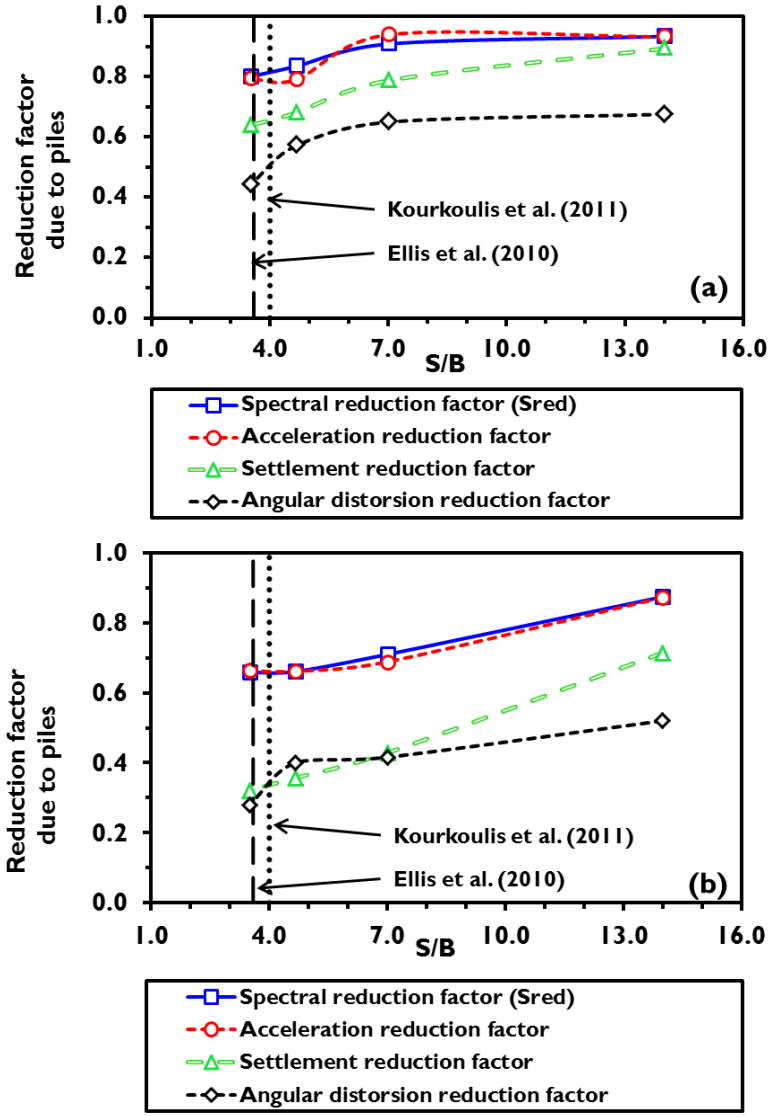

Figure (6- 11): Reduction in crest settlement and acceleration due to pile reinforcement as a function of normalised pile spacing: (a) in EQ1; (b) in EQ4

6.4 Performance of RC pile-reinforced slopes (AA04-AA07)

Now that the performance of pile-reinforced slopes has been presented for the idealised case of a purely elastic pile, Section (6.4) will describe how the performance of the slope differs when the piles have more realistic properties. After each of the RC pile tests, the piles were carefully exhumed to check for damage. If no damage was found, the piles were tested under four-point bending to determine the residual

moment capacity and bending stiffness of the section, following the cycles of cyclic loading imparted during the centrifuge test.

6.4.1 Permanent slope deformations

The seismic crest settlement was measured at the crest of the slope using LVDTs as mentioned before. Figure (6-12a) shows that the seismic crest settlement decreases with decreasing spacing ratio *S/B*. Figure (6-12b) shows these settlements normalised by the crest settlement for the non-reinforced slope (AA01) to obtain a settlement reduction factor. At the closest spacing tested, the settlement has been reduced to 66% of the value in the unreinforced slope. At the largest spacing (AA04, *S/B*=14) there is only a very small difference compared to the non-reinforced slope case and this can be attributed to the soil moving between the piles with no discernible arching effect.

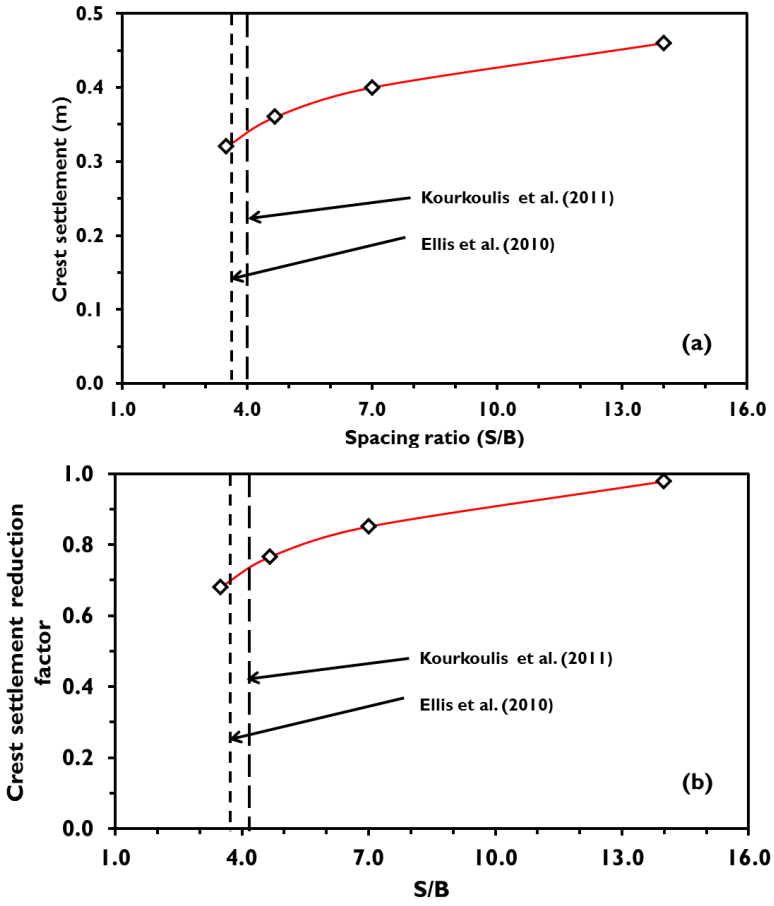

Figure (6- 12): Crest settlement (AA04-AA07).

6.4.2 Dynamic response

The effects of the piles on the accelerations within the slope were described both as a soil amplification factor (ratio of peak accelerations) and in terms of acceleration response spectra. The former is shown in Figure (6-13) for the installation of piles at *S/B* = 3.5, where the acceleration response is reduced to approximately 83% (0.62g at the crest for the non-reinforced slope case, AA01, to 0.52g for *S/B* = 3.5, AA07).

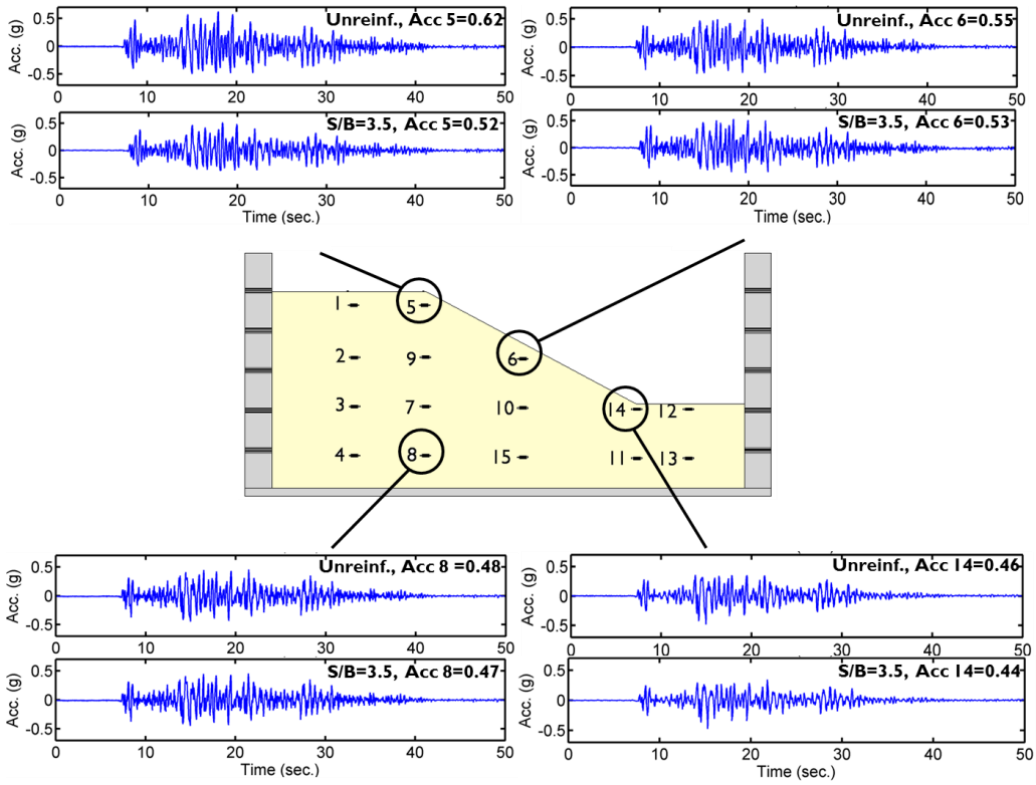

Figure (6- 13): Acceleration for selected points in the slope before and after slope stabilisation (tests AA01 and AA07)

To compare changes in peak acceleration ratio, an amplification reduction factor was defined, representing the ratio between the dynamic amplification factors from input to crest for each piled case to that of the unreinforced slope. This is shown in Figure (6-14).

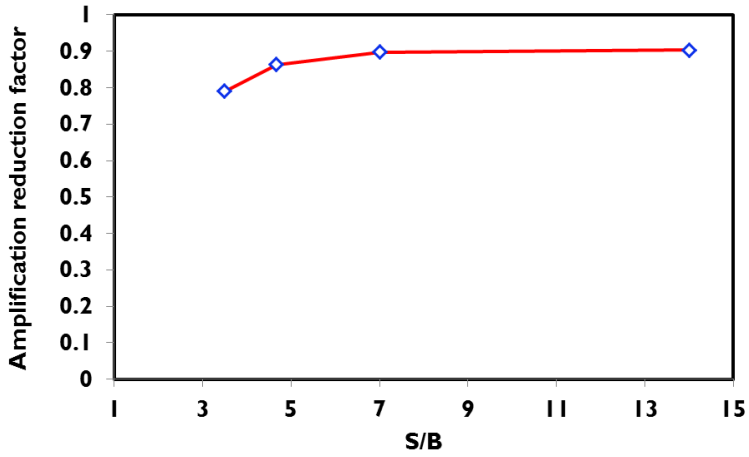

Figure (6- 14): Amplification reduction factor as a function of S/B.

ARS, using the instrument at the crest of the slope, as before, is shown in Figure (6-15). From this figure, the dynamic amplification factor for a particular case can be calculated at zero periods as it represents the peak acceleration at the crest normalised by the input peak ground acceleration for each case.

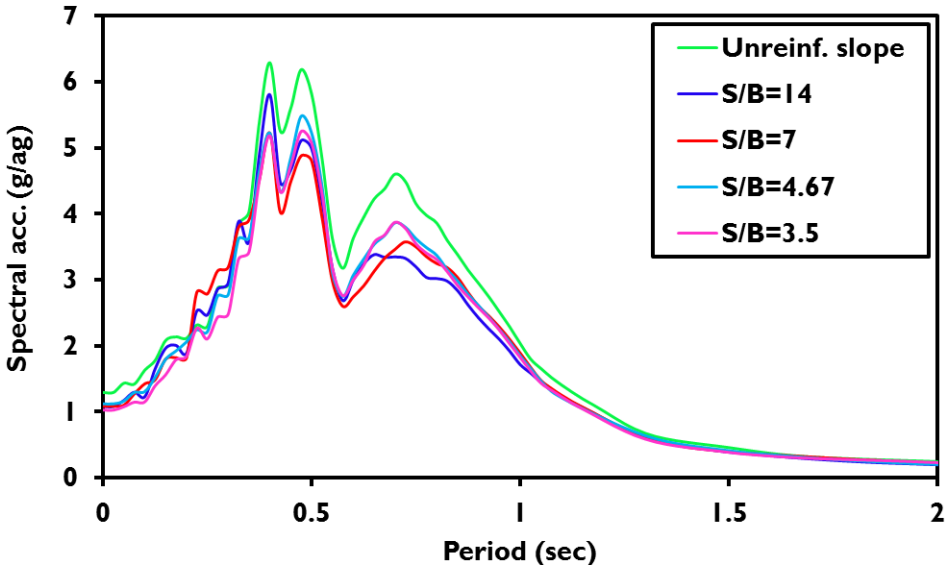

Figure (6- 15): Normalised acceleration response spectra (ARS)

By dividing the reinforced-case spectral ordinates by those for the unreinforced slope, a spectral reduction factor (S_{red}) can be determined as a function of the period of the system of interest:

$$S_{red}(T) = \frac{ARS(T)}{ARS(T)_{AA01}} \qquad (6\text{-}2)$$

Where (T) is the period; *ARS(T)* is the normalised spectral acceleration for each case; $ARS(T)_{AA01}$ is the normalised spectral acceleration for non-reinforced slope. This is shown in Figure (6-16), based on the data shown in Figure (6-15). Although there is some variation in the magnitude of S_{red} with period, it would seem a reasonable first approximation to take S_{red} as a constant for multiplying the ARS of an unreinforced slope, in the same way that site-effect (ground motion amplification) and topographic amplification factors are routinely accounted for in spectra determination. The apparent constancy of S_{red} is potentially a very useful and powerful result as it suggests that the effect of the addition of the piles could be approximated from an analysis of an unreinforced slope (perhaps conducted using a simple 2-D/plane-strain finite element model, such as that validated in Chapter 5), and accounting for the effects of the piles using a simple global reduction factor.

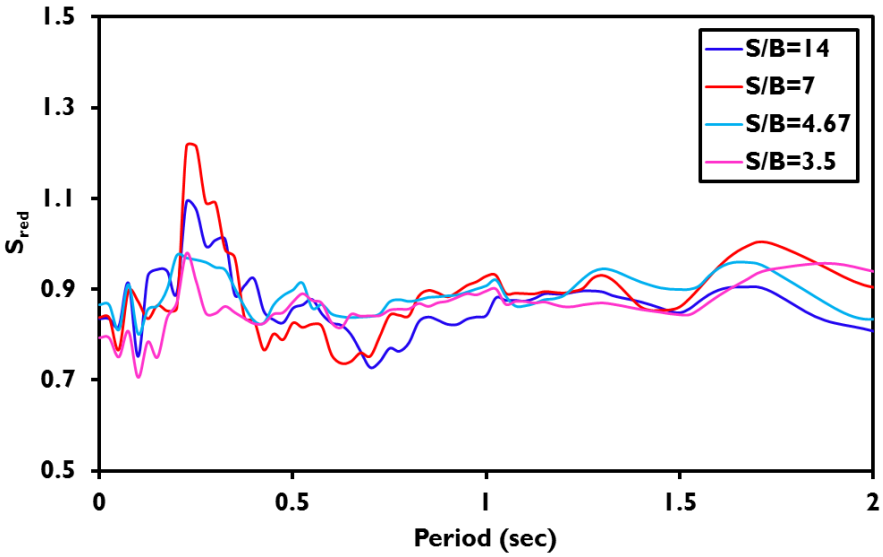

Figure (6- 16): Spectral reduction factor (Sred)

6.4.3 Degradation of the residual capacity of RC piles (AA04-AA07)

No damages were visually observed in any of the RC piles in the single earthquake tests (AA04-AA07). At first glance, this appears obvious, as the induced bending moments from the slipping soil, measured in the elastic pile tests, were less than the ultimate capacity of the 'designed' RC piles, and similar moments should be expected in the RC piles as the bending stiffness is almost identical. However, this does not tell

the whole story as due to their damageable nature, the moment capacity of the RC piles can change (reduce) during shaking.

The residual moment capacities for the RC piles used in each centrifuge test (AA04-AA07) were determined using four-point bending tests. As was expected, the residual ultimate capacities were less than the moment capacity measured (M_y) before the tests (on unused RC piles) and this can be attributed to microstructural damage in the model concrete and wire bond, induced by the strong cyclic loading, as is also observed for real concrete piles (Erdem, 2012).

Figure (6-17) shows the residual moment capacity for the two RC piles used in test AA04 (*S/B*=14). The average moment capacity of 208 kNm is lower than the average value of the pre-earthquake tests (233 kNm, Section 3.7.5.1).

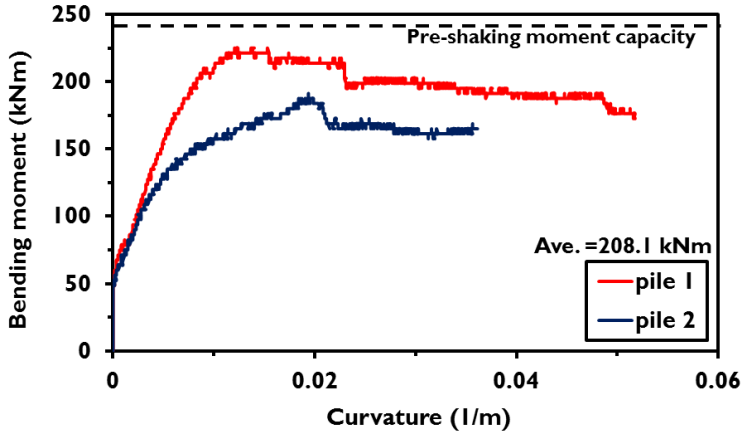

Figure (6- 17): Residual moment capacity for RC piles following 1 earthquake at *S/B* = 14 (AA04)

It was observed in Section 6.3.1 that the bending moments induced in the piles increased as *S/B* was reduced to 7.0. In Figure (6-18) it can be seen that cycles of loading around a larger average moment led to increased deterioration in the residual capacity of the piles. The repeatability of the measurements is also notable from this figure.

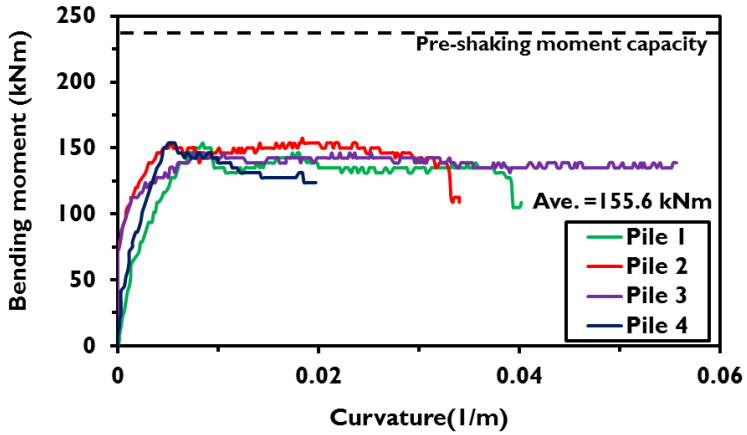

Figure (6- 18): Residual moment capacity for RC piles following 1 earthquake at *S/B* = 7.0 (AA05)

Further decreases in spacing ratio (increasing the number of piles per row) reduced total soil pressures induced by the earthquake and the consequent bending moments induced in the piles. The residual moment capacity of the piles from test AA06 (*S/B* = 4.7) was therefore higher than at *S/B* = 7.0, as shown in Figure (6-19), and higher still following test AA07 (*S/B* = 3.5) as shown in Figure (6-20).

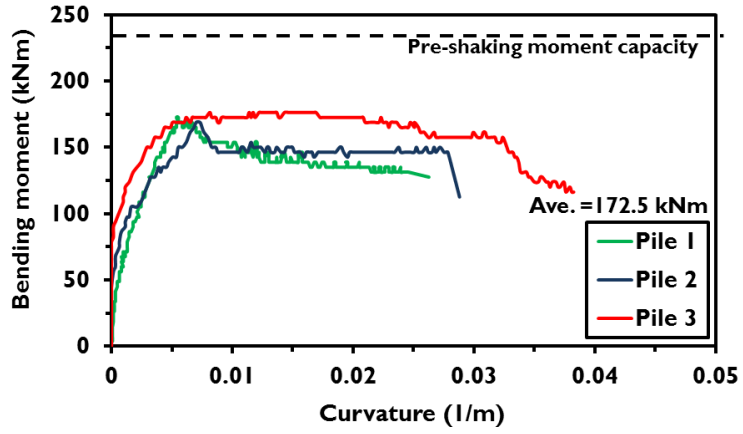

Figure (6- 19): Residual moment capacity for RC piles following 1 earthquake at *S/B* = 4.7 (AA06)

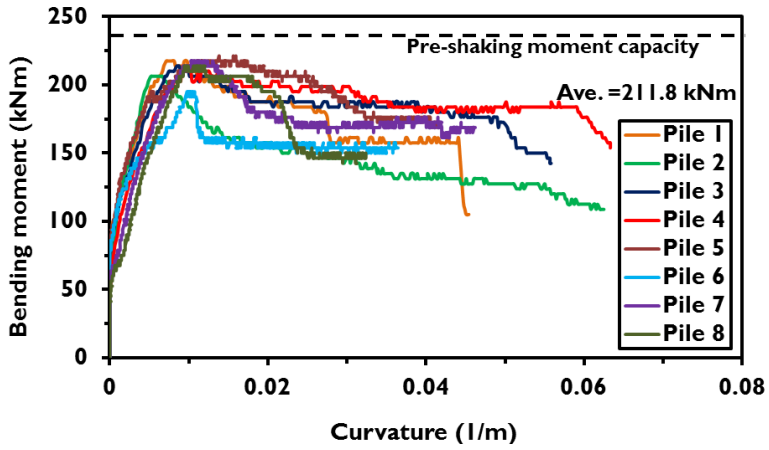

Figure (6- 20): Residual moment capacity for RC piles following 1 earthquake at *S/B* = 3.5 (AA07)

Figure (6-21) shows the residual moment capacity after each centrifuge test. Also shown in this figure are the measured maximum induced moments after EQ1 from the elastic pile tests. This suggests why no damage was observed in the RC piles tested in AA04 – AA07.

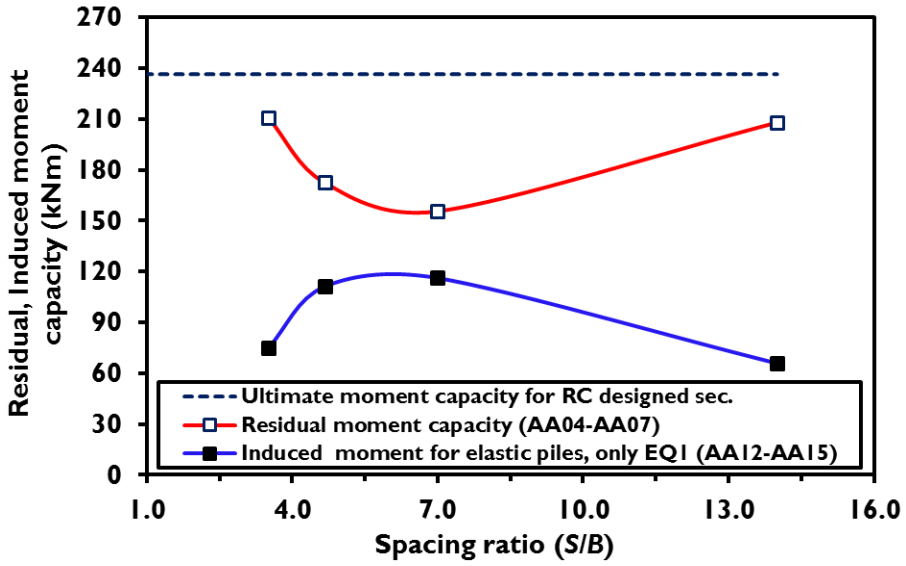

Figure (6- 21): Residual moment capacity and expected maximum induced moments (tests AA04-AA07)

6.5 Assessment of RC pile-reinforced slope performance during aftershocks (AA08-AA011).

In this group of centrifuge tests, the tests described in Section 6.4 were essentially repeated, but with four earthquake motions applied. This allows assessment of how the permanent movements, dynamic response and pile-behaviour/properties are influenced by aftershocks. All models were tested under strong four successive Chi-Chi earthquake motions (AA08-AA12).

6.5.1 Permanent slope deformations

The settlement at the crest of the slope was measured at the end of each earthquake and was accumulated as in Chapters 4 and 5. Figure (6-22) shows how the spacing ratio (*S/B*) for the pile row affects the cumulative settlement time histories, while Figure (6-23) shows directly the effect of *S/B* on post-earthquake accumulated crest settlement. Figure (6-22) suggest that initially strong reductions in movement in the initial earthquake are not necessarily followed by improved instantaneous performance in aftershocks, though in all cases the cumulative settlement was lower following the installation of the piles. As observed in the previously reported tests (Sections 6.3.1 and 6.4.1), *S/B* = 3.5 gives optimal geotechnical performance (Figure 6-23), with substantial reductions in movement.

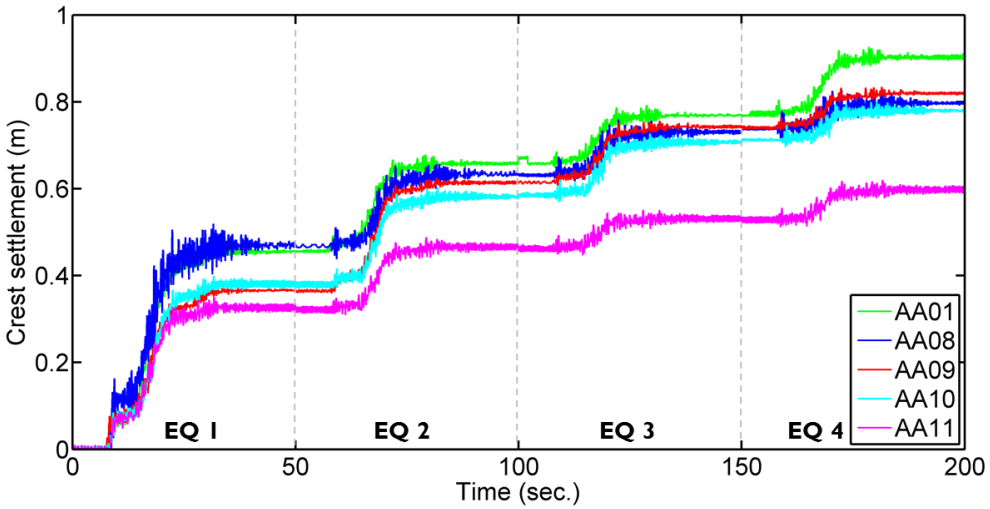

Figure (6- 22): Crest settlement for (AA08-AA11).

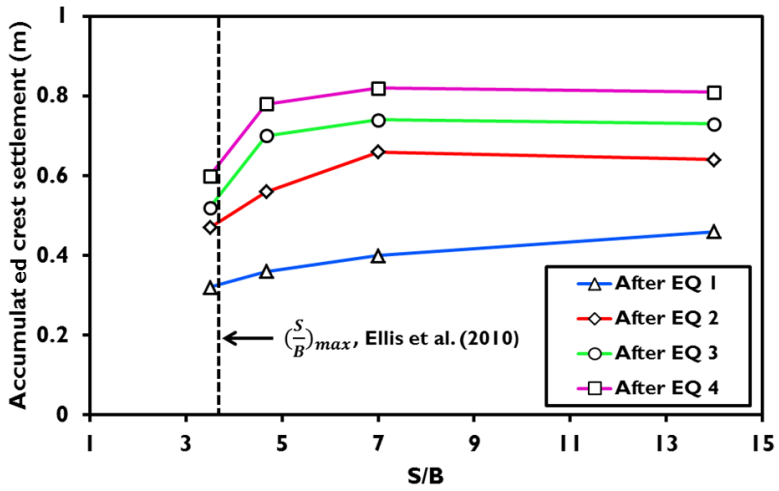

Figure (6- 23): Accumulated crest settlement as a function of *S/B*.

In Figure (6-24) the instantaneous crest settlements are normalised by the value measured for the unreinforced slope in each earthquake to give a reduction factor. It can be seen that the progressive improvement in performance with reducing *S/B* observed in EQ1 (see also Figure 6-12) becomes much sharper with further shaking, with the intermediate cases (*S/B* = 4.7 and 7) becoming less effective in aftershocks. Piles spaced at *S/B* = 3.5 however retain their good performance, even after a number of strong aftershocks.

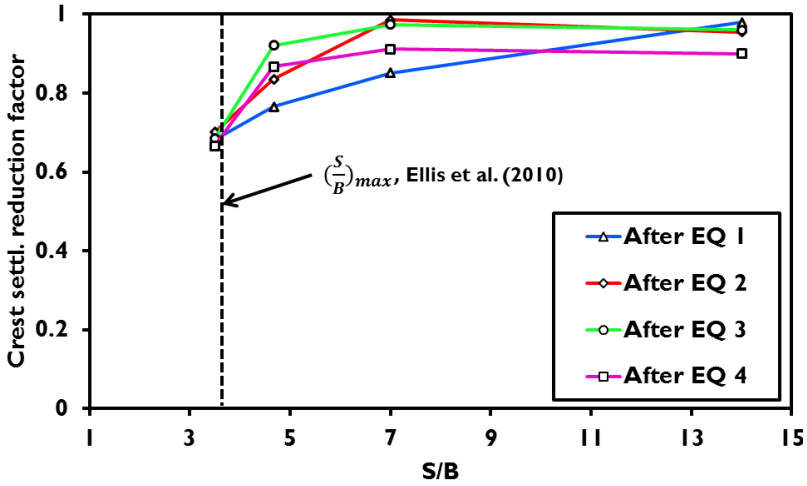

Figure (6- 24): Crest settlement reduction factor as a function of S/B.

Figure (6-25 b) shows also how the measured crest settlement for each studied case reduces with decreasing of the spacing ratio (*S/B*) for the row of stabilising piles and how the yield acceleration reduction factor increases with increasing accumulative Arias intensity, A_I (i.e. Figure 6-25 a). It should be noticed also in figure (6-25 b) that

piles are not only important during the main earthquake to stabilise slope, but also in the subsequent aftershocks.

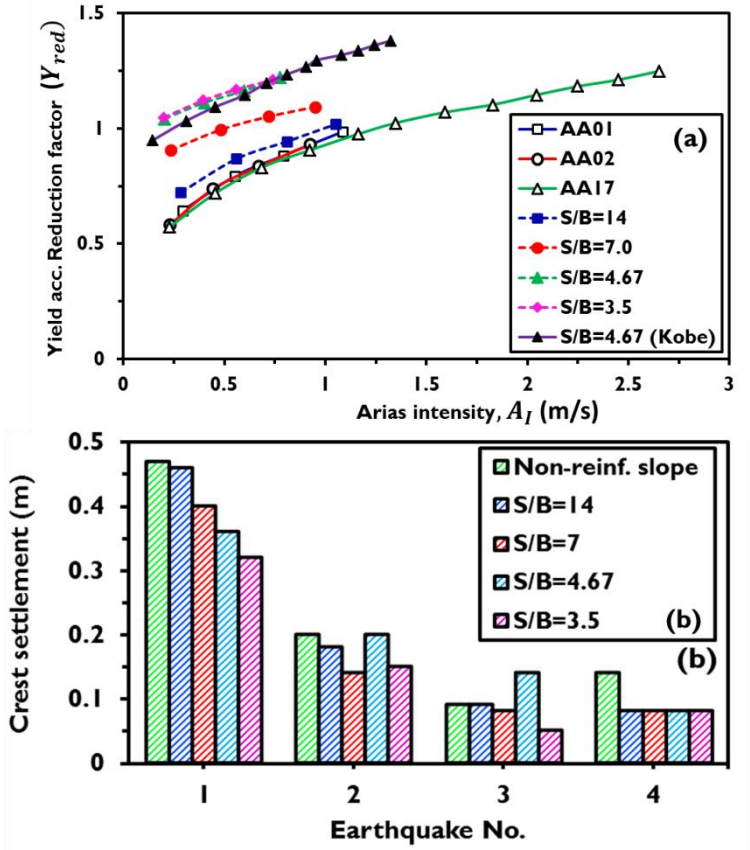

Figure (6- 25): Aftershocks effects on crest settlement for different pile spacing

6.5.2 Dynamic response

Normalised ARS for accelerations recorded at the crest of the slope for the first earthquake (EQ1) and the last earthquake (EQ4) in each test were determined and are shown in Figure (6-26). The improvement due to the piles is less apparent than in the case of the elastic piles, though it is clear that they reduce the acceleration response over for T > 0.4 s (except at the widest spacing, *S/B* = 14)

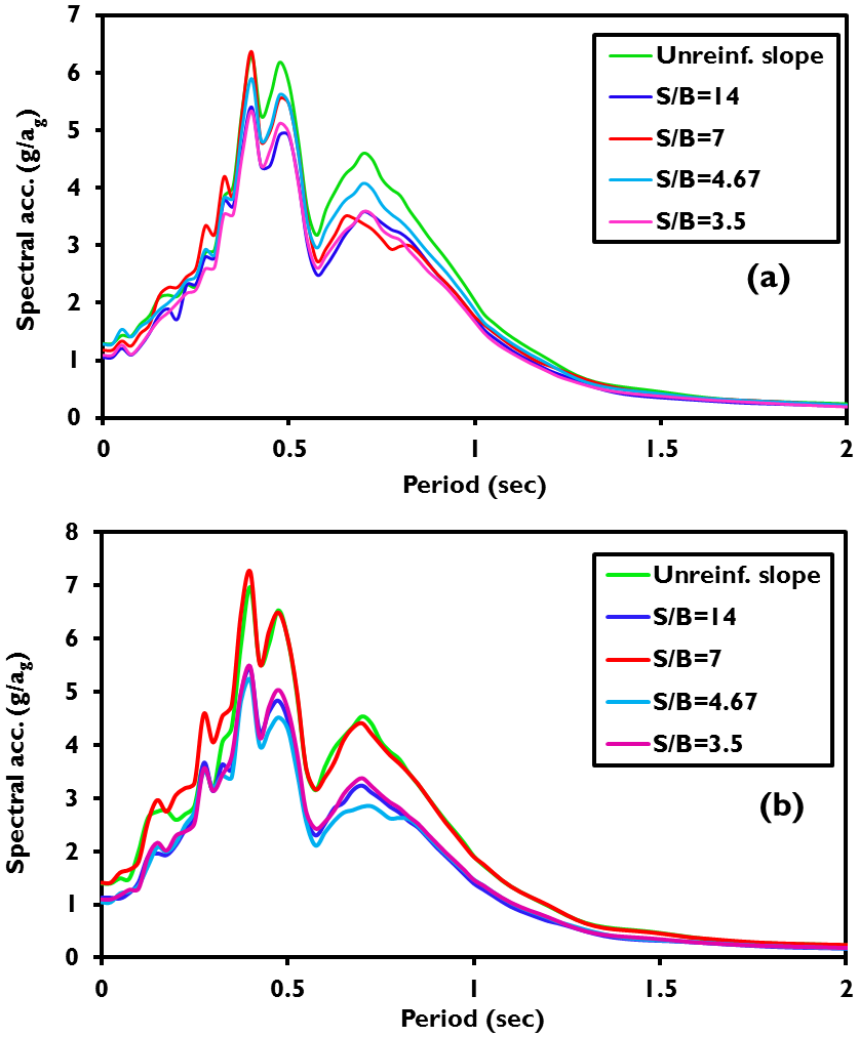

Figure (6- 26): Normalised spectral acceleration in g/a_g, (a) after EQ 1; (b) after EQ 4

The spectral acceleration reduction factors (S_{red}) were also calculated as described in Section 6.3.3 for the first and the last earthquake data as shown in Figure (6-27). These will be compared to values from the previous tests in section 6.4.2.

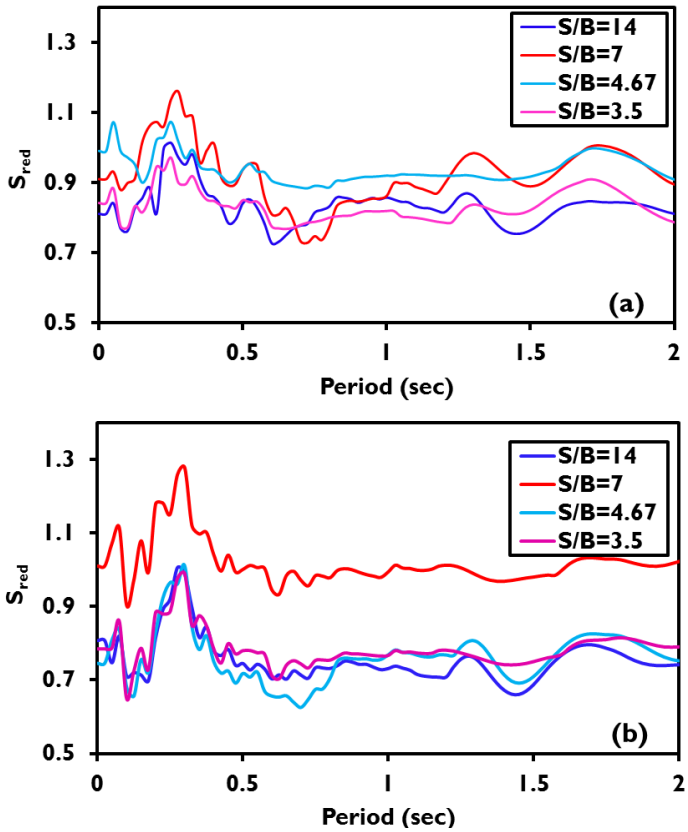

Figure (6- 27): Spectral reduction factor; (a) after EQ 1; (b) after EQ4

6.5.3 Degradation of the residual capacity of RC piles (AA08-AA11)

Determination of the residual moment capacities for the stabilising piles following the centrifuge tests with many aftershocks (four successive Chi-Chi earthquakes) were conducted as described in Section 6.4.3. The data is shown in Figures (6-28) – (6-31). One of the piles in test AA09 (*S/B* = 7) was observed to be broken (not tested) and another was cracked which is shown by the red line for Pile 2 in Figure (6-29). The piles at this spacing ratio saw the largest induced moments and most reduced residual capacities.

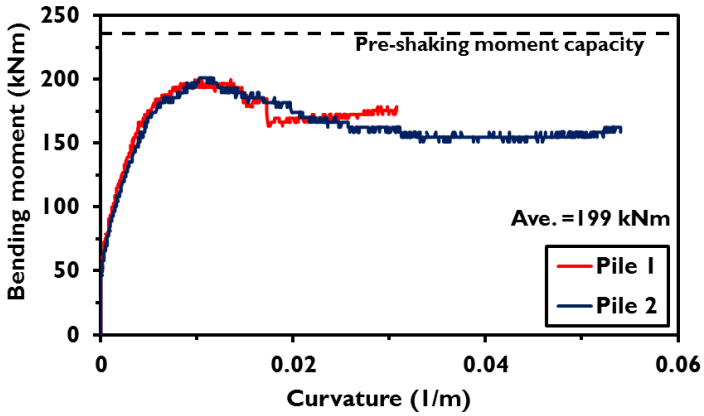

Figure (6- 28): Residual moment capacity of RC piles (After AA08)

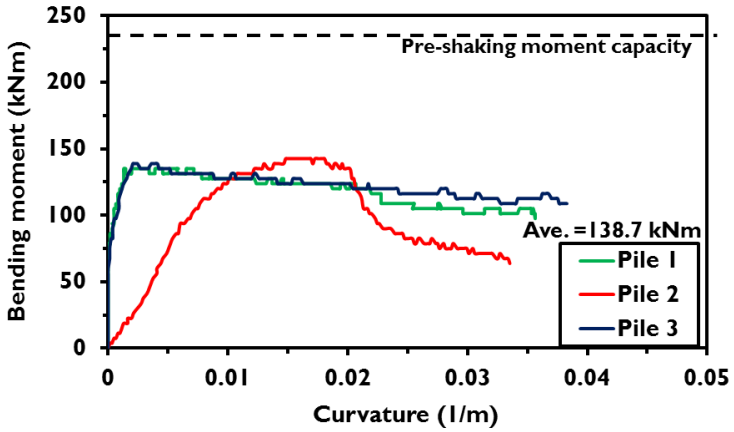

Figure (6- 29): Residual moment capacity of RC piles (After AA09)

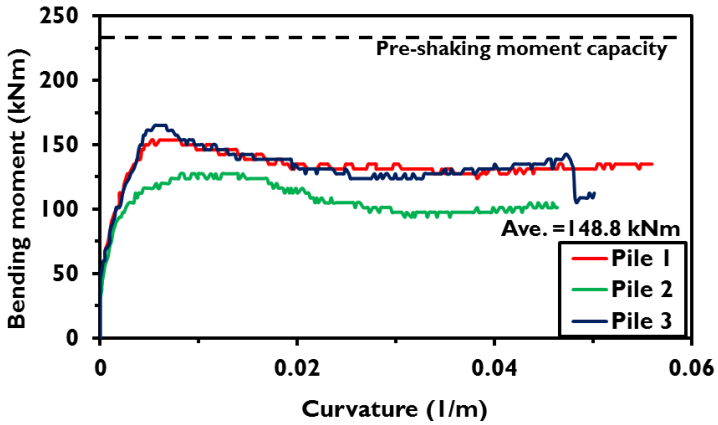

Figure (6- 30): Residual moment capacity of RC piles (After AA10)

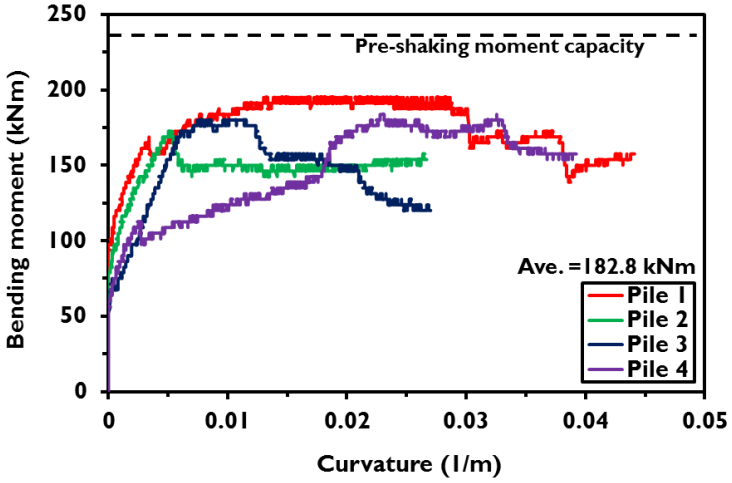

Figure (6- 31): Residual moment capacity of RC piles (After AA11)

Figure (6-32) shows how the mean residual moment capacities were reduced compared to the piles tested under a single earthquake motion (from Section 6.4.3). The variation of residual capacity with *S/B* is similar to that for the single motion

tests, but reduction is slightly larger. It was previously noted from the elastic pile tests that the induced permanent bending moments increased slightly during the aftershocks, so this appears to correlate with the magnitude of the induced moments being the main controlling factor on the amount of reduction in the residual pile capacity.

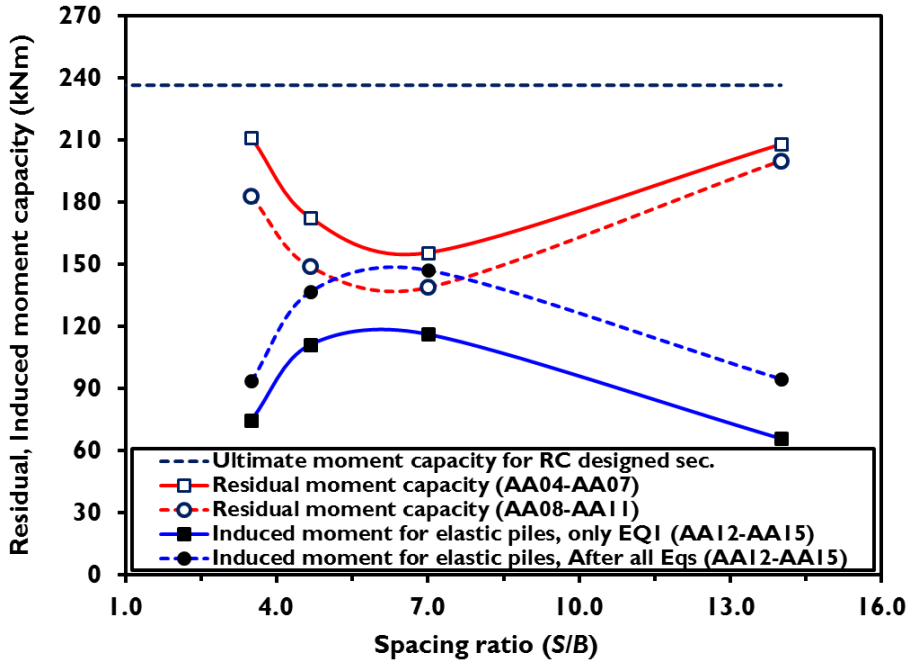

Figure (6- 32): Residual moment capacity and expected maximum induced moments (AA04-AA11)

6.6 Effects of non-linearity of pile response on slope performance

6.6.1 Permanent slope deformations

Crest settlement results for 'RC' and 'elastic' piles in all studied cases have been normalised by the crest settlement in the appropriate non-reinforced slope case and summarised in Figure (6-33a and b) for both a single large earthquake and following a sequence of strong aftershocks.

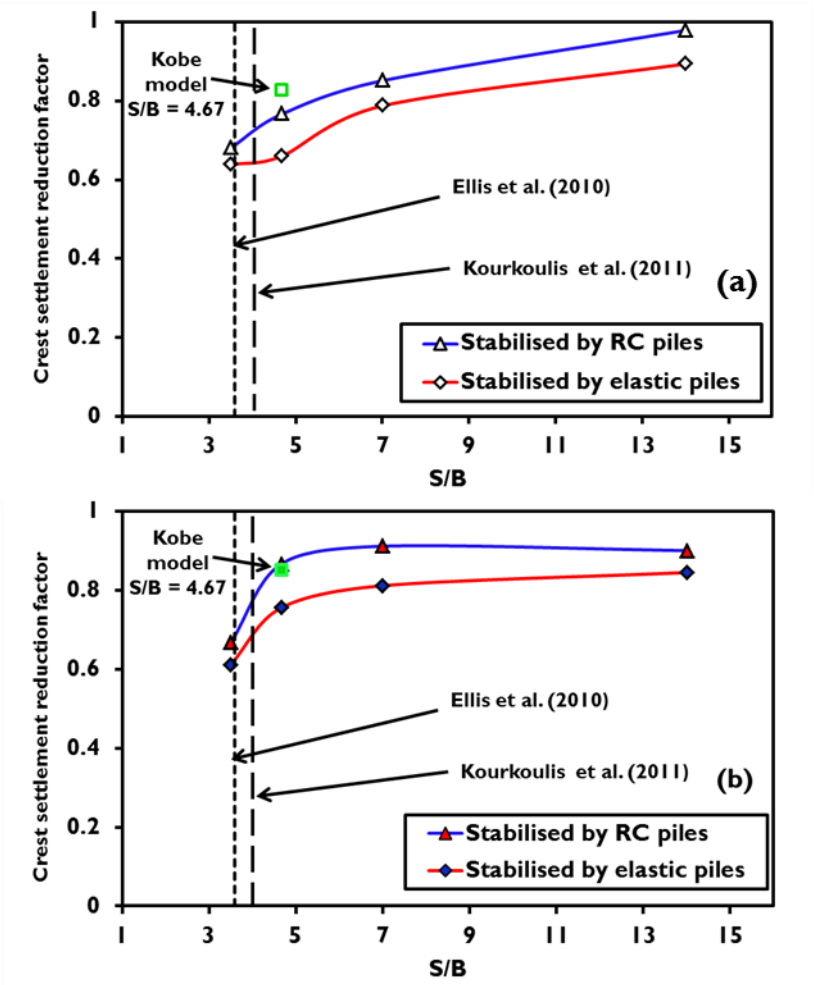

Figure (6- 33): Comparison of crest settlements for slopes with elastic and RC piles: (a) EQ1; (b) EQ4.

For a single earthquake at minimum spacing (*S/B* = 3.5), the crest settlement reduction factor was reduced by 36% for the elastic piles and by 32% RC piles. The RC piles in all cases show less improvement than the elastic piles, suggesting that not accounting for the true behaviour of the reinforced concrete (i.e. approximating as elastic) will generally overestimate performance, though would be close enough for design and decision making purposes. After strong aftershocks, the crest settlement reduction is by 39% in the elastic case and 33% for the RC case. In both cases, the piles become less effective during aftershocks at spacings greater than *S/B* = 3.5, but the results suggest that by installing at optimal spacing consistent reinforcement can be obtained which remains effective even during 'storms' of earthquake activity. The excellent agreement of the normalised results from the Kobe model compared to the main data using the Chi-Chi motion, suggests that the proportional improvements are

insensitive to input motion (though are likely to still depend on slope and pile configuration, e.g. height, slope angle and pile EI).

6.6.2 Dynamic response

Figures (6-34) and (6-35) show the comparative ARS for both 'RC' and 'elastic' piles for EQ1 and EQ4. During the first earthquake (Figure 6-34), the differences between the two pile types are relatively small. The RC piles perform less match at *S/B* = 7, which was one of the tests with the higher induced bending moments. After four earthquakes/aftershocks (Figure 6-35), this is noticeable at all values of *S/B* except for the widest spacing.

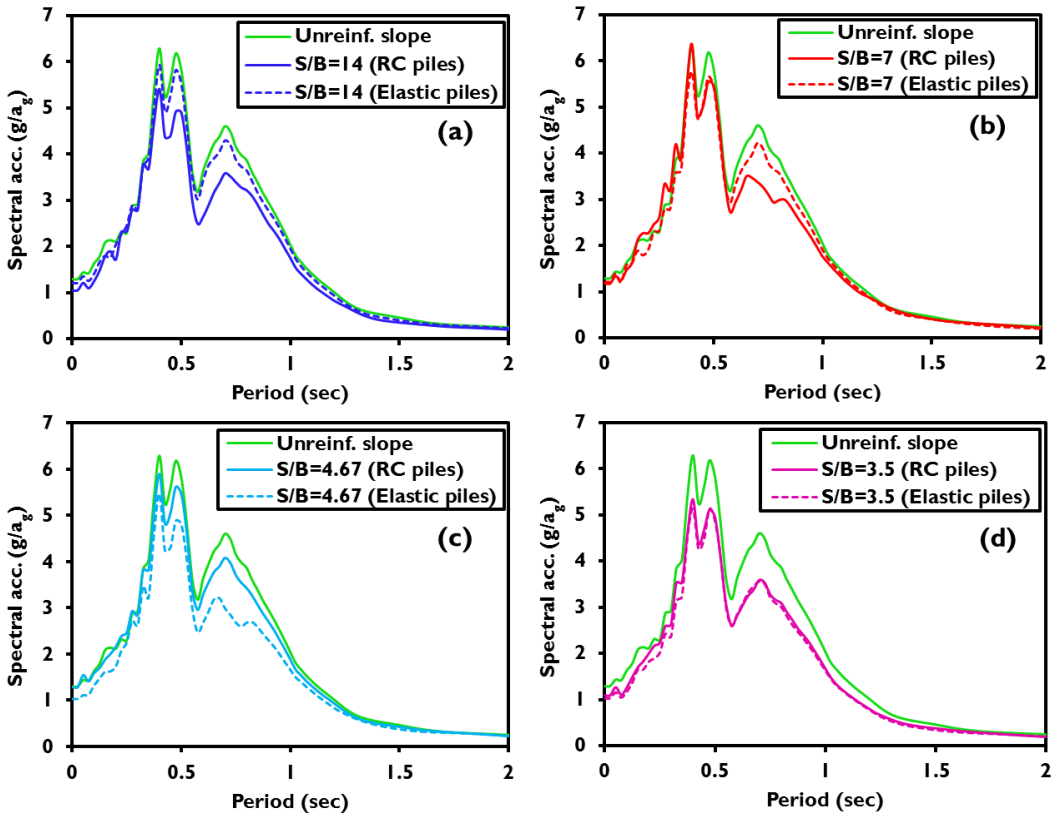

Figure (6- 34): ARS after EQ1 for: (a) *S/B*=14; (b) *S/B*=7; (c) *S/B*=4.67; (d) *S/B*=3.5

.

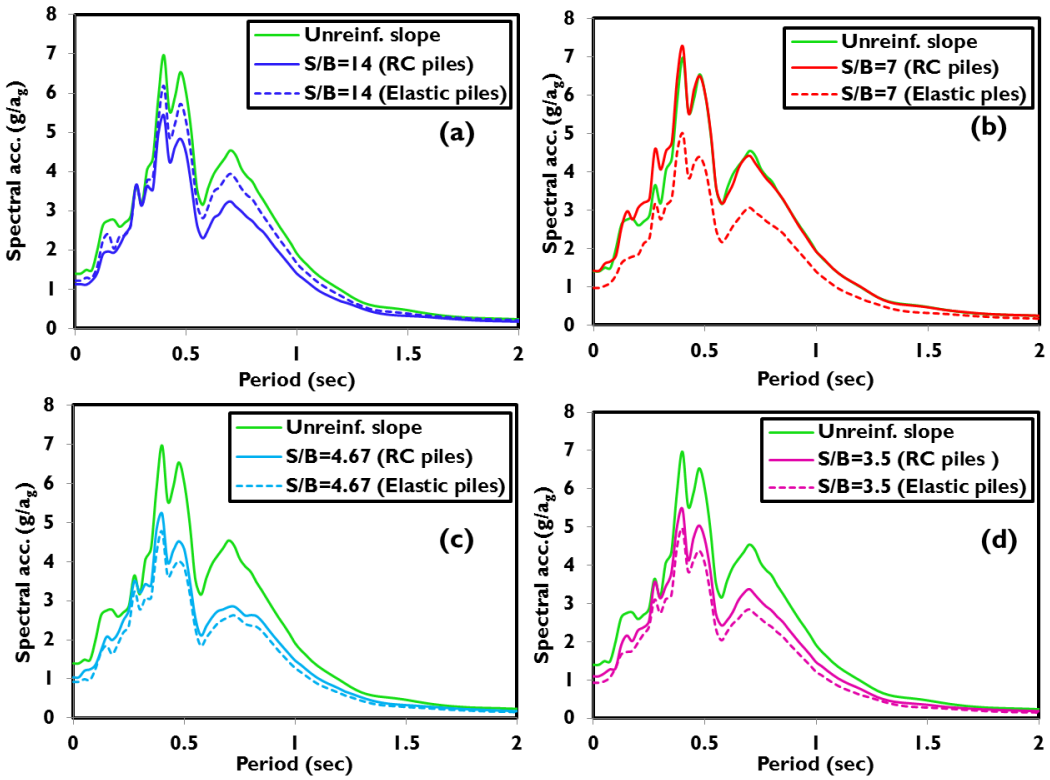

Figure (6- 35): ARS after EQ4 for: (a) *S/B*=14; (b) *S/B*=7; (c) *S/B*=4.67; (d) *S/B*=3.5

Figure (6-36) and correlates the spectral reduction effect evident in Figures (6-34) and with the RC pile deterioration observations noted in Sections 6.4.3. In the lower half of the figure, it can be seen that the residual moment capacity was reduced from the initial pre-earthquake value in all of the tests. Comparing this with the maximum bending moments measured in the elastic pile tests, it is clear that the reduction in residual moment capacity mirrors the variation in the induced moments. This is a classic indication of a fatigue-type process occurring in the RC piles. The convergence between induced moments and residual capacity is reflected in the effectiveness of the piles in reducing crest accelerations (i.e. S_{red}) in the upper part of the figure, and suggests that as the piles get close to failure, their effectiveness at reducing dynamic motions is dramatically reduced.

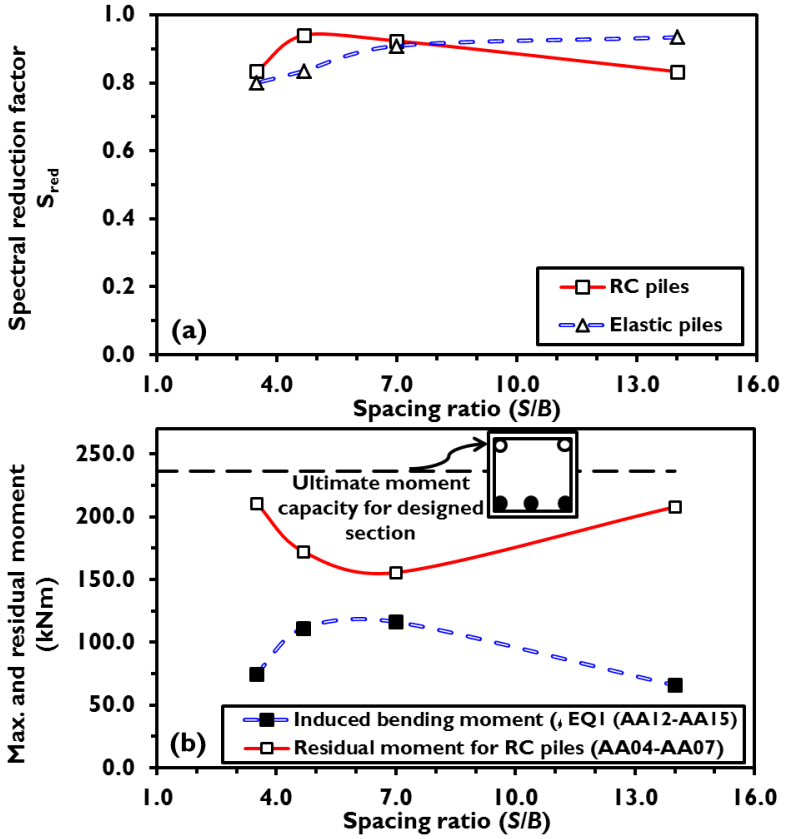

Figure (6- 36): Reduction in residual moment capacity in RC piles following a single earthquake and resulting effectiveness of pile reinforcement (EQ1)

Figure (6-37) shows a similar correlation after four earthquakes. As demonstrated earlier, there is some increase in induced moment from the aftershocks in the elastic pile tests. The additional cyclic loading at higher average moment leads to further deterioration in the residual capacity of the section and in one case (*S/B* = 7.0, test AA09) the residual capacity is just below the induced bending moment measured in the corresponding elastic test. On examination of the piles, this was the only test of those listed in Table (6-1) in which some cracking damage was seen in one of the piles. It should be noted that only some of the piles were damaged as there is some inherent variability in the capacity of the RC pile sections due to the way in which they are made (as in real concrete piles) and the induced moments were measured in a different (elastic) model. As in Figure (6-36), the convergence between induced moment and residual capacity appears to correlate with the piles becoming ineffective at reducing the dynamic motions within the slope.

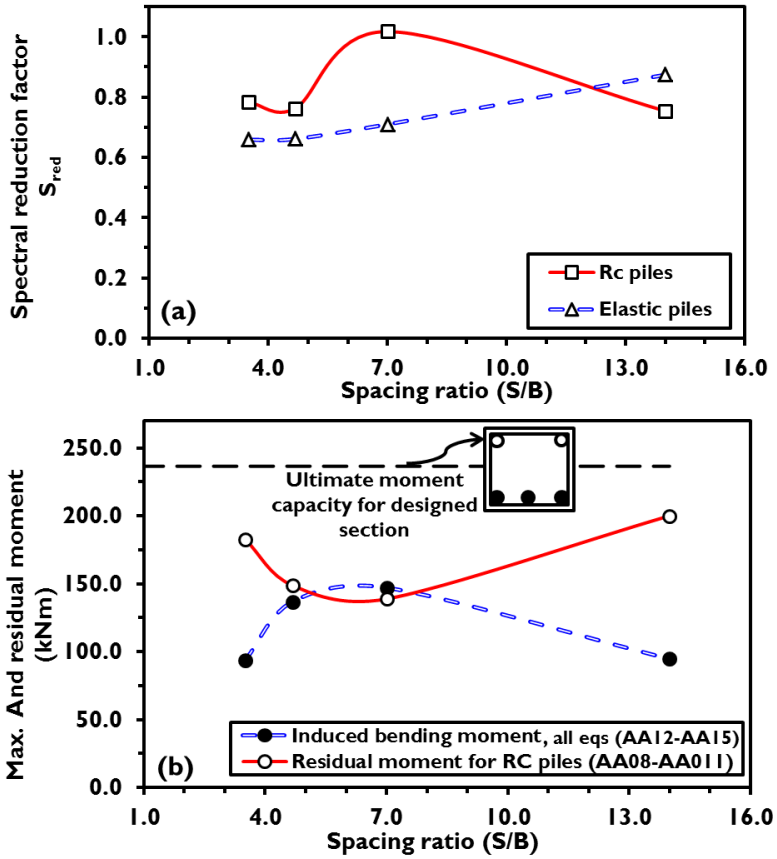

Figure (6- 37): Reduction in residual moment capacity in RC piles following four earthquakes and resulting effectiveness of pile reinforcement in EQ4

Figure (6-38a) plots normalised residual moment capacity (M_{res}) measured for the exhumed piles following the earthquake shaking as a function of the maximum induced moment in the piles (M_{max}). This data is derived from Figures (6-17) – (6-20) and Figures (6-28) – (6-31). In each case, the pre-earthquake yield moment capacity (M_y) is used in the normalisation. The points can all appear to lie along an arc between the points (0,1) and (1,0), suggesting a characteristic relationship for this particular RC section and earthquake characteristics. The 1:1 dashed line represents the condition that $M_{res} = M_{max}$, i.e. that failure will have occurred. The trend of the centrifuge data points intersect this line at $M_{max}/M_y \approx 0.6$, implying that to avoid damage due to fatigue effects, the design value of $M_y > M_{max}$ /0.6 = 1.67Mmax. Given that only one earthquake time history and one pile section were used in the testing on RC piles, it is not clear whether this result would apply to all possible design situations; however, in the absence of further information, it would be prudent to use this value (essentially a partial resistance factor in limit state design).

Figure (6-38b) shows that the residual bending stiffness (EI_{res}) measured in the same post-shaking four-point bending tests is between 50 – 80% of the pre-earthquake value (EI_{static}), which may help to explain some of the loss of dynamic reinforcement effect in Figures (6-36) and (6-37). As larger accelerations will likely cause larger permanent slips (Newmark), the loss of dynamic reinforcing effect may then be responsible for the reductions in permanent movements (Figure 6-33) compared to the case of purely elastic piles.

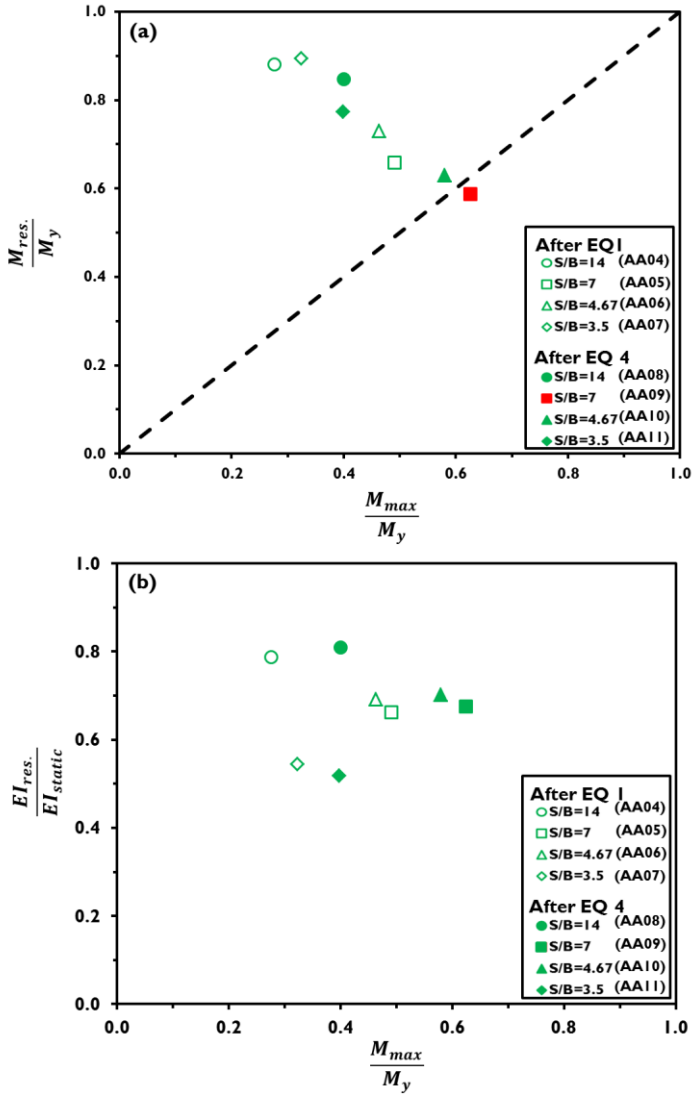

Figure (6- 38): Residual bending properties of RC piles following kinematic loading

6.7 Effects of pile detailing and performance of a slope with seismically damaged piles

The generally good performance of the model RC piles (in terms of not breaking in the tests described so far) suggested that this section could be considered to have been properly designed to resist the seismic effects, in that a sufficient moment capacity ($M_y \approx 230$ kNm) had been provided to avoid damage (in all but one pile). In order to examine the effect of not putting sufficient effort into the reinforcement detailing, a second type of reinforced concrete pile was produced. This consisted of a uniform distribution of longitudinal reinforcement (rather than concentrating this on the upslope side of the pile) and all of this reinforcement was used smooth. From Figure (3-24) it was known that such an arrangement should provide a reduced moment capacity in the region of 80 kNm.

Two further centrifuge tests were conducted using this new weaker RC pile section, denoted tests AA18 (subjected to 4 earthquake motions) and AA19 (subjected to 1 earthquake). Both tests were conducted at $S/B = 7.0$; this was chosen as this case gave the maximum induced bending moments in the elastic pile tests (see Figure 6-8). Further four point bending tests were conducted of the 'weak RC' section to verify the properties, giving an average moment capacity of 70 kNm for both upslope and downslope movements as shown in figure (6-39).

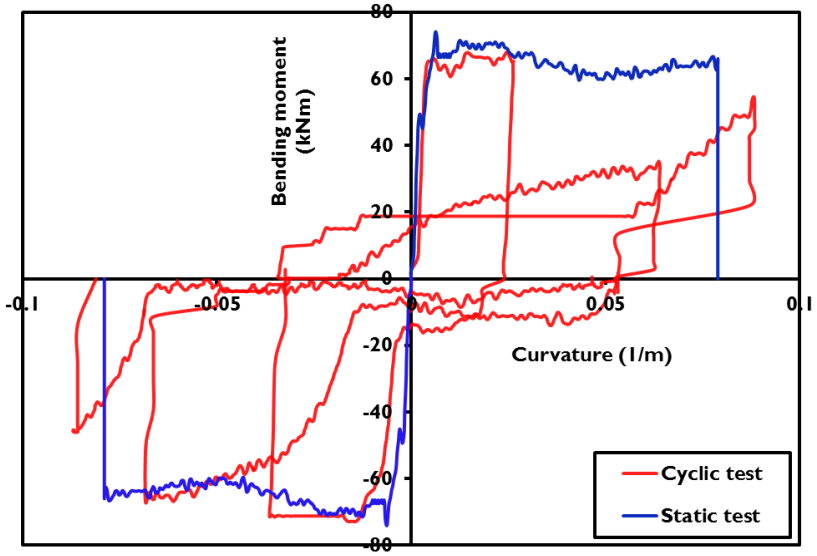

Figure (6- 39): Moment capacity for weak section.

The principal bending properties of all three model pile sections described in this thesis are summarised in Table (6-2), where it should be noted that values of the displacement ductility, μ were determined following the method outlined by Pam et al. (2001).

Table (6- 2): Summary of pile bending properties (values at prototype scale)

Pile type	**B (m)**	**EI (MNm^2)**	**M_y (kNm)**	**Ductility, μ**
Elastic	0.5	50.4	3750	>6
RC	0.5	48.9	230	5.3
Weak RC	0.5	42.2	80	3.7

Figure (6-40) shows the crest settlements measured for *S/B* = 7.0 for both the 'designed' and 'weak' RC sections (tests AA05/09 and AA18 respectively), compared to the movements of the unreinforced slope in EQ1. The displacements of the reinforced and unreinforced slopes are initially similar, as relative soil pile movement is required to generate resistance from the piles. Beyond 0.1 m of displacement the slope reinforced with the design section moves consistently ≈ 20% less than the unreinforced slope. This is consistent with Figure (6-33a). The movements in the case of the weak section however remain close to those of the unreinforced slope, though a reduction of ≈ 7% can be inferred from the figure. This strongly suggests that (i) the weak piles yielded at approximately 0.1 m crest movement in EQ1; and (ii) that once yielded the piles do still impart some improvement to the soil. This latter point is true as if the pile has not reached its ultimate capacity (it is instead yielding in a ductile manner) it can still provide an additional resisting force to the slipping soil mass consistent with that required to generate the yield moment (70 kNm in this case) in the piles. Table (6-3) summarises these differences in crest settlement for the different pile types tested at *S/B* = 7.0, along with complementary data on the influence on angular distortion and spectral reduction (S_{red}).

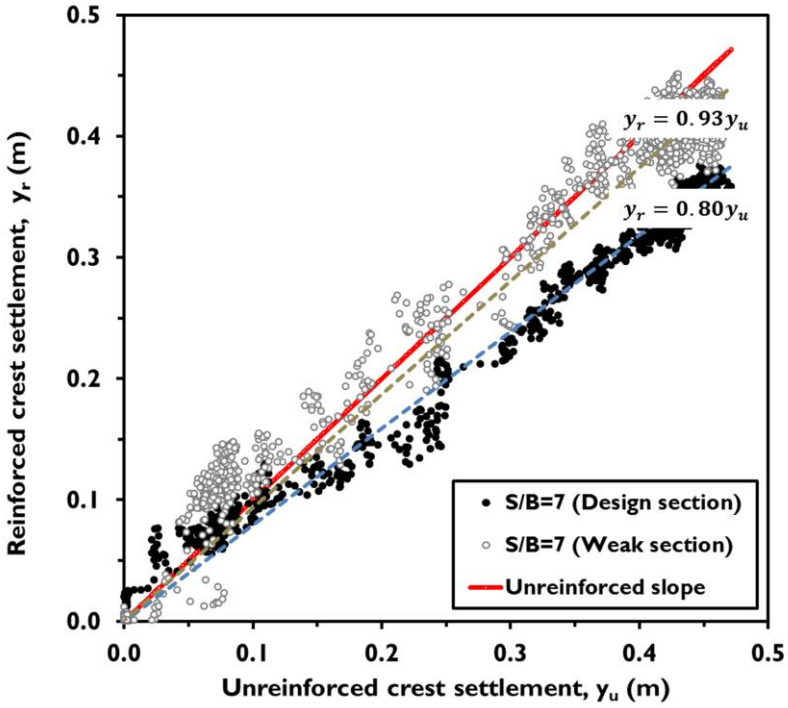

Figure (6- 40): Effect of RC section detailing on crest settlements during EQ1.

Table (6- 3): Effect of pile design on seismic slope performance (s/B = 7.0)

Pile type	Relative crest settlement	Relative angular distortion	Relative S_{red}
Unreinforced	1.00	1.00	1.00
Elastic	0.75	0.65	0.90
RC	0.80	0.69	0.92
Weak RC (damaged)	0.93	0.71	0.98

Figure (6-41) shows close-up images of the weak RC piles after the final two tests AA18 and AA19. The ruler shown at the bottom of each image has its zero at the top of the pile (ground surface). All but one of the piles show tensile cracking on the upslope face (closest to the camera), and some show compressive spalling (loss of material) on the downslope face. This damage can be seen to occur between 60-80 mm from the top of the model piles, i.e. between 3-4 m below ground surface at prototype scale. This is consistent with the depth of maximum moments shown in Figure (6-8). As significant pile damage occurred in both tests (i.e. under successive and single strong earthquakes) it confirms the inference from Figure (6-39) that the piles in test AA18 were broken during EQ1.

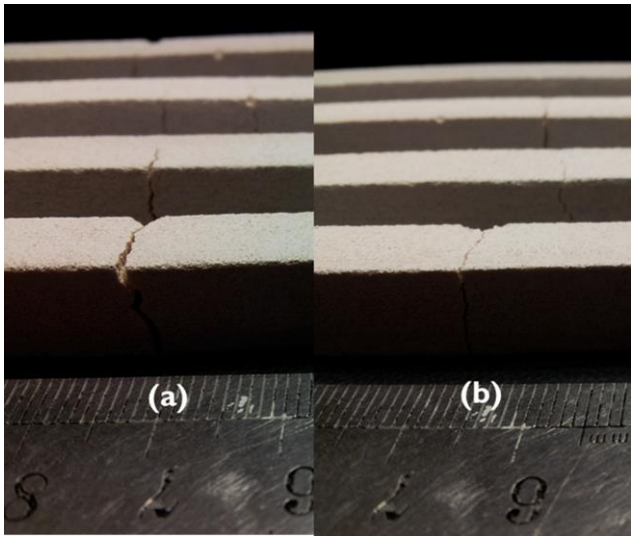

Figure (6- 41): Photographs showing pile damage around the location of maximum bending moment: (a) after four successive earthquakes (test AA18); (b) after a single earthquake (test AA19).

6.8 Summary

An extensive programme of geotechnical centrifuge testing to investigate the performance of pile-reinforced cohesionless slopes during earthquakes and after many aftershocks has been presented in this chapter. These results have been focused on the effects of the piling on the post-seismic permanent deformations of the slope and the co-seismic dynamic response. The soil-pile interaction (SPI) has been also investigated in this chapter and will subsequently be modelled in Chapter 7. The main findings are summarised below:

1- The deformation of pile-reinforced slopes is significantly influenced by the spacing along the pile row (defined by *S/B*). Settlement and angular distortion at the crest of the stabilised slope reduces as pile spacing decreases. Minimum deformations were observed at the closest pile spacing ratio (*S/B* = 3.5) while virtually no effect is observed at spacing ratios *S/B* $\geq$ 14. The behaviour at large *S/B* is likely due to the breakdown of arching between the piles. The minimum spacing tested represents that suggested for optimal performance by other authors and is considered to represent the most effective reinforcement for the least cost. At optimal spacing, permanent deformations were reduced between 30-40% compared to the unreinforced case.

2- Deformation in subsequent aftershocks is smaller for the same earthquake motion for piled slopes. This can be attributed to the geometric hardening effects previously noted in Chapter 4 for unreinforced slopes. Piles become less efficient in aftershocks at wide spacing, though maintain their effectiveness at optimal spacing (S/B = 3.5).

3- The dynamic response is also reduced as S/B reduces. This effect appears to be period-independent. At optimal spacing, reductions of up to 20% were observed in the magnitude of spectral accelerations.

4- The designed section RC piles were strong enough that they were not broken during centrifuge tests though their residual moment capacity and bending stiffness post-earthquake were observed to be reduced. If the piles are detailed so as not to break during the earthquake, modelling them as (linear) elastic provides a good first approximation to their behaviour, though elastic modelling does marginally over-estimate the degree of improvement to the slope's performance.

5- When the piles are incorrectly detailed and yield during shaking, they provide only a very small reinforcing effect to slope performance which is essentially negligible. Detailing of RC piles to resist permanent movements and account for reductions in residual capacity is therefore extremely important. It is suggested that the static moment capacity is designed to be 1.67 times the maximum downslope moment expected from the earthquake and any aftershocks (calculation of these moments will be covered in Chapter 7).

Chapter seven
Seismic performance of pile-reinforced cohesionless slopes: Development of sliding block procedure

7.1 Introduction

In the analysis of piled slopes, it is important to be able to determine (i) the reductions in seismic displacement for a given pile arrangement (e.g. *S/B*) so that the piling can be designed to give the required improvement to the geotechnical performance and (ii) internal forces (e.g. bending moments) within the piles, so that they can be structurally detailed. In this chapter, a simplified pile-soil interaction model is developed for the analysis of piles in slipping soil which can be used within a Newmark sliding block analysis. This will be incorporated into the improved methodology for unreinforced slopes from Chapter four, so that the final method incorporates both strain-dependent geometric hardening (re-grading) and strain dependent pile resistance and is also suitable for use in the events of aftershocks. This model is then validated against the centrifuge test results reported in Chapter six.

7.2 Sliding block procedure for pile-reinforced slopes

7.2.1 Formulation

The limit equilibrium formulation for the yield acceleration developed in Chapter four, which includes strain-dependent geometric hardening of the slope, is modified here to incorporate the additional component of resistance offered by the piles. For slip of a moving mass of soil (block) of length *L*, width *S* and depth *z* beneath the slope surface, the applied downslope shear stress from Figure (7-1) is:

$$\tau_{applied} = \gamma z \sin\beta \cos\beta + k_h \gamma z \cos^2\beta \qquad (7\text{-}1)$$

where the first term relates to the static shear stress due to the ground slope, and the second term relates to the additional peak dynamic shear stress induced by the earthquake. The total shear resistance to this applied shear stress is given by:

$$\begin{aligned}\tau_{ult} &= c' + \sigma' \tan\phi' + \frac{P}{Ls}\cos\beta \\ &= c' + \left(\gamma z \cos^2\beta - k_h \gamma z \sin\beta\cos\beta - u\right)\tan\phi' + \frac{P}{Ls}\cos\beta\end{aligned} \tag{7-2}$$

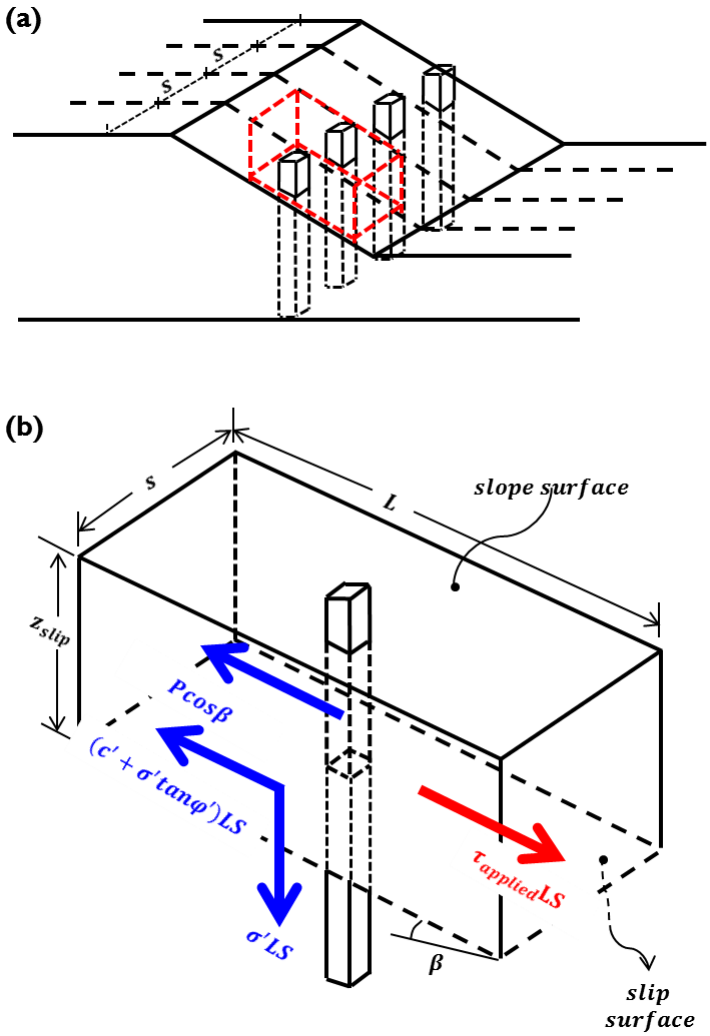

Figure (7- 1): slip mechanism in pile reinforced slope; (a) overall configuration; (b) forces acting on a pile stabilised slipping soil element

The soil yields when $\tau_{applied} = \tau_{ult}$. The value of k_{hy} at which this occurs (the yield acceleration, k_{hy}) can be determined from Equations (7-1) and (7-2) as:

$$k_{hy} = \frac{c' + \left(\gamma z \cos^2 \beta - u\right)\tan\phi' - \gamma z \sin\beta\cos\beta + \dfrac{P}{Ls}\cos\beta}{\gamma z \cos^2 \beta + \gamma z \sin\beta\cos\beta\tan\phi'} \tag{7-3}$$

In a dry cohesionless soil, c' = 0, u = 0. This allows $\cos\beta$ and γz to be cancelled from both the numerator and denominator in Equation (7-3), so that k_{hy} is dependent on the depth of the slip plane, slope geometry (length and angle), soil friction angle, pile spacing and the single pile resistance (which will be described in Section 7.3), so long as the slip plane continues to be parallel to the slope surface. Equation (7-3) therefore simplifies to:

$$k_{hy} = \frac{\cos\beta\tan\phi' - \sin\beta + \dfrac{P}{\gamma z L s}}{\cos\beta + \sin\beta\tan\phi'} \tag{7-4}$$

In Equation (7-4), φ', β, L and P are a function of shear strain i.e. slope displacement. Chapter 4 describes how the strain softening model of Matasovic et al., (1997) can be used to describe $\varphi'_{(cs)}$. A simple relationship was presented to describe the geometric effect of slip on reducing the slope angle (i.e. β). Numerically within the Newmark method, the slope angle is updated for step i+1 based on the slope angle in in the previous step (β_i) and the reduced slope height (H_i) following slope-parallel slip (d_i):

$$\beta_{i+1} = \tan^{-1}\left(\frac{H_i - d_i \sin\beta_i}{H_i \cot\beta_i + d_i \cos\beta_i}\right) \tag{7-5}$$

For the initial time step, d_0 = 0, H_i = H and β_i = β_0, as in Chapter four. In the new yield acceleration formulation in this Chapter, the geometric effect extends also to the instantaneous slip-plane length L_i, which is related to the instantaneous slope angle by:

$$L_i = \frac{H_i}{\sin\beta_i} \tag{7-6}$$

The pile resistance as a function of strain (soil slip) depends on a number of parameters describing the relative soil-pile stiffness and strength of the soil in the unstable material (as it yields around the piles). Clearly, in the initial stages of the analysis before any slip has taken place, the net additional resistance from the piles is zero. As the soil slips, the relative displacement between the soil and the pile increases, providing a progressively larger resistance to slip (P). Eventually, the resistance from the pile will reach a maximum limiting value when either the soil yields around the pile, or the pile yields structurally, whichever occurs first. A detailed soil-pile interaction (SPI) model, in terms of the relationship between P and d_i, is described in Section 7.3.

From the form of Equation (7-4) it is clear that as the soil starts to slip P will increase, while β will reduce. This will result in progressive hardening of the slope response via an increase in the yield acceleration. Even once the piles are providing the maximum resistance, the slope response will continue to be reduced compared to the unreinforced case due to (i) the constant value of P in Equation (7-4), so long as the soil or pile are yielding in a ductile way, and (ii) the continued geometric hardening. By incorporating the effects of strain fully within the model, the behaviour of a seismically damaged slope during subsequent earthquakes/aftershocks can be determined from the initial conditions (pile resistance, relative soil-pile displacement, re-graded slope angle) obtained at the end of the previous ground motion, as in Chapter four.

7.2.2 Assumptions and simplifications

For small to moderate earthquakes whose peak ground acceleration magnitude is close to (but larger than) k_{hy} (and which will therefore have only a limited amount of slip), strain softening behaviour can have a dramatic effect on computed slope displacements, with k_{hy} potentially changing continuously throughout the earthquake due to this effect as φ' changes. In larger earthquakes, where a single cycle causes sufficient slip/strain to reach critical state conditions, then the strain softening model is likely to predict only a marginally smaller slip compared to a standard (strain-hardening) analysis using a constant $\varphi' = \varphi'_{cs}$. It was demonstrated in Chapter four that the effect of the strain softening was negligible for the strong earthquakes used in the centrifuge tests (see Chapters 4). According to this, the strain softening has been

neglected in the modelling described in this chapter (i.e. the material has critical state strength from the beginning of the analysis).

It is also assumed, as in Chapter 4, that once the slope has deformed to a new, smaller value of β, the failure mechanism will continue to be of the infinite type, with a new slip surface forming parallel to the new slope surface (see Figure 4-3). It should be noted, as in Chapter 4, that the model as formulated can be used even for the case of large total slope movements (such as may accrue during a series of strong aftershocks) as the displacement increment in each individual time step will remain small, and therefore the instantaneous failure mechanism will be represented by Figure (6-1) for small displacements.

7.3 Soil-pile interaction (SPI) model

In this section, the relationship between the amount of soil slip and the pile resistance is developed. This behaviour, described as the SPI model will also enable the peak bending moments to subsequently be derived within the piles, so that they can be appropriately detailed. Given that the aim will be to ensure the piles do not break, it can be assumed that the soil in the slipping mass will yield around the piles. The interaction in this zone of soil will therefore be described using a single non-linear elasto-plastic P-y curve which will describe the force applied on the pile, P, by the slipping soil as a function of the relative displacement between the soil and the pile ($d_i - y_p$) at the position of resultant load application. The part of the pile within the 'stable' soil will be modelled using a linearised elastic response model describing the response of the pile (y_p) under the applied load P. This is shown schematically in Figure (7-2).

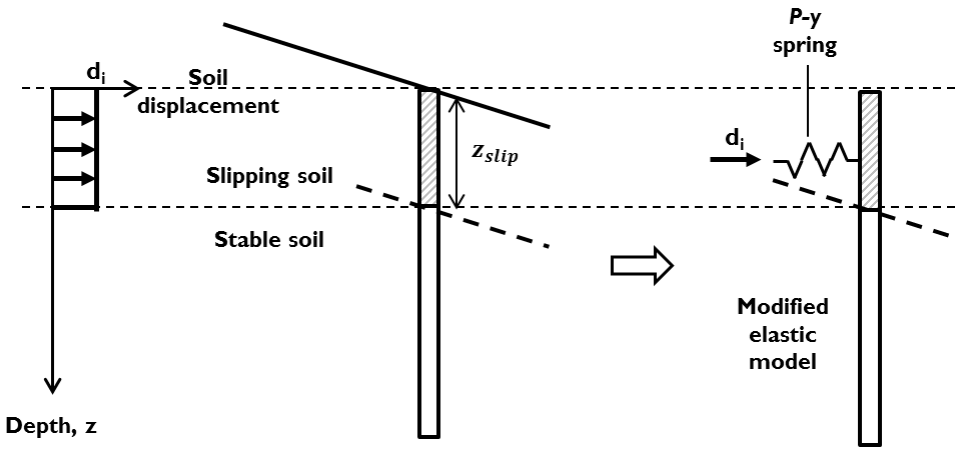

Figure (7- 2): Modelling approach.

7.3.1 Soil-pile interaction in slipping soil

p-y curves are popular for describing the non-linear relationship between soil resistance and relative soil-pile deformation. O'Neill and Murchison (1983) developed a procedure which was subsequently adopted by the American Petroleum Institute (API) to determine the load-deflection relationship (*P-y* curve) in sands. This method will be used herein within the slipping soil. The P-y curve in this procedure uses an hyperbolic tangent function to represent the non-linearity in the response. Three main coefficients are used, namely C_1 and C_2, which can be calculated as a function of the angle of internal friction (API recommended practice, 2000), and the initial subgrade reaction (k) which can also be determined as a function of the angle of friction (i.e. Figure 7-3). This relationship is written as:

$$P = Ap_u \tanh\left[\frac{kz}{Ap_u}\left(d_i - y_p\right)\right] z_{slip} \tag{7-7}$$

where P is the total soil resistance over the length of the pile within the slipping soil mass (i.e. of length z_{slip}), p_u is the ultimate soil resistance (see below) at soil yield, d_i is the soil slip, y_p is the lateral pile displacement at the location of the P-y curve, k is the initial modulus of subgrade reaction, z is the thickness of the slipping soil mass and A is a factor to account for cyclic loading. For cyclic loading, A = 0.9; A = 1.0 for monotonic loading. The ultimate capacity, p_u, is calculated as:

$$p_u = (C_1 z + C_2 D_{eq})\gamma' z \tag{7-8}$$

D_{eq} is the equivalent pile diameter (assumed to be equal to the square pile width here, i.e. $D_{eq} = B$) and γ' is the effective unit weight of the soil.

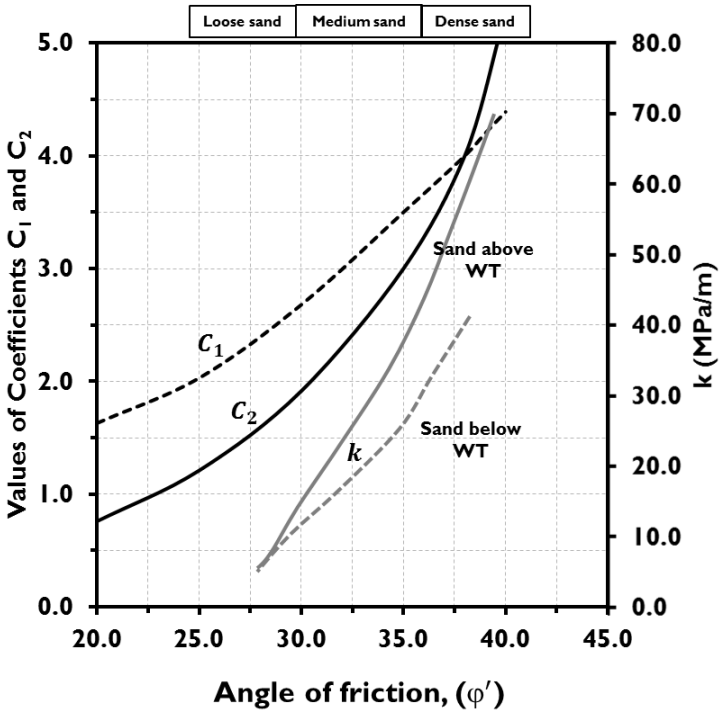

Figure (7- 3): API P-y coefficients as function of φ'.

7.3.2 Soil-pile interaction instable soil

In the stable soil, the soil is assumed to remain elastic, with the relationship between applied load (P) and pile displacement presented by Randolph (1981). Its implementation is shown schematically in Figure (7-4). Use of this method assumes that the resultant horizontal force on the pile from the slipping soil (i.e. *P-y* spring force) acts at a depth of $0.67z_{slip}$ below the top of the pile, meaning that the pile length within the stable soil is treated as a partially embedded pile acted upon by a resultant horizontal force (= $P\cos\beta$) and moment (= $P\cos\beta \times 0.33z_{slip}$) acting at the level of the shear plane. This method can account for (linear) variation of soil shear modulus with depth, and pile sections of any *EI* (through use of an equivalent elastic circular pile of Young's Modulus E_p). The resulting relationship between P and y_p is given by:

$$P = \frac{\rho_c G_c L_c}{\cos\beta\left(\frac{E_p}{G_c}\right)^{\frac{1}{7}}\left[0.54 + 0.40\frac{z_{slip}}{L_c}\right]} y_p \tag{7-9}$$

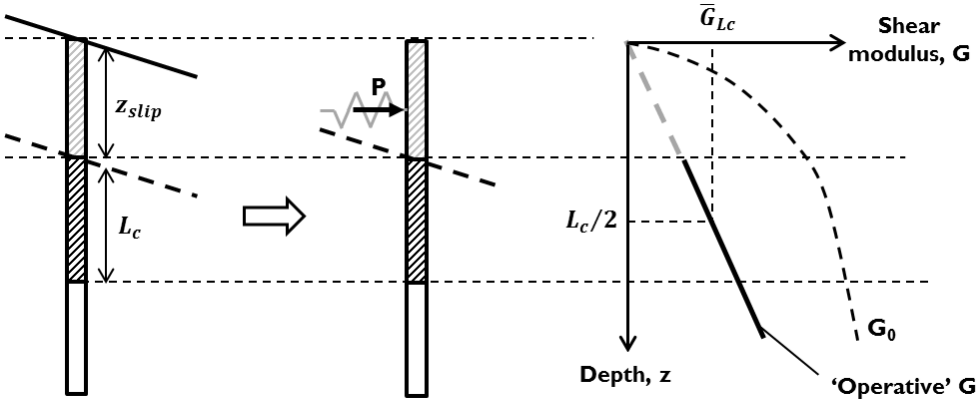

Figure (7- 4): Definition of parameters used in model for stable soil

where:

$$E_p = \frac{64(EI)_{pile}}{\pi D_{eq}^4} \tag{7-10}$$

$$L_c = D_{eq}\left(\frac{E_p}{G_c}\right)^{\frac{2}{7}} \tag{7-11}$$

$$G_c = \bar{G}_{Lc}(1 + 0.75\nu) \tag{7-12}$$

$$\rho_c = \frac{G(z = zslip + L_c/4)}{\bar{G}_{Lc}} \tag{7-13}$$

The parameter $\bar{G}_{Lc}$ is the median value of the operative shear modulus over the critical length, i.e. the value of G at a depth of $L_c/2$, and ρ_c is an homogeneity factor describing the variation of G with depth. The key modification made to this existing model in this thesis is that the 'operative' shear modulus is assumed to be the value of '*G'* as reduced to account for the effects of cyclic shearing. The analytical determination of this *G*-depth relationship is presented in Section 7.3.4. To use

Equations (7-11) – (7-13) some iteration is required due to the inter-relationships between L_c and G_c. In practice an initial value of L_c is assumed and used to determine G_c. This value of G_c is then used in Equation (7-11) to calculate an improved estimate of L_c. The procedure is then repeated until the values of G_c and L_c are consistent with each other.

7.3.3 Combined SPI model and spacing effects (pile 'shadowing')

For use in the Newmark method, i.e. for determining the instantaneous value of P in Equation (7-3) or (7-4), a direct relationship between P and slope slip d_i is desirable, so that the slip computed from the previous Newmark step can be used to obtain the current pile resistance force. This can be achieved by substitution of Equation (7-9) into Equation (7-7) for the unknown pile displacement y_p. The resulting closed-form expression can then be used to evaluate P over a fine grid of d_i values. This will give a unique curve defining the soil-pile interaction for a single pile.

When using piles in a closely spaced pile row, the zones of soil into which the piles displace relative to the soil may overlap, resulting in a reduction in the resistive force (P) available due to 'shadowing'. This is accounted for in the present analysis by applying the p-multiplier concept, i.e. by reducing the values of P in the SPI model by a factor between 0 – 1 which is dependent on the pile spacing. A number of authors have investigated p-multipliers for piles in cohesionless soils and their results are summarised in Figure (7-5). An approximate relationship was derived from this data for use within the SPI model:

$$p_m = \begin{cases} 0.235\dfrac{s}{B} - 0.168 & \dfrac{s}{B} \le 5.0 \\ 1.0 & \dfrac{s}{B} \ge 5.0 \end{cases} \qquad (7\text{-}14)$$

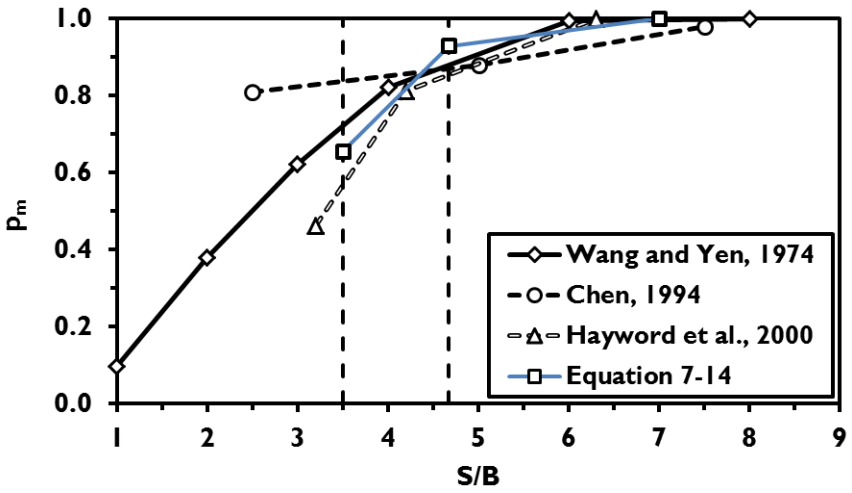

Figure (7- 5): Relationship between p-multiplier and pile spacing.

According to this concept, the measured single pile resistance from the p-y curve using API method has been modified to what it should be, based on the spacing ratio, i.e. $P = p_m \times P$(single pile).

7.3.4 Determination of operative shear modulus

In this chapter, a method of estimating the shear modulus within the stable soil is described and validated against data derived from the time-acceleration histories of the accelerometers from the centrifuge models at three main depths below the ground surface (see Brennan et al., 2006). Figure (7-6) shows time-shear stress, time-shear strain and a shear stress-shear strain cycle at peak cyclic shear strain from Test AA06. These were computed form the data of three vertical accelerometers; 6, 10 and 13 (see Figure 6-1 in chapter 6) which were located at the middle of the slope and along the centreline of the container (midway between the two central piles)

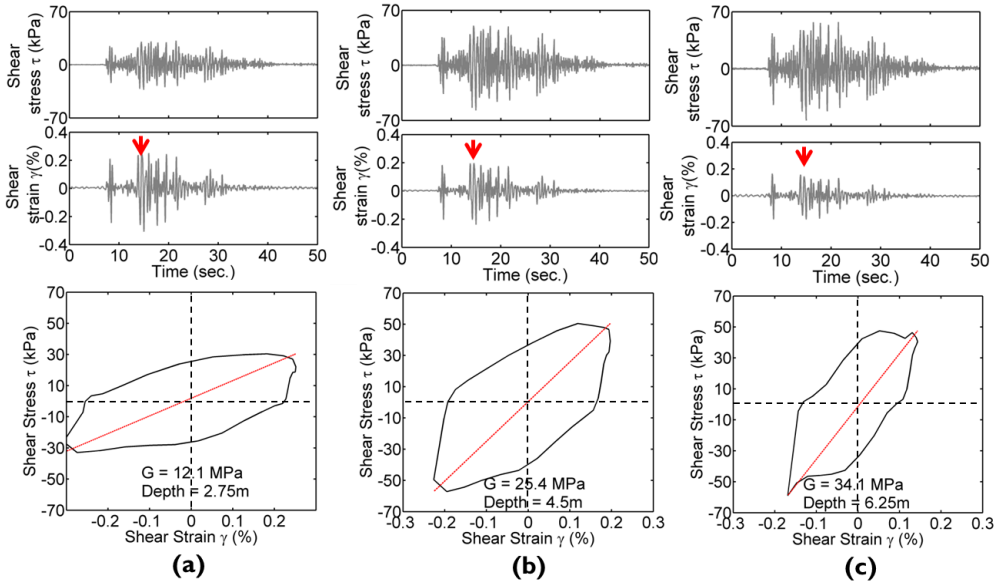

Figure (7- 6): Variation of the shear stress, shear strain and shear modulus: (a) at 2.75 m depth, (b) at 4.50 m depth, (c) at 6.25 m depth.

The 'operative' shear modulus used in the SPI is calculated based on initial shear modulus (G_o) for the soil before cyclic loading (from Hardin and Drnevich, 1972 – Equation 7-15) as well as the variation of cyclic shear stress ($\tau_{av.}$) and cyclic shear strain (γ) during the earthquake with depth using Equation (7-16).

$$G_o = 100.\left[\frac{(3-e)^2}{1+e}\right].\sqrt{\sigma_o'} \tag{7-15}$$

$$\frac{G}{G_o} = \frac{\tau_{av.}}{G_o.\gamma(\%)} \tag{7-16}$$

The representative cyclic shear stress is estimated using the equation proposed by Seed and Idriss, (1971). They assumed that the equivalent average cyclic shear stress caused by earthquake is approximately 0.65 from the maximum induced stress:

$$\tau_{av.} = 0.65.(\frac{a_{\max}}{g}).\sigma_{v_o}.r_d \tag{7-17}$$

where a_{max} is the peak ground acceleration at the soil surface, g is the acceleration due to gravity, σ_{v0} is the total overburden stresses, and r_d is a stress reduction coefficient which was calculated using the equation proposed by Idriss (1999).

$$r_d = e^{(\alpha(z)+\beta(z).M)} \tag{7-18}$$

where M is the earthquake magnitude and:

$$\alpha = -1.012 - (1.126.\sin(\frac{z}{11.73} + 5.133) \tag{7-19}$$

$$\beta = 0.106 + 0.118.\sin(\frac{z}{11.28} + 5.142) \tag{7-20}$$

where z is the depth below ground surface in meters.

The cyclic shear strain (γ) is estimated using Equation (7-21) as proposed by Pradel (1998):

$$\gamma(\%) = \left\{\frac{1 + a.e^{(b.\tau_{av.}/G_o)}}{1+a}\right\}.\frac{\tau_{av.}}{G_o}.100 \tag{7-21}$$

where

$$a = 0.0389.(\frac{\sigma_o^{'}}{P_a}) + 0.124 \tag{7-22}$$

$$b = 6400.(\frac{\sigma_o^{'}}{P_a})^{-0.6} \tag{7-23}$$

and $\sigma_o^{'}$ is the average stress and P_a is the atmospheric pressure (100 kPa)

$$\sigma_o^{'} = \sigma_v^{'}.(\frac{1+2K_0}{3}) \tag{7-24}$$

In Equation (7-24), K_o is the coefficient of lateral earthquake pressure ($1-\sin\varphi'$), and σ_v' is the vertical effective stress.

Figure (7-7) shows the variation of initial shear modulus (G_o), operative shear modulus (G) calculated using Equation (7-16) and the measured shear modulus from the centrifuge test data, from Figure (7-6). Some differences are observed between the operative and measured shear moduli, but the approximate procedure given above appears to give a rational basis for making a reasonable estimation of the operative shear modulus for analysis.

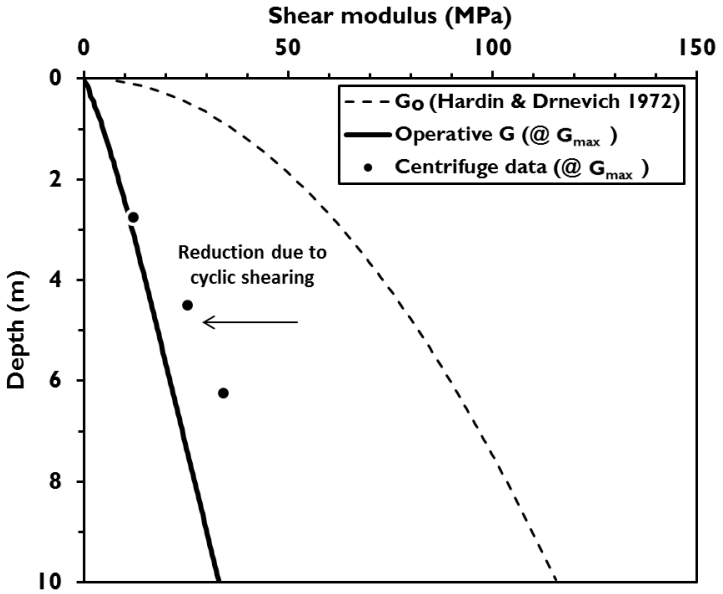

Figure (7- 7): Actual and average shear modulus.

7.3.5 Final SPI model for parameters used in the centrifuge tests

Figure (7-8) shows the P-d_i curves for pile resistance, using soil properties for the centrifuge tests. The curves are identical for S/B = 14.0 and S/B = 7.0, and are reduced in magnitude at S/B = 4.7 and 3.5 in line with Equation (7-14). It can be seen how such a curve can be used to determine the pile resistance for a given amount of soil slip within the Newmark method described in Section 7.2. It is also clear that once the soil has slipped by more than 10 mm, the pile resistance will reach a maximum. Expressing this in terms of the pile size, 0.015B, this displacement is consistent with the lower limit of previous findings by Pan et al. (2002) and Bransby

et al. (1999) which suggest that the ultimate pile resistance is mobilised within the range 0.015*D* to 0.025*D*, where *D* is the diameter of a circular pile.

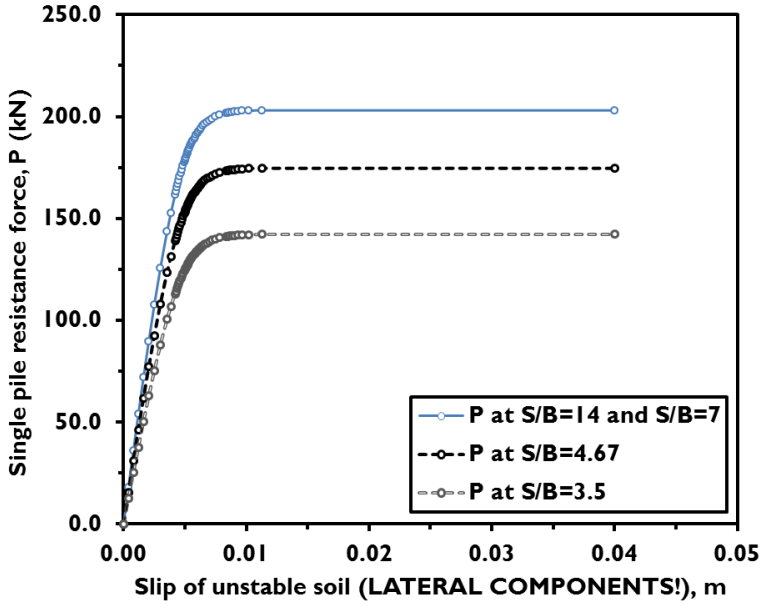

Figure (7- 8): Calculated SPI curves for centrifuge test conditions.

7.3.6 Determination of bending moment profile in piles

Once the Newmark analysis has been conducted, the variation of *P* with time will have been determined as an integral part of the analysis. Once the instantaneous load is known, it is relatively simple to determine the bending moments within the pile as they are proportional to *P* while the pile remains elastic (ideal design). Randolph (1981), as cited in Fleming et al. (2009), present normalised bending moment profiles for the pile (which apply below the slip plane in this case) for the cases of moment-only loading and shear-only loading. If the pile remains elastic, the principal of superposition can be used to account for the shear force (= $P\cos\beta$) and moment (= $P\cos\beta \times 0.33z_{slip}$) acting at the location of the slip plane depth. Above the slip plane (i.e. within the slipping soil) the bending moments are assumed to reduce linearly to zero at the ground surface (consistent with the lateral bearing capacity of the soil increasing linearly with the depth and all of the soil within this zone being at yield).

Normalised moment curves (M/PL_c) have been created as a function of normalised depth below the slip plane $\left(z - z_{slip}\right)/L_c$ and these are shown in Figure (7-9) for ρ_c =

1.0 (homogeneity factor for the centrifuge test conditions, i.e. for G increasing linearly with depth, see Figure 7-7).

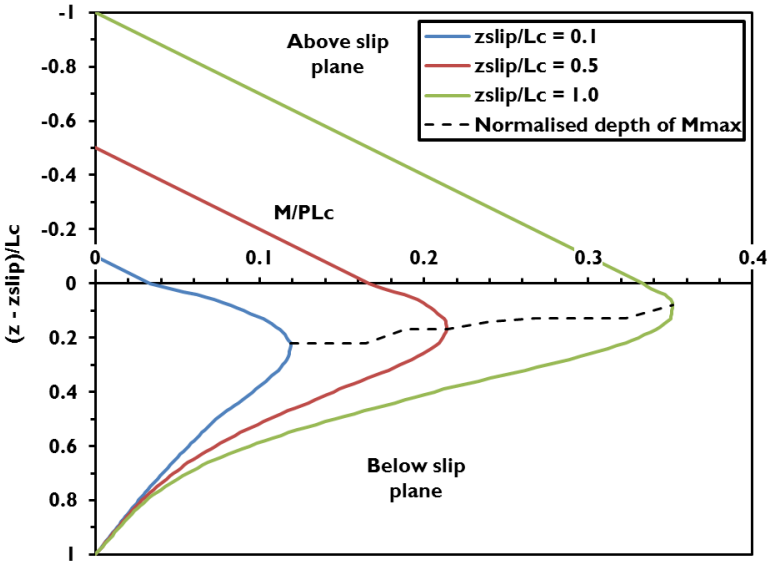

Figure (7- 9): Generalised bending moment curves for piles resisting an infinite slip.

7.4 Validation of Newmark method against centrifuge data

7.4.1 Analysis procedure

To use the Newmark method developed in the previous sections, it is necessary to know the sip plane depth, z_{slip} in order to determine the soil slip as a function of time and the corresponding bending moment distributions. In the centrifuge tests z_{slip} was not known. However, both crest settlement (which is directly linked to soil slip as described in Chapter 4) and bending moment were measured in the piles, so z_{slip} could be determined by trial and error as the value giving a good match simultaneously to both the crest settlements and maximum bending moment. The SPI curves shown in Figure (7-8) were used for these analyses.

Figure (7-10) shows the effect of pile resistance and geometric re-grading (change in β) on the yield acceleration compared to an unreinforced slope using the first earthquake (EQ1) of test AA15 as an example. Only the positive (downslope) accelerations have been shown for clarity. It can be seen how the yield acceleration is strongly influenced by the pile resistance when the ground motion exceeds the yield acceleration based on the critical strength. Motion of the slope also causes re-grading

(geometric hardening) and the yield acceleration can subsequently be seen to increase non-linearly throughout the remainder of the earthquake, leading to reduced slip velocities (and hence reduced permanent slip) compared to the case with no geometric hardening (Al-defae et al., 2013 and Chapter 4). It is also noticeable that the geometric hardening effect is less pronounced when the slope is reinforced by piles, presumably as the amount of slip has been reduced as a result of adding the reinforcement.

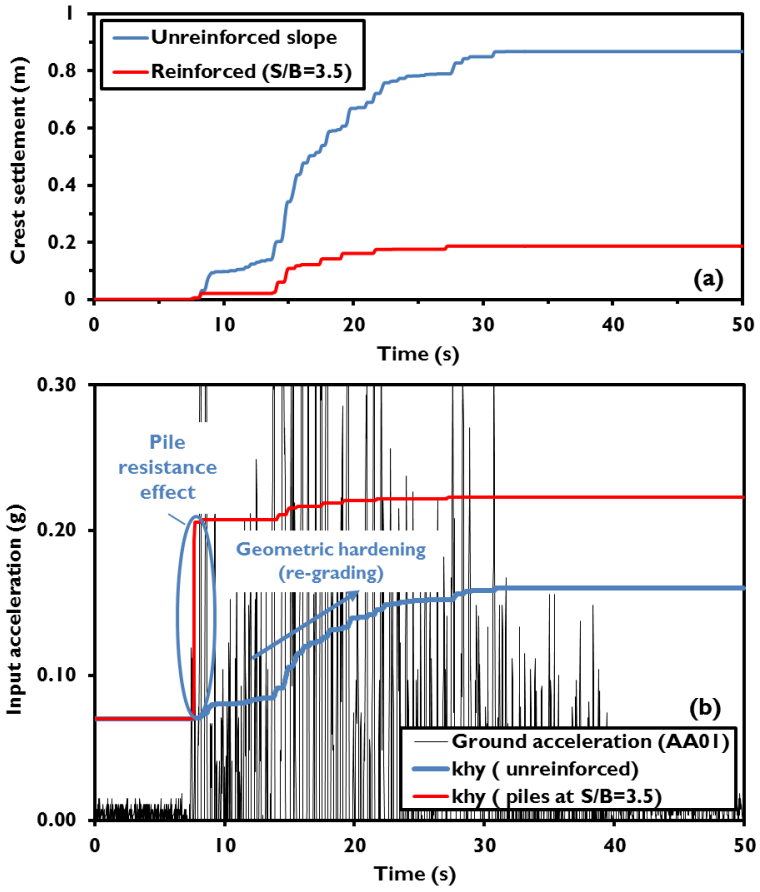

Figure (7- 10): Effect of pile resistance and geometric hardening on slope behaviour; (a) time-crest settlement; (b) time-yield acceleration

Four pile spacing ratios are considered in this section, representing those tested using the elastic instrumented piles in the centrifuge which were reported in Chapter 6. According to previous studies, there is no effectiveness for pile spacing larger than 5*D* (here 5*B*) to prevent the slipping soil due to the inability of the stresses to arch between adjacent piles (i.e. Hayward, 2000; Wang and Chen, 1974 and Kourkoulis,

2011). Thus, the results in this section are classified into two groups; the first group is referred to as 'non-effective pile spacing' (*S/B* = 7 and 14) where little if any effect of the piles is expected, while the second is referred to as 'effective pile spacing' (*S/B* = 3.5 and 4.67) where significant reduction is expected. Results for both permanent deformation (settlement at the crest of the slope) after the earthquake and aftershocks and the calculated peak bending moment in the pile (at the end of the earthquake) for both two groups were compared with the measured data from the centrifuge tests to investigate suitability of the modified Newmark procedure for piled slopes

7.4.2 'Non-effective pile spacing' results

The two larger values of pile spacing (i.e. *S/B*=14 which represented a model slope stabilised by 2 piles and *S/B*=7 which represented a model slope stabilised by 4 piles) are considered in this section. The input motion which was used in these Newmark analyses are the time-acceleration histories for accelerometer No. 8 (see Figure 6-1), as utilised in Chapter 4 for the unreinforced slopes. For the maximum pile spacing ratio (*S/B*=14), the measured bending moment at the end of EQ1 (from test AA12) is well predicted by using z_{slip} = 1.5 m. The slope was known to have displaced by more than 10 mm by the end of EQ1, so it is appropriate that the peak bending moment in the pile has reached the maximum value. The peak bending moment is compared to the centrifuge measurements in Figure (7-11). It can be observed from Figure (7-11) that the predicted bending moment increased sharply to the peak value compared to the measured moment. This can be attributed to the very stiff behaviour of the SPI curve (from the underlying *P-y* curve) shown in Figure (7-8).

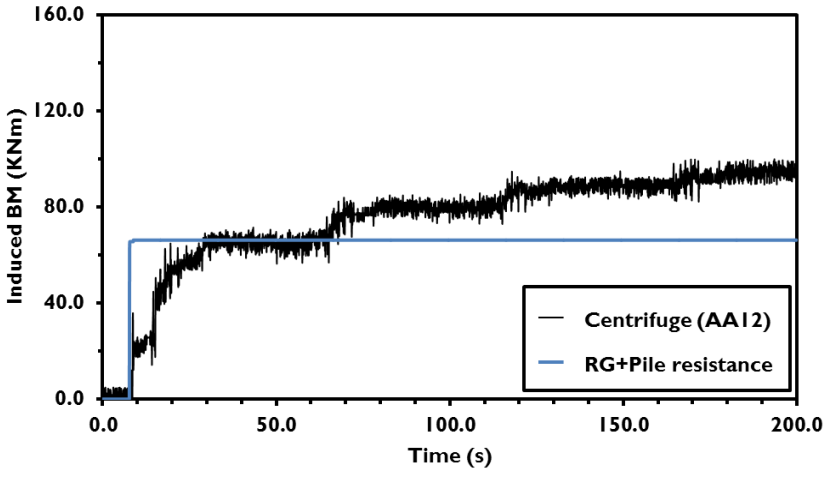

Figure (7- 11): Predicted and measured peak bending moment (*S/B*=14)

The predicted settlement at the crest was approximately 110% of the measured settlement from the centrifuge at the end of the first earthquake (Figure 7-12) while it was increased to 140% at the end of all aftershocks. This is not surprising considering the results of the unreinforced slope from Chapter 4 where the settlement was over-predicted by approximately 135% from the measured settlement after EQ1 and 150% at the end of all aftershocks. It can also be seen that the pile resistance gives only a small improvement of yield acceleration from the unreinforced case (k_{hy} = 0.07g) increasing to 0.09g at the onset of maximum pile resistance. The effect of the piles on the slope response for such a large spacing is clearly minimal.

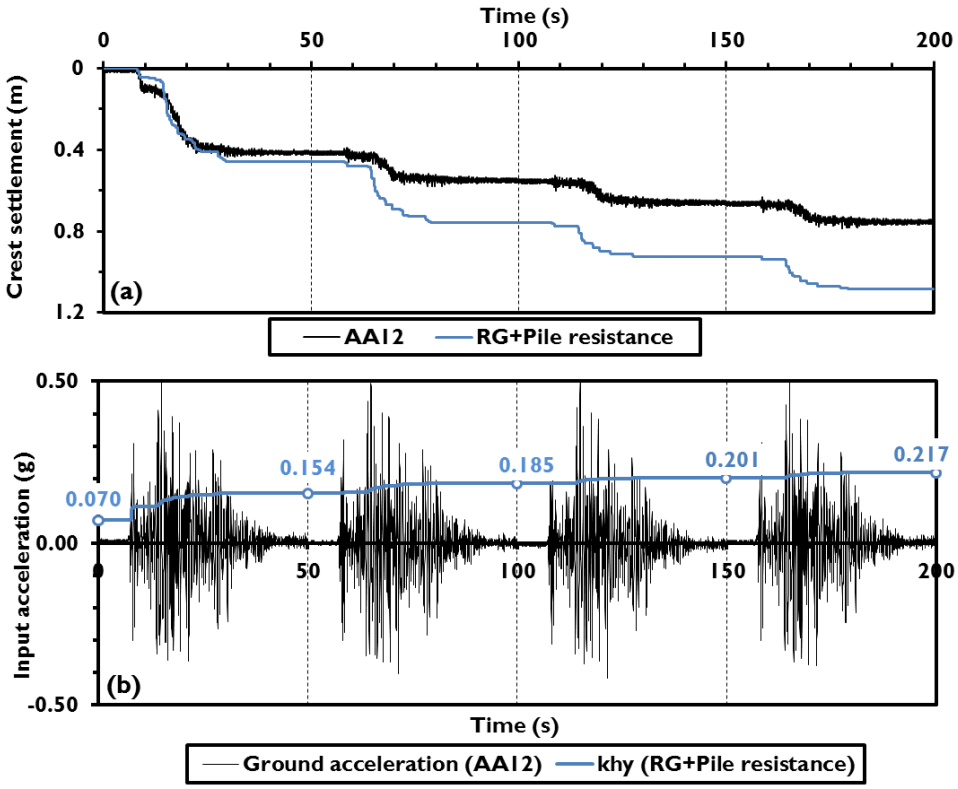

Figure (7- 12): Validation for test AA12 (*S/B* = 14): (a) Predicted and measured crest settlement; (b) variation of yield acceleration.

Decreasing the pile spacing ratio to 7, the measured peak bending moment at the end of EQ1 from the centrifuge model (i.e. test AA13) was predicted at z_{slip} = 1.75m. At the end of EQ4 the predicted moment was approximately 81% from the measured moment at the end of the fourth earthquake (Figure 7-13).

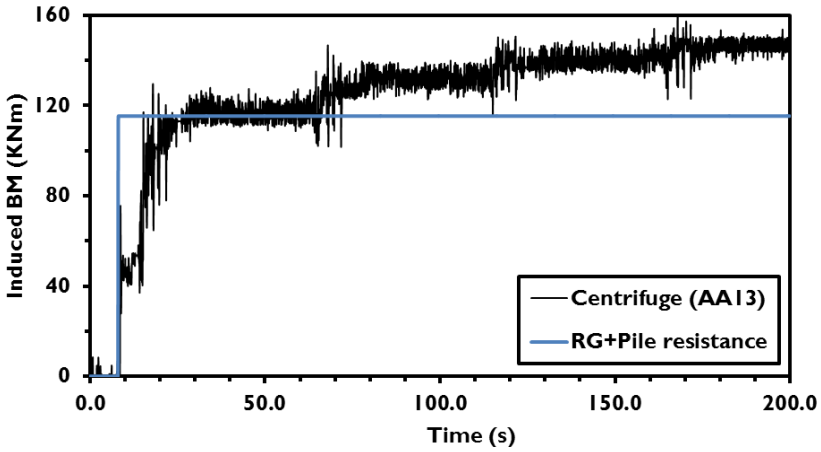

Figure (7- 13): Predicted and measured peak bending moment (*S/B*=7)

The settlement at the crest in this case was under-predicted at approximately 70% of the measured settlement from the centrifuge model at the end of EQ1 and reached approximately 95% at the end of all aftershocks (Figure 7-14).

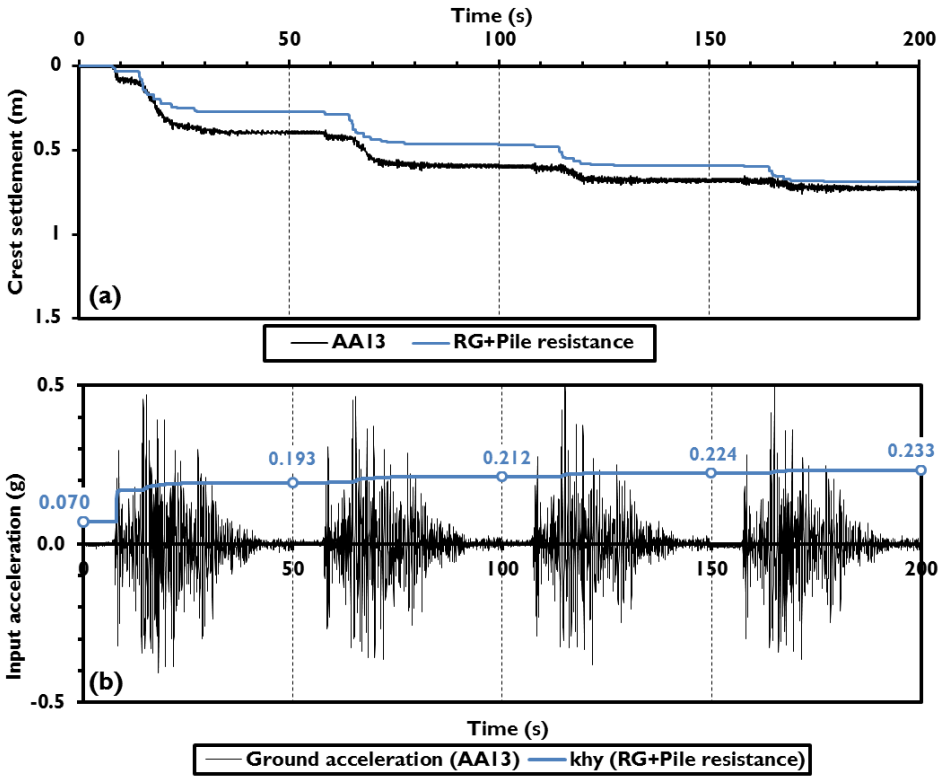

Figure (7- 14): Validation for test AA13 (*S/B* = 7): (a) Predicted and measured crest settlement; (b) variation of yield acceleration.

Under-prediction of settlement was also observed at the end of the second and third earthquakes. The improvement of the yield acceleration is more significant in this case due to larger potential pile resistance per metre length of the slope. The yield acceleration was increased from 0.07g to 0.167g at the onset of maximum pile resistance.

7.4.3 'Effective pile spacing' results

The other two pile spacing ratios considered in the centrifuge programme (*S/B* = 4.67 and 3.5) were less than 5*D* (*B* here), thus according to most of the previous studies, these pile spacing ratios were expected to be effective in improving the slope performance (i.e. reducing slip/settlement). For *S/B* = 4.67, the measured peak bending moment at the end of EQ1 from the centrifuge model (i.e. test AA14) was predicted from the Newmark procedure using z_{slip} = 1.77 m (Figure 7-15).

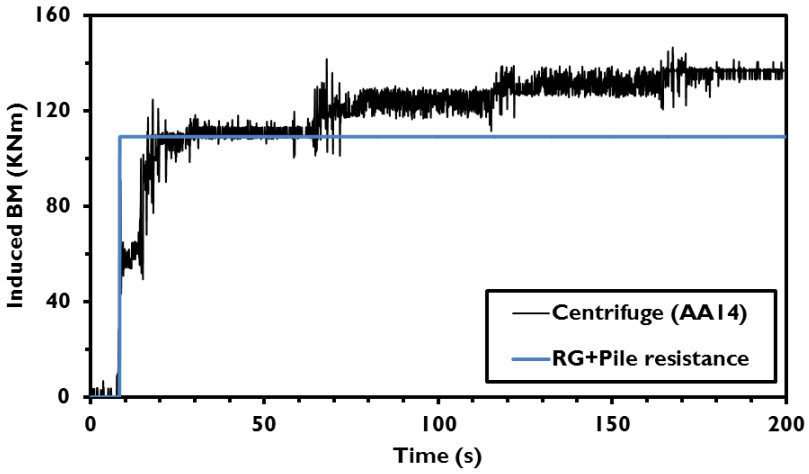

Figure (7- 15): Predicted and measured peak bending moment (S/B=4.67)

The computed crest settlement at the end of EQ1 associated with these bending moments was again under-predicted compared to the centrifuge test measurements (approximately 62% of measured), while it was more reasonable at the end of EQ4 (Approximately 91% of measured). Figure (7-16a) shows both predicted and measured crest settlement while Figure (7-16b) shows the yield acceleration variation against time.

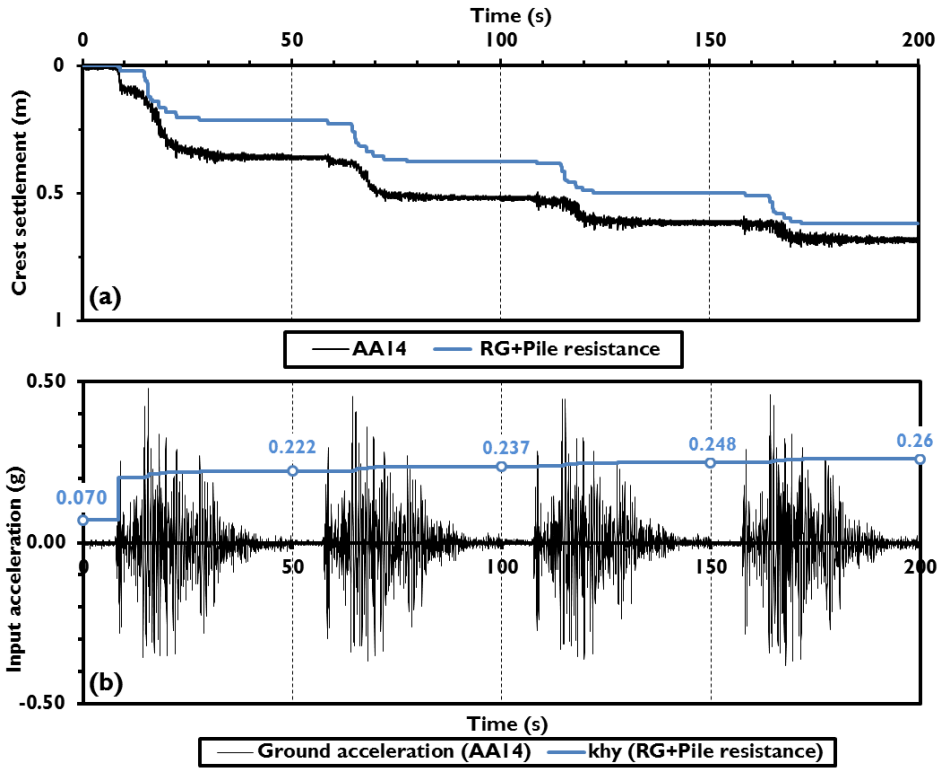

Figure (7- 16): Validation for test AA14 (S/B = 4.67): (a) Predicted and measured crest settlement; (b) variation of yield acceleration

The yield acceleration in this case was increased sharply from 0.07g to 0.203g when the peak pile resistance is first mobilised. Although the individual resistances of the piles are lower than for *S/B* = 7 due to the shadowing effect, the reduced spacing means there is still an increased overall resistance per metre length of the slope.

By decreasing the pile spacing ratio to the minimum studied value in this research, the measured peak bending moment at the end of EQ1 from centrifuge test AA15 were predicted by using z_{slip} = 1.7 m. This moment was 80% of that measured after EQ4 (Figure 7-17).

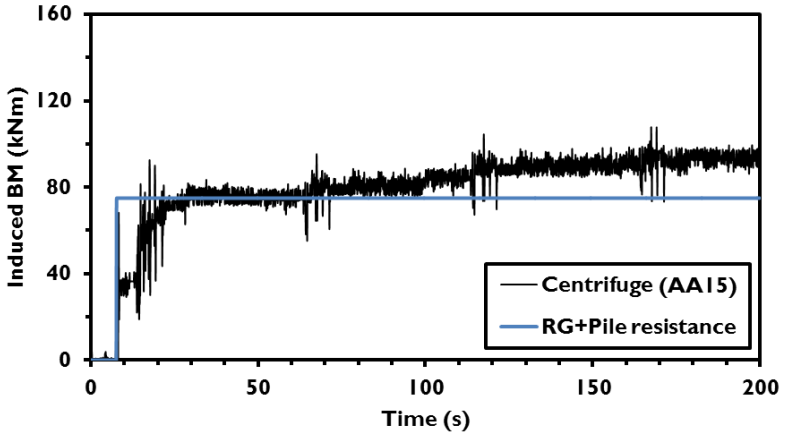

Figure (7- 17): Predicted and measured peak bending moment (*S/B*=3.5)

The computed crest settlement at this minimum pile spacing ratio (*S/B)* is compared to the measured crest settlement in Figure 7-18. The crest settlement was again initially under-predicted (approximately 60% compared to the measured crest settlement at the end of EQ1) but this improved during the subsequent earthquakes.

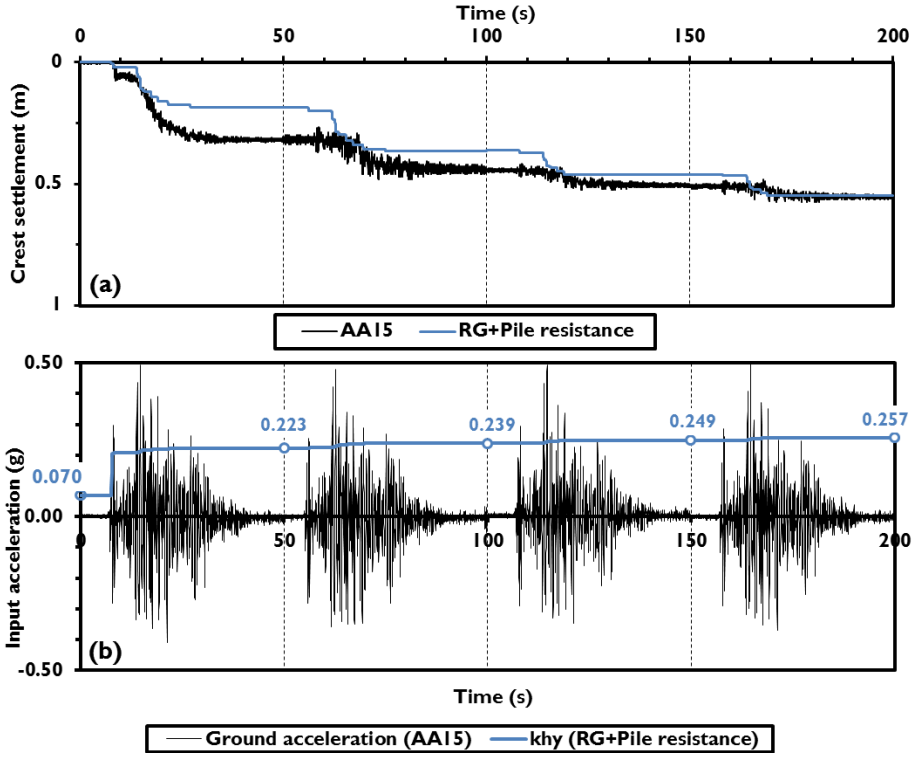

Figure (7- 18): Validation for test AA15 (*S/B* = 3.5): (a) Predicted and measured crest settlement; (b) variation of yield acceleration.

The yield acceleration was increased from 0.07g to 0.193g when the peak pile resistance is first mobilised (Figure 7-18b).

One further case considered was test AA16, where twelve time-acceleration records of the Kobe motion were applied to a model with *S/B* = 4.67. This is used here to investigate the Nemark procedure's validity under many aftershocks (twelve here), and also demonstrate that its predictive abilities are not limited to just the Chi-Chi motion. The same value of z_{slip} was used as in test AA14 (Chi-Chi motion at *S/B* = 4.67). Peak bending moment and settlement comparisons are shown in Figures (7-19) and (7-20), respectively.

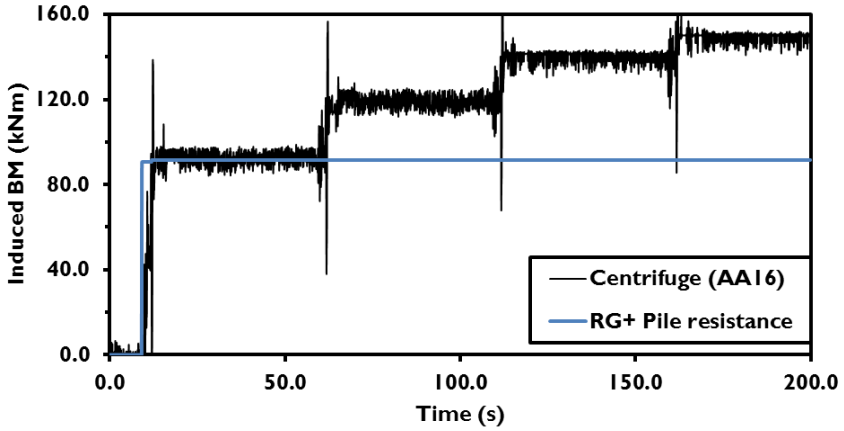

Figure (7- 19): Predicted and measured peak bending moment for Kobe model (*S/B*=4.67)

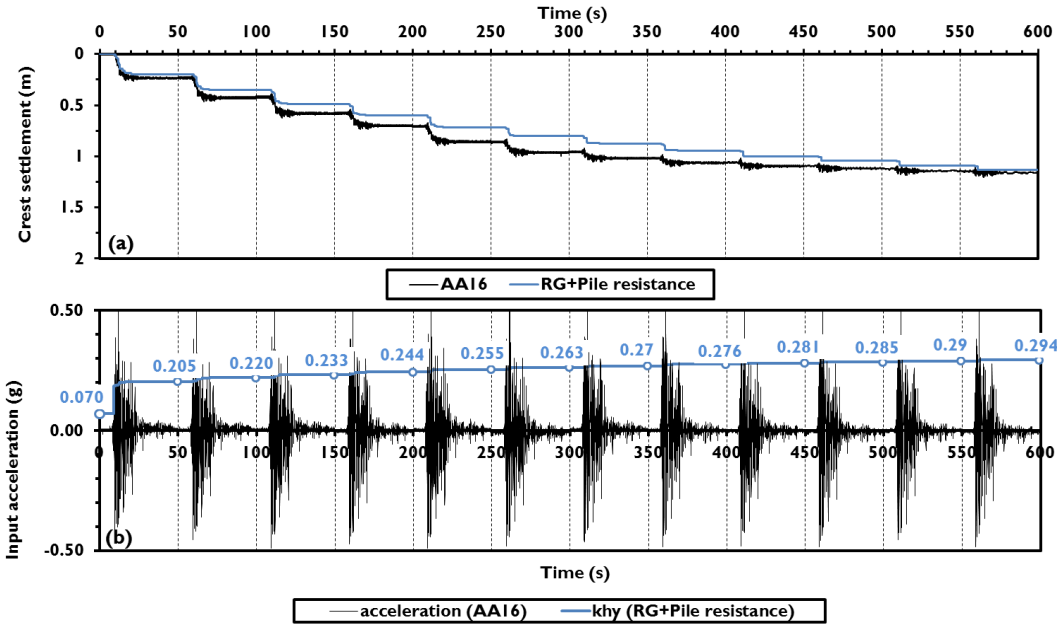

Figure (7- 20): Validation for test AA16 (S/B = 4.67): (a) Predicted and measured crest settlement; (b) variation of yield acceleration.

It can be seen from the computed bending moment for (AA16) that it was increased to more than (150%) at the end of EQ4 from that measured at the end of the EQ1. This

actually is contrasting with what was observed from all Chi-Chi- model described earlier. This attaributed to the input motion which has height spiky in very narrow range comparing with Chi-Chi earthquake.

7.4.4 Summary of model performance: crest settlement

Figure (7-21) shows both the predicted and measured accumulative and instantaneous (during a single earthquake) crest settlements for all four earthquakes and for all studied cases. It is clearly shown that the accumulative crest settlement for maximum pile spacing (*S/B*=14) is over predicted for all aftershocks and this difference between the measured and predicted values increases with further aftershocks and this was consistent with what was observed in the unreinforced case presented in chapter 4.

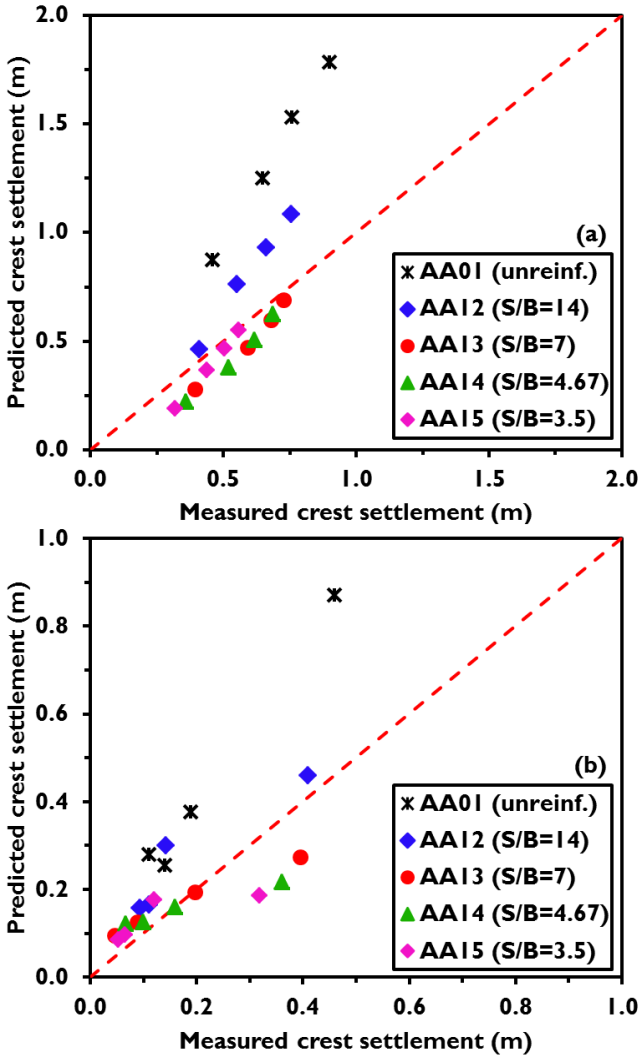

Figure (7- 21): Predicted and measured crest settlement: (a) accumulated and (b) instantaneous

The accumulated crest settlements at the end of each earthquake match reasonably well with the measured crest settlement for all cases (except *S/B*=14) especially after the end of all aftershocks (see figure 7-21 a). Figure (7-21 b) shows the instantaneous crest settlement after each earthquake. The validity of this modified procedure is shown from the crest settlement where decreasing of crest settlement after each aftershock is observed.

Figure (7-22 a) shows the accumulated crest settlement computed by the modified Newmatk's procedure for test AA12 (Kobe model) and test AA10 (Chi-Chi model). These tests have the same *S/B* ratio, but different input motions. The crest settlement is slightly under predicted for all aftershocks, but generally the match is very good and clearly applicable across different input motions and for a large amount of seismic input.

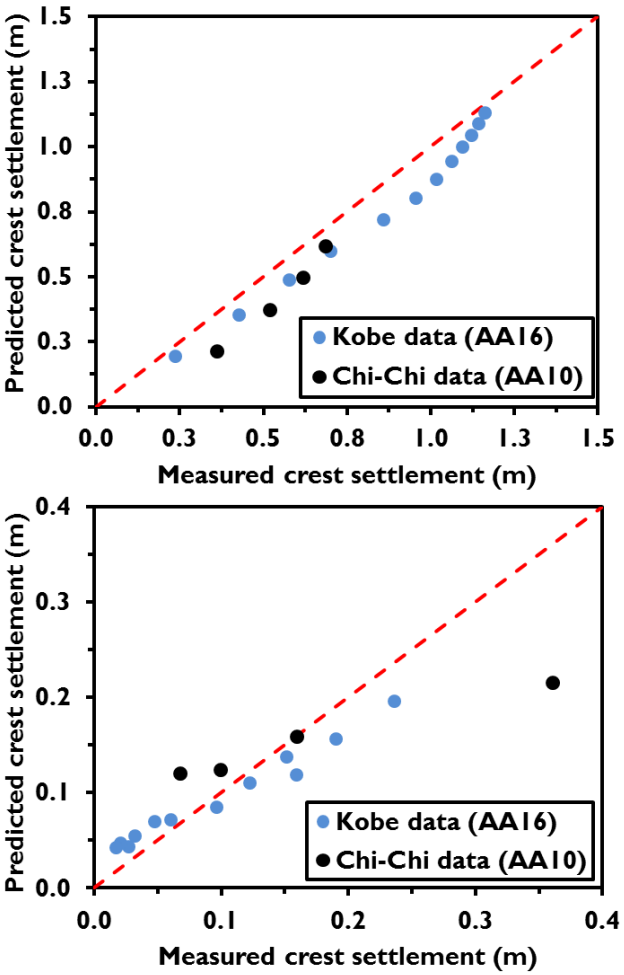

Figure (7- 22): predicted and measured crest settlement for AA10 and AA16 (S/B=4.67): (a) accumulated and (b) instantaneous

7.4.5 Summary of model performance: pile bending moments

As was explained in section 7.3.5, the bending moment along the pile has been calculated based on three main parameters: peak or mobilised pile resistance (P) at the end of the first earthquake, depth of the slip surface (z_{slip}) and critical length of the pile (L_c). Moment distributions along the piles have been determined using Figure (7-9) and compared to those measured in the centrifuge tests at the end of the first earthquake (see chapter 6). These are shown in Figure (7-23). It can be noticed that the magnitude of the peak bending moment, which occurs just below the slip plane, is slightly over-predicted and occurs at a shallower depth (predicted at 2 m depth, while it was measured from the centrifuge at 3.6 m depth).

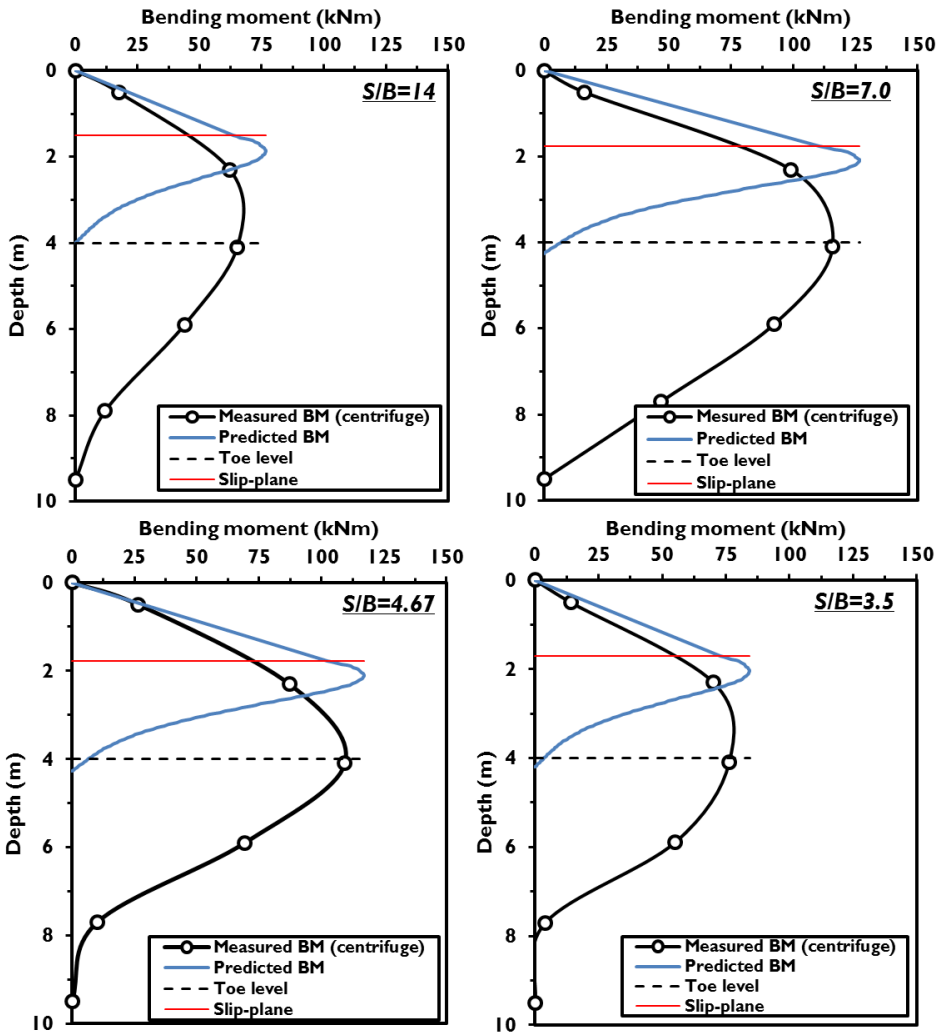

Figure (7- 23): Predicted and measured bending moments along piles, end of EQ1.

Figure (7-24) shows a comparison of the moment distributions from the Chi-Chi and Kobe models where both of them had the same pile spacing ration (*S/B* = 4.67). The same depth of the maximum moment was observed in both cases while the maximum moment magnitude predicted was slightly larger in the Kobe case.

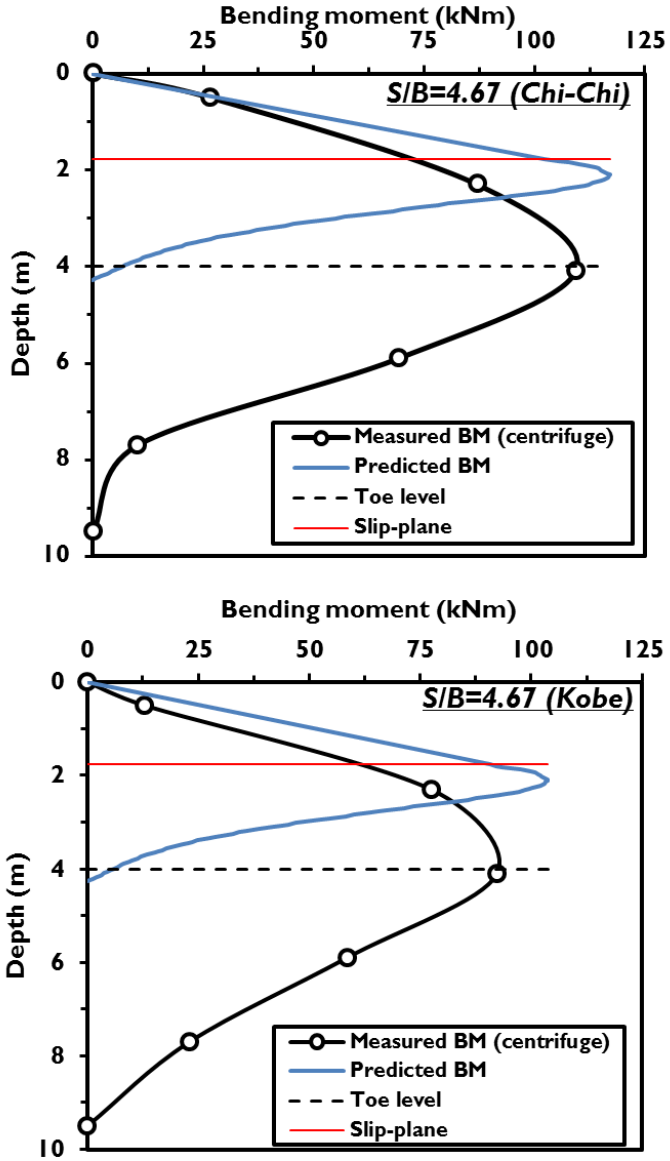

Figure (7- 24): moment distribution along pile for Chi-Chi and Kobe models (s/B = 4.67)

As shown from both Figures (7-23) and (7.24), the procedure gives a visualization about the magnitude of the maximum bending moment, but it does not give a good estimation of the moment distribution below the slip plane. This can be attributed to the effect of the critical length of the pile used in the calculation procedure. By modifying the normalised curve shown in Figure (7-9) to a new form (i.e. Figure 7-

25), by using three times the calculated critical length of the pile proposed by Randolph, 1981 both the depth of maximum bending moment and the moment distribution are well predicted. (see Figure 7-26).

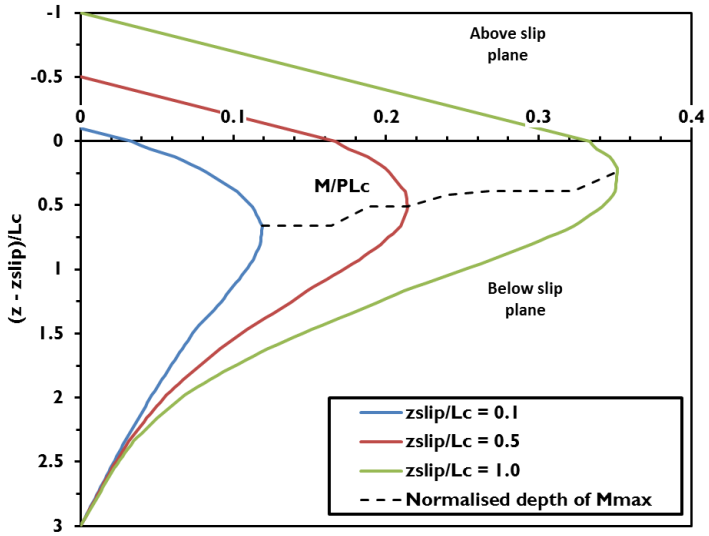

Figure (7- 25): Generalised bending moment curves for piles resisting an infinite slip

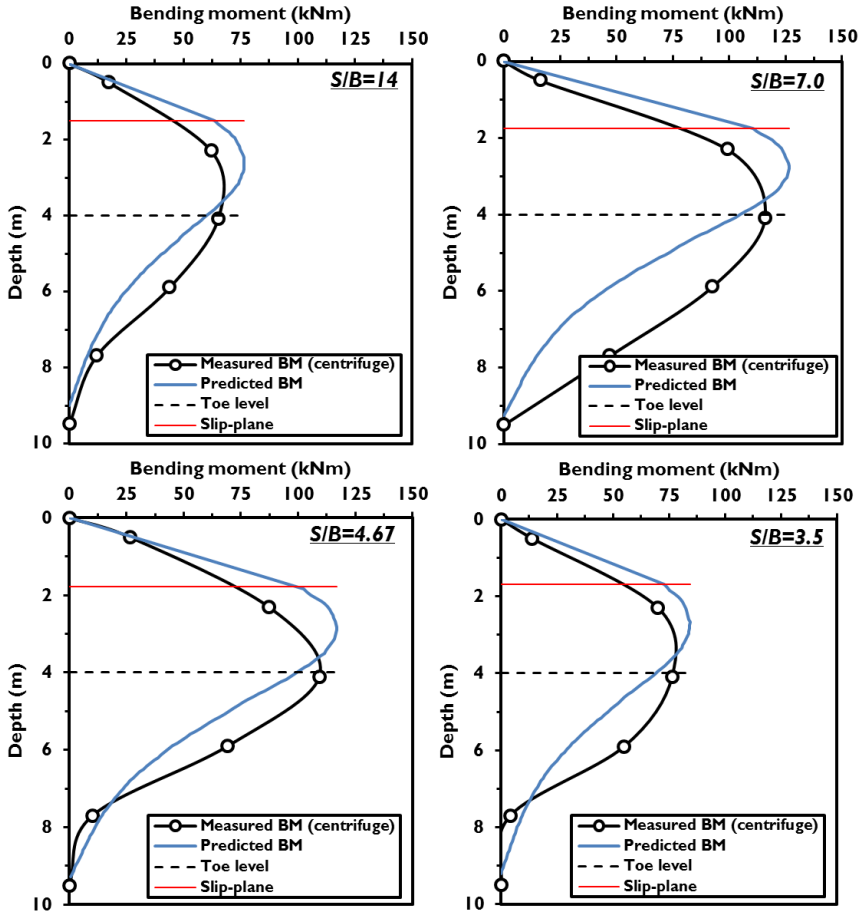

Figure (7- 26): Predicted and measured bending moments along piles, end of EQ1.

7.5 A priori determination of z_{slip}

In the forgoing validation in Section 7.4, the Newmark method was used to obtain (simultaneously) a good prediction of slope displacements and pile bending moments, allowing the empirical determination of z_{slip}. However, for practical use in design it would be more useful if an a priori determination of z_{slip} could be made. The Discontinuity Layout Optimisation (DLO) technique was therefore used to analyse the pile-reinforced slope system under pseudo-static seismic accelerations to investigate the shape of the seismic slip surface and the (initial) yield acceleration of the pile-slope system (Smith and Gilbert, 2007). As in Chapter 4, *LimitState:GEO, 2.0 software* was used to calculate the minimum upper-bound mechanism by DLO for the actual limited geometry of the centrifuge model of the unreinforced slope.

The piles were represented as 'engineered elements'. By using engineered elements, relative displacement between the soil and each node of this element is allowed, such that the soil can slip past the piles if energetically desirable. Three main parameters are required to define the properties of engineered elements: (i) lateral resistance per unit length per unit width to lateral displacement (N); (ii) pullout resistance per unit length per unit width, (T) and (iii) plastic moment resistance of the element per unit width. A linear variation with depth was assumed for both lateral resistance and pullout resistance:

$$T = T_c + T_q.\sigma'_v \tag{7-25}$$

$$N = N_c + N_q.\sigma'_v \tag{7-26}$$

The spacing ratio has been taken into account in the calculation of the parameters in Equations (7-25) and (7-26), so that they represent equivalent values per unit length of the slope. As the pile elements have their tops at the surface of the slope where both resistances are expected to be zero, thus $T_c = N_c = 0$. The depth-dependent parameters T_q and N_q are given by:

$$T_q = 4.B.(2K_o).\tan\delta \tag{7-27}$$

$$N_q = \frac{{K_p}^2}{s/B} \tag{7-28}$$

Where

B: Pile width

K_o : Earth pressure coefficient at rest condition = $1-\sin\varphi'$.

K_p : Passive earthquake pressure and be calculated using equation 7-29:

$$K_p = \frac{1}{K_a} \tag{7-29}$$

And

K_a is the active earthquake pressure and is calculated using equation 7-3:

$$K_a = \frac{1-\sin\varphi'}{1+\sin\varphi'} \tag{7-30}$$

δ : The interface angle between the soil and the pile calculated from direct shear box at critical state (see section 3-8 in chapter 3).

The variation of the angle of internal friction with depth (dilation suppression due to confining stress level) has also been taken into account in the representation of the soil model. Thus, the soil is divided into many 0.5 m thick layers over the top 8 m of soil such that each layer can be given a different angle of friction. Figure (7-27) shows how the angle of friction vary with depth (effective stress) based on the results from the direct shear box tests conducted in Chapter 3.

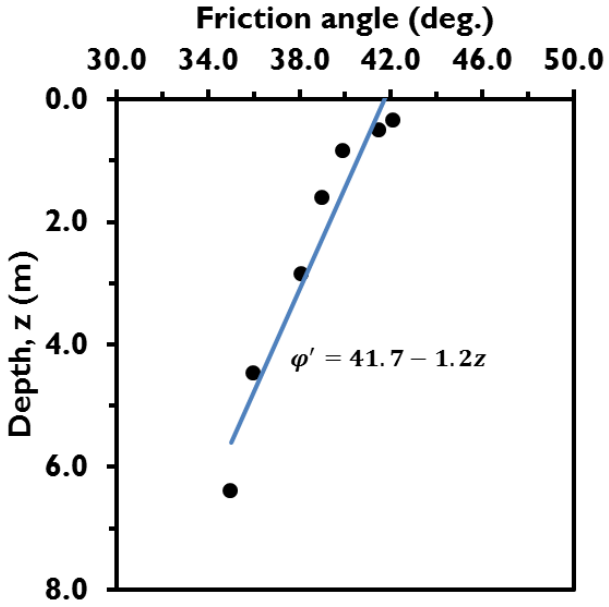

Figure (7- 27): Soil friction angle as a function of depth

The moment capacity of the RC model piles was used in determining the plastic moment resistance (M_p). This was divided by the pile spacing to represent the equivalent moment resistance per unit length of the slope.

Figure (7-28) shows the failure mechanism for the pile-reinforced cohesionless slope at different spacing ratios using the variation of the angle of the friction with depth. It can be seen that the failure mechanism is different from case to other. The slip surface is appearing along the whole slip surface and 'through' (past) the piles at *S/B* = 14. As the pile spacing reduces to *S/B* = 7.0, it is changed to two symmetric slip failures either side of the pile. With further reductions of *S/B* the critical mechanism involves only the soil upslope of the pile. These observations can be attributed to the flow of the soil through piles at larger pile spacing whereas the piles restrain the soil around them as they become closer together. The depth of the slip surface is observed to be approximately 1.5m below the surface in each case and this is broadly consistent with what was investigated from the modified Newmark's procedure (see Figure 7-29).

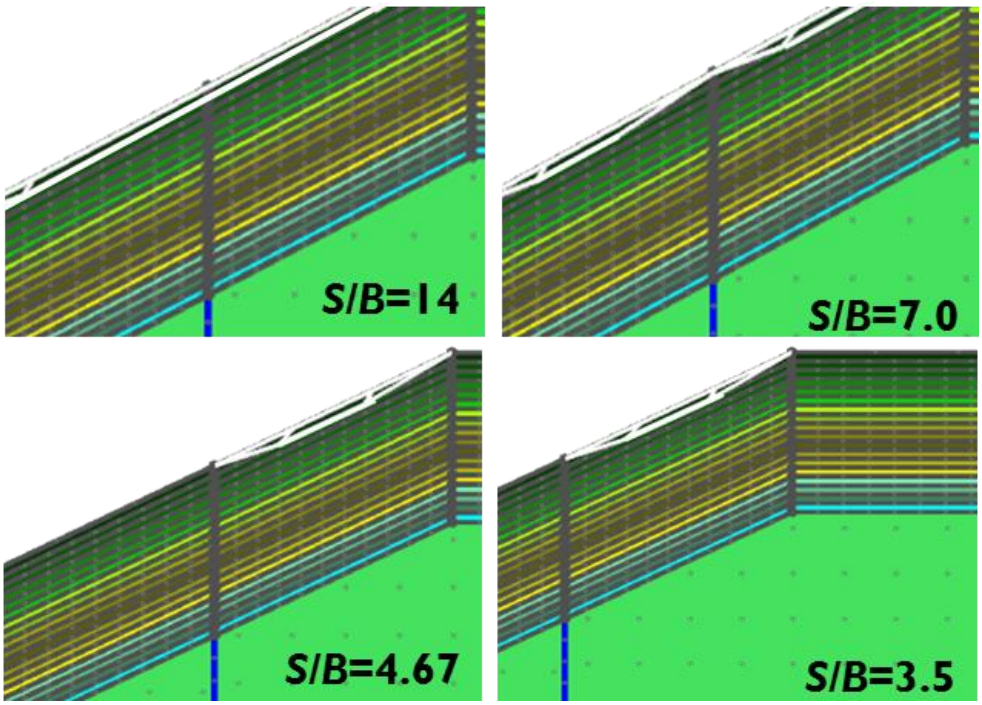

Figure (7- 28): Failure mechanisms for piled-slope computed from DLO for seismic case

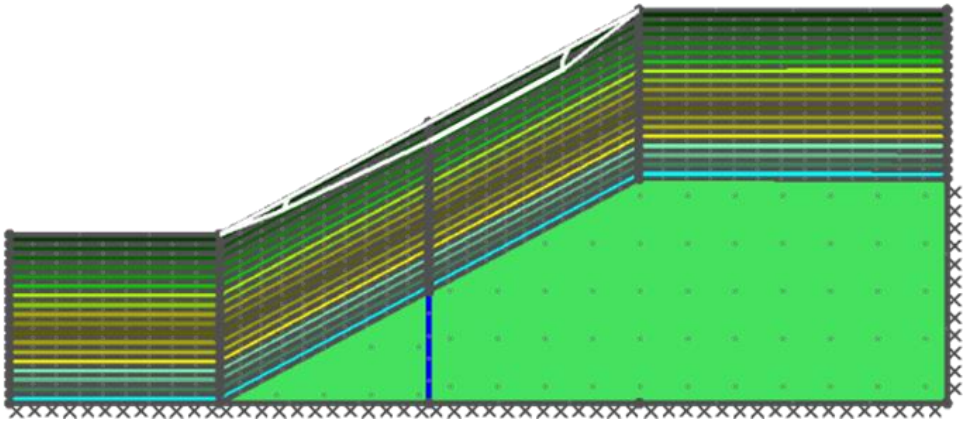

Figure (7- 29): Depth of slip surface

The yield accelerations in each case were also determined using DLO. Table (7-1) shows the static factor of safety and the yield acceleration for all cases. Compared to the Newmark-derived yield accelerations at the onset of full pile resistance, the DLO predictions are much higher and appear not to be significantly influenced by *S/B*. It should be noted however that the Newmark method is used to predict performance to large displacement, and hence critical state strength parameters were used. The DLO only finds the instantaneous slip mechanism assuming that the pile can mobilise its resistance with no relative slip (i.e. when soil properties are at peak). The use of critical state strength everywhere (i.e. both on the slip plane and in the SPI) is a simplification in the Newmark method and it is expected that the initial position of the slip plane will actually be controlled through soil-pile interaction when there is negligible relative soil-pile movement and the soil is at peak strength (i.e. as predicted from DLO). This slip plane is then thought to be maintained throughout further shearing during which (and for the majority of the earthquake) the soil parameters will have softened to critical state. Therefore, it is thought that the DLO analyses can be used to estimate the slip plane position, but that the yield acceleration should be calculated through the Newmark model where the effects of pile strength mobilisation and re-grading can be taken into account.

Table (7- 1): Static and dynamic slope stability data

s/B	*F* (DLO)	k_{hy} (DLO)	k_{hy} (Newmark)*	z_{slip} (DLO)	z_{slip} (Newmark)
Unreinf.	1.61	0.21g	0.07g	0.50 m	N/A
14	1.66	0.2599g	0.09g	1.50 m	1.50 m
7.0	1.66	0.2635g	0.167g	1.50 m	1.75 m
4.67	1.66	0.2635g	0.203g	1.50 m	1.77 m
3.5	1.66	0.2635g	0.193g	1.50 m	1.70 m

*Values at onset of maximum pile moment, including re-grading effect

7.6 Summary

The modified Newmark procedure which was developed in Chapter 4 for predicting slip in unreinforced cohesionless slopes has been modified in this chapter to be applicable to pile–reinforced cohesionless slopes. A summary of the key results and observations are given below:

1- The Newmark method gives reasonably good predictions of permanent seismic slope deformation at all pile spacing ratios, both in initial earthquakes and following many strong aftershocks and for different input motions.

2- The pile spacing ratio (*S/B*) played an important role in the deformation of the stabilised slope during earthquake loads. This was consistent with the observations from the centrifuge tests reported in Chapter 6.

3- The peak pile resistance was generally mobilised at very small amounts of seismic slip, and therefore within a very short time for the strong earthquakes considered. This can be attributed to the high stiffness of the P-y curve used in the slipping soil. Future developments to the Newmark method could consider alternative *P-y* formulations to improve this .

4- In contrast to the unreinforced slope, the depth of the slip surface played an important role in determining the magnitude of slope deformation and the response of (bending moments within) the stabilised pile, as the calculated peak pile resistance (limited by the slipping soil) is dependent on the slip depth.

5- The depth of the slip surface in unreinforced slopes was approximately 0.5m from Chapter 4. Application of the developed Newmark method for pile-reinforced slopes to prediction of the centrifuge test results from Chapter 6 suggested that the presence of the piles increased the slip depth to 1.5 m in case of $S/B = 14$ and between 1.7 – 1.77 m at closer spacing.

6- The DLO technique appears to give a reasonable a priori estimate of the slip plane depth in the case of pile-reinforced slopes which is required for the Newmark method. This must be done using peak strength parameters and accounting for the suppression of dilation (reduction in peak strength) with depth. However, yield accelerations should be determined using the Newmark formulation where strain dependency can be taken into account.

Chapter eight
Conclusions, remarks and recommendations for further research

8.1 Overview

In this thesis, nineteen successful dynamic centrifuge tests were reported and interpreted, considering unreinforced and pile-reinforced cohesionless slopes. This was supported by Finite Element modelling procedures for predicting unreinforced slope behaviour and new validated Newmark procedures for use in design.

All dynamic centrifuge tests were implemented using 1:50 scale models at 50- g level and accelerations, dynamic response and permanent deformations were measured. Two kinds of pile models were used to stabilise cohesionless slope in this study, RC pile models (made of cementations plaster mortar and reinforcing steel wire), which were damageable and elastic model piles (aluminium alloy) which were instrumented to measure induced seismic bending moments.

8.2 Improved Newmark procedure for unreinforced slopes

The dynamic centrifuge tests included in Chapter four were for unreinforced cohesionless slope. An analytical solution was developed to determine the seismic displacement (permanent settlement) of the slope and to investigate the effects of soil strength properties and how the yield acceleration of slopes changes with time during earthquakes and aftershocks. The following key conclusions have been drawn:

1- A fully strain-dependent formulation of the seismic yield acceleration of a granular slope has been developed, for use in a modified Newmark sliding-block procedure. Reduction in slope angle with slip/strain (re-grading or geometric hardening) has been incorporated alongside an existing strain-softening/hardening formulation. The new model allows for greatly-improved prediction of slope movement under multiple strong earthquakes as it implicitly contains the strain history (seismic memory) of the slope, and

therefore permits both the response of slopes under strong aftershocks, and the whole-life performance of a slope to be quantified.

2- The model has been validated against centrifuge test data for a dry cohesionless sandy slope under the action of both multiple sequential recorded ground motions from recent strong earthquakes, and under harmonic shaking. It has been demonstrated that the effects of geometric hardening are much more significant than those of strain hardening/softening in the soil when the ground motions are strong and there are many of them (as would be the case for real slopes over their design life).

3- Though predicted displacement (settlements) of the slope were over predicted compared to the centrifuge results, the new procedure gives better results than the previous state-of-the-art (just shear strain softening behaviour).

4- The sliding block model is useful in preliminary design due to the limited soil property data required and low computational effort compared to more complex models (e.g. Finite Elements).

8.3 Finite Element modelling of unreinforced slopes

A set of constitutive model parameters for an advanced non-linear model simulating HST95 sand has been used in chapter five within Plaxis 2D to predict the centrifuge test results. Simulations with this model were compared with an existing model (Brinkgreve et. al, 2010), validated against centrifuge data and compared to the new analytical solution described in Section 8.2. The key conclusions are outlined below:

1- The validated Finite Element model procedures give a more complete picture of seismic slope response. These procedures can be used to undertake detailed analyses on optimal slope designs, based on preliminary designs developed using the improved sliding-block procedure described above.

2- The elasto-plastic constitutive model required parameters which could be specified based only on relative density using existing correlations, or using routine laboratory tests to develop a soil-specific model.

3- The new procedures offer significant benefits for use in routine design. It was demonstrated that the use of soil-specific parameters gave far improved predictions, particularly of permanent settlement, compared to existing correlations, which over-predicted settlements, particularly in subsequent earthquakes (aftershocks). This highlights the value of performing adequate site investigation.

4- The FE models gave comparable predictions of permanent movements at the slope crest to those using the improved sliding block model developed in chapter four, capturing the decay in ground displacement (geometric hardening) observed in the centrifuge tests.

5- FEM is able to additionally quantify the dynamic performance of the soil and the ground deformation profile (angular distortion) at the crest. This would provide the necessary information to make a detailed study of the seismic hazard posed to infrastructure located at the slope crest, and would therefore be complimentary to the sliding block models, being useful in the later stages of detailed design.

6- It was observed that the FE models generally over-predicted the magnitude of dynamic ground motions in the slopes which was ascribed to difficulties in modelling shear wave interaction with the sloping ground surface. It has additionally been shown that Eurocode 8 recommendations for topographic amplification effects may not be period independent and may result in under-predictions of the dynamic response of supported infrastructure.

7- In developing the soil-specific model used in this study, a complete characterisation has been made for the HST95 sand used in physical modelling experiments at the University of Dundee over a wide range of relative density; the constitutive parameters so derived will be useful in numerically simulating future static and dynamic geotechnical problems.

8.4 Centrifuge modelling of pile-reinforced slopes

In Chapter six, the effect of a discretely spaced row of piles on seismic slope performance was evaluated by testing fourteen centrifuge models of pile-reinforced

slopes. The 1:2 dry sandy slope used in the unreinforced slopes was subject to same ground motions recorded in the 1999 Chi-Chi earthquake, with the pile type and pile spacing being varied between tests. Three different pile types were investigated, including a conventional 'elastic' model, a 'designed' model reinforced concrete (RC) section with a moment capacity larger than the seismically induced bending moments, and a 'weak' model RC section consisting of nominal longitudinal reinforcement, which was weaker than the induced moments. The tests described represent the first use of a novel technique of modelling reinforced concrete at very reduced scales (1:50) for the study of seismic soil-structure interaction problems within a geotechnical centrifuge. The following conclusions have been drawn:

1. As elastic piles are spaced more closely, they have increasingly significant effects in reducing settlement and angular distortion at the crest and in reducing the magnitude of dynamic ground motions at the crest. Existing recommendations for the maximum spacing of the piles to make use of arching effects appeared to correlate with optimal reinforcement of the slope observed in the tests, and it is suggested that these could be used in determining pile layouts. Reductions of up to 35% in permanent movements and 20% in accelerations were recorded at S/B = 3.5.
2. Tests on more realistic piles using model reinforced concrete demonstrated that even if the piles are designed with a sufficient moment capacity to remain elastic, non-linearity within the cyclic response and fatigue effects combine to reduce the beneficial effects of the soil-pile interaction, particularly as the induced moments become close to the residual capacity of the section. However, reductions of 30% in permanent movements and 15% in accelerations were still observed at the optimal spacing (S/B = 3.5).
3. From the induced bending moments measured in the elastic piles and the measured slope settlements it is shown that elastic soil-pile interaction is replicated accurately by the model RC piles, so long as the induced bending moments are below the moment capacity of the model RC section. It is therefore verified that the elastic behaviour of the model concrete translates to prototype scale.
4. It has been observed that realistic bending properties can be achieved in the model RC piles and that the SSI within the boundary value problem

considered is largely indistinguishable from one using purely elastic elements. This suggests that the model RC will be particularly useful in studying (dynamic) soil structure interaction problems, replicating correct pre-failure behaviour, but also being able to sustain damage at realistic loads (bending moment capacity) and show representative post-failure behaviour (ductility).

5. If the pile is not structurally detailed to resist the seismically induced bending moments, the piles will break, though the ductile yielding of the piles will still impart some additional resistance to the slope in subsequent strong shaking (e.g. aftershocks).

8.5 Improved Newmark procedure - pile-reinforced slopes

The improved Newmark procedure presented in Chapter 4 was modified in chapter 7 (without strain softening behaviour and by incorporating strain-dependent pile resistance) to allow prediction of permanent seismic deformation in piled slopes. Only slope hardening (re-grading) effects were taken into account in this extension to the model. It was investigated how piles and pile spacing affect slope deformation, depth of slip surface and induced moment. The main important findings are presented below:

1- The seismic permanent deformation of the slopes was strongly influenced by the mobilisation of the pile resistance due to relative soil-pile movement. The displacement was observed to reduce clearly with decrease in pile spacing.

2- The pile resistance mobilised its peak resistance within a very short time when the slope started to slip reaching the ultimate resistance at soil lateral displacement of approximately 0.025D (here B) and this was identical with what was observed by others (e.g. Bransby et al. 1999).

3- In contrast to the solution for unreinforced slopes presented in Chapter four, the depth of the slip surface played an important role in variation of both bending moment and the permanent deformation (seismic displacement) of the pile-reinforced slope.

4- The depth of the slip surface can be determined by DLO technique; this was approximately 1.5m below the ground surface for all pile spacing values

(except *S/B*=14). Very similar values were determined based on back-calculating the centrifuge test results using the analytical solution.

5- This solution, even if has not given a very good prediction of distribution of the bending moment along the pile (the critical length of the pile appeared to be longer than originally predicted), gives excellent results in terms of the seismic permanent deformations at the crest and the magnitude of the maximum bending moment within the piles.

6- The calculated displacements were over predicted at pile spacing *S/B=14* whereas they were under predicted as the pile spacing decreases. The best prediction was observed for the minimum pile spacing (i.e. *S/B*=3.5).

8.5 Suggestions for further research

Based on the conclusions given in Sections 8.2 – 8.4, the modified procedures developed in this thesis are recommended for use, particularly in the preliminary design stages. The suggested further research work is outlined below:

1. Further study is required including constructed infrastructure at and near the crest of the slope to investigate how this may influence the overall failure mechanisms, site effects and dynamic behaviour.

2. More FEM (e.g. using Plaxis 3D and the same constitutive model parameters presented in the 2D modelling in chapter four) could be used to model the pile reinforced slopes modelled in the centrifuge. This would provide a tool for detailed design to complement that developed for unreinforced slopes. It could then be used to investigate in further detail how pile spacing affects slope and pile performance during earthquake events.

3. Different positions of stabilising piles within the slope could be tested to understand what is the best position for piles to be installed to give optimal reinforcement (e.g. piles installed near the toe of the slope or near the crest of the slope). Both centrifuge and 3D finite element modelling are recommended.

4. Different soil types, slope angles and slope heights should be considered, particularly ground water flow and consequent pore pressure effects besides cases where failure may be rotational, more than translational.

5. The lateral forces acting on piles due to soil movements is recommended to be measured by using the earth pressure sensors (fixed along the upslope face of the pile) besides the instrumented piles to better understand the soil-pile interaction .

References

Al-Defae, A.H., Caucis, K. and Knappett, J.A. (2013). Aftershocks and the whole-life seismic performance of granular slopes. *Géotechnique*. 63(14):1230-1244.

Al-Defae, A.H. and Knappett, J.A. (2013). Centrifuge modelling of the seismic performance of pile-reinforced slopes. *Journal of Geotechnical and Geoenviornmental engineering, ASCE* (*accepeted*).

Al-Defae, A.H. and Knappett, J.A. (2011). Small-scale modelling of reinforced concrete piles. *Proceeding of conference of Iraqi cultural attaché for engineering sciences.*1-2/10/2011. UCL.London.UK.

Al-Defae, A.H. and Knappett, J.A. (2012). Seismic displacement of cohesionless slopes: geotechnical centrifuge modelling. *Young Geotechnical Engineering Symposium,YGES2012*. University of Leeds, England, UK.

Al-Defae, A.H. and Knappett, J.A. (2014). Stiffness matching of model reinforced concrete for centrifuge modelling of soil-structure interaction. *8th International Conference of Physical Modelling in Geotechnics, 8ICPMG,* (*accepted*).

Anastasopoulos, I., Gazetas, G., Bransby, M., Davies, M. & El Nahas, A. (2007). Fault rupture propagation through sand: finite element analysis and validation through centrifuge experiments. *Journal of. Geotech. Geoenviron. Engng.* 133(8): 943–958.

Abdoun, T., Dobry, R., O'Rourke, T. and Goh, S.H. (2003). Pile response to lateral spreads: Centrifuge modelling. *Journal of Geotechnical and Geoenvironmental Engineering, ASCE,* 129(10): 869-878.

Adachi T., Kimura M., Tada S., (1989). Analysis on the preventive mechanism of landslide stabilizing piles, *Proceeding of the 3rd International Symposium on Numerical Models in Geomechanics (NUMOG III),* Niagara Falls: 691–698.

Ambraseys, N. & Srbulov, M. (1995). Earthquake induced displacements of slopes. *Journal of soil Dynamic and Earthquake Engineering*, 14(1): 59-71.

American Petroleum Institute (API) (2002). Recommended practice for planning, designing, and constructing fixed offshore platforms. *API Recommended Practice 2A* (RP-2A-WSD), 21 Edition.

Ashford, S.A., Sitar, N., Lysmer, J. and Deng, N. (1997). Topographical effects on the seismic response of steep slopes. *Bulletin Seismology Society*. AM87, No.3:701-709.

ASTM3080-72 Standard. (2000). Test method for direct shear test of soil. American Society of Testing and Material.

Ausilio, E., Conte, E. & Dente, G. (2001). Stability analysis of slopes reinforced with piles. *Journal of Computers and Structures*, 28(8): 591-611.

Banerjee, P.K. & Davies, T.G. (1978). The behaviour of the axially and laterally loaded single piles embedded in non-homogeneous soils. *Géotechnique*, 28(3): 309-326.

Barton, Y.O. (1982). Laterally loaded piles in sand: Centrifuge tests and finite element analysis. *Ph.D Thesis*, University of Cambridge, UK.

Bazant, Z.P. & Yu, Q. (2005). Designing against size effects on shear strength of reinforced concrete beams without stirrups: II. Verification and Calibration. *Journal of Structural Engineering*, 131(12): 1886-1897.

Bellezza, I. & Pasqualini, E. (2005). Parametric study of the stability of the slope reinforced with piles. *Proceeding of the 16th International Conference on Soil Mechanics and Geotechnical Engineering*, Balkema, Rotterdam Vol.3: 1319-1322.

Bertalot, D. (2013). *Behaviour of shallow foundations on layered soil deposits containing loose saturated sands during earthquakes*. *PhD Thesis*, University of Dundee, UK

Bertalot, D., Brennan, A.J., Knappett, J.A., Muir Wood, D. and Villalobos, F.A. (2012). Use of centrifuge modelling to improve lessons learned from earthquake case histories. *Proc. 2nd European conference on Physical Modelling in Geotechnics, Eurofuge 2012*, 23-24 April, Delft, the Netherlands.

Bertalot, D. and Brennan, A.J. (2012). Influence of bearing pressure on liquefaction-induced settlement of shallow foundations. *Géotechnique* (In press).

Bolton, M.D. (1986). The strength and dilatancy of sands. *Géotechnique*, 36(1): 65-78.

Bouckovalas G., D., and Papadimitriou B., A. (2005). Numerical evaluation of slope topography effects on seismic ground motion. *Journal of Soil Dynamic and Earthquake Engineering*. 25(5):547-558).

Bosscher J., Gray D., 1986. Soil arching in sandy slopes, *Journal of Geotechnical & Geoenvironmental Engineering*, ASCE. 112(6):

Boulanger, R.W., Curras, C.J., Kutter, B.L., Wilson, D.W. and Abghari, A. (1999). Seismic soil-pile-structure interaction experiments and analysis. *Journal of Geotechnical and Geoenvironmental Engineering*, ASCE, 125(9): 750-759.

Bransbay, M.F. (1996). Difference between load-transfer relationships and laterally loaded pile groups: Active p-y or Passive p-y. *Journal of Geotechnical Engineering*, 122(12):1015-1027.

Bransby, M.F. (1999). Selection of *p-y* curves for the design of single laterally loaded piles. *International Journal for Numerical and Analytical Methods in Geomechanics*, 23(15):1909-1926.

Bransby, M.F., Brown, M.J., Knappett, J.A., Hudacsek, P., Morgan, N., Cathie, D., Maconochie, A., Yun, G., Ripley, A.G., Brown, N. and Egborge, R. (2011). Vertical capacity of grillage foundations in sand. *Canadian Geotechnical Journal*, 48(8): 1246-1265.

Bransby, M.F. & Springman, S. (1999). Selection of load-transfer functions for passive lateral loading of pile groups. *Journal of Computers and Geotechnics*, 24(3): 155-184.

Bray, J.D. and Rathje, E.M. (1998). Erathqake-induced displacements of solid-waste landfills. *Journal of Geotechnical and Geoenvironmental Engineering Division*, ASCE. 124(3): 242-245.

Brennan A.J., and Madabhushi, S.P.G. (2009). Amplification of seismic accelerations at slope crests. Canadian Geotechnical Journal. 45(5): 585-594.

Brennan, A.J., Thusyanthan, N.I. and Madabhushi, S.P.G., (2005). Evaluation of shear modulus and damping in dynamic centrifuge tests. *Journal of Geotechnical and Geoenviornmetnal Engineering, ASCE.* 131(12): 1488-1497.

Brinkgreve, R.B.J., Engin, E. and Engin, H.K. (2010). Validation of empirical formulas to derive model parameters for sands. In: T. Benz and S. Nordal (Eds.) Numerical methods in geotechnical engineering, CRC press/Balkema.

Broms, B.B. (1964). Lateral resistance of piles of cohesionless of soils. *Journal of Soil Mechanics and Foundation Engoneering Devision, ASCE*, 90(3): 123-158.

BSI (1990). BS1377, Part 4 – Maximum and minimum dry density for granular soil. British Standards Institution, UK.

BSI (2005a). Eurocode 8: Design of structures for earthquake resistance – Part 1: General rules, seismic actions and rules for buildings, EN 1998-1:2004. British Standards Institution, UK.

BSI (2005b). Eurocode 8: Design of structures for earthquake resistance – Part 5: Foundations, retaining structures and geotechnical aspects, EN 1998-5:2004. British Standards Institution, UK.

Cai, F. and Ugai, K. (2000). Numerical analysis of the stability of a slope reinforced with piles. *Journal of Soil and Foundations*, Japanese Geotechnical Society. 40(1): 73-84.

Cai, F. and Ugai, K. (2003). Response of flexible piles under laterally linear movement of the sliding layer in landslides. *Canadian Geotechnical Journal*, 40(1): 46-53.

Carder, D. (2009). Improving the stability of slope using a spaced pilling technique. TRL Report, *Transportation Research Laboratories*, UK.

Carder, D.R. & Barker, K.J. (2005). The performance of a single row of spaced bored piles to stabilise a London clay on the A12. *Transport research laboratory*. TRL642.

Carter, D.P., (1984). A non-linear soil model for predicting lateral pile response. Report. Civil Engineering Dept., Univ. of Auckland, New Zealand. No.359.

Chandrasekaran, V. S. (2003). Centrifuge modelling in earthquake geotechnical engineering. *CPFTEGE report*.

Chang, C.J., Chen, W.F. & Yao, J.T.P. (1984). Seismic displacements in slopes by limit analysis. *Journal of Geotechnical Engineering, ASCE*, 110(7): 860-874.

Chen C.Y., Martin G., (2002). Soil-Structure interaction for landslide stabilizing piles. *Journal of Computers and Geotechnics*, 29(5):363-386.

Chen L.T., Poulos H.G., 1997. Piles subjected to lateral soil movements. Journal of Geotechnical and Geoenvironmental Engineering, ASCE. 123(9): 802-811.

Chen, X. L., Kato, N., Tsunaki, R., and Mukai, K. (2009). Prediction of slope failure due to earthquake, *Chinese Science Bulletin*, Institute of Geology, Chinese earthquake administrations, Beijing, China.

Chlimintzas, G.O. (2003). Seismic displacements of slopes using multi-block sliding technique. *Ph.D Thesis*, Civil Engineering Dept., Soil Mechanics and Engineering Seismology, Imperial College London (University of London). UK.

Chow, Y.K. (1996). Analysis of piles for slope stabilisation. *International Journal of Numerical and Analytical Methods in Geo-mechanics*, 20(9): 635-646.

Craig, R.F. and Knappett, J. A. (2012). Craig's soil mechanics, *Spon Press, Taylor & Francis Group*, London and New York.

Cox, W. R., Reese, L. C., and Grubbs, B. R. (1974). Field testing of laterally loaded piles in sand." Proceeding of the sixth Offshore Technology conference, Paper 2079, Houston, Texas: 459-472.

Davis, L.L. and West, L.R. (1973). Observed effects of topography on ground motion, *Bulletin of the Seismological Society of America*, 63(1): 283-298.

Davies, M.C.R. (1981). Centrifuge modelling of embankments on clay foundations. *Ph. D Thesis*, University of Cambridge, London, UK.

David,M. Wood (2004). Geotechnical modelling. *Taylor and Francis Group*, Oxford, London, UK.

De Beer E., Carpentier R., 1977. Methods to estimate lateral force acting on stabilizing piles. *Journal of Soils and Foundations, Discussion*. 17(1):

Decourt, L. (1991). Load- deflection prediction for laterally loaded piles based on N-SPT values. *4th International proceeding for piling and deep foundation*, Balkima, Rotterdam. Vol 2: 549-555.

Ding, T. (2006). Seismic slope safety- determination of critical slip surface using acceptability criteria. *Ph.D Thesis*, Department of Civil and Environmental Engineering, Imperial College, University of London, London, UK.

Donovan, N.C. (1969). Research Brief, sol dynamic speciality section. *7th International Conference on Soil Dynamics and Foundation Engineering*, Mexico City.

Drnevich, V. P., Hall, J. R. and Richart, F. E. (1966). Large amplitude vibration effects on the shear modulus of sands. *Repot for Waterways Experiment Station, Corps of Engineering, U.S. Armay Contract* DA-22-079-Eng-340, University of Michigan.

Duncan, J. M. & Wright, S. G. (2005). Soil strength and slope stability. *John Wiley & Sons, Inc.*, Hoboken, USA.

University of Dundee, (2002). Dundee centrifuge manual. Dundee. UK.

Ellis, E. A., Durrani, I.K. & Reddish, D.J. (2010). Numerical modelling of discrete pile rows for slope stability and generic guidance of design. *Géotechnique*, 60(30): 185-195.

Erdem, S. (2012): Impact load-induced microstructure damage of concrete made with unconventional aggregates. *Ph.D. Thesis. University of Nottingham*. UK

Fleming, W.G. K., Weltman, A.J., Randolph, M.F. and Elson, W.K., (2009). Piling engineering. *3rd Edition*. Halsted Press, New York, NY100116, USA.

Gilhooly, Y.P. (2008). Modelling of reinforced concrete beams. *MSc. Thesis*. Civil Engineering Division, University of Dundee, UK.

Hardin, B.O. (1965). The nature of damping in sands. *Journal of Soil Mechanic and Foundation Engineering Division*, ASCE, 91(SMI):63-67.

Hardin, B.O. and Black, W.L. (1968). Vibration modulus of normally consolidated clay. *Proceeding of Soil Mechanics and Foundation Engineering Division*, ASCE. 94(SM2):353-369.

Hardin, B.O. and Drnevich, V.P. (1972). Shear modulus and damping in soils: Design Equation and Curves. *Journal of Soil Mechanics and Foundation Engineering Division, ASCE*. 98(SM7):667-692.

Hassiotis, S., Chameau, J.L. & Guanaratne, M. (1997). Design method for stabilisation of slope with piles. *Journal of Geotechnical and Geoenviornmental Engineering*, ASCE. 123(4): 314-323.

Havenith, H.B., Vanini, M., Jongmans, D., & Faccioli, E., (2003). Initiation of earthquake-induced slope failure: Influence of topographical and other site specific amplification effects. *Journal of Seismology*. 7(3): 397-412.

Hayashi, H., Nishikawa, J. & Taniguchi, K. (1998). Sesmic behaviour of road embankements. *Proceeding of the Centrifuge 98.* Balkima, Tokyo, Japan. Vol. 1: 243-248.

Hayward, T., Lees, A., Powrie, W. & Smethurst. (2000). Centrifuge modelling of a cutting slope stabilised by discrete piles. *TRL471 report, Transport Research Laboratory*, Berkshire, UK.

Higgins, T. (2007). Small scale modelling of reinforced concrete beams. *MSc. Thesis*, Civil Engineering Devision, University of Dundee, UK.

Hynes-Griffin, MM. E. & Franklin, A.G. (1984). Rationalising the seismic coefficient method. *Final Report, Miscellaneous Paper GL-84-13. Army Engineer Waterways Experiment Station, Vicksburg, MS. Geotechnical Lab.*

Idriss, I.M. 1999. An update to the Seed-Idriss simplified procedure for evaluating liquefaction potential. *In Proceedings, TRB Workshop on New Approaches to Liquefaction*, FHWA-RD-99- 165, FHWA, Washington, D.C.

Ishibashi, I. and Zhang, X., (1993). Unified dynamic shear moduli and damping ratios of sand and clay. *Journal of Soils and Foundations*. Japanese society. 33(1):182-191.

Ito, A.T. & Matsui, T. (1975). Method of estimate lateral forces acting on stabilising piles. *Japanese Society of Soil Mechanics and Foundation Engineering*, 15(4): 43-59.

Ito, A.T., Matsui, T. & Hong, W.P. (1981). Design method for stabilising piles against landslide: One row of piles. *Japanese Society of Soil Mechanics and Foundation Engineering*, 21(1): 21-37.

Ito, T., Matsui, T. and Hong, W.P. (1982). Extended design method for multi-row stabilising piles against landslides. *Journal of Soil and Foundation*, 22(1): 1-13.

Iwasaki, T., Tatsuoka, F. and Takagi, Y. (1976). Dynamic shear deformation properties of sand for wide strain range. *Report of Civil Engineering Institute*, CEI, No.1085, Ministry of Construction, Tokyo, Japan.

Jibson, R.W. (1993). Predicting earthquake-induced landslide displacements using Newmark's sliding block analysis. *Transportation Research Record*, **1411**: 9-17.

Jibson, W.W. and Corne, A. J. (2001). Observations and recommendations regarding landslides hazards related to the January 13, 2001 M-7.6 EI-Salvador earthquake. *USGS Report*, 01-171.

Kavazanjian, E.Jr, M.N., Hadj-Hamou, T. & Sabatini, P.J. (1997). Design guidance: Geotechnical Earthquake Engineering for Highways. Vol. 1, Design Principles. *US Department of Transportation*, Washington, USA.

Keefer, D. K. (1984). Landslides caused by earthquakes. Journal of Geological society of America, Bulltin, 95(4): 406-421.

Khazai, B. and Sitar, N. (2004). Evaluation of factors controlling earthquake-induced landslides caused by the Chi-Chi earthquake and comparsion with the Northridge and Loma Prieta events. *Journal of Engineering Geology,* **71**(1-2)**:** 79-95.

Khoo, E. Okumura, T. and Lee, F.H. (1994). Side friction effects in plain strain models. *Centrifuge 94*, Leung et al., (EDS), Balkima, Rotterdam.

Kim, J. and Sitar, N. (2004). Direct estimation of yield acceleration in slope stability analyses. *Journal of Geotechnical and Geoenviromental Engineering,* **130**(1): 111-115.

Kinmond, S. (2009). Small scale modelling of reinforced concrete slabs. Msc. Thesis, Civil Engineering Devision, University of Dundee, UK.

Kishida, H. and Takano, A. (1970). The damping in the dry sand. *Proceeding of the 3rd Japan Earthquake Engineering Symposium*. Tokyo, Japan.

Knappett, J.A. (2010). Centrifuge modelling considerations. *Lecture Notes.*

Knappett, J.A. and Craig, R.F. (2012). Craig's Soil Mechnics, 8th Edition. Taylor and Francis/Routledge, UK.

Knappett, J. A., Reid, C., Kinmond, S. & O'Rielly, K. (2011). Small- scale modeling of reinforced concrete structural elements for use in geotechnical centrifuge. *Journal of Structural Engineering,* ASCE. 137(11): 1263-1271.

Kobayashi, Y. (1981).Causes of fatalities in recent earthquakes in Japan. *Journal of natural disaster science.* 3(2): 15-22.

Kong, F. K. & Evans, R. H. (1987). Reinforced and pre-stressed. *3rd. edition , Ean Spon,* London, UK.

Kourkoulis, R., Gelagoti, E., Anastasopoulos, I. and Gazetas, G. (2011). Stabilisation of seismically unstable slopes using piles: Parametric Analysis. *5th International Conference on Earthquake Geotechnical Engineering*, Santiago, Chile, Vol.1.

Kok, S.T. and Bujang, B.K.H. (2008). Numerical modelling of laterally loaded piles. *American Journal of Applied Sciences*, 5(10): 1403-1408.

Kramer, S.L. (1996). Geotechnical earthquake engineering. *Prentice Hall, Upper Saddle River*, New Jersey, USA.

Kramer, S.L. (2008). Performance-Based Earthquake Engineering: Opportunities and Implications for Geotechnical Engineering Practice. Keynote Paper, *Fourth Conference on Geotechnical Earthquake Engineering and Soil Dynamics*, ASCE, Sacramento. Vol. (5):1-32.

Kuhlemeyer, R.L. (1979). Static and dynamic laterally loaded floating piles. *Journal of Geotechnical Engineering Division, ASCE,* 105(2): 289-304.

Kutter, B. (1994). Recent advance in centrifuge modelling of seismic shaking. *Proceeding of the International Conference on Recent Advance in Geotechnical Earthquake Engineering and soil Dynamic*, St. Louis, Missouri. Vol. 2: 927-942.

Lauder, K. (2011). The Performance of Pipeline Ploughs. *Ph.D. Thesis*, University of Dundee, UK.

Lee, C.Y., Hull, T.S., & Poulos, H.G. (1995). Simplified pile-slope stability analysis. *Journal of Computers and Geotechnics*. 17(1):1-16.

Lee, E.M. & Jones, D.K.C. (2004). Landslide risk assessment, *Thomas Telford LTD*, London, UK.

Leroueil, S., Locat, J., Vaunat, J., Picarelli, L. &Faure, R. (1996). Geotechnical characterisation of slope movements. *Proceeding of the 7th International Symposium on Landslides*. Trondheim, Norway, Balkima. Vol. 1.

Liang, L.F., (1988). Back analysis of lateral load tests on piles. *Report.* Civil engineering Dept., Univ. of Auckland, New Zealand. No. 460.

Liang, R.Y. (2002). Drilled shaft foundations of noise battier walls and slope stabilisation. Ohio Departement of Transportation and the U.S. Department of Transportation, Federal Highway Administration and The University of Akron,Akron, Ohio 44325-3905.

Liang R, Sanping, Z., 2002. Numerical study of soil arching mechanism in drilled shafts for slope stabilization. *Journal of Soils and Foundations*. Japanese Society **42**(2):83-92.

Lighthall, P. (1979). Dimensionless charts for critical acceleration and static stability of earth slopes. *M.Sc. thesis*, Civil Engineering, Soil Mechanics and Seismology Section, Imperial College, London, UK.

Litle, W. A. & Paparoni, M. (1996). Size effect in small-scale models of reinforced concrete beams. *Journal of American Concrete Institute*, ACI. 63(11): 1191-1204.

Lo Presti, D.C.F., Pallara, O., Fioravante, V. and Jamiolkowski, M. (1998). Assessment of quasi-linear models for sands. In R. Jardine, M. Davies, D. Hight, A. Smith and S.

Stallebrass (Eds.), Pre-failure deformation behaviour of geomaterials, *Thomas Telford*, UK: 363-372.

Loukidis, D., Bandini, P. and Salgado, R. (2003). Stability of seismically loaded slopes using limit analysis. *Géotechnique*, **53**(5): 463-479.

Madabhushi, S., Haigh, S. & Subdei, B. (2002). Seismic behaviour of steep slopes. *Proceeding of the International Conference of Physical Modelling in Geotechnics.* Balkima, Newfoundland, Canada. Vol.2: 489-494.

Madden, P. (2008). Slope stabilisation using Piles: mini-centrifuge modelling. *MSc. Thesis*. Civil Engineering Division, University of Dundee, UK.

Maghsoudi, A.A. & Sharifi, Y. (2009). Ductility of high strength concrete heavily steel reinforced members. Scientia Iranica, *Transaction A: Civil Engineering*, 16(4): 297-307.

Mahlhaus, H.B. and Vardoulakis, I. (1987). The thickness of shear bands in granular soils. *Géotechnique*, **37**(3): 271-283.

Makdisi, F.I. & Seed, H.B. (1978). Simplified procedure of estimating dam and embankment earthquake-induced deformations. *Journal of Geotechnical and Geoenviornmental Engineering Division*, ASCE, 104(7): 849-867.

Mansur, M.A. & Islam, M.S. (2001). Interpretation of concrete strength for nonstandard specimens. *Journal of Materials in Civil Engineering*, ASCE. 14(2): 151-155.

Martin, G.R. and Chen, C.Y. (2005). Response of piles due to lateral slope movement. *Journal of Computers and Structures*. 83(8-9): 588-598.

Massey, C. & Ian. (2010). The dynamics of reactivated landslides: Utiku and Taihape, North Island, New Zealand. *Ph.D Thesis, Faculty of Social sciences and Health-Geography dept*. Durham University, UK.

Matasovic, N., Kavazanjian, E. and YAN, L. (1997). Newmark deformation analysis with degrading yield acceleration. *Proceeding of Geosynthetics.* Vol. 2, Long Beach, California, USA, March 1997: 989-1000.

Matlock, H., (1970). Correlation for design of laterally loaded piles in soft clay. *Proceedings, Second Annual Offshore Technology Conference*, Houston, Texas, 1(Oct.1204): 577-594.

Matsushida, K., Kishida, H. and Kyo, K. (1967). Experiments on damping of sands. *Summarised of The Technical Report*, Transactions of the Architectural Institute of Japan.

McDonnel, P. (2008). Small-scale modelling of beam columns. *MSc. Thesis*, Civil Engineering Devision, University of Dundee, Dundee, UK.

Meen-Wah, G. and Hsien-Te, C. (2009). Seismic response of Renyitan earth-fill dam. Journal of Geotechnical Engineering, 4(2): 41-50.

MuirWood, D. (2002). Some observations of volumetric instabilities in soils. *International Journal of Soilds and Structures.* **39**(13-14): 3429-3449.

Murthy, V.N.S. (2003). Geotechnical engineering: principles and practices of soil mechanics and foundations engineering. Mrcel Dekker AG, Basel, Switzerland.

Newmark, N.M. (1965). Effect of earthquakes on dams and embankments. *Géotechnique,* 15(2): 139-159.

Ng Carles, W.W., Li, X.S. (2004). Centrifuge modelling of loose embankments subjected to uniaxial and bi-axial earthquakes. *Journal of Soil Dynamics and Earthquake Engineering*, 24(4): 305-318.

Oda, M. and Kazama, H. (1998). Microstructure of shear bands and its relation to the mechanism of dilatancy and failure of dense granular soils. *Géotechnique,* **48**(4): 465-482.

Okamoto, S. (1984). Introduction to earthquake engineering. University of Tokyo, 2nd Edition (P630).

O'Neill, M.W., and Murchison J.M. (1983). "An evaluation of p-y relationships in sand," *A Report to the American Petroleum Institute*, PRAC 82-41-1, The University of Houston-University Park, Houston, Texas.

Ovesen, N.K. (1979). The measurements, selection and use of design parameters in geotechnical engineering. *Proceeding of the 7th European Conference of Soil Mechanics and Foundation Engineering*, Brighton, England, Vol.4:319-323.

Pam, H.J., Kwan, A.K.H. & Islam, M. S. (2001). Flexural strength and ductility of reinforced normal-and high-strength concrete beam. *Proceeding of the Institution of Civil Engineers, Structures and Buildings*, ICE, 146(4): 381-389.

Pan, J.L., Goh, A.T.C., Wong, K.S. and The, C.I. (2002). Ultimate soil pressure for ples subjected to lateral soil movement. *Journal of Geotechnical and Geoenvironmental Engineering Division*, ASCE. 128(6): 530-535.

Paolucci, R., Faccioli, E. and Maggio, F., (1999). 3D response analysis of an instrumented hill at Matsuzaki, Japan, by a spectral method. *Journal of Seismology*. 3(2): 191-209.

Parise, M. & Jibson, R.W. (2000). A seismic landslides susceptibility rating of geologic units based on analysis of characteristics of landslides triggered by the 17 January, 1997 Northridge, California Earthquake, *Journal of Engineering Geology*, 58:251-270.

Park, R. (1988). Ductility evaluation from laboratory and analytical testing. *Proceeding of the 9th World Conference on Earthquake Engineering.* Tokyo, Japan, Vol. 3:605-616.

Perry, J. (1989). A survey of slope condition on motorway earthquake in England and Wales. *Transportation Research laboratory*, TRL, UK.

Poulos, H.G., (1971). Analysis of piles in soil undergoing lateral movement. *Journal of Soil Mechanics and Foundations,* ASCE. 99(SM5): 391-406.

Poulos, H.G., (1971). Behavior of laterally loaded piles: I- single piles. *Journal of Geotechnical and Geoenvironmental Engineering Division*, ASCE. 97(5): 711-731.

Poulos, H.G., (1973). Behavior of laterally loaded piles: II Pile group. *Journal of Soil Mechanics and Foundations,* ASCE. 97(SM5).

Poulos, H.G. (1995). Design and reinforcing piles to increase slope stability. *Canadian Geotechnical Journal,* 32(5): 808-818.

Poulos, H.G. & Davis, E. H. (1980). Pile foundation analysis and design. *John Wiley and Sons*, New York, USA.

Pradel D. (1998). Procedure to evaluate earthquake-induced settlements in dry sandy soils. *Journal of Geotechnical & Geoenvironmental Engineering*, ASCE, 124 (4): 364-368.

Prater, E.G. (1979). Yield acceleration and seismic stability of slopes. *Journal of Geotechnical Engineering Division,* ASCE, 105(5): 682-687.

Randolph, M.F. (1981). The response of flexible piles to lateral loading. *Geotechnique*, 31(2): 247-259.

Randolph, M.F. and Houlsby, G.T. (1984). The limit pressure on a circular pile loaded laterally in cohesive soil. *Geotechnique*. 34(4): 613-623.

Rathje, E.M. and Bray, J.D. (1999). An examination of simplified earthquake-induced displacement procedures for earth structures. *Canadian Geotechnical Journal,* **36**(1): 72–87.

Reese, L.C., Wang, S.T. & Fouse, J. L. (1992). Use of drilled shafts in stabilising a slope. *Proceeding of the Stability and Performance of Slopes and Embankments Conference*, Vol. 2: 1318-1338.

Reese, L.C., Cox, W.R., and Koop, F.D. (1974). Analysis of laterally loaded piles in sand. *Proceeding of the VI Annual Offshore Technology Conference*, Houston, Texas, USA, Vol.1: 473-485.

Rollins, K.M., Olsen, R.J., Egbert, J.J., Jensen, D.H., Olsen, K. G. & Garrett, B. H. (2006). Pile spacing effect on lateral pile group behaviour: Load testing. *Journal of Geotechnical and Geoenvironmental Engineering*, ASCE, 132(10): 1262-1271.

Rollins, K.M., Peterson, K.T. and Weaver, T.J. (1998). Lateral load behaviour of full-scale pile group in clay. *Journal of Geotechnical and Geoenvironmental Engineering, ASCE*, 124(6): 468-478.

Rowe, P.W. (1962). The stress-dilatancy relation for static equilibrium of an assembly of particles in contact. Proc. Royal Soc. A, 269:500-527.

Santos, J.A. and Correia, A.G. (2001). Reference threshold shear strain of soil – its application to obtain a unique strain-dependent shear modulus curve for soil. *Proc. 15th Int. Conf. Soil Mechanics and Geotechnical Engineering*, Istanbul, Turkey, Vol.1: 267-270.

Sarma, S.K. (1973). Stability analysis of embankments and slopes. *Géotechnique*, 23(3): 423-433.

Samra, S.K. (1979). Stability analysis of embankments and slopes. *Journal of Geotechnical Engineering*, ASCE, 105(12): 1511-1524.

Sarma, S.K. (1981). Seismic displacement analysis of earth dams. *Journal of Soil Mechanics and Foundation Engineering*, ASCE, 107(12): 1735-1739.

Satoh, H., Ohbo, N. and Yoshizako, K. (1998). Dynamic test on behaviour of pile during lateral ground flow. *Proceeding of the Centrifuge 98*, Rotterdam, Balkima, Vol.1: 337-382.

Schanz, T., Vermeer, P.A. and Bonnier, P.G. (1999). The hardening-soil model: Formulation and verification. In R.B.J. Brinkgreve, Beyond 2000 in computation geotechnics, Balkema, Rotterdam, 281-290.

Schofield, A. N. (1981). Dynamic and earthquake geotechnical centrifuge modelling. *Proceeding of the International Conference on Recent Advance in Geotechnical Earthquake Engineering and Soil Dynamic*, St.Louis, Vol.2:1081-1100.

Schofield, A.N. and Zeng, X. (1992). Design and performance of an equivalent shear beam (ESB) container for earthquake centrifuge modelling. *Technical Report* CUED/D-SOILS, TRL245. Cambridge University, UK.

Seed, H.B. (1979). Consideration in the earthquake resistant design of earth rock fill dams. *Géotechnique*, 29(3): 215-263.

Seed, H.B. and Idress, I. M. (1970). Soil moduli and damping factors for dynamic response analysis. *Report of Earthquake Engineering Research Centre*, EERC, No. EERC-70/10. University of California, Berkeley, USA.

Seed, H.B., and Idriss, I.M. 1971. Simplified procedure for evaluating soil liquefaction potential. *Journal of Soil Mechanic and Foundation Division*, ASCE, 97 (9): 1249–1273.

Silver, M.L. and Seed, H.B. (1969). The begavior of sands under seismic loading conditions. *Report of Earthquake Engineering and Research Centre*, EERC, No. EERC 69-16. University of California, Berkeley, USA.

Skempton, A.W. (1985). Residual strength of clays in landslides, folded strata and the laboratory. *Géotechnique,* 35(1): 3-18.

Smith, C.C**.** and Gilbert, M. (2007). Application of discontinuity layout optimization to plane plasticity problems. *Proc. Royal Soc A: Mathematical, Physical and Engineering Sciences*, 463 (2086), October: 2461-2484.

Soil Mechanic and Foundation Division. (1958). Glassory of terms and definitions in soil mechanic: *Report of the Committee on Glossary of Terms and Definitions in Soil Mechanics and Foundation Division*. 84(4): 1-43.

Sonnenberg, R. (2008). Centrifuge modelling of root reinforced slopes. *Ph.D thesis,* Civil Engineering Division, University of Dundee, Dundee, UK.

Spillers, W.R., and Stoll, R.D. (1964). Lateral response of piles. *Journal of Soil Mechanics and Foundation Division*, ASCE, 90(6): 1-9.

Stewart, D.I. (1989). Ground effect on in –situ wals in stiff clay. *Ph.D thesis*, Emmanuel College - Cambridge University, London, UK.

Taji, Y., Sato, M. and Yanagisawa, E. (1998). Modeling of prototype soil-pile structure system during seismic groun liquefaction. *Proceeding of the Centrifuge 98*, Rotterdam, Balkima, Vol.1: 283-288.

Tandjiria, V., The, C.I. and Low, B.K. (2000). Reliability analysis of laterally loaded piles using response surface. *Journal of Structural Safety*. 22(4): 335-355.

Taylor, R.N. (1994). Geotechnical centrifuge technology, *Blackie Academic*, London, UK.

Terzaghi, K. (1950). Mechanism of landslides. *Geological Society of America*, Engineering Geology (Berkey) volume: 83-123.

Terzaghi, K. (1955). Evaluation of coefficient of subgrade reaction. *Geotechnique*. 5(4): 297-326.

Vesic, A.S. (1961). Beam on elastic subgrade and the Winkler hypothesis. *Proceeding of 5th International Conference of Soil Mechanic and Foundation Engineering.* Paris, Vol. 1: 845-850.

Viggiani, C. (1981). Ultimate lateral load on piles used to stabilise landslides. *Proceeding of the 10th International Conference on Soil Mechnaics and Foundations Engineering*, Stocholm, Vol. 3: 555-560.

Wang, W.L., and Yen B.C. (1974). Soil arching in slopes. *Journal of Geotechnical and Geoenvironmental Engineering,* ASCE. 100 (GT1). 61-78.

Wartman, J., Bray, J. and Seed, R. (2003). Inclined plane studies of the Newmark sliding block procedure. *Journal of Geotechnical and Geoenvironmental Engineering*, **129**(8): 673–684.

Wartman, J., Seed, R. and Bray, J. (2005). Shaking table modeling of seismically induced deformations in slopes. *Journal of Geotechnical and Geoenvironmental Engineering*, **131**(5): 610–622.

Wassel Al-Bodour (2010). Development of design and analysis method for slope stabilisation using drilled shaft. *Ph.D Thesis*. University of Akron,USA.

Wei, W.B. & Cheng, Y.M. (2009). Strength reduction analysis of slope reinforced with one row of piles. *Journal of Computers and Structures*, 36(7):117-1185.

Weissman, G.F. and Hart, R.R. (1961). The damping capacity of some granular soils. *Symposium Proceeding of Soil Dynamic*, ASTM, Special Technical Publication No. 305:46-54.

Wilson, R.C. & Keefer, D.K. (1983), Dynamic analysis of slope failure from the 6 Augest 1979 Coyote Lake, California earthquake. *Bulletin of the Seismological Society of America*. 73(3): 863-877.

Wilson, R.C. & Keefer, D.K. (1985). Predicting areal limits of earthquake-induced landsliding in evaluating earthquake hazard in the Los Angeles region. *U.S. Geological Survey Professional Paper* 1360: 317-345.

Won, J., You, K., Jeong, S. & Kim, S. (2005). Coupled effects in stability analysis of pile-slope system. *Journal of Computers and Structures*, 32(4): 304-315.

Yin, Y., Wang, F. & Sun, P. (2009). Landslides hazards triggered by the 2008 Wenchuan earthquake, Sichwan, China. *Bulletin of Landslides*, 6(2): 139-152.

Yu, Y., Deng, L., Sun, X. & He, L. (2008). Centrifuge modelling of dry sandy slope response to earthquake loading. Bulletin of Earthquake Engineering, 6(3): 447-461.

Yu, Y.Z., Deng, L.J., Sun, X. and Lu, H. (2010). Centrifuge modelling of dynamic behaviour of pile-reinforced slopes during earthquakes. *Journal of Central South University of Technology*, 17(5): 1070-1078.

Zeng, X. & Schofield, A. N. (1996). Design and performance of an equivalent-shear-beam container for earthquake centrifuge modelling. *Géotechnique*, 46(1): 83-102.

Zolfagari, A.R., Heath, A.C. and Mccombie, P.F. (2005). Simple genetic algorithm search for critical non-linear failure surface in slope stability analysis. *Journal of Computer and Geotechnics*. 32(3):139-151.